Universitat Autònoma de Barcelona
Departament de Física
Tesi doctoral en Física
Curs Acadèmic 2014-2015

Limits to the Violation of Lorentz Invariance using the Emission of the Crab Pulsar at TeV Energies Discovered with Archival Data from the MAGIC Telescopes

Candidat
Daniel Garrido Terrats

Director
Dr. Lluís Font Guiteras

Co-director
Dr. Markus Gaug

Limits to the violation of Lorentz invariance using the emission of the Crab pulsar at TeV energies discovered with archival data from the MAGIC telescopes

Daniel Garrido Terrats

April 22, 2015

I hereby declare

that I am the only author of this thesis,

that the data presented in this thesis are property of the MAGIC collaboration if not otherwise stated,

that I authorize the Universitat Autònoma de Barcelona to lend this thesis to other institutions or individuals for the purpose of scholarly research.

Daniel Garrido Terrats

Contents

Introduction

The unification of gravity with the rest of the fundamental forces of Nature is a problem that has puzzled scientists since the beginning of the 20th century. Albert Einstein himself devoted the last years of his career trying to answer the following question: is there a single physical theory that can account for all forces we observe, including gravity?

The most complex part of this problem probably is the incompatibility of the quantum theory, that governs the smallest scales, with gravitation, that rules the largest scales. A unified theory should be able to account for both scales at once, and at the same time solve the mysteries that lie beyond the limits of current General Relativity theory and Quantum Field theory, namely the behavior of spacetime at the singularities inside black holes and at the moment of the Big Bang. The quest for such a Quantum Gravity theory is the holy grail of physics for the 21st century, although some attempts such as loop quantum gravity or string theory have have succeeded to solve some of its multiple problems.

From an experimental point of view, physicists try to look for tests and experiments that can shed some light into the problem. One of such proofs consist in testing the limits of validity of a special relativity principle known as Lorentz invariance. Many experimental setup have been used to check this symmetry of Nature and one of these states that, if this principle is not met in some extreme scenarios, one of the expected manifestations would be the measurement of a dependency of the speed of light with the energy of the photons. Astronomical sources could provide for such a proof: if some delay is measured between photons with different energies that were simultaneously emitted by a far away object, that would be the first clear signal of a quantum gravity effect, given that any other reason for such a delay could be discarded. Even if no delay is measured, important constraints can be set with such lack

of observation, which will limit the parameter space where Quantum Gravity theory candidates should develop.

This thesis try to attack that problem following this approach, and the source we used to such limit photon delays is the Crab pulsar. This object is a highly-magnetized, fast-spinning neutron star that lies at the center of the Crab nebula, the remaining of a supernova explosion that was observed in the 13th century. Its emission is not continuous but in the form of two short, consecutive flashes that repeat about 30 times every second with great precision, which are perfectly synchronization in every energy band of the electromagnetic spectrum where this source has been detected, from radio to very-high-energy gamma-rays. Thanks to this extremely accurate changes in its flux, the Crab pulsar is one of the best candidates to limit the variations of the speed of light, even though it is in our galactic neighborhood.

The Crab pulsar was detected by the ground-based MAGIC and VERITAS telescopes up to energies of 400 giga-electronVolts. However, our ability to limit any breaking of the Lorentz symmetry is tightly related to the highest energy band in which we are able to detect it, so a major effort has been done to extend its spectrum up to the highest possible energies. To achieve this goal, an analysis of the largest dataset of Crab pulsar observations by the MAGIC telescopes was performed, which expanded across seven years and containing more than 300 hours of good quality data. This titanic effort was done by part of the MAGIC collaboration, and the part of its development and results that was performed by the author of this thesis are reported here, together with the results of the global analysis.

Once the definitive set of photons from the Crab nebula, together with the inner pulsar, was obtained, the testing of the Lorentz invariance violation was executed. The expected effect of this symmetry breaking is the change of the time of arrival of the Crab pulses for different photon energies. Therefore, we compared the arrival times of the one of the two pulses (the one reaching higher energies), both in the low- and in the very-high-energy gamma-ray bands. This violation of the fundamental physical principle was also limited using a more sophisticated approach, the so-called *maximimum likelihood method*: the energy scale for such violation was found such that the statistical likelihood of those events to be described by a certain pulsar model, was maximized, where the expected photon delay was taken into account by this model. The reported

limits are very close to the order of magnitude of the current best limits to a quadratic energy dependence for such delay. Besides, this is the first time this method is applied to a periodic astrophysical source, which is completely background-dominated by the photons of the surrounding nebula.

The outline of this thesis has been structured according to the following chapters:

Chapter 1 gives an introduction to the field of gamma-ray astronomy, where the basic principles of gamma-ray production, extinction and detection are described and the most prominent gamma-ray emitters in the Universe are briefly explained.

Chapter 2 describes the cosmic rays and their interaction with the Earth atmosphere, which forms the basement technique for their indirect detection from the ground, as well as for gamma-ray photons. The imaging atmospheric Cherenkov technique is explained, together with a description of the telescopes used to the observations that are presented later, the two Florian Göbel MAGIC telescopes. The general analysis process of the data taken by this instrument is detailed.

Chapter 3 explains the basic principles of the physics of pulsars and describes the specific characteristics of the Crab pulsar, together with the current theories that explain its emission but focusing in the highest energies.

Chapter 4 gives all the information regarding the analysis of the Crab pulsar data taken by the MAGIC telescopes during a two year period when only one telescope was operative. The results obtained from the analysis of the archival mono MAGIC data are detailed, as well as those obtained from the global Crab pulsar analysis (not reported in this thesis). We also discuss these results and its consequences on the current gamma-ray emission models of the Crab pulsar are explained.

Chapter 5 provides a theoretic context to the current theories to be a Quantum Gravity candidate. The the phenomenology related to the Lorentz invariance violation is described, together with a list of the previous limits that have been set to the space of parameters where such effect could be found. We highlight the limits obtained from astrophysical sources by other gamma-ray facilities around the world.

Chapter 6 explains how limits to the violation of the Lorentz invariance were derived from the very-high-energy emission of the Crab pulsarr. The implementation and characterization of the maximum likelihood method for LIV tests is described, together with the two sets of limits to the Lorentz invariance that were obtained. We discuss these results in the context of the previous limits set by other experiments using the Crab pulsar and also other sources.

Chapter 7 contains a summary of the obtained results on both of the topics of this thesis, i.e. the discovery of unprecedentedly high energy emission from the Crab pulsar and the limits to the violation of Lorentz invariance derived from it.

Chapter 1

Gamma-ray astronomy

The electromagnetic radiation spectrum expands for more than 28 orders of magnitude in frequency (ν) or in wavelength (λ), from the extremely low frequency radio signals with frequencies of just a few Hertz ($\nu \approx 10^0$ Hz or $\lambda \approx 10^8$ m) up to the most energetic gamma rays (from now on γ-rays) with frequencies even as high as of $\nu \approx 10^{28}$ Hz or $\lambda \approx 10^{-20}$ m. A photon is considered a γ-ray if it has frequency higher than $\sim 10^{19}$ Hz or, equivalently, an energy higher than 10^2 keV ([1]).

The idea of doing astronomy using γ-rays was born at the beginning of the 20th century but it took several decades until it proved successful. Now we know that the sky contains many interesting sources in this band of the electromagnetic (EM) spectrum and several techniques have been developed to explore it. In this first chapter we will describe the basic principles that rule γ-ray production and absorption, as well as the main types of astronomical sources that produce the γ-rays that scientists are able to observe.

But, before that, a comment about the usual conventions in this new field of science is required. For instance, in γ-ray astronomy, as well as in X-rays, we use to refer to the energy of the incoming photon instead of characterizing it by its wavelength or its frequency, like astronomers in other energy bands do. Energies are expressed as multiples of the electron-Volt, eV, a choice of units that is shared with those branches of astronomy that are in close relation with

[1] One electron-Volt (eV) is the energy an electron gains when traveling through a region where there is a 1 V difference in the electric potential. Thus, 1 eV $\approx 1,602176 \cdot 10^{-19}$ J

this discipline: it is common to use units of keV $= 10^3$ eV and MeV $= 10^6$ eV in X-ray astronomy, GeV $= 10^9$ eV and TeV $= 10^{12}$ eV for γ-ray telescopes and PeV $= 10^{15}$ eV or even EeV $= 10^{18}$ eV for cosmic-ray detectors. Within the γ-ray regime itself, astronomers also distinguish three sub-regions of the spectrum, a convention that we will often use throughout this thesis: high energy γ-rays (HE), from 0.1 MeV up to ~ 10 GeV; very high energy γ-rays (VHE), with energies between 10 GeV and 10 TeV and UHE γ-rays, whose energies lie above 10 TeV.

1.1 Gamma-ray production and absorption mechanisms

In order to understand the physical processes that govern γ-ray sources, we must first explain the basic principles of every physical mechanism that is able to produce γ-rays, as well as those processes that can absorb them. A brief description of those mechanisms will be given in this section but a more detailed description can be found in [1, 2]. These interaction processes are, namely:

- Electron-positron annihilation
- Bremsstrahlung radiation
- Synchrotron radiation
- Curvature radiation
- Direct and inverse Compton scattering
- Synchrotron-self-Compton
- Neutral pion decay
- Pair production

1.1.1 Electron-positron annihilation

This process occurs anytime an e^- collides with its antiparticle and vice versa:

$$e^- + e^+ \longrightarrow \gamma + \gamma \tag{1.1.1}$$

Two γ-rays are therefore produced, whose energy is 0.51 MeV each if measured in the center of masses reference system (hereafter, RS). A boost transformation has to be applied, multiplying by a Lorentz factor $\gamma = (1 - \beta^2)^{-1/2}$

(where $\beta = v/c$ is the particle speed in units of the speed of light c), in order to estimate the energy of those γ-rays when we observe this interaction from a different RS, like the laboratory frame, i.e. when the target particle is at rest.

1.1.2 Bremsstrahlung radiation

This german word for *braking radiation* describes those photons emitted by a charged particle when it gets deflected by an electric field, usually that of another charged particle. Although bremsstrahlung radiation is a general term, it usually refers to the radiation emitted by electrons that are slowing down when traveling through matter, due to the interaction with the electric field of the atomic nuclei. In the most common astrophysical scenarios, electrons are moving at relativistic speeds and they have a power law spectrum with spectral index $-\Gamma$. In this kind of situation, the emitted radiation also shows power law spectra but with a harder spectral index[2] of $-\Gamma + 1$.

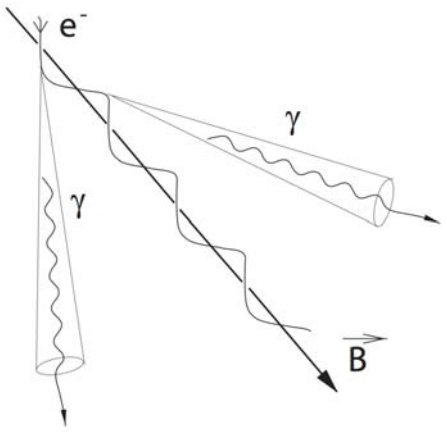

Figure 1.1: Schematic of the interaction between a charged particle and a magnetic field where synchrotron radiation is produced. The charged particle, an electron in our case, spirals around the magnetic field line $\vec{B}$ and emits photons up to γ-ray energies in a cone tangentially to its direction of motion.

1.1.3 Synchrotron radiation

When a relativistic, charged particle is moving in the presence of a magnetic field this kind of radiation is produced. However, if the particle is non-relativistic, the radiation emitted is known as *cyclotron* or *gyro* radiation. The charged

[2] In X- and γ-ray astronomy, a rather counterintuitive convention is used: the term *harder* refers to a less steep spectra, i.e. a spectral index closer to 0, since the resulting fraction of high energy particles is higher. On the contrary, when a spectra gets steeper, i.e. with a higher index in absolute value, is said to be *softer* since the fraction of particles with the highest energies gets smaller.

particle gets accelerated due to the Lorentz force in a centripetal fashion that makes it rotate around the magnetic field lines (see figure 1.1). Synchrotron radiation is emitted along the tangent of the circular motion and mainly within an angle $\theta \approx mc^2/E$ around the direction of movement at every instant, if m and E are the particle mass and energy respectively. If α is the angle between the magnetic field $\vec{B}$ and the speed of the particle $\vec{v}$, it will then move along an helicoidal path with radius

$$r = \gamma mc\ v \sin\left(\frac{\alpha}{eB}\right) \tag{1.1.2}$$

where γ is the Lorentz factor of the charged particle. The change in internal energy U per unit time or emitted power is given by

$$\frac{dU}{dt} = -\frac{3e^2}{2c^3}\gamma^4 \left(\frac{c^2}{r}\right)^2 \tag{1.1.3}$$

whereas a photon produced by synchrotron radiation has a characteristic energy of

$$E_c = \frac{3}{2}\gamma^3 \frac{\hbar}{r} \tag{1.1.4}$$

This is not the most common γ-ray creation mechanism since the energy of the emitted photons is much lower than the energy of the radiating particle. But in certain astrophysical scenarios γ-rays are produced through this process (see §1.2). When a population of charged particles whose energies are power-law distributed with spectral index $-a$, the spectrum of synchrotron radiation is also a power-law but its spectral index is $-(a+1)/2$ instead.

1.1.4 Curvature radiation

This form of radiation is similar to synchrotron radiation that was previously described: it is emitted by relativistic, charged particles in the presence of magnetic fields but only when they are forced to follow curved magnetic field lines. This situation occurs, for instance, when a charged, relativistic particle spiral around the magnetic field line emitting synchrotron radiation. This energy loss produces that the radius of its path shrinks until a ground state of minimal energy is reached. However, since it is centripetally accelerated to follow the field line curvature it will also emit curvature radiation at the same time.

The characteristic energy of a photon emitted by curvature radiation by a particle with a Lorentz factor γ that is moving along a path with curvature radius ρ is

$$E_c = \frac{3}{2}\gamma^3 \frac{\hbar c}{\rho} \tag{1.1.5}$$

whereas the emitted power is

$$\frac{dU}{dt} = -\frac{e^2}{6\pi\epsilon_0\ c^3}\gamma^4 \left(\frac{c^2}{\rho}\right)^2 \tag{1.1.6}$$

The energy distribution of its radiation is peaked at a frequency of $\nu_m = \frac{c\gamma^2}{2\pi\rho}$, and its flux can be described by the expression

$$F(\nu) \propto \begin{cases} \nu^{1/3} & \text{for } \nu < \nu_m \\ e^{-\nu} & \text{for } \nu < \nu_m \end{cases} \tag{1.1.7}$$

1.1.5 Direct and Inverse Compton scattering

Compton scattering occurs when a charged particle interacts elastically with a photon so, in the case of an electron

$$\gamma + e^- \longrightarrow \gamma + e^- \tag{1.1.8}$$

When the energy exchange is favorable to the charged particle (the particle gains energy while the photon energy is reduced) the process is called *direct* Compton scattering (hereafter, CS). The opposite case, when the photon is up-scattered by the charged particle, is called *inverse* Compton scattering (from now on ICS). If the energy of the particle is high enough it can scatter photons up to γ-ray energies.

In an ICS event with initial photon and electron energies E_γ and E, respectively, and using m as the electron mass, one has to distinguish between two regimes: the non-relativistic or *Thomson* regime, where $E_\gamma E \ll (mc^2)^2$, corresponds to the classical case whereas the ultra-relativistic or *Klein-Nishina* regime, where $E_\gamma E \gg (mc^2)^2$, takes into account quantum-kinematical effects. Besides, in some situations a single photon can undergo several ICS interaction processes, extracting a big fraction of the charged particle energy. For this to happen, the radiation and magnetic energy densities must be comparable [2].

1.1.6 Synchrotron-self-Compton

This kind of emission (from now on, SSC) is a combination of the previous two mechanisms, where the synchrotron emission by ultra-relativistic, charged particles is so efficient that an intense radiation field is created. These photons act as targets for ICS by the same charged particles that produced them in the first place, thus photons are able to reach even higher energies than in a simple synchrotron emission process. Due to interactions between several generation of particles, this process produces typical duplicated features in the source spectra.

1.1.7 Neutral pion decay

The hadronic production channel plays a crucial role in the production of γ-rays in astrophysical sources. The neutral pion π^0 has a rest mass of 135 MeV and a very short lifetime of $8.4 \cdot 10^{-17}$ s, much shorter that the charged π^+ and π^- ($2.6 \cdot 10^{-8}$ s). Thus, it quickly decays into two γ-rays

$$\pi^0 \longrightarrow \gamma + \gamma \tag{1.1.9}$$

with 99% probability but there is also a small chance (1% probability) that it produces an $e^- e^+$ pair instead

$$\pi^0 \longrightarrow e^- + e^+ + \gamma \tag{1.1.10}$$

Most hadronic interactions produce π^0 and in high energy interactions, neutral, positive and negative charged pions are produced in the same amount. Whilst charged pions eventually decay into muons or sometimes into electrons and their corresponding neutrinos, their longer lifetimes allows them to interact with other particles before doing so.

The most common interactions producing neutral pions are those of protons with other nuclei, X, like the ones from interstellar gas

$$p + X \longrightarrow \pi^0 + k \cdot \pi^{\pm} + Y \tag{1.1.11}$$

and those of protons with photons via photo-pion production

$$p + \gamma \longrightarrow \Delta^+ \longrightarrow p + \pi^0 \tag{1.1.12}$$

Each photon in equation 1.1.9 carries half of the particle energy and, for the case of relativistic pions, these photons are beamed in the same direction the primary particle was moving. Besides, a population of nuclei with a power-law energy distribution with spectral index $-\Gamma$ will produce via π^0 decay γ-ray emission with a softer spectral index of $-(\Gamma + 1)$.

1.1.8 Pair production

This physical process occurs when a high-energy photon decays into an $e^- e^+$ pair. Photons traveling through empty space do not undergo this process. Only those moving within a medium do so, usually in the vicinity of an atomic nucleus. The incident γ-ray actually interacts with a virtual photon, the one produced by the intense electric field of the charged, ambient particle. This reaction

$$\gamma + \gamma \longrightarrow e^- + e^+ \tag{1.1.13}$$

the inverse of the electron-positron annihilation process described in §1.1.1, can only occur when the energies of the two interacting photons, E_1 and E_2 fulfill the following condition

$$E_1 \cdot E_2 > \frac{1}{2}(m_e c^2)^2(1 - \cos\phi) \tag{1.1.14}$$

where ϕ is the collision angle between the two photons. After averaging over all possible collision angles, one can see that this reaction has a maximum for

$$E_1 \cdot E_2 \approx 3.7(m_e c^2)^2 \tag{1.1.15}$$

For γ-rays, we can model this process as an energy loss proportional to the incident photon energy,

$$dE_\gamma/dx = -E_\gamma/X_{\gamma,0} \tag{1.1.16}$$

where $X_{\gamma,0} \approx 47\text{g/cm}^2$ is the mean free path of a the photons on air. We should remember the following rule of thumb, which will be useful later in §2.2: in the atmosphere, this process is only triggered for photons with energies above a critical energy of $E_c \approx 20$ MeV.

1.2 Sources of gamma-rays in the Universe

Since the opening of this new EM window, γ-ray astronomy has evolved into a mature discipline in just a few decades. It allows us to look at the same sky our ancestors have been staring at for thousands of years but we can do it now with new eyes. What we see is shown for instance in figure 1.4 (at least for the low energy γ-rays observed by the LAT detector on-board of the Fermi satellite, details in §1.3.1). In this section we intend to describe the basic characteristics of some of the sources in this plot, which are the usual observation targets of γ-ray telescopes. We will start with extragalactic sources and we will finish with those ones locating in our galaxy. We will give a more extended description for the case of pulsars, since the analysis of the one at the center of the Crab nebula is a main topic of this thesis.

1.2.1 Active galactic nuclei

It is generally considered that every galaxy in the Universe has a high probability to contain a supermassive blackhole (SMBH) in its center, with masses between $10^2 M_\odot$ and $10^9 M_\odot$ or more. Around 1% of all galaxies show a very bright central region, much brighter than the emission produced by the rest of the stars in the galaxy combined, so they are called active galaxies or **active galactic nuclei** (hereafter, AGNs). They are the brightest steady sources in the Universe but their related phenomenology is so varied that there is no set of common observational properties for all AGNs: some have a continuous spectrum, others show narrow emission lines or variable spectral features; some AGNs experience sudden increases of their luminosity in time scales of the order of days, others are completely stable.

All these properties have led to a complex classification of AGNs, producing an extensive "zoology" formed by quasars, quasi-stellar objects, blazars, Seyfert galaxies, low-ionization nuclear emission-line regions (LINERs), radio galaxies, BL Lacertae, optically violent variable quasars (OVV) and several other subtypes. Many models have been proposed that try to account for the emission of some of these families of astrophysical sources. But the most favored ones are those claiming that we are looking the same family of objects under different orientations with respect to our line of sight, allowing us to observe different parts of the AGN emission regions [5]. A general schematic view of the current AGN model is shown in figure 1.3. According to it, an AGN is usually composed

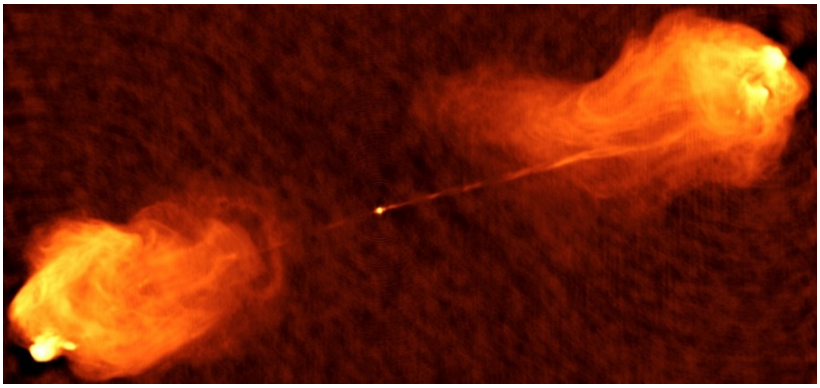

Figure 1.2: Radio image of the jets in the active galaxy Cygnus A taken with the VLA observatory. A complex filamentary structure within the giant lobes was discovered, as well as several hotspots. Image courtesy of NRAO/AUwe [3].

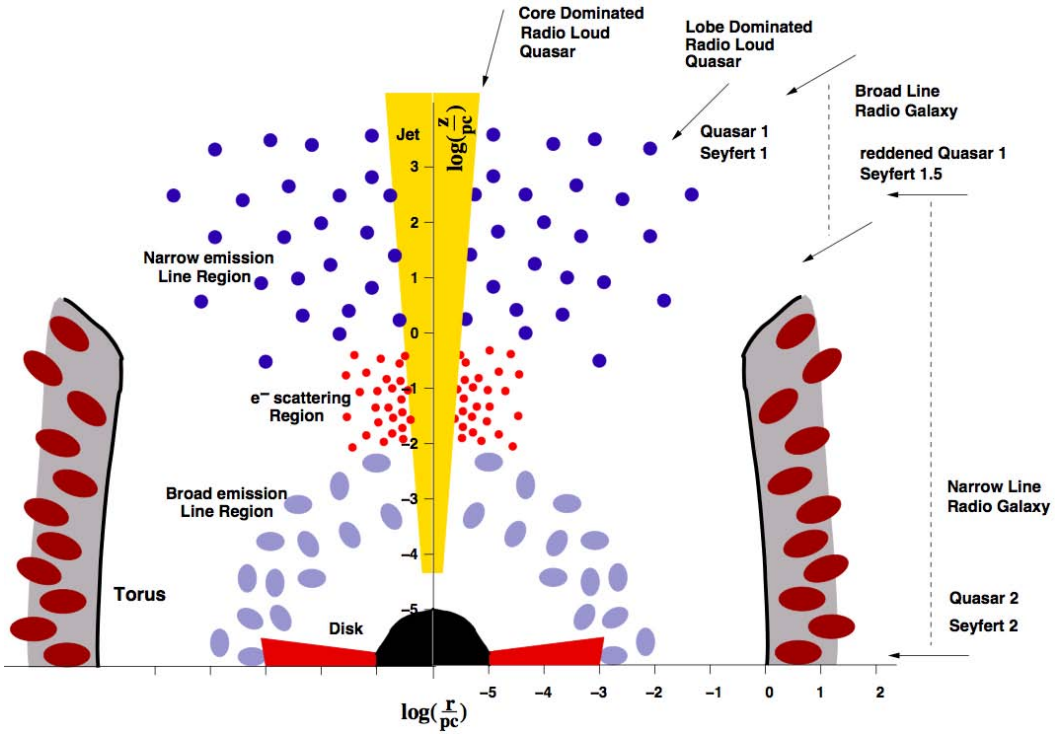

Figure 1.3: Scheme with the diverse substructures forming an AGN, according to the currently accepted unification model. Figure taken from [4].

by the following structures:

- A **SMBH** with a mass of the order of $10^3 - 10^{10} M_\odot$ and a radius up to several times the size of the solar system. It attracts any matter around it and powers the observed emission of the AGN.

- An **accretion disk** is formed around the central SMBH as matter falls spiraling towards it. Similarly to microquasars (§1.2.5), matter forming the disk gets heated as it gets close to the horizon, becoming a highly ionized plasma that emits thermal radiation in all the EM spectrum, with a maximum emitted power in X-ray energies.

- **Jets** are present in almost 10% of the AGN population. They are extremely collimated plasma flows that inject ultra-relativistic particles into the intergalactic medium. These jets can be up to several Mpc long and they usually end up in huge particle clouds or blobs caused by turbulence in the particle flow, like the giant radio lobes of Cygnus A shown in figure 1.2. They are believed to be composed mainly by electrons with a small fraction of light hadrons while the most favored emission mechanism is synchrotron self-Compton. However, the details of jet formation and the mechanism dominating along its propagation are still poorly understood.

- A **torus-shaped structure** surrounding the accretion disk has been confirmed by observations. It is formed of dust obscuring the optical emission from the disk and reemitting it in the infrared and radio wavelengths. Several theories try to explain its formation: it may be formed by the merging of multiple interstellar clouds, or induced from the interstellar matter by the local magnetic field, or it may be formed by the sum of winds of many of stars flowing with the torque exerted by the merger of the two SMBH after the collision of the two host galaxies [4].

- The **broad emission region**, a shell cloud located close to the accretion disk that emits ionization lines as it is illuminated by the disk emission. The lines are broadened by the Doppler effect of this fast-moving cloud ($< 10^7$ m/s).

- The **narrow line region** is formed by slower clouds ($< 10^5$ m/s) that are located further away from the central region. Their lower speeds produce

a weaker Doppler effect so emission lines are not so broadened as those produced in the previous region.

- A **sphere of electrons** at a very high temperature surrounds the accretion disk and it is a powerful X-ray emitter.

The production of γ-rays in AGNs is located both in the accretion disk and along the ultra-relativistic jets. In the former, there is a highly efficient conversion of mass into energy, up to 10% of the inward-falling matter. Moreover, those AGNs whose jets point directly towards the Earth (quasars and blazars) are the most distant sources of VHE radiation that we are able to detect. This allows us to set important constraints on the amount of extragalactic background light present in intergalactic space, responsible of the absorption of γ-rays along their travel towards our detectors, producing a maximum visibility distance that is known as the *γ-ray horizon*.

1.2.2 Gamma-ray bursts

In the decade of 1960 a network of satellites known as Vela was deployed to detect and monitor any nuclear explosion on the Earth by measuring the associated γ-ray emission. This allowed the live detection of any violation of the Nuclear Tests Ban Treaty, an international prohibition of nuclear weapons tests on the surface of the Earth or in the atmosphere. But they detected something completely unexpected: a mean of 1 γ-ray explosion per day was being detected but it was not coming from the Earth surface but from random directions in the Cosmos. They named this phenomena **gamma ray bursts** (from now on, GRB) and they usually appear in regions of the sky where no star had been detected, neither before of the GRB nor after it.

GRBs can be described by the following properties:

- Their observed durations extend over 4 orders of magnitude: from a few milliseconds up to several minutes. We can distinguish between short GRBs (less than 2 s long) and long GRBs (more than 2 s with an average duration of 30 s). There are about 2-3 GRB per day.
- They appear isotropically in the sky and they are located at cosmological distances of the order of Gpc ([3]) and they typically show extreme redshifts

[3] 1 Gpc $\approx 3.1 \cdot 10^{25}$ m

of $z > 1$.

- GRBs are the brightest, non-steady sources of γ-rays in the sky. Their intrinsic luminosity is of the order of 10^{45} W, which is 9 orders of magnitude higher than a typical galaxy like the Milky Way.

- Most of their energy is emitted in the hard X-ray band and in the LE γ-ray regime, with a clearly non-thermal spectrum. After the burst, a longer emission at lower energies can be detected for some GRB, the so-called *afterglow*. Its spectrum extends down to radio wavelengths and the afterglow can last up to a year while its brightness slowly decreases. This afterglow allowed the precise determination of the distance of many GRBs.

- Their lightcurve profiles are very complex and little common features have been able to found: some are single-peaked, others are multi-peaked, some show a long pause between peaks.

Nowadays, we believe that the origin of the long kind of GRBs is explained by the **Hypernova model**: a massive, Wolf-Rayet star of tens of times the solar mass and likely belonging to the second or third generation of stars, exhausts the stellar material after a few Myr and collapses in a scaled up version of a SN known as hypernova, releasing about 100 times more energy than the average SN and forming a blackhole in the process. How the short kind of GRB are produced is still unknown but current models involve merging of two NSs forming a blackhole or the merger of a NS and a blackhole. Multi-wavelength campaigns are needed to confirm or discard any of them. Besides, these kind of events also produce an intense gravitational wave. So the solution to the question on what causes short GRBs is probably to be found in the still unexplored window of gravitational wave astronomy.

1.2.3 Diffuse gamma-ray emission

When we look at the sky with our γ-ray detectors we are able to spot the disk of the galaxy very easily, like in figure 1.4. It is clearly seen as a bright band in the middle of the picture and it is composed of two main contributions: the bright spots produced by bright and resolved γ-ray sources like SNR, pulsars or microquasars, but also a quite uniform background glow all along the galactic

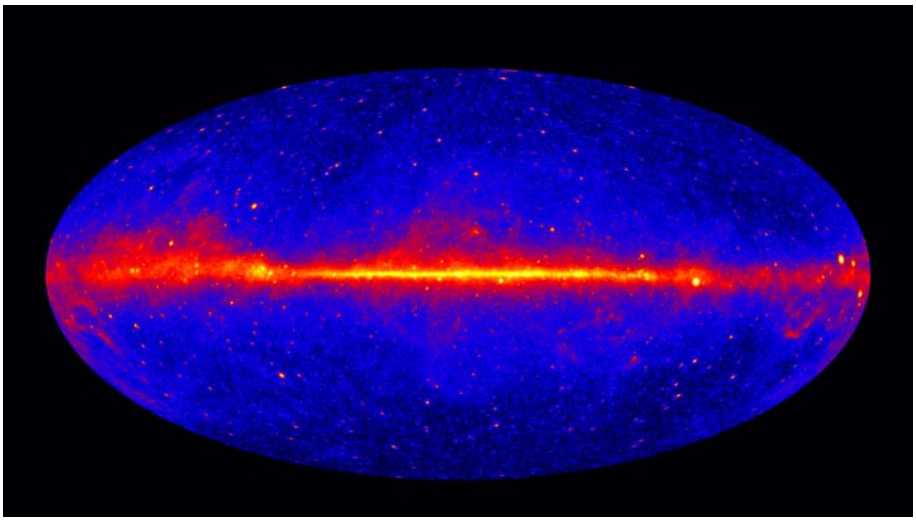

Figure 1.4: A view of the full sky at γ-ray energies above 1 GeV. This is the result of 5 years of Fermi observations. The disk of our galaxy is clearly visible, together with a tens of individual γ-ray sources, shown as bright spots. Image credit: NASA/DOE/Fermi LAT Collaboration.

plane. These γ-ray photons are produced by unresolved γ-ray sources and form what we call the galactic **diffuse emission**.

Diffuse galactic emission has been successfully modeled as the combined γ-ray emission from several contributions. The main one being the collision of high energy CRs with interstellar matter nuclei via the neutral and charged pions decay channels (see details on §1.1). There are also identifiable lines of emission by some radioactive elements, for instance the ^{26} Al line detected by the COMPTEL experiment [6], shown in figure 1.5. The annihilation of $e^- e^+$ also contributes to the global galactic diffuse emission. Finally, high energy electrons traveling through regions with high photon density up-scatter those photons into γ-rays via inverse-Compton

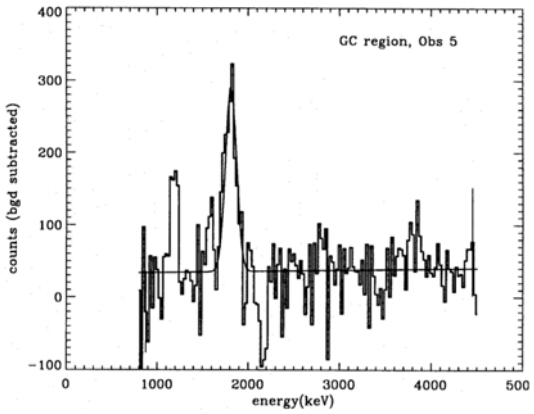

Figure 1.5: The energy spectrum measured in the galactic plane by COMPTEL for photon energies between 0.8 MeV and 4.5 MeV. A clear line is visible at 1.809 MeV, associated with the radioactive isotope ^{26}Al in interstellar space. Taken from [6].

(see §1.1).

1.2.4 Supernova remnants

After the outer layer of a stellar object is ejected in a supernova event (from now on, SN), the expelled material can continue traveling through space for thousands of years at relativistic velocities and injecting heavy nuclei to the interstellar medium. An expanding shell structure or remnant of the supernova (hereafter, SNR) is formed. As example we can mention the Crab nebula itself or the one created by SN 1572, one of the few supernova events in history that was visible with the naked eye. This supernova was observed in the 16th century by the famous astronomer Tycho Brahe and the associated SNR was named after him (see figure 1.6).

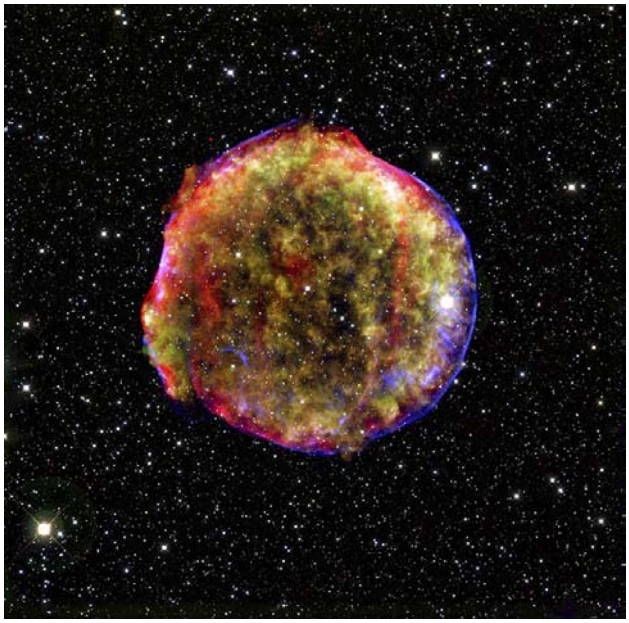

Figure 1.6: Composite image of the Tycho SNR, located in the Cassiopeia constellation and formed by the explosion of a type-Ia supernova in 1572. The image combines exposures of the FoV in X-rays (*yellow, green, blue*), infrared *red* and optical (*white*). Image credit: NASA/CXC/SAO (X-ray), NASA/JPL-Caltech (Infrared), MPIA, Calar Alto, O.Krause et al. (Optical).

If there is any interstellar material surrounding the supernova the expanding matter in the shock will interact with it, slowing it down and usually producing an intricate, asymmetric morphology. This complex interaction produces abundance of γ-rays but their origin is still unclear. Several studies at different wavelengths favor a hadronic origin for such HE photons via pion decay [7]. Furthermore, the dynamic and time evolution of the shock and the surrounding dust clouds positions SNRs as strong candidates to solve the long-standing mystery of the origin of CRs [8].

1.2.5 Microquasars

Binary, tertiary or even higher multiplicity stellar systems account for up to 80% of all star systems in our Galaxy. Among those, microquasars are just a small fraction, where one of the two is a very compact object, a neutron star (from now on, NS) or a black hole of a few solar masses. The name of *microquasars* was chosen because these kind of binary systems show very similar features to quasars, a sub-type of AGN galaxies, but the scale of the former is several orders of magnitude lower than the scale of the latter. Interestingly, astrophysicists have discovered certain features in the structure and evolution of quasars by observing the characteristics of microquasars.

A special feature of these systems is that the distance between the two stellar objects is small enough for the Roche lobes[4] of the massive star to be filled and, therefore, stellar material flows from it towards the compact object. Matter falls spiraling inwards and an accretion disk is formed. Extreme gas temperatures are reached due to shear forces and viscosity dissipation, produced by the differential rotation within the accretion disk and turbulences appear driven by magnetic instabilities. The hot gas of the disk radiates huge amounts of energy from radio to γ-rays. Besides, another component of the EM emission of these objects is produced by the two *jets* or collimated flows of relativistic particles, that escape the system in opposite directions, perpendicularly to the rotation plane.

The jet formation process is still not completely understood but it is likely linked to the extreme spacetime bending produced by the rapidly spinning compact object and to the turbulent instabilities in the matter flow at the center of the accretion disk, close either to the NS surface or to the blackhole horizon. Correlations have been found between drops of the X-ray emission from the disk (the one produced by its hottest, most inner part) with sudden bright spots in the jet that travel along it. This is probably caused by the inner part of the disk entering the event horizon of the blackhole while the remaining material is ejected into the jet [9].

The emission of these kind of objects extends across the entire EM spec-

[4]The Loche lobes are a geometrical space region defined by all the points around a binary star system where the gravitational pull of the two objects balances out. It is tear-drop shaped, with a tear centered in each object and sharing their vertex in the first Lagrangian point.

trum but neither all of them emit photons at every energy nor their emission is steady. Due to their complex morphological characteristics, several emission processes can take place depending on multiple parameters, like the position of the compact object with respect to the companion star, the alignment of the jets with our line of sight, the collision of these jets with the stellar winds or the star itself or the varying size of the accretion disk. This variability allows us to test acceleration and absorption models for high energy particles.

1.2.6 Pulsars

Pulsars are a very interesting source of γ-rays in the galaxy: they are fast-spinning, high magnetized NSs, which were left after the SN explosion of its progenitor star. However, since they are one of the two main topics of this thesis, we will not describe them here but in a dedicated chapter later on (chapter 3).

1.3 Gamma-ray detection techniques

Detectors of γ-rays can be classified into two basic kinds according to their detection principle: direct or indirect detectors. Each type performs best in a certain range of the γ-ray band. The first kind of instruments are usually placed within artificial satellites orbiting around the Earth so they are commonly referred to also as **space-born** γ-ray detectors; whereas the second type is always installed on the surface of the Earth and therefore they are known as **ground-based** γ-ray detectors. We will see how these instruments work and their main technical features in the two following sections.

1.3.1 Space-born telescopes

The atmosphere is opaque to certain wavelengths, as one can see from the atmospheric opacity in figure 1.7. This includes γ-ray wavelengths so, if one wants to directly detect this kind of radiation, detectors must be placed at very high altitudes using balloons or on-board of satellites, orbiting around the Earth. If one chooses the second option there is an intrinsic limitation on their effective collection area (~ 1 m^2), due to two facts: first, γ-rays cannot be focused like other kinds of EM radiation; second putting any instrument in orbit is a very expensive procedure, so budget constraints are the limiting factor on their size. However, these instruments are able to provide high quality data

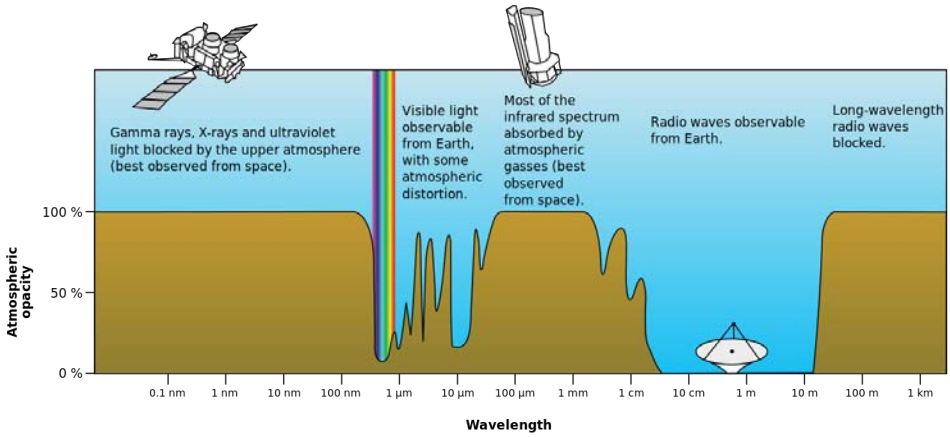

Figure 1.7: Atmospheric opacity for EM radiation as a function of the photon wavelength. The main windows to directly detect EM radiation from the Universe are optical, long-wavelength infrared and radio. Image credit: NASA.

due to an excellent background rejection and high energy and angular resolution.

Space-born γ-ray telescopes have become operational since the first light of Explorer 11, a satellite that managed to detect 22 γ-rays out of 9 hours of data in 1962 [10]. Later on, experiments like OSO-3, SAS-2 and especially COS-B proved this was a fruitful field for scientific research, showing that numerous violent events emit in the highest energy bands. The new observational window to our Universe triggered the interest of many scientists and astronomers around the world and the first catalogues of γ-ray sources were produced. Other important γ-ray detectors on-board of satellites include the CGRO space observatory, HETE-2[5] and Swift[6], AGILE[7], INTEGRAL[8] and Fermi[9], the latest four currently in operation.

All these instruments are sensitive to the region of the EM spectrum between 0.1 MeV and 30 GeV approximately, and they use different detection techniques depending on which energy band they are trying to observe. The least energetic γ-rays, i.e. below 0.5 MeV, are measured in a similar fashion as X-rays: scintillator counters and solid state detectors are used since the main interaction the photon suffers with the instrument is through photoelectric absorption. For photons below 30 GeV, Compton scattering dominates over other interactions, but pairs of e^-e^+ are also produced. Instruments working in this energy range

[5] http://space.mit.edu/HETE/
[6] http://swift.gsfc.nasa.gov/
[7] http://agile.rm.iasf.cnr.it/
[8] http://sci.esa.int/integral/
[9] http://fermi.gsfc.nasa.gov/

measure the energy of the Compton-scattered e^- as well as the energy of the deflected photon with a scintillator. For higher energy photons pair production is the dominating interaction, thus this kind of instruments consist in: a converter, where the photon creates a e^-e^+ pair; a tracker, where one can follow the trajectory of each lepton and derive the incoming direction of the primary photon; and a calorimeter, a region where leptons are stopped and their energy is measured.

1.3.2 Ground-based telescopes

A different approach consists in placing the instrument on the Earth surface, which is the one followed by ground-based γ-ray telescopes, which are able to detect higher energy radiation than space-born detectors. The reason for this is two-fold: first of all, γ-ray fluxes decrease very fast with energy (see more details in §2.1), so telescopes on-board of satellites, with their reduced detection surface are insensitive to energies above a few tens of GeV; secondly, ground-based telescopes have effective collection areas larger than space-born detectors (of the order of $10^4 - 10^5$ m^2), because even a γ-ray entering the atmosphere hundreds of meters away from the telescopes still produces detectable effects at the position of the telescopes. Because of that, they have a much bigger chance of detecting the scarce photons with the highest energies, i.e. they are more sensitive in that energy regime.

However, this technique also has important drawbacks. For instance, since these instruments cannot operate neither under strong light conditions (during daytime or strong moonlight) nor during bad weather situations, the effective observation time is very much reduced with respect to telescopes on-board of satellites. Also the background is higher and harder to reject, especially at the lowest energies these telescopes are able to operate, and their energy and angular resolution is not as good as the one from space telescopes.

Ground-based detectors can not detect the messenger particle directly because they are absorbed by the higher layers of the atmosphere. They are designed for the indirect detection of those particles, so they can be classified into those detecting secondary products of the interaction between the primary and the air molecules, like for the CR detectors AUGER[10], AGASA[11], and

[10] http://www.auger.org/

[11] http://www-akeno.icrr.u-tokyo.ac.jp/AGASA/

KASKADE[12]; or detectors of tertiary particles like fluorescence photons (AUGER and HiRes[13]) or Cherenkov photons, the so-called IACTs. These instruments are based on the detection technique known as **Imaging Atmospheric Cherenkov** technique, which will be explain in detail later on in chapter 2. Some examples of this type of instruments are telescopes MAGIC[14], VERITAS[15], HESS[16], HEGRA and Whipple. We will not elaborate on the details of each of these techniques except for the one used by the MAGIC telescopes. Extensive reviews dedicated to each topic are available, detailing the different techniques, as well as their reported performance [11–15].

[12] https://web.ikp.kit.edu/KASCADE/
[13] http://www2.keck.hawaii.edu/inst/hires/
[14] https://magic.mpp.mpg.de/
[15] http://veritas.sao.arizona.edu/
[16] https://www.mpi-hd.mpg.de/hfm/HESS/

Chapter 2

The IACT technique and the MAGIC telescopes

In the first part of this chapter we describe the chain of interactions that are triggered by the arrival of a high energetic particle to the upper part of the Earth atmosphere, but we will focus mainly on the particular case where this cosmic ray happens to be a γ-ray photon. In the second part of the chapter, we describe the technique used to detect this kind of photons using ground-based instrumentation.

2.1 Cosmic rays

The upper part of the Earth atmosphere is continuously hit by all sorts of energetic particles arriving from the Cosmos. We know them as **cosmic rays** (CRs) and they were discovered by Victor Hess at the beginning of the 20th century [16]. They are still the most energetic particles ever observed: we have measured CRs up to energies of 10^{11} GeV, as shown in figure 2.1. If we consider the the most artificially accelerated particles, those moving inside the Large Hadron Collider (LHC) at the European Organization for Nuclear Research (CERN [1]) and we compare their energies of ~ 10 TeV, we can see that the energy difference is outstanding: up to 8 orders of magnitude. The most energetic ones have the same energy as a tennis ball moving at 100 km/h ! But they are incredibly scarce: only 1 of these particles reaches a km^2 of the Earth surface every century. we can only humbly accept that human beings still have a lot to

[1] from its name in french, *Conseil Européenne pour la Recherche Nucléaire*.

learn from Nature about efficient particle acceleration.

A new kind of astronomy has developed in the last few decades to solve the mysteries of CR origin and dynamics: **CR astronomy**. It is a main player on the multi-messenger approach to astronomy and it is particularly interesting when we are able to detect the highest energy ranges of the CR spectrum: the so called ultra high energy CRs (UHECR) for energies above millions of TeV (10^{18} eV) and the most energetic ones, the extremely energetic CRs (EECR), for energies above the theoretical Greisen-Zatsepin-Kuzmin limit of $5 \cdot 10^{19}$ eV. The energy of these kind of particles allows them to travel in an almost straight line from their production location, because intergalactic magnetic fields are not intense enough to deflect them.

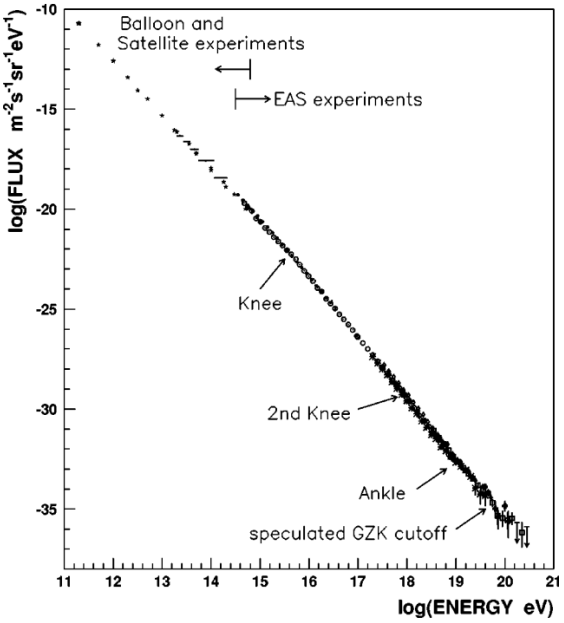

Figure 2.1: The CR spectrum as measured by several kind of instrumentation: space- or air-born experiments for low energies and ground-based indirect detectors for high energies. The flux can be modeled by three energy power-laws, i.e. it is proportional to $E^{-3+\delta}$, where δ is zero/negative/positive for particles with energies below the knee/above the knee/above the ankle. CR energies, expanding over 10 orders of magnitude in energy and more than 25 orders of magnitude in flux, probably the widest magnitude span ever seen in Nature for a single phenomena. Taken from [17].

As an example of CR telescope we will briefly describe the Pierre Auger Observatory. Formed by an array of 1,600 water tanks separated 1.5 km from each other, they cover an extension of $3,000$ km^2 in the Argentinian region of Pampa amarilla. Each tank contains $12,000$ L of water together with some photomultiplier tubes (PMTs hereafter) that detect the light emitted by the secondary particles interacting with water molecules. These secondary particles

are a by-product of the interactions of CR with air molecules, a process known as *shower* that is explained in §2.2. In this way, the type, energy and incoming direction of those secondary particles can be determined, as well as the properties of the primary particle: the CR that triggered the shower interaction. However, after seven years of flux integration, the Pierre Auger Collaboration has not found any correlation between the arrival directions of CRs and large-scale anisotropies, neither with nearby extragalactic objects [18].

The flux of CRs arriving to the Earth is much higher than any γ-ray source in the sky, hadron-induced showers represent a constant and loud background noise for γ-rays observations. In order to build a successful γ-ray astronomy, a technique to distinguish between hadronic and EM showers has been developed, which we will describe together with the complete MAGIC data analysis chain in §2.5.

Besides, the nature of the incident CR has a major influence in the chain of interactions that are triggered when those particles reach the upper layers of the Earth atmosphere. We can distinguish between showers induced by protons or other nuclei in **hadronic showers** and γ-ray- or $e^{\pm}$-induced showers, also known as **EM showers**. In the former, tens of species of secondary particles are produced. In the latter, however, only $e^{\pm}$ and γ-rays are produced. Let's start by describing in detail the physical processes that make both kind of showers possible.

2.2 Extensive air showers

When an ultra-relativistic CR or γ-ray arrives to the Earth, a series of chained interactions take place in the upper part of the atmosphere in what is known as **extensive air shower** (from now on EAS). The primary particle usually collides with a nitrogen, an oxygen or an argon nuclei at a typical altitude of $5 - 25$ km above the sea level (from now on a.s.l.), which strongly depends on its energy: the more energetic the particle is, the deeper it can travel through the atmosphere and the lower the interaction point is located. The product of these interactions are two or more secondary particles and, since the primary is very energetic, the secondaries also travel almost at the speed of light in vacuum. These particles suffer further interactions with air nuclei, producing even more particles in a multiplicative cascade consisting of thousands and even millions of

secondary particles. This process only reaches an end when, down in the lower atmosphere, the energy of each particle falls below a certain threshold and no more particles are produced. All the particles in the cascade travel almost in the same direction as the initial CR, known as **shower axis**, and they all arrive almost at the same time, scattered in a ~ 100 m circle [19]. The highest density of particles is found at the center of this circle which is known as **shower core**.

2.2.1 Electromagnetic showers

EM showers are the ones triggered by a γ-ray, an electron or a positron and they are the simplest kind of EAS since they are principally composed of e^-, e^+ and γ-rays. These showers are governed by three main interaction processes: $e^{\pm}$-pair production by photons, bremsstrahlung and ionization-energy loss of e^+e^-. When the primary particle enters the atmosphere, two different interaction processes with a nucleus in the atmosphere may occur: if the primary is a γ-ray, it will quickly interact with the intense electric field close to the nuclei and a $e^- - e^+$ pair will be produced; if the primary is an e^- instead, it will radiate via bremsstrahlung, producing high energy photons.

These two processes occur alternatively and they are reasonably well described by the *Heitler model* [20]. This model assumes an incident particle with energy E and the products of the interaction are 2 particles with energy $E/2$. After i interactions or *generations* we obtain 2^i particles with energy $E/2^i$ (see figure 2.2, *left*) and this process continues up to the **shower maximum**, when the average energy of the particles falls below the critical energy.

The Heitler model correctly predicts that the number of particles at the shower maximum is proportional to the energy of the primary E and also that the number of secondary particles grows exponentially with the shower length; moreover, the distance between the impact altitude and the shower maximum altitude depends logarithmically on E, which means that the higher the energy of the primary particle, the deeper it will travel through the atmosphere before triggering an EAS. Showers produced by γ-rays with energies between 30 GeV and 30 TeV reach their maxima above the MAGIC location at 2200 m a.s.l. However, the Heitler model does not account for the fluctuations from shower to shower, which can be significant even between showers produced by particles with the same energy: about 40% for 100 GeV showers and about 20% for 1 TeV showers.

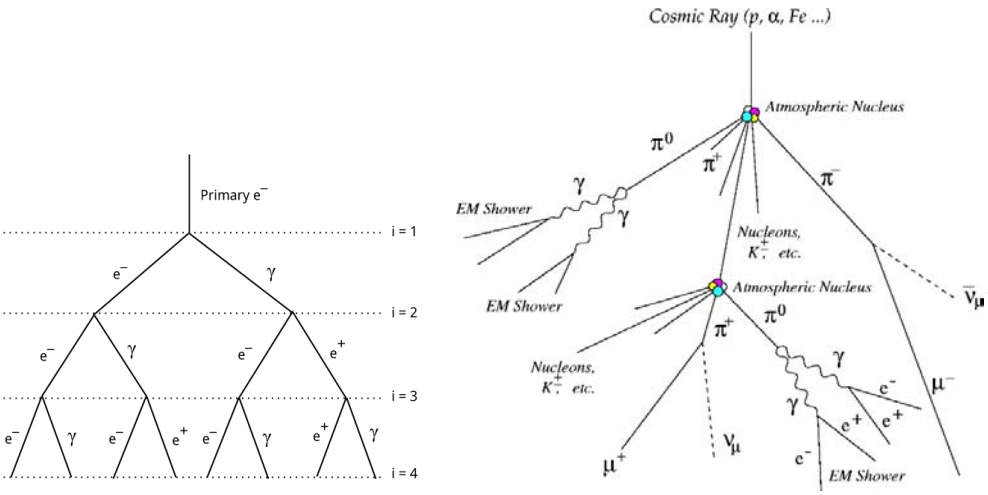

Figure 2.2: *Left)* Heitler model scheme for an e^--induced EM EAS. The different generations of secondary particles are marked with different values of the parameter i, a the mean distance between two consecutive generation is one radiation length. *Right)* Schematic for a hadron-induced EAS. Taken from [21].

2.2.2 Hadronic showers

When the primary particle is a hadron (hydrogen, helium or heavier element nuclei), the number of species of secondary particles and the possible interactions is much bigger than in the case of a purely EM shower. A hadronic **shower core** is formed by the surviving parts of the primary CR, if any, and by the secondary particles with the longest life-spans (τ): charged pions ($c\tau = 7.8$ m), kaons ($c\tau = 3.7$ m) and baryons. The most abundant secondary particles are neutral pions (together with charged pions) but these particles are short-lived ($c\tau = 25$ nm). They quickly decay into two γ-rays (99% probability) so they start purely EM sub-showers from lower altitudes. Since other particles also decay into π^0, this particle is the main responsible for the production of the EM component of hadronic showers. One can see a schematic view of the interactions that occur in a hadronic shower in figure 2.2 (*right*), and the emission of Cherenkov light at different heights obtained from the MC simulation of a 1 TeV proton and a 5 TeV iron nucleus can be seen in the center and right plots of figure 2.3, respectively. The shower continues until the energy per nucleon gets down to ~ 1 GeV, the pion production threshold. A hadronic shower penetrates deeper into the atmosphere than an EM shower of the same energy and the fluctuations in the number of particles are bigger than in the pure EM case.

We can group the types of particles that form a hadronic shower in three groups. The first one is the **hadronic component**, the core of the shower that we have described before. These particles can transfer a high transversal mo-

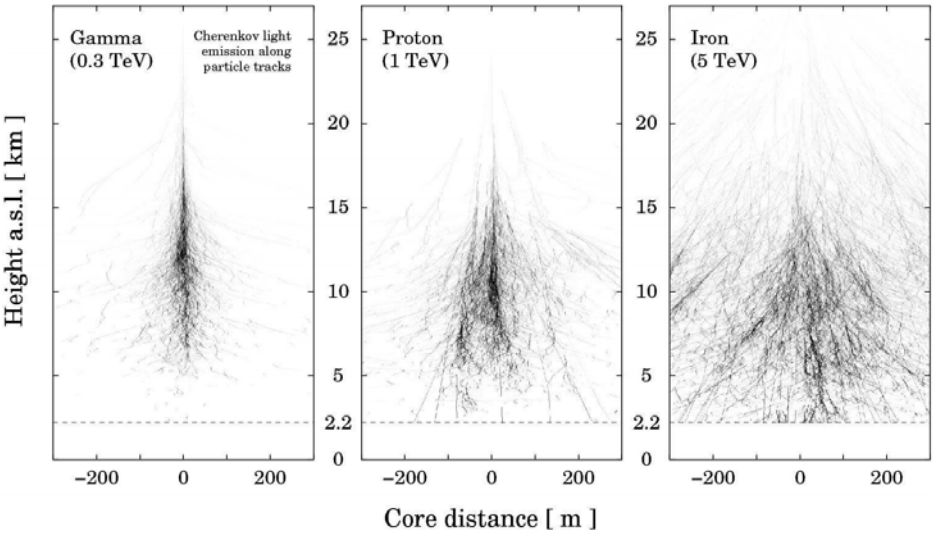

Figure 2.3: Cherenkov light emission as a function of altitude (Y axis) and core distance (X axis) for three kinds of EAS: an EM shower induced by a 300 GeV γ-ray (*left*) and two hadronic showers induced by a 1 TeV proton (*center*) and a 5 TeV iron nucleus (*right*). Darker black lines represent stronger emission of Cherenkov photons. Taken from [22].

mentum to their decay and interaction products, increasing the shower spread. Secondly, the **electromagnetic component** consists of the EM sub-cascades of the shower, i.e. the electrons, positrons and γ-rays from the decay of π^0, and it is the dominant component in the final stages of shower development[2]. The third component consists in the muons and neutrinos from pion and kaon decay. Muons are able to travel long distances from the shower that produced them and they can even reach the ground. They produce a very clear circular pattern, such as those shown in figures 2.20 and 2.21 as seen by the MAGIC telescopes (*right columns*). They are normally used to calibrate the ability of Cherenkov telescopes to focus light on its focal plane.

2.2.3 Cherenkov light production

Hadronic and EM showers are triggered by particles traveling very close or at the speed of light, respectively. Secondary particles in those showers will still be moving at ultra-relativistic speeds. In fact, those particles will be traveling through a dielectric medium faster than the phase velocity of light in that medium: Considering that the speed of light in the air is $v_p = c/n$, where $n(\lambda)$ is the wavelength-dependent refraction index of the air[3], thus primaries

[2] These EM sub-cascades, when casted transversally to the hadronic shower axis, are very similar to pure EM showers and this produces an irreducible background signal for Cherenkov telescopes, undistinguishable from pure EM showers.

[3] At ambient pressure, $n \simeq 1.0003$

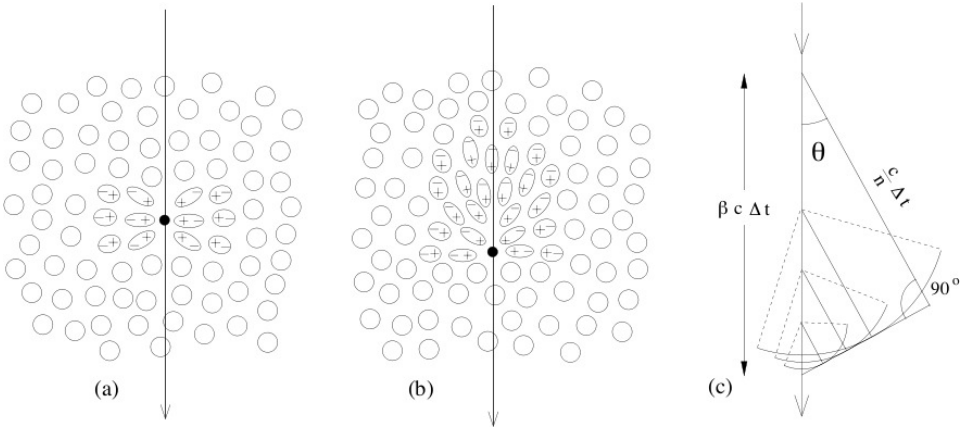

Figure 2.4: Reaction of the atmospheric molecules when a charged particle travels through them at non-relativistic speed (*a*) and at ultra-relativistic speed (*b*). Schematics of the Cherenkov wavefront formation (*c*).

and secondaries usually travel faster than 99.997% of the speed of light for the energies that we are considering. In this situation, a special kind of radiation will be emitted as these particles travel along the atmosphere: the so-called **Cherenkov radiation**. This EM shock-wave was discovered in 1934 by Cherenkov and Vasilov and it is the analog of the sonic shock-wave that follows a supersonic jet along its path: the medium is perturbed by an object that is traveling faster than the speed at which the medium can reach (see figure 2.4).

The condition that a charged particle with rest mass m has to fulfill to produce Cherenkov radiation (that it travels faster than the phase speed of light in the medium) can be expressed with the following equation:

$$\frac{v}{c} > \frac{v_p}{c} = \frac{1}{n(\lambda, T)} \tag{2.2.1}$$

Which can also be seen as a constrain or threshold in the particle total energy:

$$E > \frac{mc^2}{\sqrt{1 - \left(\frac{1}{n(\lambda,T)^2}\right)}} \tag{2.2.2}$$

Thus, lighter particles emit Cherenkov radiation at smaller energies than the heavier ones. For electrons and positrons, the only Cherenkov light emitters in EM showers, they need an energy higher than 20 MeV to start emitting Cherenkov radiation at 2200 m a.s.l. and more than 80 MeV at 20 km height.

Cherenkov radiation is emitted in the direction of the emitting particle,

forming a cone with an opening angle described by

$$\cos(\Theta) = \frac{c}{v\ n(\lambda)} \approx 1 \Rightarrow \Theta \approx 0 \tag{2.2.3}$$

In the case of EM showers, the Cherenkov light cone is very narrow, of $\Theta \sim 1^{\circ}$ at 2200 m and even less at higher altitudes. Since Cherenkov emission occurs along the track of the particle, the total amount of Cherenkov light arriving to the ground is the superposition of multiple concentric cones and it is contained within a circle of ~ 120 m radius known as the **Cherenkov light pool** (see figure 2.5). When the shower axis is not perfectly vertical but coming from a certain zenith angle, the Cherenkov photon distribution is shaped as an ellipse. All Cherenkov photons arrive approximately at the same time: for a typical EM shower, they arrive within $3 - 10$ ns, in what is sometimes called a Cherenkov flash. Hadronic showers can have longer flashes.

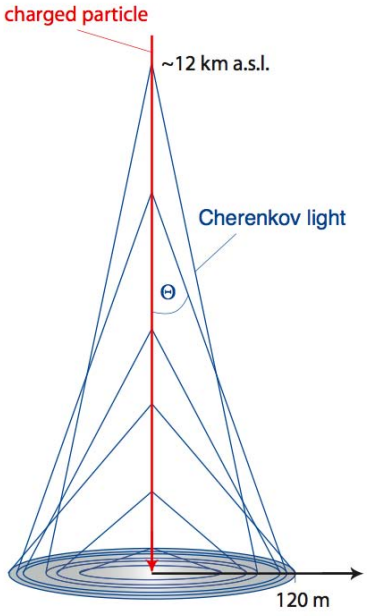

Figure 2.5: Geometric scheme of the overlapping of Cherenkov photons emitted at different heights As a result, a light pool of ~ 120 m is produced on the ground. Figure taken from [23].

Cherenkov light spectrum can be described using the Frank-Tamm formula

$$\frac{d^2N}{d\lambda dx} = \frac{2\pi\alpha}{\lambda^2}\left[1 - \frac{c^2}{v^2 n(\lambda, h)^2}\right] \tag{2.2.4}$$

where x is the path length traveled by the emitting particle, $\alpha = 1/137$ is the fine structure constant and $n(\lambda, h)$ is air refractive index at the wavelength of the emitted Cherenkov photon, λ, and h is the emission height.

2.2.4 Cherenkov light extinction

But not all the produced photons can reach the telescope: there is a considerable fraction of Cherenkov photons that is lost during the propagation between their production altitude and the observation point. They can be scattered out of the FoV or absorbed by different kinds of air molecules. Several components

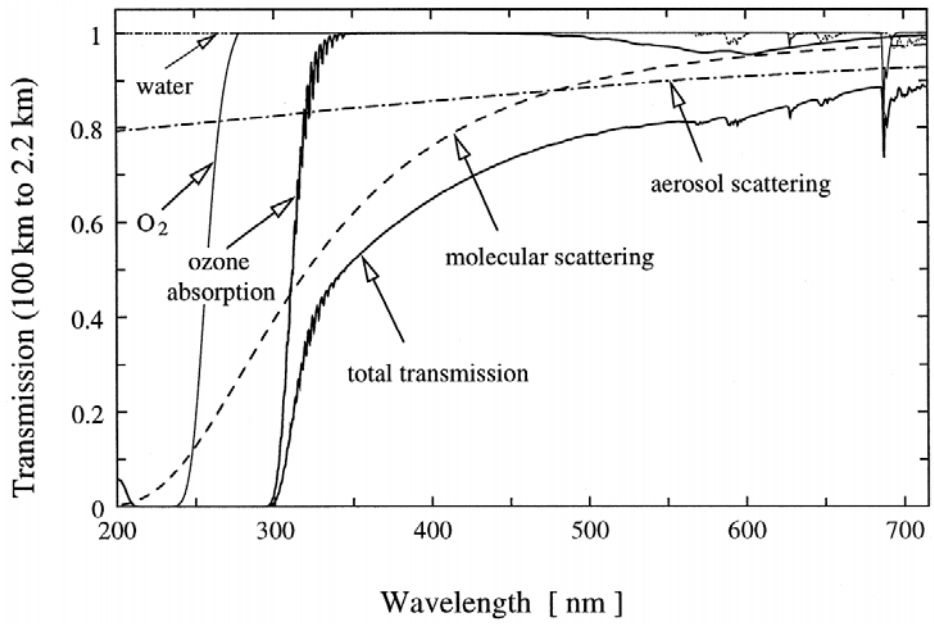

Figure 2.6: Transmittance of the atmosphere as a function of radiation wavelength, i.e. fraction of the photons of a certain wavelength that are able to reach the MAGIC height (2.2 km) from their production position (100 km, but equivalent to light coming from infinity for our purposes). This is not exactly the transmittance of that would be measured for Cherenkov light since its production site is much lower in altitude, at $\sim 10 - 20$ km but it is a good approximation. Taken from [24].

in the Earth atmosphere are also contributing to this attenuation. Figure 2.6 shows the overall absorption of light coming from infinity (or 100 km, which are equivalent in our case) as a function of the light wavelength (lower, solid line), as well as the different contribution to this reduction of the transmittance.

Rayleigh scattering is due to the interaction of the Cherenkov photons with particles smaller than their wavelength, i.e. air molecules. The efficiency of this scattering process is proportional to λ^{-4}, thus the shorter wavelength photons are strongly suppressed by it. This is shown in figure 2.6 as a dashed line: as one can see, this interaction scatters away completely photons with $\lambda < 200$ nm and it produces about 40% attenuation at $\lambda \approx 350$ nm.

Particles with a diameter comparable or greater than the wavelength of Cherenkov light, the so-called *aerosols*, suffer a different elastic interaction known as **Mie scattering**. This effect is very hard to model, since it depends on the shape, density and size distribution of the scattering particles, which can span over a wide range of values. However, for big scattering particle Mie scattering is not very wavelength-dependent, as shown by the dash-dotted line in figure 2.6. Aerosols at La Palma are usually a mix of sea salts from the Atlantic ocean, ice crystals from passing clouds, dust and microscopic sand particles

(especially during a *calima* event[4]) or rather seldom chemical haze produced by anthropogenic activities in Europe and in Northern Africa.

Second order contributions to the absorption of Cherenkov light are produced by ozone molecules, which is only significant at UV wavelengths, and absorption in the infrared band by water and CO_2 molecules. Besides, multiple interactions may scatter shower particles far away from its axis. The Cherenkov light produced by them creates a halo around the Cherenkov lightpool and it may end up out of the telescope FoV.

A last key factor that determines the spectra of an EAS is the *zenith angle* of the observation: the higher the zenith angle (close to the horizon), the longer the distance from the emission point to the telescopes and the higher the probability that some of the above-described events occur. Since they mainly affect at short wavelengths, a high zenith angle also makes the Cherenkov spectra shift towards longer wavelengths, i.e. Cherenkov light becomes redder.

2.3 Imaging Atmospheric Cherenkov technique

In order to measure the γ-ray emission of astrophysical sources from the ground, an indirect detection technique has been developed: the **Imaging Atmospheric Cherenkov technique** or IACT.

The first successful IACT telescope (or simply IACT) was the Fred Lawrence Whipple telescope[5]. This 10 m dish γ-ray telescope paved the road to ground-based γ-ray astronomy. It was built in 1968 and it took the scientists working there 20 years to detect the brightest, steady γ-ray source that is now used as stelar candle, the Crab Nebula [25]. It takes nowadays less than 17 minutes to detect this same source using the MAGIC telescopes with a reliable statistical significance [26]. But, in doing so, they were the pioneers that opened a new observations window to the Universe by solving the hardware issues and developing the analysis tools that IACTs requiere.

There are several facts that make this detection technique so challenging:

- First of all, the bulk of Cherenkov emission is located in the near UV and

[4]Massive haze intrusion in the atmosphere of the Canary islands that occurs when wind coming from the east carries huge quantities of dust from the nearby Sahara desert.

[5]http://www.sao.arizona.edu/FLWO/whipple.html

the optical EM band. But regular optical telescopes are not suited to detect the Cherenkov flashes because of their *brevity*: a faint flash that last for only ~ 10 ns can not be detected with CCD cameras, the standard tool in optical astronomy. The shortness of the signal requires a detector with a very fast response. This requirement was fulfilled with the use of **photomultiplier tubes** (hereafter **PMTs**), which are the commonly used detectors in particle physics.

- Second, showers are *very faint*, especially at energies below 100 GeV, so the light detectors (PMTs) also need to be extremely sensitive, almost down to detecting individual photons. This translates into the need to use high amplitude gains, so a few photons are able to produce an intense electrical signal. Applying a high voltage of the PMTs of the order of the 10^3 V is therefore required.

- The spectra of most γ-ray sources can be modeled using a power-law function with an index that is usually between -2 and -4. This means that their flux at VHE is very low: a 100 m circle surface perpendicular to the direction of the source can be traversed by only a few hundreds of γ-rays per hour for the brightest sources whereas for the faintest ones, this flux can go down to a few tens of γ-rays *per year*. Such tiny fluencies require massive collection areas.

- The detectors used by IACTs are very sensitive so, even in the darkest nights, they are constantly triggered by ambient light. These background photons are abundant and their origin is diverse.

    1. **Night-sky background** or NSB is the combination of the light coming from stars, galaxies, the moon, zodiacal light, distant lightning and also from human activities in nearby cities or cars passing by the telescopes. The average photon flux arriving from a region of the sky with no bright stars is of the order of 10^{12} ph/sr/m^2 within the wavelength range we are interested in.

    2. γ-rays are not the only particles triggering EAS. For instance, cosmic **electrons** trigger the exact same kind EM showers than γ-rays do. Electrons arriving in the direction of our candidate source constitute an irreducible background for any IACT observation.

3. High energy particles like **muons** or **hadrons** also produce showers in the atmosphere. The former can be easily distinguished by their characteristic ring-shaped image in the camera plane. The latter are the most abundant species in CRs and they are at least 10^4 times more abundant than VHE photons, even when we observe the brightest γ-ray sources. However, the showers they induce in the atmosphere have a different morphology and time-development features, and methods have been developed to reduce them during the analysis of the recorded data.

4. There also exists a **diffuse γ-ray** background that is produced by all the unidentified γ-ray sources in our galaxy. Therefore, it is another irreducible contribution that is especially important when we observe galactic sources or extragalactic sources that happen to be behind the plane of the Milky way.

Several techniques have been developed to discard most of the background in IACT observations. The first source of background light, the NSB, triggers pixels randomly, with no correlation between their positions in the camera plane. An individual threshold for each pixel is set in order to prevent that they become the dominant signal of our detector. Since light produced in EAS usually has a compact spatial distribution, several topological criteria are also applied to distinguish actual showers from pure NSB events (see §2.4.4). The rest of the background sources on the above list are a not so easily discarded by such criteria, since they all produce atmospheric showers similar to the ones we are trying to detect. But none of them has a preferred arrival direction, i.e. they are isotropically distributed. However, γ-ray-induced EM showers point in a preferred direction: the position of the emitting source. We will explain the details on how we do this in §2.5.3 but we can already understand that this fact is crucial to discard a big fraction of the background shower events from the actual signal.

Considering all these facts, IACT telescopes design has to be carefully planed and it is strongly dependent on the kind of sources we will be trying to observe. For instance, if one wants to be the first one to detect GRBs from the ground, one has to consider that they emit mostly lower energy γ-rays. These photons produce very faint Cherenkov flashes at high altitudes in the atmosphere and their Cherenkov light has to travel through a big fraction of the atmosphere,

where extinction is also higher. These two facts make GRB events to look faint in the camera of an IACT. In order to detect this kind of sources, we need to have big reflective surfaces to collect as much Cherenkov light as possible of every single shower. This will rise the building costs, which will strongly limit the number of Cherenkov telescopes. This is the approach followed by the 2 $\varnothing 17$ m MAGIC telescopes that we describe in §2.4.

On the other hand, close-by AGNs and most galactic sources emit VHE γ-rays, which produce bigger EAS that develop deeper in the atmosphere. The greater number of produced Cherenkov photons and the smaller atmospheric extinction makes this kind of showers easier to detect from the ground and thus, we do not require such big reflective surfaces. However, fluxes at these energies are extremely low, so we need to cover a bigger detection area. This problem was solved using a bigger number of IACT telescopes with a smaller mirror area but distributed over a bigger region. This approach was followed by for instance H.E.S.S., with their array of 4 $\varnothing 10$ m telescopes (now with an additional $\varnothing 24$ m telescope, H.E.S.S. II) and by the small size telescopes within the future Cherenkov telescope array (hereafter, CTA).

2.4 The Florian Göbel MAGIC telescopes

In this section we will introduce the telescopes that were used to collect the data presented in this thesis, namely the MAGIC telescopes. We will explain how they work, what their main subsystems are and we will describe in detail each step of the MAGIC data analysis chain.

The *Florian Göbel* MAGIC telescopes is a system two IACTs located at the Canary island of La Palma, in Spain ($28°45'$ N, $17°53'$ W, 2225 m a.s.l.), within Observatorio del Roque de los Muchachos (ORM). This observatory is maintained by the Instituto de Astrofísica de Canarias (IAC), whose headquarters are at La Laguna, in the nearby island of Tenerife. The system is currently being operated by an international collaboration composed by more than 150 astronomers, physicists and engineers. It is mainly founded by the funding agencies BMFB and MPG (Germany), INFN (Italy), MICINN (Spain) and the ETH Zurich (Switzerland) [27]. In this section we will describe its subsystems with some detail.

The project was originally conceived in 1998 by some of the scientists op-

erating the HEGRA telescopes[6], the previous generation of IACTs. MAGIC's main goal was to lower the energy threshold to close the gap between satellite ($\sim$ 10 GeV) and ground-based (100 GeV) γ-ray astronomy [28]. Since such low-energy events produce faint Cherenkov flashes, a big collection area was needed to detect them, as well as a high quantum efficiency of the photomultiplier tubes in the camera. The other, closely-related goal was the first detection of a GRB by a ground-based facility.

To accomplish the first goal, a Cherenkov telescope with a $\varnothing 17$ m diameter segmented disk was built between 2002 and 2003, obtaining a total reflective surface of 234 m^2. It was the biggest Cherenkov telescope in the world for almost a decade, until H.E.S.S. upgraded their system in 2012. MAGIC's second goal required GRB observations to start as early as possible after the arrival of the trigger signal, provided by space-born detectors. To do so, an innovative light-weight structure was designed and the readout electronics were moved out of the camera itself and placed in a dedicated building close to the telescopes. This fact allows MAGIC to precisely reposition towards any point in the sky in few tens of seconds.

In 2005 the construction of a second telescope started, namely MAGIC-II. Regular observations with the two telescopes at the same time did not start until 2009, when MAGIC became a stereoscopic system. This second telescope was basically a clone of the first one but with some improvements in the hardware and the readout electronics [29]. In order to make the two telescopes identical, in summer 2011 both MAGIC-I and MAGIC-II readout electronics were updated with the latest version of the Domino Ring Sampler chip (DRS v4 or DRS4) [30]. Later on in summer 2012, the upgrade of the MAGIC telescopes was finished with the upgrade of the MAGIC-I trigger and camera, to match the characteristics of that of MAGIC-II.

2.4.1 Structure & drive

Since one of the goals of the MAGIC telescopes was to detect fast transient events like GRBs, fast and accurate repositioning was required. Because of this, a very light structure was build and light materials were used whenever possible, achieving a weight of only 72 t. At regular speed, MAGIC can point towards any position in the sky in less than 100 s. But in the so-called GRB-mode, i.e.

[6] http://www.mpi-hd.mpg.de/hfm/CT/CT.html

Figure 2.7: *Left)* Lateral view of the MAGIC-I telescope. In the bottom half of the picture one can see the metallic fiberguides that connects the first MAGIC telescope (in the background) with the control house. *Right)* Foundations of the MAGIC-I telescope. The base structure (*center*), the mirrors (*top*), the rail (*bottom*) and part of the mast (*bottom-left*) are visible.

whenever an alert for an observable GRB is received, MAGIC enters a fully automatic operation mode, saving precious time by skipping any human input. This allows the telescopes to reposition in less than 20 s in special, fast-movement mode.

The structure of the MAGIC telescopes is an altitude-azimuth mount that consists of 3 layers, holding the reflective system and the camera. The complete space frame weighs only ~ 5.5 t, 25 t with mirrors. The base is an hexagonal-shaped frame composed of 7 m long, carbon fiber-epoxy tubes connected with aluminum dots, which are shown in figures **??** (*right*) and 2.8. On top of it and in opposite positions one can find two modular pyramids sustaining the elevation axis of the telescope. The mirrors are hold by a complex disk structure, formed by smaller and thiner carbon fiber tubes. Both parts can be seen on figure 2.7: the dark, thick tubes at the center of the image and the white-painted, thin tubes at the right, respectively. As we can see in the schematics of figure 2.8 (*left*), there is also a metallic, arch-shaped mast (*green*) holding the camera and 10 pairs of steel cables (*black*) fix it to the pyramidal towers (*blue*). These cables also stabilize the camera against vibrations and wind-induced oscillations. On the back of the mirrors, the mast becomes a circular rail for the elevation movements and it also holds the counter-weights for the heavy camera (marked with green boxes in figure 2.8, *right*). The whole telescope structure is rigid:

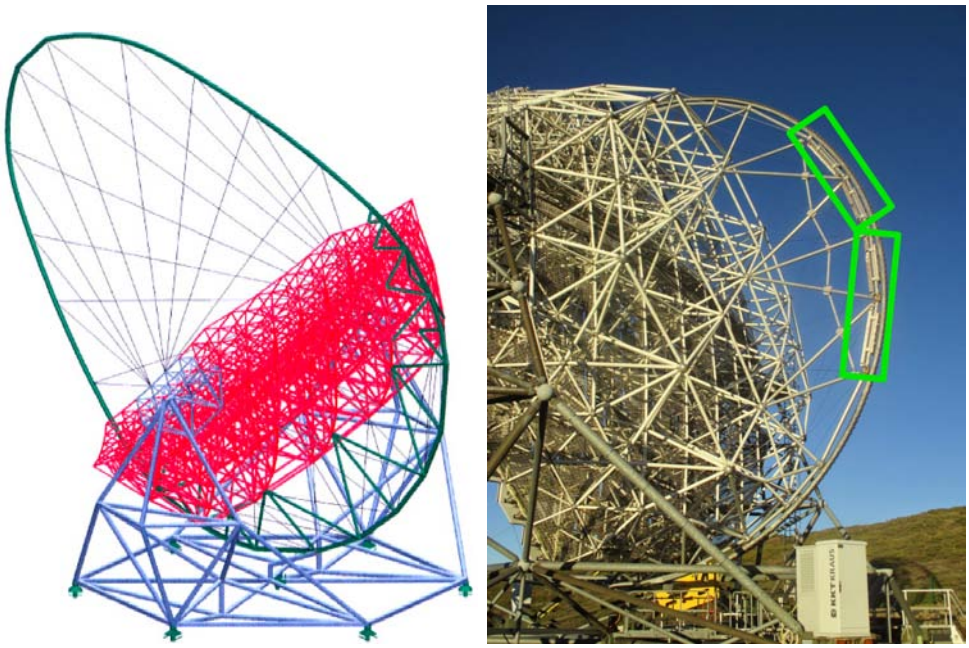

Figure 2.8: *Left)* Schematics of the MAGIC telescope structure. The hexagonal base and the two pyramids are shown in blue, the mast is painted in green, as well as the steel cables and the auxiliary tubes holding it to the disk structure, marked in red. *Right)* Structure of the MAGIC telescopes (in this case MAGIC-I) and backside of the elliptic mast that holds the camera, as well as the the counter-weights, marked with two green boxes, placed on it.

it deforms less than 3.5 mm in any position, according to design specifications. Besides, it is also light (only ~ 60 tn without other components) and modular, so it could be eventually unmounted and mounted back again.

The above described structure is placed on top of a $\varnothing 20$ m rail with less than 8 mm deviation from the circular shape [31]. Fixed to it there is a chain with six bogeys that allow the azimuth rotation of the telescopes. This rotation is powered by two, 11 kW servo-motors placed on two of those bogeys, in diametrically opposed positions next to the support towers. A third motor located on the arch base allows the telescopes to vary its elevation.

The elevation can be set to any value between -10° and 160° and the azimuth can be set between -90° and 318° (where 0° marks the horizontal and the geographical north respectively). The telescopes could also be used in the so-called *reverse mode*, i.e. with an elevation bigger than 90°. The accessible movement range is limited both by software and hardware. The presence of hardware end-switches directly connected to the drive electronics guarantees a fast but controlled emergency deceleration to avoid hitting any structure surrounding the telescopes during repositioning.

Figure 2.9: *Left)* One of the six mechanical bogeys that move along the metallic rail following the chain at the bottom of this picture. It allows for a complete azimuth rotation of the telescope. Two of the tubes that form the support structure for the mirrors and the camera can be seen on top. *Right)* The zenith rotation drive is located at the center of the structure, behind modular structure supporting the reflective surface. The white the carbon-fiber tubes can be seen on the top-right corner of this picture.

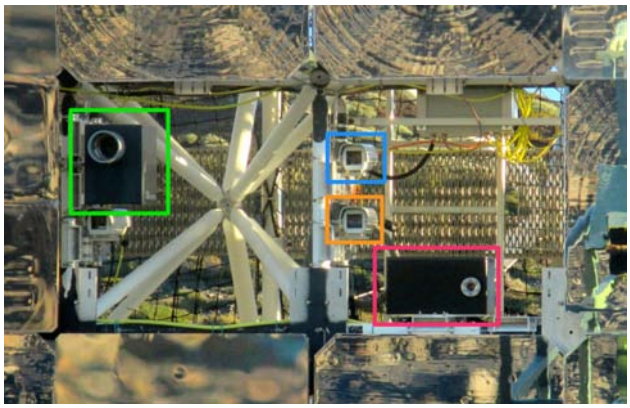

Figure 2.10: The two central mirrors of MAGIC-I are occupied by several cameras and sensors, marked by color boxes: the SBIG camera (green), the starguider camera (blue), the T-Point camera (orange) and the calibration box (pink). The same instruments can be found also in the center of MAGIC-II reflective surface. The white camera below the SBIG camera was part of an old sub-system that was used in the past but it is currently disabled.

A pointing precision of less than 0.022° is achieved using two absolute shaft-encoders that are responsible for the constant measuring of the pointing position of the system. They are calibrated using the so-called *starguider camera*, a 4.6° FoV, high-sensitivity, CCD camera mounted at the center of the reflective surface (marked in blue on figure 2.10) that compares the telescope's pointing position with respect to the background stars. To do so, the starguider camera monitors the position of a set of LEDs forming a ring around the telescope camera and, at the same time and thanks to its wide FoV, it identifies a group of bright stars. The starguider information is stored within the data file so corrections for any possible mispointing can be

introduced later in the analysis of the affected data.

2.4.2 Mirrors

The reflective system of the MAGIC telescopes is $\varnothing 17$ m mirror, with a total reflective surface of 236 m^2. The focal length is also 17 m, so the relative aperture of the optical system is $f/D = 1$. The Cherenkov flashes last only between 1 and 3 ns but there is still some structure in the Cherenkov light front. To keep this information and include it as part of the analysis, the MAGIC mirrors where designed with a paraboloid shape. Therefore, the relative arrival times of each Cherenkov photon of the EAS is conserved. This shape also improves several other performance aspects, like reducing the minimum trigger rate by recording less NSB photons or increasing the signal-to-noise ratio of Cherenkov events against NSB events.

The reflector is composed of 247 tessellated square facets of 1 m-side. Each unit contains a single aluminum mirror in the case of MAGIC-II, whereas for MAGIC-I there are 4 smaller, square aluminum mirror tiles of 0.5 m side length each. However, these mirrors where not produced with the same techniques and because of that they have a different internal structure. All the small 0.25 m^2 mirrors in MAGIC-I consist of an aluminum mirror on top of a honeycomb structure. However, there are two kinds of 1 m^2 mirrors in MAGIC-II. 143 of them are a scaled-up version of the MAGIC-I tiles. The resting 104 panels are glass-honeycomb-glass sandwich with an aluminum coating. All the mirrors are covered with a protective quartz coating and polished with a diamond milling machine to make the surface reflective and guarantee a roughness below 10 nm. All the individual mirrors show a PSF between 3 and 6 mm, well below the size of a single pixel in the camera, and the overall reflectivity of the system is approximately 80% for light with typical Cherenkov wavelengths between 300 and 650 nm. Besides, each mirror segment is equipped with an internal heating system to avoid dew and ice formation.

Since the telescopes are not covered by a protective dome like most ground-based astronomical facilities, a degradation of their reflectivity is expected during MAGIC operation lifetime. A partial re-aluminization was carried out in 2014 for MAGIC-I mirrors. However, perfect reflectivity is not required for IACTs to

Figure 2.11: Mirrors of both MAGIC telescopes. *Left)* MAGIC-I hexagonal distribution of square mirrors. One can see that the two central mirrors are missing. The front side of the camera as well as the author of this thesis can be both seen in the reflection. *Right)* The set of mirrors mounted in MAGIC-II. The camera mast can be seen in the lower and upper left corners. The two central mirrors are also missing in order to place several cameras and sensors. The black dot at the center of the inner mirrors are the mounted lasers used approximately once per year to check the correct alignment of the mirrors.

work efficiently because the reflected images are recorded with cameras with only a thousand pixels.

Active mirror control

While tracking a source, the telescopes suffer small deformations because the gravitational loads are different for each zenith position. To avoid the consequent defocusing, an *Active Mirror Control system* (AMC) was installed to allow on-the-fly individual mirror alignment. To do so, each mirror segment is fixed to the carbon structure at 3 points. One of these joints is fixed while the other two connect with two stepping motors that can realign each segment individually with 20 μm precision [32]. The mirrors are oriented according to some predefined look-up tables (from now on, LUTs) that only depend on the zenith angle, and this is usually done during repositioning to maximize the observation time. A dedicated software controls the entire system, constantly monitoring each facet and realigning it during the observations if needed. Thanks to it an optical point-spread-function (from now on, PSF) of only 12 mm can be reached[7].

[7]The point-spread-function is defined as the size of the spot in the focal plane of the imaging system for light of an unresolved source coming from infinity. It measures the ability of the reflective surface to focus parallel light rays, which is directly related with the quality of the recorded images.

The AMC also corrects for all the optical aberrations that smear the shower image, like astigmatism, spherical aberration or tessellation aberration, except for one: the coma aberration, which makes the off-axis images look a few percent larger. Since the AMC cannot correct for it, the only way to take it into account is to include it within the MC simulation of the telescopes. Besides, the AMC allows us to select the focal length of the entire reflective system. Since shower maximum is located at around 10 km a.s.l., the mirrors are usually focused to this distance. But we can also use the AMC to calibrate our system, for instance by focusing an image in the camera plane of a source at infinite, like a star.

2.4.3 Camera & calibration system

After the Cherenkov photons produced by an EAS are reflected by the MAGIC mirrors, most of them end up reaching the camera of the telescope. The MAGIC cameras are hermetic, 850 kg, 0.81 m deep, $\varnothing 1.46$ m cylinders. In the side facing the telescope one can find a UV-transparent, circular, plexiglass window and two movable lids to cover the detector during daytime. An efficient IACT camera needs: a high quantum efficiency (QE) of its individual sensors or "pixels" (PMTs in our case) and ultra-fast response is also very important, since Cherenkov flashes last only a few nanoseconds.

PMTs are the responsible for converting the Cherenkov light into an electrical signal. Each camera contains 1039 PMTs that are $\varnothing 1$ in and have a 0.1° FoV, whereas the entire camera has a 3.5° FoV. These pixels are the R10408 6 stage model produced by Hamamatsu[8], and they have a high peak QE of 34%. The main components are an hemispherical photocatode and 6 dynodes, their output direct current during a dark night is ~ 1 μA and they work at a constant high voltage (HV) of about 1250 V. They have a fast signal response of only 1 ns FWHM and a gain of $3 \cdot 10^4$, which is relatively moderate compared to PMTs used in other particle detectors but it is needed in order to perform observations under moderate moonlight conditions (although always below 75% moon phase).

The PMTs of the old MAGIC-I camera form an hexagon of around 1 m size

[8] http://www.hamamatsu.com/

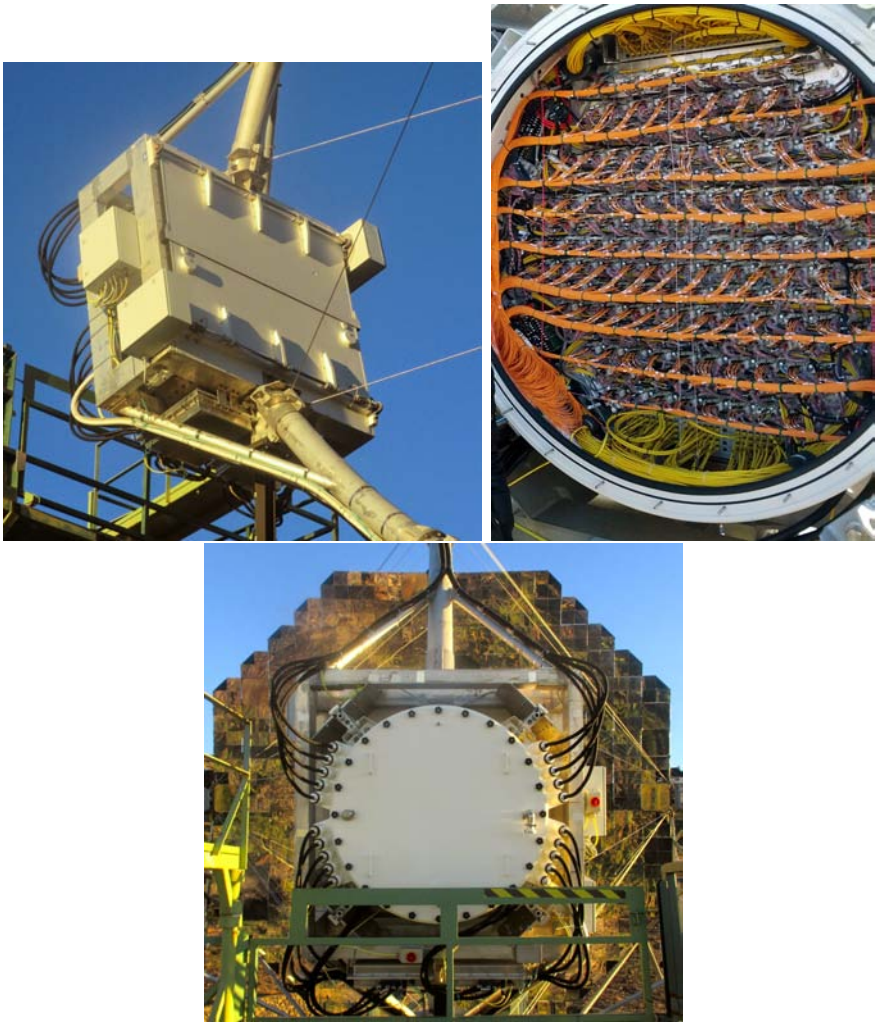

Figure 2.12: *Top-left*) Front side of MAGIC-I camera with its lids closed. The two supporting masts can be seen in the lower and upper sides of the camera, as well as the steel cables that assure the rigidity and stability of the structure during observations. *Top-right*) MAGIC-I camera backplane after removing its cover. The back of the individual pixels can be seen, as well as the orange fiber optics that carry the signal to the readout electronics located in the nearby building. *Bottom*) The backplane of MAGIC-I camera and the reflective surface on the background.

whereas the MAGIC-II and the new MAGIC-I camera have a circular array of pixels of $\varnothing 1.2$ m. They are grouped in 169 clusters, making them easier to maintain and exchange. Each 7-pixel cluster also has its own pulsar board, a generator of fake pulses mimicking the signal produced by a Cherenkov flash and that allows for testing the electronics and calibrating the response of the PMTs, even during daytime. The electrical signal coming from the PMT is pre-amplified and sent to a Vertical Cavity surface Emitting Laser (VCSEL) to convert it into an optical signal. VCSELs require constant working temperature, so the whole camera is stabilized at around 14° thanks to a 8 kW water cooling system.

There is also a slow control system to receive commands from the Camera Control software, *CaCo*, and to read the input from the different camera sensors. Other auxiliary systems like the power distribution cables, a low voltage (LV) to power up the HV generator and a liquid cooling system, a vital component that provides the temperature stabilization the VCSELs require to have an stable response and performance.

In the space between the PMTs one can find Winston cones light-guides to collect the rest of the light that did not enter the PMT, minimizing the dead area between them. They also avoid that light that is not coming from the reflector enters the PMTs. In the outermost ring of the camera, a set of 7 special clusters contain hybrid photo-detectors (HPD), an improved design of PMTs with up to 50% QE, and used for testing purposes. There is an additional special pixel located in the center of the camera that is also able to perform to optical observations, the so-called *central pixel*. It was first installed in MAGIC-I to perform simultaneous observations of the Crab pulsar and it was useless for normal observation of showers. However, this pixel was changed, together with the necessary electronics, for a new one that was able to perform also regular observations. A twin pixel was also installed at the center of the MAGIC-II camera and it only makes sense to use them in on-source observation mode (for details see section 2.4.8).

Finally, the optical signal is transmitted through multi-mode optical fibers, which can be seen as the orange cables in figure 2.12 (*top-right*), the best way to transmit the signal between distant locations without significant losses. 1296 optical fibers are installed between the camera and the nearby building, known as the Control or Counting House (CH), where the rest electronics including the

camera readout are placed. They are packed in bundles of 72 fibers, each of them 162 m long and they are protected inside a rigid guideline, which is visible in the lower half of figure 2.7.

Finally, the calibration system is located at the center of the MAGIC reflective surface inside the calibration box, marked with a pink box in figure 2.10. Its goal is to illuminate the pixels of the camera with homogeneous light flashes of known duration and intensity. In this way, a conversion factor between the signal recorded by the electronics in the CH (described in the next section 2.4.4) and the flux arriving at the camera can be computed. The old calibration system for MAGIC-I was composed of 64 LEDs emitting short pulses ($3-4$ ns long) at 670, 460 and 520 nm wavelengths. The new calibration system for both telescopes uses a Nd-YAG laser that shoots light pulses 0.7 ns wide. Its intensity can be varied from 1 to 1000 photo-electrons (phe) in every pixel by changing the position of two rotating filter wheels with different attenuation factors. In order to illuminate the camera plane uniformly, an integrating sphere in front of the laser diffuses the light evenly. The data recorded by the camera during each one of these calibration events is stored on disk thanks to a special calibration trigger signal sent down the trigger branch by the two trigger calibration units (TCU), one for each telescope, located inside the CH. Since the laser shots are randomly delayed, a pin-diode is placed between the laser and the camera and it tells the TCU when the laser has been shot. The calibration trigger is send to the prescaler board, that centralizes all trigger inputs and takes the final decision to record or discard the data (see section 2.4.4).

2.4.4 Receivers and trigger system

Once the optical fibers have reached the CH, they are plugged in the receiver boards (or just receivers), where photo-diodes are responsible for converting the optical signal back into an electric signal. At this point the signal is divided in two: the digital trigger branch and the analogue readout branch. In order to process all the camera pixels, each receiver board has 24 independent channels to read the input from 24 optical fibers. The receiver outputs are 3 L0 trigger cables (8 channels each) and 24 analog channels for the signal itself. The receivers are installed in groups of 9 in a commercial VME crates installed in groups of 3 inside standard racks and locked cabinets. Since receivers require a constant temperature to work, there are dedicated, always-on air cooling units

on top of each cabinet. An image of all these components can be seen in figure 2.13. The receivers are also used to measure the individual pixel rates (IPR) as well as the pixel mapping.

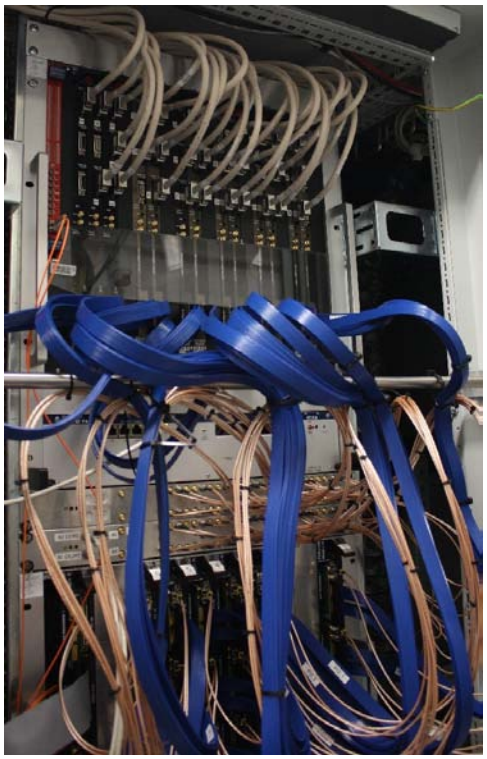

Figure 2.13: Receiver boards installed on the racks. PULSAR boards containing the DRS4 chips can be seen at the bottom.

The next step in the signal processing is the trigger system. This system is a complex, multilevel decision device that is responsible for the selection of the Cherenkov shower signal hidden under several sources of noise. The trigger tells the data acquisition system (or DAQ) when to store the signal produced by the camera in coincidence with an EAS. The digital trigger signal is produced by the receiver and transmitted to the trigger system, where it is processed by several trigger logics or *trigger levels*. The **level zero trigger** (L0) checks that the signal of an individual pixel is higher than a programmable threshold during a limited time interval. If any pixel in the camera fulfills this condition, a trigger signal is generated by the receivers and is further processed by the next trigger level. If this is not the case, the event will never trigger the data acquisition system and will not be saved to disk. This L0 digital signal is a square-shaped, 1-level digital signal whose width and delay can be programmed for both MAGIC-I and MAGIC-II electronics.

The signal is then processed by the L1 trigger, which is a more complex topological trigger. It measures temporal and spatial information of the event and is a very efficient way to distinguish between events that only contain background light from the night sky (or NSB) and Cherenkov events: whereas NSB events trigger each pixel randomly, photons from a Cherenkov shower are distributed in a rather compact way and they only last for a few nanoseconds. The L1 trigger takes advantage of this difference and selects only those events where

a certain set of neighboring pixels have survived the L0 trigger within a limited time window. This logic is known as *x Next Neighbor topology* (xNN), where x stands for 2, 3, 4 or 5. The trigger signal of each pixel is not processed individually by the L1 trigger but in groups of 19 pixels which are called *macrocells*. These macrocells display a precise spatial configuration in the camera plane: 19 overlapping, hexagonal-shaped regions containing 36 pixels each. There is 1 pixel row in common with the next macrocell and all of them cover the 547 innermost pixels of the camera. This means that the effective trigger region has a 2.5° FoV. Each macrocell signal is processed by a single L1 trigger board.

The MAGIC collaboration developed an intermediate trigger level, the so-called L2, for MAGIC-I. It was based on a deeper topological analysis of the shower images [33]; however, its insufficient performance forced the collaboration to discontinue this project. A new the trigger logic for IACTs in the stereo era has been designed, simulated and tested, the so-called *topo-trigger*, and it is now under commissioning phase within the MAGIC collaboration [34].

Every macrocell output is merged and sent to the next level of trigger decision: the stereo-coincidence or L3 trigger. The processing of the previous trigger data and the production of the L3 signal is done by a multi-purpose PULSAR (pulser and recorder) motherboard. This 9-unit VME board was developed by the University of Chicago and has been used in several high-energy particle experiments [35]. A L3 trigger occurs when there is a L1 trigger for each telescope within a limited time window, 200 ns long. When observing in stereo mode, events that only triggered one telescope are not triggering L3 and they are therefore discarded. To account for the arrival time difference of the Cherenkov shower to each one of the telescopes a zenith- and azimuth-angle dependent delay must be introduced in the L1 trigger that arrives first, in order to wait for the L1 trigger of the second telescope. This is done with a specific delay board.

This VME board, together with other auxiliary boards (pre-scaler, delay, converter and scaler boards) constitute what it is known as the MAGIC global trigger system (GTS). The GTS can manage, sync and merge up to 8 trigger sources but only 5 are currently being used: L1, L3, calibration, pedestal and pulse injection triggers. Before entering the readout, all these trigger signals are sent to the prescaler board, an electronic board that can eventually apply

pre-scaling factors to specific trigger sources. This board also synchronizes the L1 and L3 trigger signals so the pulse lies inside the readout window. It is responsible for sending the final trigger to the data acquisition system.

Finally, there is a complementary trigger level called analog **sum trigger** (ST). This experimental trigger channel was developed by MAGIC when there was only a single telescope, between 2007 and 2010, but it could not handle observations neither in wobble mode (see section 2.4.8) nor in stereo mode. In 2014, a new stereo-compatible version was installed and commissioned. This new ST has been operational since late 2014 until today and it can only work when pointing directly to the source position (on-mode), like the old ST. It works in parallel to the L1 trigger but its working principle is somehow different: it sums the analog signal coming from a subset of pixels or "patches", smaller than L1 macrocells, and it applies a threshold to this combined value. However, PMTs can liberate high spurious signal spikes due to the release of a proton in the first dynode. This proton travels back tot he photocatode and liberates a large amount of electrons. The resulting spikes on the signal were high enough to trigger the ST patch by themselves, even when there was no signal coming from the rest of the pixels in the patch. This problem ruined the performance of the ST but it was solved applying a cut or ceiling to the signal of each pixel: above the so-called *clipping level*, the pixel was saturated and any further excess of charge is not used in the summation. In this way, and after a fine tuning of the clipping levels to maximize the performance, the ST managed to lower the energy threshold of the observations by a factor 2, down to 25 GeV [36]. Everything paid off when MAGIC discovered the first pulsar in the γ-ray sky, the Crab pulsar [37], thanks to the ST.

2.4.5 Readout and data acquisition system

After receiving a positive trigger signal, the next step in the signal processing is to read the data in every pixel of both MAGIC-I and MAGIC-II telescopes and then store them to disk. This is done by the readout system together with the data acquisition (DAQ) software, the so-called *DominoDAQ* [21]. The old MAGIC-I readout was based on fiber-optic multiplexing readout system (MUX) with commercial flash analogue-to-digital converters (FADCs). The MUX system merged the signals coming from 16 channels into a single one by arranging them sequentially, in intervals of 40 ns. This analog output signal was sent to the FADCs, where the digitization took place at a sampling frequency of 2 GHz

and only the 50 samples or slices where the pulse was located were stored to disk. The dead-time of the entire system was about 25 μs.

The MAGIC-II readout, as well as the new MAGIC-I readout system, use instead the 4th version of the domino ring sampler (DRS4) chip. Each DRS4 chip has 1024 capacitors arranged as a ring and each of them is charged by the analogue signal during a certain amount of time controlled by a special clock. When the last capacitor is filled the sequence starts over from the first capacitor. Thus, at a 2 Gsample/s operation frequency, the signal is overwritten every 512 ns. When a trigger arrives, the sequence is stopped and the charge in each capacitor is read sequentially at 33 MHz and digitized by an ADC. After some improvements by the MAGIC collaboration on the original chip performance, a dead-time of 27 μs could be reached. Since the shower Cherenkov flash lasts only for a few tens of ns, in order to reduce the amount of data produced by the MAGIC telescopes, the pulse position on the DRS4 ring is found by the firmware and, out of the 1024 slices of the sampled pulse, only 60 of them are stored for further processing. Each DRS4 chip has 8 channels that process every pixel individually and the chips are placed in groups of 4 mezzanines in each PULSAR boards, which are placed in the VME crates, very close to the receiver boards. This is needed to avoid signal dispersion when using long cables. Therefore, each PULSAR board can process up to 96 channels. The DRS4 chips behave linearly but their performance is temperature-dependent. As a consequence, the readout electronics need to be switched on ~ 2 hours before data taking for the temperature to stabilize. Besides, it is necessary to perform regular calibration of these chips, which is done once per night before observations start. In this way, the pedestal offset of each chip is individually estimated and subtracted from the measured signal, later on.

L3 deadzone

The DRS4 chips provide fast digitization of the analogue signal while keeping costs low. Its ring structure together with the 2 Gsample/s speed translate into an intrinsic memory buffer of 512 ns. However, the time needed for the trigger signal to propagate and for the signal to be read, digitized and stored is around ~ 300 ns. A maximum delay of ~ 200 ns that can be applied to the signal before the data start to be overwritten. When observing in stereoscopic mode, a delay between the two telescopes is always required to keep the signals synchronized: the shower front reaches one telescope first and then there is a time gap created

by the Cherenkov light traveling to the second telescope and getting reflected to the camera. The duration of this gap depends in the position the telescopes are pointing in the sky and it is maximum when both telescopes are pointing along the same line (towards NW or SE) but are not facing one another. Since they are separated by a 85 m distance, there is a maximum possible delay between the signal of both telescopes of 283.5 ns. It only affects high zenith angle observations, higher than $45°$, in the case of telescopes pointing along the line between them. The previously stated maximum delay can only be reached when telescopes are pointing towards the horizon (zenith angle $= 90°$).

As a consequence, some regions of the sky cannot be observed with both telescopes in coincidence mode, because the delay between the MAGIC-I trigger and the MAGIC-II trigger is so big that the charging of DRS4 ring already starts from the initial position. In the MAGIC collaboration this design flaw is known as the **L3 trigger deadzone** and has been recently solved by reducing the sampling speed.

2.4.6 Atmospheric monitoring instrumentation

The weather monitoring is a task that telescope operators have to perform in order to determine the feasibility of the data taking and, more importantly, to ensure the safety of the staff and the infrastructure. To do so, operators have several instrumentation live-monitoring the weather conditions at the MAGIC site. A dedicated team within the MAGIC collaboration, the atmospheric and calibration (ATCA) working group, was formed in 2011 to coordinate all the tasks related to the maintenance of the existing weather monitoring hardware and its controlling software, to deploy new instrumentation and to exploit all the data gathered by these instruments [38].

All the weather information produced by those sensors is collected and displayed in a public webpage[9] (from now on, the WS webpage) that other telescopes at the ORM observatory can also use. Some other measures, retrieved from other facilities at the ORM, are also shown there for commodity. At the same time, a dedicated piece of software name *ATCAguard* displays all the available weather data and alarms the operators of changing or dangerous atmospheric conditions when certain conditions are met (see section 2.4.8 for details about MAGIC operating conditions).

[9] http://www.magic.iac.es/site/weather/

Figure 2.14: *Left)* The weather station device used by the MAGIC collaboration; it measures the wind speed and direction, the air humidity and atmospheric pressure. *Right)* The weather station (foreground) is mounted at the top of a steel pole installed in the roof of the CH. MAGIC-I can be seen in the background.

The most important piece of instrumentation is the **weather station** that one can see in figure 2.14. This commercial WDS 1MV device by Reinhardt GmBH[10] is located at the roof of the CH, on top of a 2 m mast. It is equipped with a set of sensors that measure air temperature and dew point, humidity, wind-speed, wind direction and speed of the wind gusts every 2 second and this information is transmitted through a serial cable to the CH. At the same time, these values are plotted in the WS webpage following a three-color code warning system for adverse atmospheric conditions (see figure 2.15). Since this is a critical subsystem several spare weather stations are kept at the CH anytime.

A dedicated piece of hardware is used to monitor the aerosol content of the atmosphere and its vertical distribution: a single wavelength **LIDAR system**. This device, pictured in figure 2.16, is located under a small dome at the roof of the CH and is composed of a 532 nm, micro-power, Nd-YAG laser, a $\varnothing 60$cm mirror with a 1.5 m focal length, a hybrid photo-detector (HPD), a robotic equatorial mount and a computer with a FADC card for the treatment and transmission of the signal to the central control. The LIDAR tracks the MAGIC pointing position while avoiding its FoV, and fires a set of short, 0.5 ns pulses, each of them carrying an energy of 5.1 μJ [39]. The pulsed light interacts with aerosol molecules via Mie scattering and some of it is reflected backwards,

[10] `https://www.reinhardt-testsystem.de`

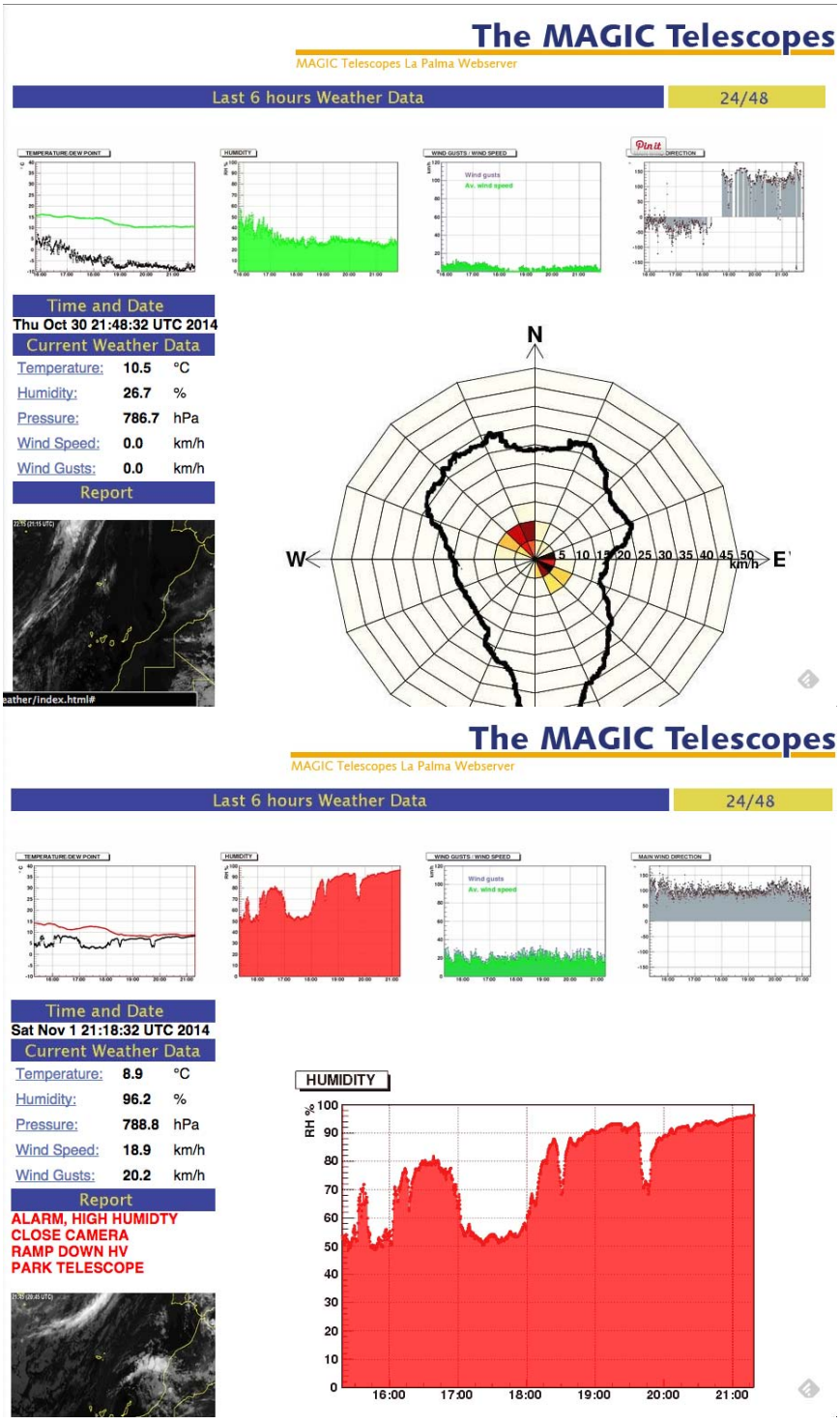

Figure 2.15: *Top)* The MAGIC weather monitoring webpage shows good weather conditions: little wind and low humidity. *Bottom)* The plots on the MAGIC weather monitoring webpage turn red when the humidity or the windspeed limits are reached. Some warning messages remind the operators about the basic procedure to follow in these circumstances.

Figure 2.16: *Left)* Lidar device used by the MAGIC collaboration for a live monitoring of the aerosol content of the atmosphere. *Right)* The LIDAR tower with its remotely-operated dome closed. MAGIC-I can be seen on the background.

towards the reflective surface of the LIDAR. The back-scattered light is collected and detected by the HPD and the signal is later on processed. The higher the cloud base, the longer for the return signal to arrive to the LIDAR; the thicker the aerosol over-density, the bigger the amount of back-scattered light. Thus, one can infer the position and thickness of the aerosol layers, the most common of them being clouds and, in the summer season, *calima* (dust intrusions from the nearby Sahara desert).

The LIDAR system is not critical for the operation of the telescopes but it is a very useful and precise way of estimating the quality of the data and correcting for it. When the MAGIC telescopes operate under non-optimal weather conditions, the LIDAR information could be used to calibrate the atmosphere: correcting reconstructed energy and effective areas, that are degraded by the presence of aerosols above the MAGIC telescopes. The LIDAR system was regularly used during operations since 2011 and the transmission of the atmosphere as a function of the height above the telescopes has been monitored. The procedure to correct the MAGIC data and its integration in the MAGIC standard data analysis procedures are still ongoing [40].

Another instrument monitoring the air quality since the first light of the telescope is the **pyrometer**. This commercial device, model KT19.82 manufactured by Heitronics, is a remote thermometer: it measures the infrared radiation emitted by the cloud base and, assuming that the air is an ideal gas, whose temperature is linearly decaying and that it is totally transparent to in-

frared wavelengths, it estimates the height of the cloud. Traditionally, MAGIC has used the pyrometer to estimate a custom parameter known as *cloudiness*, a simple tool to understand weather conditions at the site. Its value varies between 0% and 100%, where 0% means a perfectly clear atmosphere and 100% means that the sky is completely covered by clouds. However, recent studies have shown that this parameter is generally well correlated with the transmission obtained with the LIDAR system at the site.

Finally, there are other instruments that help the MAGIC observers to judge the state of the atmosphere and the general air quality but only qualitatively, because its data are not integrated into the MAGIC observational data and no strong criterion is relying on them, like the high-sensitivity, optical *all-sky camera*. Some plots and weather information are also gathered from public services and displayed on the MAGIC WS webpage: the dust content of the air at ground level is directly measured by the neighbor TNG telescope, the MeteoSat images for the Canary Islands and the EumetSat images for high and mid altitude clouds around the archipelago.

2.4.7 Other subsystems

Timing system: Composed by a high-precision rubidium clock together with a GPS device, the timing system is needed to precisely measure the triggers arrival time. The rubidium clock is an oscillator that is able to provide a precision of 10^{-11} s every second but only for short time-scales, so it need an auxiliary timing system to keep it synchronized in the long run. The GPS system, with a precision of the order of 10^{-9} s keeps the rubidium clock from losing synchronization over longer time periods. Once per second, it forces the clock time to have the same value as the measure provided by the GPS receiver. A binary time label or *time-stamp* is assigned to each recorded shower. The combination of both systems is able to reach a 1.5 μs precision [41].

Central Control software: A complex LabView® piece of software is responsible for gathering all the information from the different subsystems, sending orders to them via TCP/IP connections and acting as graphical interface between the MAGIC telescopes and its direct users, the operators. This central control (CC) program was known as *Arehucas* while MAGIC was still a single telescope system but it was renamed to *SuperArehucas* (SA) when the second

Figure 2.17: Interface of the central control software of the MAGIC telescopes, *SuperArehucas*. On the left half (purple rectangle), the values of several parameters of MAGIC-I (top) and MAGIC-II (bottom) cameras can be monitored. In this picture, the pixel charge of a randomly selected event is shown every 1 second in the big, main panel, whereas the smaller ones show the pixel dark current (DC) and logarithmic pixel rates. In the right half (green rectangle), all the MAGIC subsystems can be monitored and information is distributed in two columns, one for each telescope. For instance, the current source each telescope is pointing (usually the same for both) is marked with a blue box; next to it the drive status is displayed and the weather conditions are shown right above it; the L1 trigger status and configuration is marked with red boxes, together with the L1 and prescaler rates; the L3 trigger rate is shown in between and marked with a yellow rectangle.

telescope started to operate. Its user interface is shown in figure 2.17. In order to simplify the work of the MAGIC staff at the site, several automatic procedures are implemented within SA, such as a list of tasks to start up and to shut down the system. It shows warnings on malfunctioning subsystems, communication problems or abnormal trigger rates as well.

GRB alert system: This program runs in the background during MAGIC operations and it receives triggers from the Gamma-Ray Coordinates Network (GCN) or Transient Astronomy Network (TAN). When a GRB trigger is received, it checks that the MAGIC observational constraints are met, like the position in the sky, the time of the day and the distance to the moon. If an ongoing GRB passes these criteria, the GRB is observable so this system sends an alert to the CC and then the MAGIC telescopes are set to automatic GRB mode. This implies that the operators have no longer control of the system and the telescopes are automatically pointed towards the GRB position in "fast-movement mode" and they start the observation. In this way the MAGIC collaboration tries to minimize the time interval between the start of a GRB and the beginning of the MAGIC observations, by reducing human interaction to a minimum. If no mechanical problem occurs, the telescopes stays observing in this mode for 4 hours and only if the observational criteria stay fulfilled.

2.4.8 Operating the telescopes

The MAGIC telescopes are operative all-year-long since their first light in 2004, with the only exception of 3 every 28 days: during full-moon, the day before and the day after, where the background light is too intense for the telescopes to operate. Observations were stopped also for the periods where major hardware change were ongoing, like the recent 2012-2013 upgrade.

The telescopes are managed during nighttime by a shift crew, formed by 3-4 members of the MAGIC collaboration. Depending on the level of expertise and technical skills, crew members act as regular operator, as deputy shift leader or as shift leader (SL), in increasing order of experience operating the telescopes. The shifts are 4, 3 and 3 weeks long for each kind of shifter respectively. Usually, a MAGIC member joins his or hers first shift as operator, when he/she learns all the basic working routines and responses to emergency situations but has no real responsibility. For the next shift, he/she is upgraded to deputy SL and shares the responsibility of operating the telescopes and of transferring to operators the basic know-how, but he/she is not accountable for the ultimate

safety responsibility. After two shifts, he/she will be promoted to SL and will be the person responsible for any decision on the site concerning operating the telescopes, as well as the safety of the staff. To avoid long working nights, especially in winter time, shifters usually organize themselves in different working schedules for each night, either working the first half of the night (until around 1 am), the second half or the full night. One every four days is off for every member of the crew.

The MAGIC telescopes take up to ~ 1800 h of data during dark nights and up to ~ 600 h of twilight or moderate moonlight data every year. The time allocation committee (TAC) is responsible for selecting the best sources to observe among all the proposals made by the members of the MAGIC collaboration and trying to obtain the maximum scientific output within the available time. However, on average about 40% of the available time is lost due to adverse weather conditions or technical problems. All these data in raw format need about 250 TB of storage per year and they are kept on magnetic tapes. The reduction of these data is performed on site and is sent to the MAGIC database at PIC ("Port Infraestructures Científiques", catalan for Scientific Infrastructures Port), in Barcelona (Spain).

During the single-telescope era, MAGIC could only perform observations in mono mode. Since the beginning of operations of the second telescope, stereoscopic observation is the default observation mode. These observations can be done in two ways. The first mode consists in pointing the telescopes directly towards the position of the candidate source. This observation mode is known as **on mode**. Since an unbiased estimation of the background is also needed, the telescopes are pointed towards a close-by position in the sky where no known γ-ray source is present. Under the assumption that the background is the same in both sky regions, the signal is estimated as the difference between the on and the off regions.

In order to minimize the amount of time spent estimating the background for each source, and considering that the background usually varies during a single night (for instance, because of the varying atmospheric conditions) and along the trajectory of the source in the sky, the false-source tracking mode, also known as **wobble mode**, was proposed as a solution [42]. A schematic

view of this second observation mode can be seen in figure 2.18, which is the current standard mode for regular MAGIC observations: the telescopes do not point directly towards the candidate source position but to a close by region, 0.4° away from it, known as wobble 1 (W1, see figure 2.18 *Top*). To compensate for any asymmetries in the background and in the camera response, the telescopes are then pointed to new region of the sky, opposite to W1 with respect to the source and known as W2. Usually, the telescopes are then pointed towards two other wobble positions, perpendicular to the previous W1-W2 pair and also centered on the assumed source position. This new wobble pair is called W3-W4. The telescopes point towards each wobble position during the same amount of time, 20 minutes each, and then then observations start over: telescopes are pointed towards W1 and this procedure is repeated. In this way, MAGIC observes both the source and the background *at the same time*, while keeping a maximum degree of symmetry.

During the first years of operations of the MAGIC telescopes only two wobble positions were used, namely W1 and W2. The pointing changed between these two positions also every 20 minutes but the exposure of the camera had a smaller degree of symmetry. In order to reduce the systematics of our measurements, the other two wobble positions were added but in some situations observations are carried out using the previous configuration with only two wobble. For instance, there are cases were the candidate source is located in a crowded FoV, where stars or other γ-ray sources enter the trigger region of the telescopes.

This often happens with sources in crowded parts of the sky, like near or within the galactic plane or for the Crab nebula itself, the source under study in this thesis: a Be star known as Zeta Tauri, ζ Tauri or 123 Tauri is just 68 arcmin away from the Crab position in the sky so, if one wants to keep symmetric observation positions, the telescopes can only wobble along the axis perpendicular to the line between the Crab and ζ Tauri. Thus, only two wobble positions can be used because these are the only two positions in the sky which are equidistant to both stars. The selection of the number of wobble position, their axis and their distance to the candidate source has to be planned carefully, especially for sources located in populated regions of the sky. In the analysis presented latter in chapter §4, all the analyzed data was taken either in on or in wobble mode, in this case always with two wobble positions.

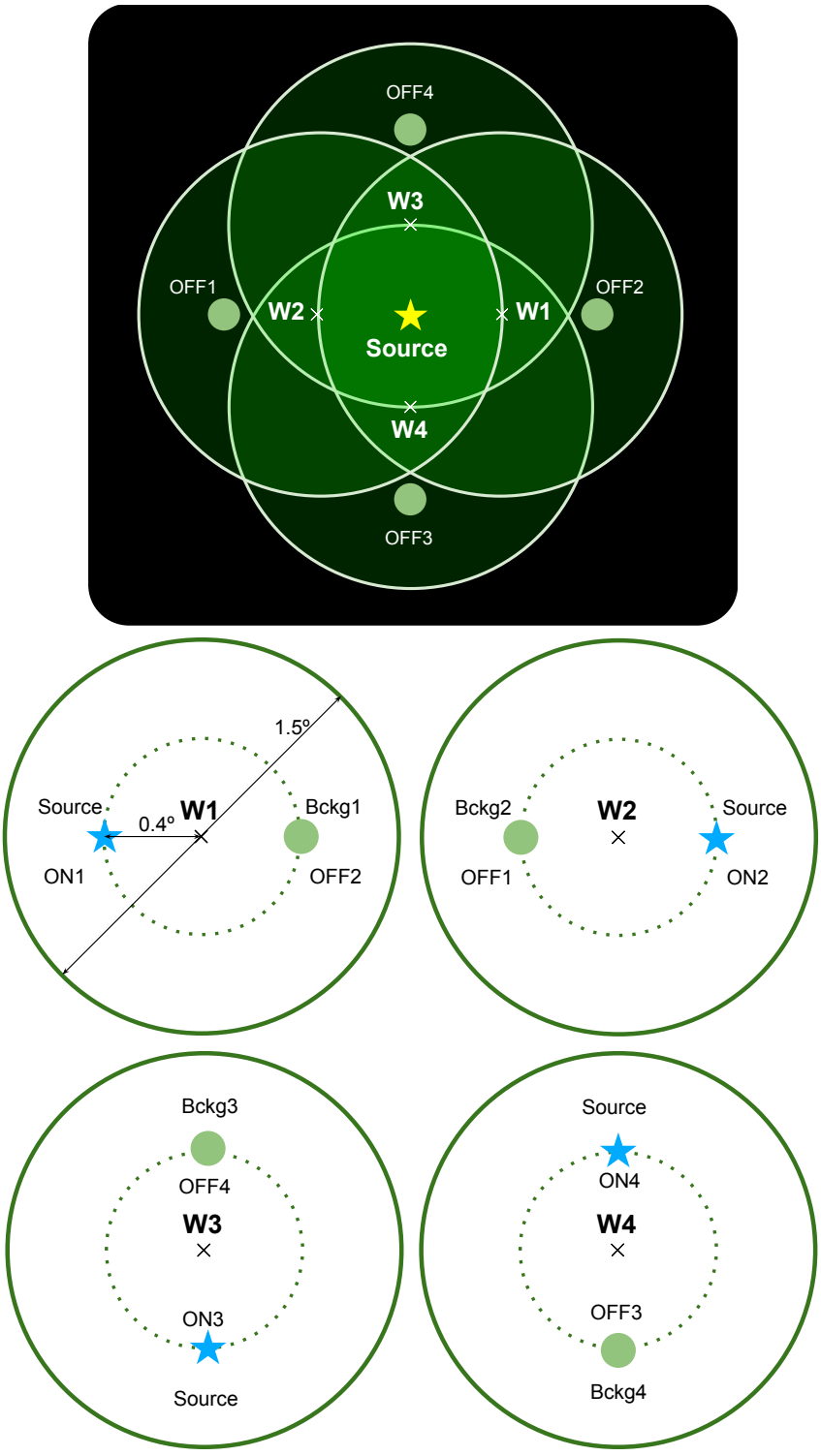

Figure 2.18: *Top)* Schematic view of the 4 standard wobble positions W1, W2, W3 and W4 in the region around the candidate source position, at $0°$, $180°$, $90°$ and $270°$ respectively. The off signal is estimated from the regions marked as OFF1, OFF2, OFF3 and OFF4. The big, green circles represent the MAGIC FoV. *Bottom)* Schematic view of each wobble position. In order to remove any asymmetry, the background region in W1 (right side of the camera plane) is used as off signal for W2 observations and viceversa. In this way, both the source and its corresponding background are located in the same position on the camera plane.

The usual operating rates in optimal, dark observing conditions are between $10,000 - 20,000$ Hz for the individual level 1 trigger in each telescope, whereas the coincidence level 3 trigger rate is much lower, between $200 - 350$Hz. These events surviving the L3 trigger are recorded by the DAQ system to be further analyzed later. But a fraction of them are only accidentals, i.e noise random events that happen to trigger both telescopes at the same time just by chance. An upper limit to this fraction can be computed taking into account the individual L1T rates (R_{L1M1} and R_{L1M2} respectively) as well as the time-coincidence window of 180 ns between the two telescopes with the DRS4 sampling electronics, 100 ns for each telescope with a minimal overlap of 20 ns. The so-called **accidental trigger rate**, R_{acc}, is then

$$R_{\mathrm{acc}} = R_{\mathrm{L1M1}} \cdot R_{\mathrm{L1M2}} \cdot 180 \text{ ns} \tag{2.4.1}$$

During the darkest nights of observation, when we observe a low zenith angle source, the moon is set and there are no clouds reflecting ambient light, the accidental rate is usually below ~ 20 Hz, less than 10% of the recorded events rate. But under adverse conditions like a bright FoV (for instance a source in the galactic plane), intense moonlight or light scattering by high altitude clouds, the rate of accidental stereo triggers can raise up to a considerable fraction of the recorded event rate and it can even dominate it. In the latter case, it is no longer useful to continue with the data taking since the telescopes are only recording noise events, which will be discarded during the analysis process described in §2.5. Data taken under these sub-optimal conditions also show an increased energy threshold, so usually HE sources are scheduled during moon time or proposed as alternative sources in case weather conditions do not allow for LE observations of other sources. There are also some recommended operating limits concerning the proper rate values but, for the moment, the final responsibility on whether to keep on or stop observing belongs to people operating the MAGIC telescopes each night. The design of a smart-scheduling system is ongoing, which will use all the available information on the observation conditions and will re-define on-the-fly the best sources to observe at each time of the night.

2.5 The MAGIC analysis chain

The data taken by IACT telescopes such as MAGIC contain information on the EAS produced within a certain region of the sky. Among of the recorded events, most of them are just part of the dominant background of any ground-based γ-ray observation: hadronic showers and cosmic electrons (see §2.3).

To infer the flux, spectra, morphology and time variability of a candidate γ-ray source, one has to reduce its background as much as possible and to estimate the probability that the surviving, γ-like shower events were in fact induced by the emission of our candidate source. If this is not the case, one is still able to set limits on the γ-ray source emission by means of upper limits to its flux. All this is done following a series of sequential analysis steps that we describe in this section. All these steps are executed using a dedicated **MAGIC analysis and reconstruction software** suite (hereafter, MARS) [43], written in C++ language and which works under the ROOT framework [44].

2.5.1 Signal processing

The first step in the data processing scheme is to convert the sampled digital signal back into a number of photoelectrons and pulse arrival time in each pixel. This task is performed by a piece of software within the MAGIC software suite, known as `callisto`, which stands for "calibrate light signals and time offsets" [45]. For the analysis of the data recorded using only DRS4 chips, i.e. after the 2013 upgrade of the MAGIC telescopes, a new calibration software is used, known as `sorcerer` ("simple, outright raw calibration; easy, reliable extraction routines").

In order to do so, one has to measure the pedestal level of each readout signal line, as well as the equivalent charge in ADC counts of each photoelectron. To solve these problems dedicated *pedestal* and *calibration* runs are taken at the beginning of each observation, as well as interleaved events taken at 25 Hz during the observations themselves to monitor the evolution of the signal transmission and readout performance during the night. The signal of a Cherenkov flash shows a pulsed shape in each of the affected pixels and a "sliding window" algorithm looks for these pulses. One can see how one of these Cherenkov flashes looks like in a given pixel in figure 2.19.

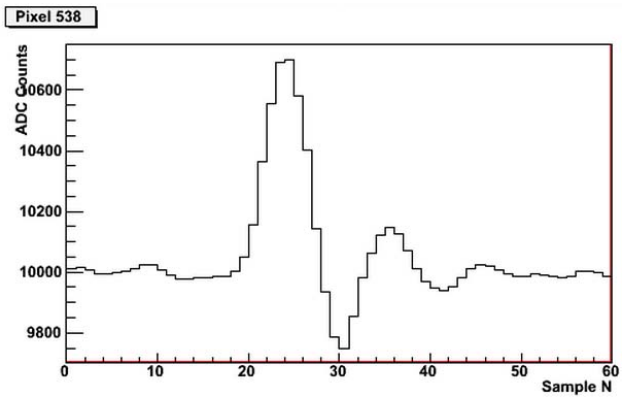

Figure 2.19: Sampled pulse event as it is recorded by a single pixel of one of the MAGIC cameras in 2014. The number of counts given by the FADC are plotted on the Y axis, whereas the X axis shows the 60 time slices in the DRS4 memory containing the signal.

Once we have extracted the signal in each pixel during the optimized time window, we would like now to calibrate our instrument, i.e. to know which is the number of photoelectrons (from now on, phe) associated to the digital signal. This is done by means of the so-called excess noise factor method or "F-factor method" [46]. The charge or number of phe in a pixel, Q, follows a Poisson distribution (with a standard deviation $\sqrt{Q}$) and its value can be deduced from its number of ADC counts, N (with a measured standard deviation σ by means of the squared F-factor:

$$Q = F^2 \frac{\bar{N}^2}{\sigma^2} \tag{2.5.1}$$

where the F-factor has been previously measured in the lab using "single phe spectra".

The calibration of the files is a delicate part of the analysis chain that requires a precise set of input parameters and response-characterization files for the hardware that was actually used to record those events. It is automatically done at the telescope site by the on-site analysis computers and a 95% reduction of the data file size respect to raw data is achieved. Both raw and calibrated data are transferred every morning after observations to the central data distribution center PIC in Barcelona (Spain).

2.5.2 Image cleaning

Now we have an image in the camera, with a charge in photoelectrons and an arrival time for each pixel and for every recorded event, like those shown in the top row of both figures 2.20 and 2.21, for MUX and DRS4 data respectively.

The next step is to select those pixels that contain useful information about Cherenkov flashes and to discard those which only contain noise. This process is called **image cleaning** and it is performed by the `star` software within MARS, which stands for "standard analysis and reconstruction".

There are two main image cleaning methods that have proven efficient for this task: the so-called *absolute* cleaning and the *sum* cleaning. In both cases we look for two kinds of pixels in every event image: *core* and *boundary* pixels. The criteria to determine whether a pixel is core, boundary or none varies for each method. In the absolute cleaning method, core pixels are those whose charge is above a certain threshold (usually 6 phe or 9 phe for MAGIC-I or MAGIC-II respectively) and whose pulse arrival times lie within 4.5 ns away from the mean arrival time of their surrounding pixels. Each group of contiguous core pixels is called an *island*. Boundary pixels are those contiguous to a core pixel, with a charge above 3 phe (4.5 phe) for MAGIC-I (MAGIC-II) and with an arrival times less than 1.5 ns away from the mean arrival times of the neighbor core pixels. Finally, the rest of the pixels are defined as unused. In the sum cleaning method, every pixel in a xNN group is labeled as core if their total charge is above a certain threshold, which depends on the value of x of the trigger logic. It also has to fulfill this condition within a certain time-window away from the mean arrival time of the xNN group. After such a cleaning, we obtain a shower image like the one shown in the second row of figures 2.20 and 2.21.

The above defined thresholds were found after an optimization to obtain the best Crab nebula sensitivity. If one chooses lower threshold values one would start being sensitive to lower energy γ-ray events but at the price of a higher number of *spurious islands*, created by upward random fluctuations of the NSB. This makes the image reconstruction that we will explain in the text section much worse. This also happens when the NSB level is high, like for data taken during moon or at twilight, so higher cleaning levels need to be used to properly analyze those data. Using those definitions of core pixels, we can assure that less than 6% of the pure-noise events survive and a big majority of them are rejected. And about 80% of the triggered events survive the image cleaning in both telescopes and these are the only events that are further processed. The rest of them are discarded.

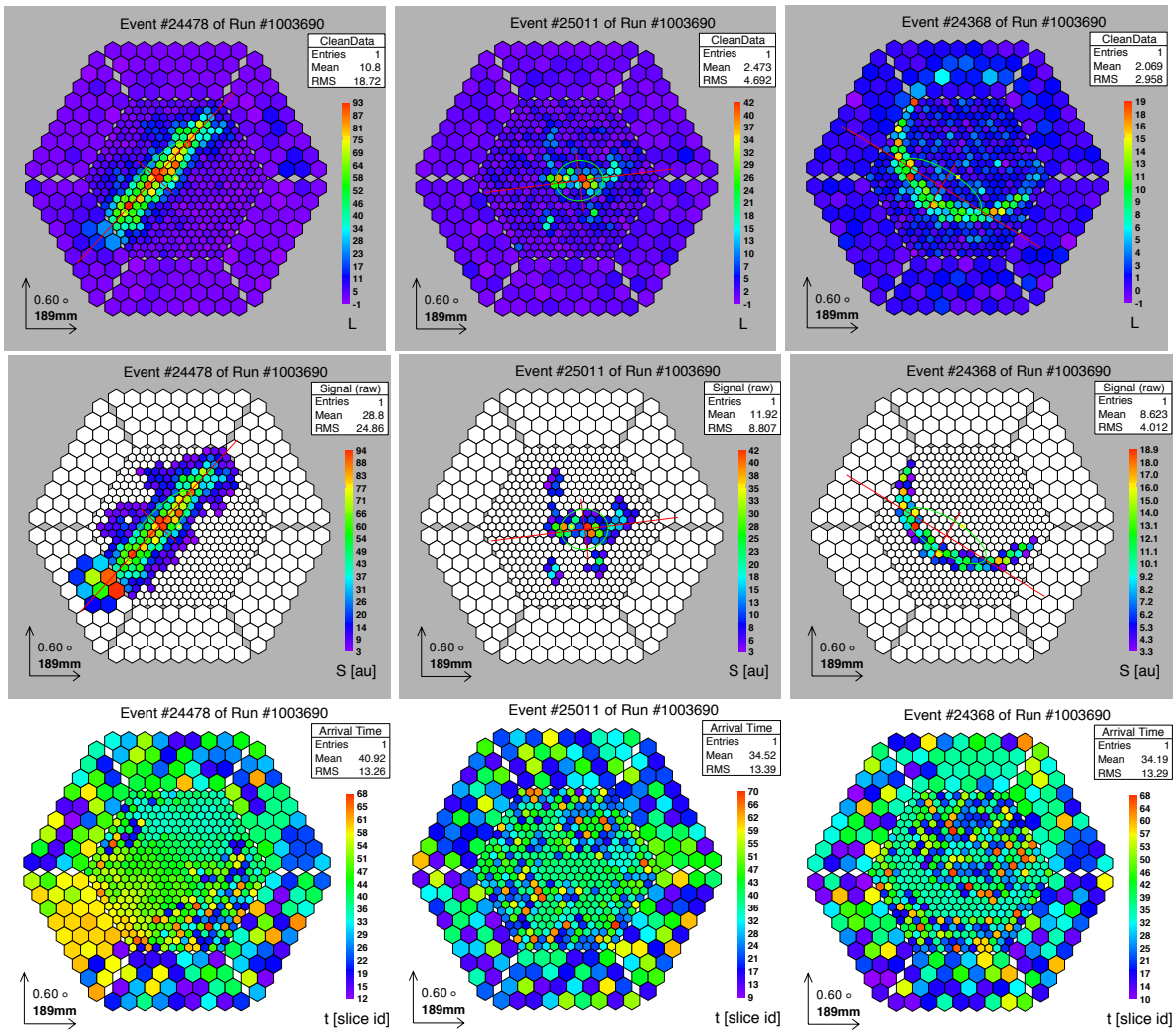

Figure 2.20: Examples of shower images recorded by MAGIC when it still was a stand-alone telescope using MUX sampling electronics. The charge distribution before (*top*) and after (*middle*) image cleaning are shown, as well as the arrival times distribution (*bottom*). Candidate events for γ-ray (*left*), hadron (*center*) and muon (*right*) induced EAS were selected as an example. The compact shape of the image produced by the γ-like event, with just 1 island, is clearly different from the more disperse image of the hadron-like event, where islands are more numerous. Ring-shaped shower image, most likely produced by a muon. The left picture shows the charge of each pixel in the camera, which is proportional to the Cherenkov light intensity; the right-top picture shows the arrival times of the signal in each pixel and a synchronous, ring-shaped region can also be seen, coincident with the ring on the left image.

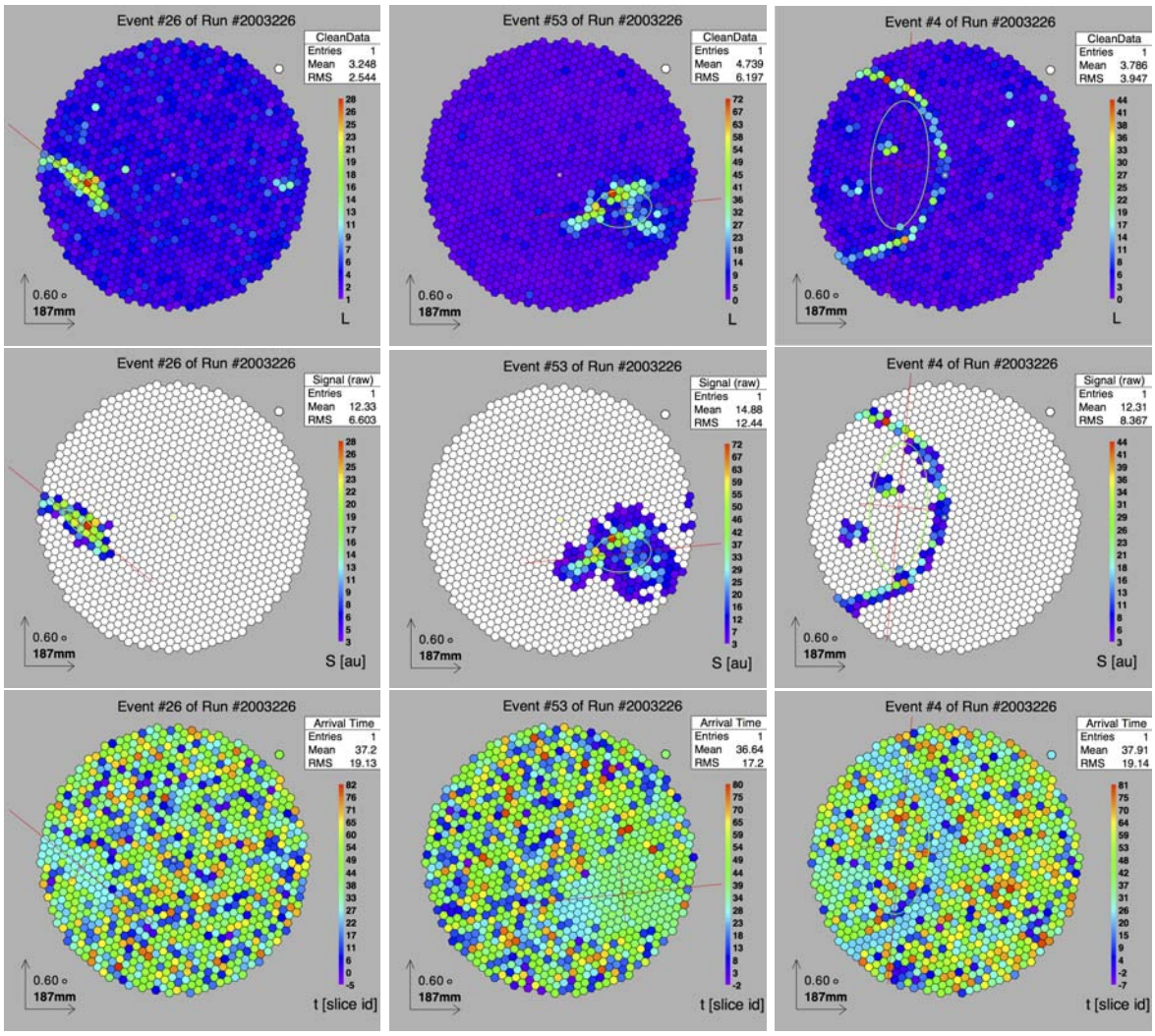

Figure 2.21: Examples of shower images recorded by MAGIC-II, using DRS4 sampling electronics. The charge distribution before (*top*) and after (*middle*) image cleaning are shown, as well as the arrival times distribution (*bottom*). Candidate events for γ-ray (*left*), hadron (*center*) and muon (*right*) induced EAS were selected as an example.

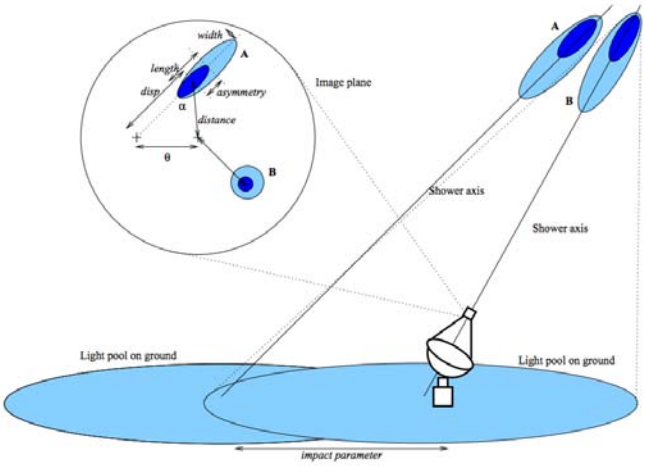

Figure 2.22: Scheme of two EAS, A and B, with different incoming direction and their projection into the camera plane. Some of the Hillas parameters are marked. Taken from [47].

2.5.3 Hillas parameters

After the image cleaning, we compute a set of parameters for each events that describe the morphologic features of the the charge distribution, like the image shape and orientation, as well as the arrival time distribution of the signal, among other parameters. Some of the geometrical ones are known as the **Hillas parameters** [48] and these describe the first, second and third order momentum of the charge distribution in the image. The computation of those parameters for each recorded event is also done by the `star` software. Some of the most relevant parameters are described in the following list:

- `Size`: sum of all the pixel charges in the shower image. It is proportional to the Cherenkov light produced by the shower and, in first order approximation, to the energy of the primary γ-ray.
- `ConcentrationN`: sum of charges of the N brightest pixels divided by the `size`.
- `Center of gravity (CoG)`: the first order momentum or image centroid, computed as the mean position of the pixels weighted by their charge.
- `Asymmetry*`: distance between the CoG and the pixel with the maximum charge value. It is positive when this pixel is closer to the assumed source

position than the CoG and negative in the opposite case.

- `Width`: second order momentum of the charge distribution corresponding to the longitude of the minor axis of the fitted elipse. It measures the lateral development of the shower.

- `Length`: second order momentum of the charge distribution corresponding to the longitude of the major axis of the fitted elipse. It is a projection of the shower axis on the camera plane.

- `Distance`*: angular separation of the CoG of the shower and the expected source position.

- `Alpha` (α)*: angular distance between the main axis of the elipse and the line connecting the CoG of the shower and the expected source position (the center of the camera for on-mode observations). Background events have random orientations whereas events coming from the candidate source use to have small values of α.

- `M3Long`: third order momentum in the charge distribution. It measures the asymmetry of the light distribution along the major axis of the elipse. Cherenkov light produced at the beginning of an EM shower is usually located towards the inner part of the camera whereas light produced at the end of the shower is located farther from the camera center, since is observed under a larger angle.

- `LeakageN`: fraction of the image charge within in the N outer rings of pixels.

- `Number of islands`: number of clusters of core pixels of the image. Hadrons, especially at high energies, use to produce wider showers and sometimes secondary hadrons develop their own subshowers, increasing the number of islands in the camera image. γ-ray showers are more compact, so their images usually have a single island.

- `Time gradient`: correlation measurement between the arrival time in each pixel and its position along the major axis of the ellipse. Its value is obtained with a linear fit of these two parameters and it corresponds to the speed of the arrival time variations along the major axis of the elipse.

- `Time RMS`: RMS of the arrival times of all the pixels in the image.

- `Disp`: distance along the major axis of the ellipse from the projected to the real source position for each shower.

Parameters marked with (*) require an extra assumption: the position of the candidate source we are observing on the camera plane. That is why they are called *source-dependent parameters*. All of these parameters have been calculated for MAGIC data but, since the second telescope became operational, a new set of stereo parameters started to be computed to fully benefit from the new hardware setup. These stereo parameters allow us to have a better understanding of the 3-dimensional development of the shower. The most relevant of them are listed below. A schematic description of some is shown in figure 2.23.

- `Estimated source position`: Intersection point of the ellipses axes of the two shower images.

- `Impact point`: the intersection point between the shower axis and the ground plane, it can be determined if one computes the intersection points of the major axis of the two ellipses, taking into account the relative position of the telescopes (see figure 2.22 *right*).

- `Impact parameter`: The minimum distance between the shower axis and the pointing direction of each telescope. In mono data, this parameter is estimated by the `Distance`.

- `Maximum height`: height of the maximum Cherenkov light production within the shower. It can be estimated combining the position of the CoG in both cameras along the shower axis.

- `Theta squared` (θ^2): squared angular distance between the expected and estimated source position for each shower. γ-ray-induced showers from the observed source have small values of θ^2 whereas background events are randomly distributed, i.e. random θ^2 values. This parameter can also be computed for events observed with just one telescope but the uncertainty in the estimation of the source position is much bigger in this case, so it is not as efficient in mono mode as it is in stereo to perform the background rejection.

The distributions of those parameters may be quite between hadron- and γ-induced showers. This allows us to discard an important fraction of the

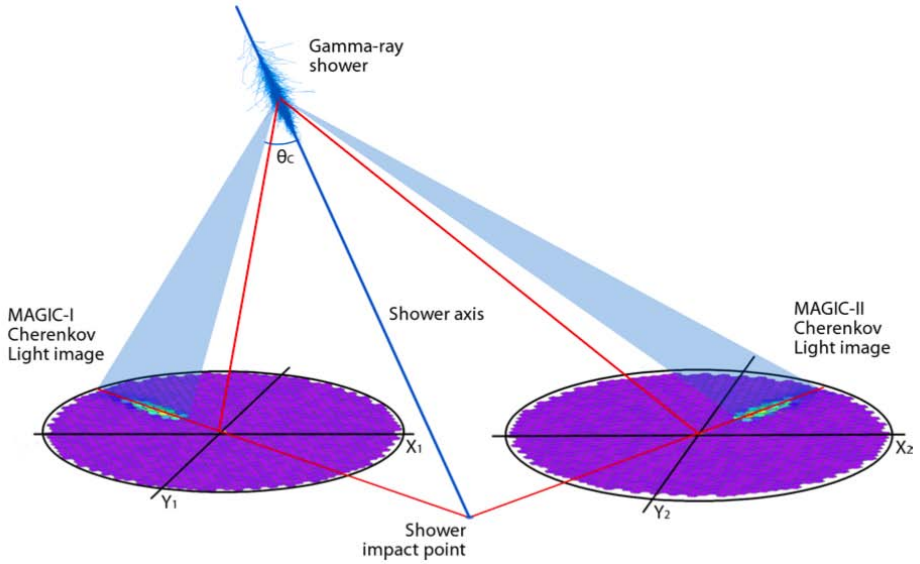

Figure 2.23: Schematics of the shower axis and shower impact point, as well as the projection of the shower image in the camera plane in stereo observation mode. Taken from [41].

background applying specific cuts on the variables that have a bigger separation power. A dedicated multi-classification algorithm known as **random forest** (from now on, RF) has been implemented for this task, as we describe in section §2.5.5.

The value of the `disp` parameter is also found using a dedicated multi-dimensional RF decision algorithm [49]. Once the `disp` value is found for a certain shower, there are two positions along the image major axis where the estimated source position could be. This degeneracy is broken in a different way for mono and for stereo observations. In the former case, directional and symmetry measurements such as the `Asymmetry` or the `M3Long` parameters have been used to decide between the two possibilities. For stereo observations, a more refined method is used instead: the distance between the 4 possible pairs of estimated source positions (two for each telescope, as shown in figure 2.24) is computed and the pair with the minimum separation distance is selected. The final position is calculated as the weighted mean of those two values. If the minimum minimum distance is above a certain threshold then that event is discarded. This threshold efficiently rejects a big fraction of hadron events.

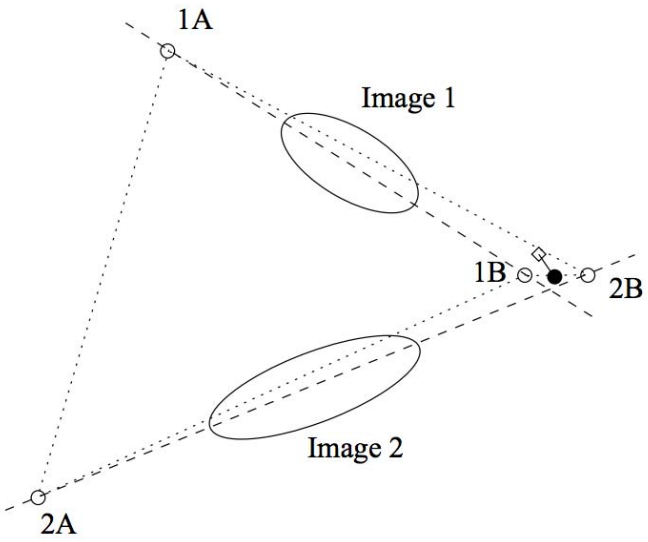

Figure 2.24: The 4 possible impact points for an event are represented with empty circles, two for each telescope along the shower axis (dashed line). The real impact point is marked as an empty diamond. The distance between every pair of points is computed (the length of the dotted line), and the pair with the minimum value is selected, in this case pair 1B-2B. The estimated impact point is marked with a filled circle. Taken from [26].

A new set of Hillas parameters was designed by Dr. M. Gaug and Dr. K. Berger, the so-called **dynamic variables**. These new version of the usual parameters showed a significant improvement in the posterior background rejection efficiency.

2.5.4 Quality selection

IACT telescopes are affected by several natural phenomena that deteriorates the quality of a given observation. During the analysis process some selection criteria has to be applied on the data to discard the affected nights, otherwise one may degrade the instrumental sensitivity of the telescopes. There is no standard set of criteria to do this data quality selection that works always and for every source. Along MAGIC lifetime, analyzers get experience in what parameters are the most reliable data quality estimators that maximize the achieved sensitivity of the instrument. The usual checks analyzers do for an efficient data selection are:

- Find which data are affected by **technical problems** like faulty subsystems, a wrongly set observational configuration, data taken during the commissioning of a major hardware change or any other kinds of test data[11].

[11] Usually data taken to check the performance of some subsystem are labelled as test. But

- **Adverse atmospheric conditions** are usually discarded by checking the logbook, i.e. the notes written by the shifters during data-taking, at least for the most extreme cases. A usual selection parameter is the cloudiness described in §2.4.6 and usually a maximum-value is set, so any data taken with a cloudiness above it is discarded by default.

- A common selection criteria is to use **cuts on the event rate**, since non-optimal weather conditions are usually correlated with the actual L3T rate at which the data are recorded. Analyzers usually discard data where the rate of events is far away from the mean rate, i.e. above or below it by one or two standard deviations. This is usually done after applying a certain `size` cut so we do not take into account energy range where trigger rates are influenced by NSB photons. Since the actual rate depends on the zenith angle of the observation, some correction is also needed. This is done by means of up-scaling the measured rate by a factor $\cos^m(ZA)$, where ZA is the zenith angle and m is an index between 0.3 and 1.5.

- **Cuts on certain Hillas parameters** are also a rather efficient way to distinguish between γ-ray-induced EAS and background events that survive the cleaning process. The most used quality cuts are applied to the `size` of the showers, the mean values of width or length mean values or their dispersion values or RMS [50].

2.5.5 Energy, Disp and Hadronnness estimation

After the analysis of the low-level data, the main source of background is the hadronic CR showers that are fare more abundant than the γ-ray events. The separation between these two components is performed by estimating a new parameter for each event: its **hadronness**, of its similarity to a hadron-induced event in opposition to a γ-like event. The method to assign a value of hadronness to every event using a previously *grown* RF method will be described in the next paragraph. The same computational method is used to estimate two other crucial parameters: the event energy and the geometrical `disp` value, defined in §2.5.3. The growth and training of these RFs is done by the `Osteria` (`Coach`) software within MARS for mono (stereo) data. The final decisional trees are the output of these tools, which are then applied to the data using the

this may not be the case for old data, when the observational procedures were not as mature as they are nowadays.

`melibea` software, which stands for MErge and Link Image parameter Before Energy Analysis.

γ-hadron separation

A machine-learning technique is used to distinguish between the γ-ray- and the hadron-induced EAS images recorded by MAGIC. A set of multi-decisional classification trees known as random forest [51] are produced for each data sample with the use of MC simulations and background data from off or undetected sources, in the so-called *training* of the RFs.

Since the images of the showers in the camera plane strongly depend on the zenith angle of our observations, the off and MC samples have to be carefully selected so that the zenith angle distribution matches as much as possible that from the data one is trying to analyze. It also has to be taken into account that the off sample was taken using the same hardware and observational configuration as the data to be analyzed, so that the images produced by hadrons of similar energy are alike. Afterwards, these RFs are applied to the actual events, and a hadronness value is assigned to each of them. The distribution of this parameter is peaked at 1 for hadronic events and it is peaked at 0 for γ-ray events. Later on, a selection based on a maximum hadronness value is applied.

Observation mode	
Mono	**Stereo**
`Width`	$\texttt{Width}_t$
`Length`	$\texttt{Length}_t$
$\log_{10}\left(\frac{\texttt{Size}}{\texttt{Width}\cdot\texttt{Length}}\right)$	$\texttt{Impact}_t$
`Conc`	$\texttt{Size}_t$
`Dist`	`MaxHeight`
$\pm$`M3Long`	$\|$`P1Grad`$\|$
`RMSTime`	
$\pm$`P1Grad`	

Table 2.1: Standard training parameters for γ-hadron separation RF, both for mono and stereo epochs in MAGIC. Subindex $t = 1\ ,\ 2$ stands for the parameter measured by each telescope, MAGIC-I or MAGIC-II respectively.

The training of these RFs consists of applying a set of cuts on a set of predefined parameters, which the program selects arbitrarily and chooses the most efficient cut value on that parameter to distinguish between the γ-rays and the hadron sample. About 100 such decisional trees are usually produced. Each of them begins with applying a cut to both samples for a randomly selected parameter within the candidate parameters list. The actual value of the cut is chosen in such way that the Gini index between the two samples is maximized.

In a second step, the same action is performed with a different randomly selected parameter within the list.

This iterative process continues until each branch either contains only one component, hadron or γ-ray, or when the number of events falls below a minimum threshold of 3 events. Then, a separation power is assigned to each of the final branches, $h = N_{had}/(N_{had} + N_\gamma)$, where N_{had} is the number of remaining hadronic events and N_γ is the number of remaining γ-ray events.

Observation mode	
Mono	**Stereo**
$\texttt{Width}$	$\texttt{Width}_t$
$\texttt{Length}$	$\texttt{Length}_t$
$\log_{10}(\texttt{Size})$	$\log_{10}\left(\frac{\texttt{Size}_t}{\texttt{CherenkovDensity}}\right)$
$\log_{10}\left(\frac{\texttt{Size}}{\texttt{Length}\cdot\texttt{Width}}\right)$	$\frac{\texttt{Impact}_t}{\texttt{CherenkovRadius}}$
$\texttt{Conc}$	$\texttt{CherenkovDensity}$
$\pm\texttt{fP1Grad}$	$\|\texttt{fP1Grad}\|$
$\texttt{Dist}$	$\texttt{CherenkovRadius}$
$\texttt{True Energy}$	$\texttt{True Energy}_t$
$\texttt{Leakage1}$	
$\texttt{Zenith angle}$	

Table 2.2: Standard training parameters for energy estimation RF, both for mono and stereo eras in MAGIC.Subindex $t = 1$, 2 stands for the parameter measured by each telescope, MAGIC-I or MAGIC-II respectively.

Once the training is done, one has to assign a hadronness value H to every event. To do so, the set of cuts that form the i-th tree are applied to a given event, which ends up classified into a branch with a separation power of $h = h_i$. This process is repeated for each of the N_{trees} trees in the RF, so one obtains a list of separation powers $\{h_i\}$ for this event. Its hadronness H is then computed as the mean value of this list, $H = N_{\text{trees}}^{-1} \sum_i^{N_{\text{trees}}} h_i$. Values of $H \approx 1$ mean that the event has ended up in the branches where the hadrons got classified during the training, so it is a good hadron candidate. On the contrary, values of H close to zero mean we have a γ-like event. There is a subset of the Hillas parameters described in §2.5.3 that have proven to be more useful in the γ-hadron separation process than others, so they are used as training variables (see table 2.1).

Energy & Disp estimation

The estimation of the energy of each event can be done in two different ways: either using look-up tables (LUTs) that have been previously constructed using

MC, or training a dedicated RF to do this estimation. An estimated energy is calculated from the shower image in each telescope separately. Afterwards, a mean estimated energy is computed that is properly weighted with the inverse of the error in the estimation of the individual energies.

Observation mode	
Mono	**Stereo**
Width	$\texttt{Width}_t$
Length	$\texttt{Length}_t$
$\log_{10}(\texttt{Size})$	$\log_{10}\left(\frac{\texttt{Size}_t}{\texttt{CherenkovDensity}}\right)$
$\log_{10}\left(\frac{\texttt{Size}}{\texttt{Length}\cdot\texttt{Width}}\right)$	$\frac{\texttt{Impact}_t}{\texttt{CherenkovRadius}}$
Conc	CherenkovDensity
$\pm$fP1Grad	$\|$fP1Grad$\|$
Dist	CherenkovRadius
True Energy	$\texttt{True Energy}_t$
Leakage1	
Zenith angle	

Table 2.3: Standard RF training parameters for the disp estimation, both for mono (*left*) and stereo (*right*) MAGIC observations. Subindex $t = 1\ ,\ 2$ stands for the parameter measured by each telescope, MAGIC-I or MAGIC-II respectively.

Once all these RFs or LUTs have been created, one can apply them to the data and assign to every event a hadronness value, two energy values and two disp values, one per telescope. This is done by the melibea software within MARS.

A hadronness cut is an efficient way to discard a big part of the hadronic background in our data. The actual value of the hadronness has to be optimized for the source one intends to analyze. The sets of hadronness cuts that were used in the analysis presented in this thesis are explained later on in §4.5.

2.5.6 Extracting the signal

As explained in previous chapters, the EAS produced by γ-rays are vastly outnumbered by those produced by other types CRs. After the data cleaning and the hadronness cuts, most of the hadron-induced showers are discarded with the hadronness cut described in the last section. To determine which of the remaining events are produced by our candidate source, one has to take profit of their unique characteristic: for a regular source, this is the orientation of the shower image on the camera. Showers induced by the γ-rays from the source will have a preferred direction, towards the candidate source position. However, background events like those produced by highly-energetic electrons or by hadrons with low values of the hadronness parameter will be randomly oriented.

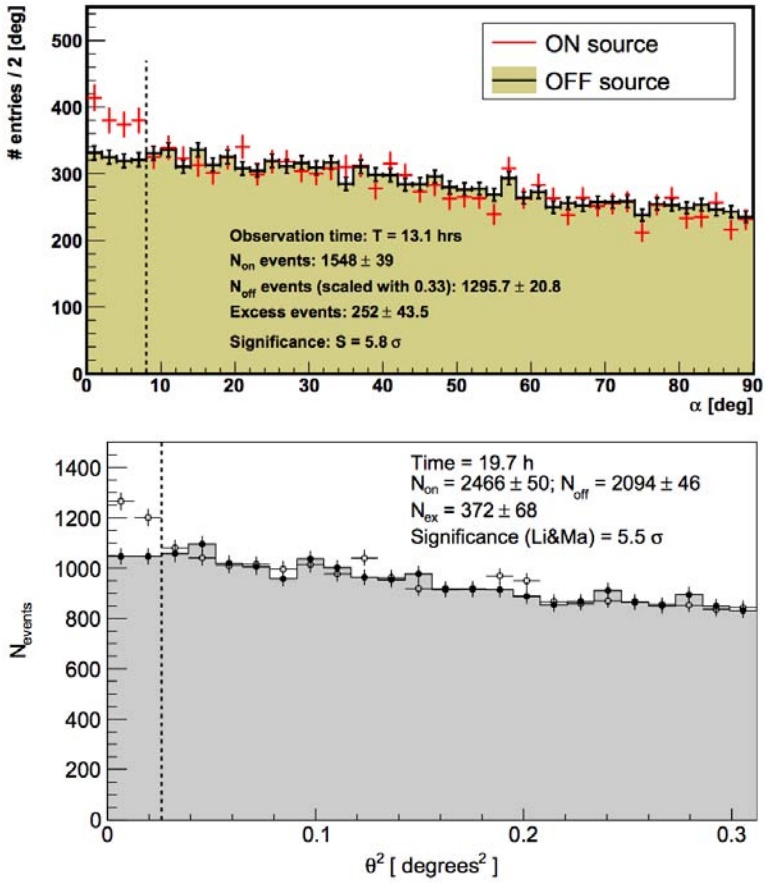

Figure 2.25: Distributions of the geometric parameters $|\alpha|$ (*top*) and θ^2 (*bottom*) for two detected γ-ray sources. Red and black points (empty and filled circles) represent the on and off regions in the left (right) plot, respectively.

The last step in the extraction of the signal from an IACT data is to perform a cut on the image orientation parameters α or θ^2, for mono and stereo observations, respectively[12] (see §2.5.3). In case of observations in on-source mode, the EAS produced by those γ-rays will point towards the center of the camera, which is the location of the source in the camera plane. In wobble mode, γ-ray-induced showers from our source will be oriented towards a region with a certain offset from the camera center. One must check the distribution of the $|\alpha|$ parameter for the on and off data, which should be approximately flat for the off region and, if our candidate source is actually a γ-ray emitter, peaked at zero for the on region (see figure 2.25. Otherwise, off and on distributions will be statistically identical and no detection can be claimed.

Once we obtain those distributions for the candidate source, it is crucial to

[12]For the sake of brevity, from now on we will only refer to $|\alpha|$ distributions.

compute the total amount of on ($N_{\rm on}$) and off events ($N_{\rm off}$), and to obtain from them the statistical significance of our signal with respect to the local background. To do so, a software named `odie` is used. The main task performed by `odie` is to select the $|\alpha|$ cut that optimizes the signal-to-noise ratio: any looser cut will include increase the number of on events but they will mostly add background events; tighter cuts will reduce the amount background but we will also be discarding a considerable fraction of our (usually scarce) signal. Typical cut values are 8° for $|\alpha|$ distributions and ~ 0.02 deg^2 for θ^2-distributions, always considering point-like sources[13].

At this point of the analysis one knows the values of $N_{\rm on}$ and $N_{\rm off}$ for our source. An additional quantity is needed: the ratio μ between on and off observation time. With these 3 ingredients one can now apply the Li&Ma formula for the significance of a signal when the number of events is small [52]:

$$\sigma_{\rm LiMa}(N_{\rm on}, N_{\rm off}, \mu) = \sqrt{2\left[N_{\rm on}\ln\left(\frac{1+\mu}{\mu}\cdot\frac{N_{\rm on}}{N_{\rm on}+N_{\rm off}}\right) + N_{\rm off}\ln\left(\mu\cdot\frac{N_{\rm off}}{N_{\rm on}+N_{\rm off}}\right)\right]} \tag{2.5.2}$$

The case of signal detection for pulsars is however, a completely different story: there is no geometrical difference between the events emitted by the pulsar and those from the surrounding nebula. Therefore, the definition of the off-region is based on a time criteria: the off events are those emitted when the pulsar is not facing towards the Earth; and vice versa: the on events are those emitted while the pulsar beam is pointing in our direction. One needs to define the on-region as a certain interval of pulsar phases where emission is expected, as well as the off region, where no emission is foreseen. Then, one can check the number of events in the on region (the signal) and subtract the number of events in the off (the background). In the case of pulsars, the on-off ratio μ corresponds to the ratio between the phase widths of the on and off regions. Those definitions depend on the pulsar one is analyzing and the details for the Crab pulsar case are given in next chapter, §2.5.7.

Thus, for pulsar analysis we can not use Odie to optimize the analysis cuts.

[13] Virtually all γ-ray-sources in the region of the sky that is available to MAGIC are below its angular resolution. So, they are all unresolved and appear like point-like sources in the camera plane, with the only exception so far of the W51 region [8].

A custom algorithm has to be applied, which will be described in §4.5.

2.5.7 Assigning phases and building the lightcurve

Pulsar analysis is based on the measurement of a periodic signal. The distinction between on and off signals is based on the arrival time of the γ-ray apart from their incoming direction in the night sky. Since the pulsar signal is repeated every $T \approx 33.5$ ms, it is more convenient to use the **pulsar phase** ϕ instead of the time t as the variable used to represent the pulsar lightcurve. The phase is defined as the fraction of a complete rotation that the pulsar had spin at the moment of arrival of the γ-ray, i.e. the *face* that the pulsar was showing us at the time each event was recorded. To perform this conversion between arrival time and pulsar phase, a set of look-up tables known as **pulsar ephemeris** were created by the Jodrell Bank Center for Astrophysics [53]. They measured the arrival time of the first pulse, that defines phase $\phi_0 = 0$, for the first day of each month at 12:00 a.m., since February 1982 until today. They have also measured the pulsar frequency ν and its first and second derivatives, $\dot{\nu}$ and $\ddot{\nu}$. Both quantities are needed to compute the phase ϕ of a photon that arrives at time t, measured from the reference system (from now on, RS) of the MAGIC telescopes[14]. To do so, we use the following Taylor expansion:

$$\phi = \phi_0 + \dot{\nu} \cdot (t_{\rm bar} - t_{\rm eph}) + \frac{\ddot{\nu}}{2} \cdot (t_{\rm bar} - t_{\rm eph})^2 \qquad (2.5.3)$$

This expression is valid for $t_{bar} - t_{eph} \approx 0$, i.e. for arrival times close to the ephemerides measurement performed at time $t_{\rm eph}$. Note that we are using here $t_{\rm bar}$ as the arrival time of the γ-ray. Since the MAGIC telescopes are located at a certain position on the rotating Earth surface, which in turn is being accelerated along its orbit by the gravity of the Sun, the local RS is not apt to estimate the phase of each Crab pulsation. We use instead the simplest available inertial RS: since the relative velocity between the Sun and an isolated pulsar like Crab can be considered constant for time scales of years which are under consideration in our analysis, we can transform our local time coordinates t to the RS of the solar system centre of masses or **solar system barycenter** (SSB), $t_{\rm bar}$.

This transformation has to take into account several correction factors which

[14] In coordinated universal time or UTC

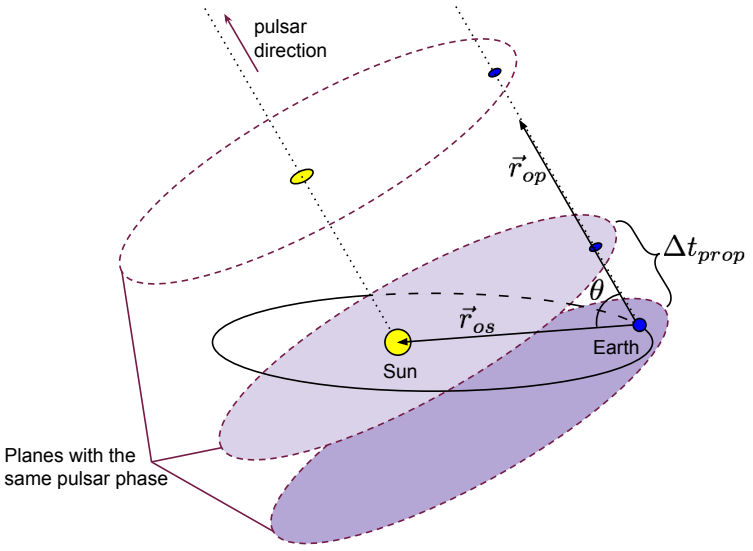

Figure 2.26: Schematic view of the different reference systems involved in the time corrections needed to compute the phase of an event. The origin of vectors $\vec{r}_{\rm os}$ and $\vec{r}_{\rm op}$ is the position of the observatory in the surface of the Earth, which could not be shown here.

we briefly describe here. Further details can be found elsewhere [54]:

$$t_{\rm bar} = t + \Delta t_{\rm prop} + \Delta t_{\rm Shap} + \Delta t_{\rm rel} + \Delta t_{\rm TDT} \tag{2.5.4}$$

- $\Delta t_{\rm prop}$ is the time delay of the pulsar signal between the SSB and the Earth position. The origin of this delay is depicted in figure 2.26.

- $\Delta t_{\rm rel}$ is the delay predicted by the combination of two relativistic effects: first, the time dilation due to the gravitational potential of the Earth; second, the time shift due to the speed of Earth moving around the Sun.

- $\Delta t_{\rm Shap}$ is the so-called Shapiro delay [55]. It is the delay produced by the photons entering the gravitational field of the Sun and it can be precisely calculated as $\frac{2GM_\odot}{c^3}\ln(1+\cos\theta)$, where θ is the angle between the direction of the Sun and of the Crab pulsar seen from the MAGIC observatory (represented in figure 2.26). This delay is of the order of $\sim 10^{-3}$ s but it depends on the relative position of the Earth with respect to the Sun, as one can tell from the dependence on the θ parameter.

- $\Delta t_{\rm TDT}$ is the time difference needed to change from UTC time to a more appropriate RS for the Earth ephemeris, the so-called terrestrial dynamical time (TDT). This delay is a fixed quantity of 32.184 s plus an integer number of *leap seconds*, which are artificial 1 s delays that are introduced ever few years in the UTC time to correct for small instabilities in the

rotation of the Earth. For instance, by the time of writing of this thesis, a leap second will be introduced at midnight of June 30th 2015.

The computation of all these factors for each recorded event is done in a highly automatized mode by means of a dedicated software developed by the MAGIC collaboration known as **PSearch** [54].

Once the phase of each event is computed, one should check whether the source shows any kind of periodic behavior. A special kind time analysis is used in the case of pulsars: since we can not see individual pulses at γ-ray energies like you can do in optical or in radio, it is useless to measure the number of events as a function of time. Instead, one should build the **phaseogram** of the pulsar, which is equivalent to the previous quantity by after integrating millions of pulsar rotations. An example of such plot can be seen in figure 3.9.

The regions of the phaseogram where we want to look for the pulsed signal, in comparison with the off region where we do not expect any pulsed emission pulsed have to be defined *a priori*. For the case of the Crab pulsar, this region will be defined later in equation 4.6.1.

Once the pulsar phaseogram is build and the on and off regions are defined, one can finally test if the source emission is modulated, in our case to the pulsar period $T = 0.0336$ s. To do so, a set of periodicity or uniformity tests can be applied, which will be briefly explained here. More detailed descriptions can be found elsewere [54]. The goal of all these tests is to discard the null hypothesis situation, which is that the signal is flatly distributed among all the possible values of the phase, $\phi \in [0, 1)$. These tests already implemented within a MARS class called `MHPhase`, and the signal significance measured with all of them can be easily retrieved.

The most simple periodicity test is the Pearson or χ^2 test. It uses the phaseogram information but binned in N events, so we will use ϕ_i for the number of events in the i-th phaseogram bin. In the large sample limit, the test statistic can be computed as

$$\chi^2 = \sum_i^N \frac{(\phi_i - \langle\phi\rangle)^2}{\langle\phi\rangle} \tag{2.5.5}$$

where $\langle\phi\rangle = \sum_i^N \phi$ is the mean phase value. If our data contains a clear periodic

signal, a large value of χ^2 will be obtained. This is especially useful when there is a narrow, single peak in our phaseogram.

To avoid the dependence of our test statistic with the number of bins N, the unbinned, Fourier-based Z_m^2 test was proposed, where m is the selected number of harmonics. Although the probability distribution of the Z_m^2 test is statistically the same as that of the χ^2 test, the bigger the value of m the more sensitive this test is to thinner pulses in our phaseogram.

Since there is no ideal value of the number of harmonics m for the Z_m^2 test to be optimally sensitive to any possible peak width, a last uniformity test is used: the so-called H-test. Based on the previous test, its test statistic can be computed as

$$H = Z_M^2 - 4M + 4 \tag{2.5.6}$$

where M is the number of harmonics that maximizes the value of H. Even though there is no analytical expression for the probability distribution of H, MC simulations have showed that it is a powerful periodicity estimator for a wide range of pulse shapes.

2.5.8 Flux estimation

Once the signal is detected, one would like to know what is the γ-ray flux from the source and whether it is stable or not with time. Let's first define the concept of **flux**, Φ, from a γ-ray source: it is the rate of γ-rays per unit of area perpendicular to the incoming direction and can be computed as:

$$\Phi = \frac{d^2 N_\gamma}{\mathrm{d}t_{\mathrm{eff}} dA_{\mathrm{coll}}} \tag{2.5.7}$$

In the international system of units or SI (from french *Système International d'unités*) it has units of $[\Phi] = [L]^{-2}[T]^{-1} = \mathrm{m}^{-2}\ \mathrm{s}^{-1}$. However, astronomers often use cgs units: $[\Phi] = \mathrm{cm}^{-2}\ \mathrm{s}^{-1}$.

These are other useful concepts derived from the flux definition and which will be of useful later:

- The **differential energy spectrum** (hereafter, DES) is defined as the flux per unit of γ-ray energy

$$\frac{\mathrm{d}\Phi}{\mathrm{d}E} = \frac{\mathrm{d}^3 N_\gamma}{dt_{\mathrm{eff}}\, \mathrm{d}A_{\mathrm{coll}}\, \mathrm{d}E} \tag{2.5.8}$$

and its units in γ-ray astronomy are $\left[\frac{\mathrm{d}\Phi}{\mathrm{d}E}\right] = \mathrm{m}^{-2}\ \mathrm{s}^{-1}\ \mathrm{TeV}^{-1}$.

- The **integral flux**, i.e. the total flux in a wide energy band, for instance above 200 GeV

$$\Phi_{E>200\ \mathrm{GeV}} = \int_{200\ \mathrm{GeV}}^{\infty} \frac{\mathrm{d}\Phi}{\mathrm{d}E}\,\mathrm{d}E \tag{2.5.9}$$

- The **spectral energy density** or distribution (hereafter SED) measures the power of EM radiation per unit area of a source and is defined as

$$E^2 \frac{\mathrm{d}\Phi}{\mathrm{d}E} = E^2 \cdot \frac{\mathrm{d}^3 N_\gamma}{\mathrm{d}t_{\mathrm{eff}}\,\mathrm{d}A_{\mathrm{coll}}\,\mathrm{d}E} \tag{2.5.10}$$

  and its units are $\left[E^2 \frac{d\Phi}{dE}\right] = \mathrm{TeV\ m}^{-2}\ \mathrm{s}^{-1}$ and it is a useful quantity because it allows us to easily notice small features in the spectra of a source, which may be easily overlooked when we analyze the DES of a source. Since most γ-ray sources exhibit a power-law spectra, one can quickly see if its spectral index is bigger or smaller than -2 because the SED shows a positive or negative steepness, respectively.

- When the integral flux is derived for a series of consecutive time periods, one can observe the evolution of the source flux with time. In this way one obtains the so-called **lightcurve** of a source (from now on, LC). However, pulsars are a special case: they are very stable emitters so we are usually not interested in their flux with respect to time but as a function of the pulsar phase instead, the so-called phaseogram or phase-folded LC, explained in the previous section. When discussing about pulsars, we will use both terms, LC and phaseogram, interchangeably throughout this thesis.

All these quantities are computed by the software programs `fluxlc` and `flute` for mono and stereo data from a chosen γ-ray source, respectively. In the case of pulsars, an especial mode computes the number of background events as those coming from the off region of the phaseogram. Even if the source is not detected, one can still set limits to the γ-ray flux arriving from that region of the sky: anything brighter than those limits should have been detected with our instrument, considering our current sensitivity. So only a faint emission would be possible. These **flux upper limits**, either integral or differential, can also be computed by these two pieces of software.

This high-level analysis of the data begins with the computation of the DES. One needs to divide the events in several energy bins. Since usually γ-ray sources emit photons in a power-law fashion, it is natural to use regular bins in a logarithmic energy scale. In this analysis we have used 30 logarithmically-spaced energy bins between 5 GeV and 50 TeV. Then, for each of those bins one needs to calculate:

- The **number of detected γ-rays**, N_γ, is estimated from the difference between the number of events in the *on* and in the *off* regions, $N_{\rm on} - N_{\rm off}$. Remember that, since the off signal for a pulsar is not defined as a different region of the sky we do not use the θ^2 or α distributions but the pulsar phase distributions, ϕ.

- The **effective collection area** of the telescope, $A_{\rm coll}$, that is estimated from the MC the total simulated area scaled down by the γ-ray detection efficiency:

$$A_{\rm coll}(E) = \epsilon_\gamma(E) \cdot A_{\rm tot} = \frac{N_\gamma^{\rm surv}(E)}{N_\gamma^{\rm sim}(E)} \cdot A_{\rm tot} \tag{2.5.11}$$

  As shown in the previous equation, the efficiency ϵ_γ is computed as the fraction of simulated events surviving the analysis process and the applied cuts, $N_\gamma^{\rm surv}$, with respect to the total number of simulated γ-ray events, $N_\gamma^{\rm sim}$. In order to have an unbiased estimation of the effective collection area, these cuts are not the same as those applied in the signal detection process that was explained in §2.5.6. Thus, a new set of cuts needs to be found and this is done by means of efficiency criteria: `fluxlc` will try that the amount of events in each energy bin after the cut reaches a given threshold fraction of the simulated events. In the case of the Crab pulsar, this threshold is 90% whereas to estimate the emission of a more conventional source, like for instance the surrounding nebula, this threshold can be lowered down to 60% and 70% for the α and hadronness cuts, respectively. A plot of the efficiency as a function of the energy derived from the MC can be seen in figure 4.8 (*left*).

- The **effective observation time**, $t_{\rm eff}$, is different from the *elapsed time* between the beginning and the end of the observations because two factors have to be taken into account. First of all, there use to be *gaps in*

the data due to interrupted observations, usually caused by: the need to pause data taking to execute the calibration and pedestal runs; due to long observations that expand several nights; due to worsening weather conditions that force the MAGIC operators to postpone the observations. The second factor is the existence of a *dead time* of the system, i.e. a short time period after receiving a positive trigger signal during which the recording of the event is being executed by the DAQ system. During this time, the telescope is not available to process any new events, which is especially relevant for high event rate experiments like IACTs. For MUX-based receivers, the dead time is 26 μs whereas for the DRS2 and DRS4 systems it is 500 μs and 27 μs, respectively. Since the triggers are approximately Poisson-distributed, the time difference between consecutive events will decay exponentially.

The estimation of the measured flux or the flux upper limits is performed using the standard software in MAGIC `fluxlc`. This tool was deprecated when the second MAGIC telescope started operations as it can only deal with mono data. A new software called `flute` is used to analyze stereoscopic data and this is the tool that the stereo Crab pulsar analysis team had to use instead.

`Fluxlc` requires several inputs to work. First of all, the actual Crab data after being processed with `melibea`. For on-source observations, also off data at `melibea` level had to be provided, keeping in mind that it can not be the same sample as the one used to train the γ-hadron separation with `osteria`. Also some MC is needed to estimate the effective collection area of our instrument after cuts. Apart from that, the applied α and hadronness cuts are automatically computed by `fluxlc` from an efficiency criterium instead of using the optimized cuts.

Another useful physical magnitude in γ-ray astronomy is the number of γ events detected by the telescopes per unit time, the so-called **gamma rate**. Since our effective collection area has a strong dependence on the zenith angle where our instrument is pointing, this rate has to be estimated within a certain range of zenith angles. The gamma rate is computed in a similar way as one

does for the source lightcurve:

$$\text{Gamma Rate} = \frac{N_{\text{exc}}}{t_{\text{eff}} \cos^{1.26}(ZA)} \tag{2.5.12}$$

where t_{eff} is the effective observation time needed to obtain the N_{exc} excess events and ZA is the mean zenith angle in our data. The zenith angle correction is elevated to an index 1.26. This number was chosen following previous studies on the subject although others use different values to apply the ZA correction to different magnitudes. If the source is bright enough, like in our case with the Crab nebula, one can compute the number of excess events as $N_{\text{exc}} = N_{\text{on}} - \nu \cdot N_{\text{off}}$, where the ν parameter is again the on-off observation time ratio and where N_{on} and N_{off} are the number of events above a certain energy threshold for the on and off regions respectively.

Chapter 3

Physics of the Crab pulsar

Pulsars were discovered in 1967 by Mrs. Jocelyn Bell during her PhD thesis, together with Dr. Anthony Hewish, her PhD director. She was observing the night sky with a custom radio telescope at Cambridge university, manually inspecting the lengthy logs and looking for patterns in the received signal. When she discovered a signal repeating regularly every ~ 1 s, she first thought that could be a signal of intelligent life so she named the anomaly LGM1, for *Little Green Men 1*, but the source she serendipitously discovered is now catalogued as PSR B1919+21. Later on, other regular signals were found so the hypothesis of a contact with an alien civilization was discarded. These signals were identified as rotating neutron stars and they were named **pulsars**, due to their unique regularly pulsating signal. Her discovery was awarded with the 1974 Nobel prize in Physics but, in a controversial decision, only her PhD director received the prize, since Jocelyn Bell was a PhD student at that time. However, she was awarded later on with multiple academic and scientific honors.

Since then, about 2300 pulsars have been discovered so far, according to the ATNF pulsar catalogue [1] [56], mainly in radio wavelengths. A general picture of their composition, structure and emission mechanisms have been established over the decades. In this chapter wegive a concise review of their main characteristics before explaining the peculiarities of the Crab pulsar. The physical processes that produce the observed emission, according to the current models, will also be explained here.

[1] http://www.atnf.csiro.au/people/pulsar/psrcat/

3.1 General characteristics of pulsars

A pulsar is a highly-magnetized, spinning NS. Whereas the existence of NSs was already predicted in 1934 [57], pulsars were the first direct evidence of their existence. They are stellar remnants of a supernova explosion produced by the collapse of a massive star ($M > 8M_{\odot}$), a picture first predicted by Pacini in 1967 [58] and later confirmed by Gold [59]. They have the strongest magnetic fields as well as the most intense gravitational fields ever observed in Nature (after blackholes). For this reason, pulsars are excellent objects to test the most fundamental laws of physics.

Pulsars emit two collimated radiation beams and only when these beams point towards the Earth we are able to detect them. This explanation of the periodicity of their signal is provided by the so-called **lighthouse model**, due to the similarity with the apparent pulsation in the light coming from a lighthouse. Their EM emission is produced mainly by non-thermal processes and most of it is emitted only in radio wavelengths. Just a few pulsars have been detected in the optical band and about 100 of them have been detected in X-rays. A thermal component is detected at these short wavelengths and sometimes no radio counterpart has been found. Also more than 100 pulsars have been recently detected in γ-rays by the LAT instrument onboard of the Fermi satellite [60], which are shown in figure 3.1.

During their formation, the supernova explosion expelled most of the stellar material and only the core of the star remained: an object with a mass between 1.4 to $2M_{\odot}$ and a radius between 10 and 20 km. It has a complex internal structure and its density varies several orders of magnitude between the surface, where $\rho \sim 10^6$ g/cm^3, and the core, where $\rho \sim 10^{15}$ g/cm^3. The density of a NS at its center is slightly higher than the density of an atomic nucleus. These incredible mass concentrations mean that just 1 cm^3 of NS material (a teaspoon) is up to one hundred million tons heavy!

A pulsar is stable because the positive degeneracy pressure of neutrons balances the gravitational negative pressure. But if the mass of the progenitor star would have been a few solar masses higher, the inner pressure would not have been enough to compensate the heavy gravitational pull and a black hole would have been created. Theorized quark stars would be an intermediate stage before the final collapse into a black hole.

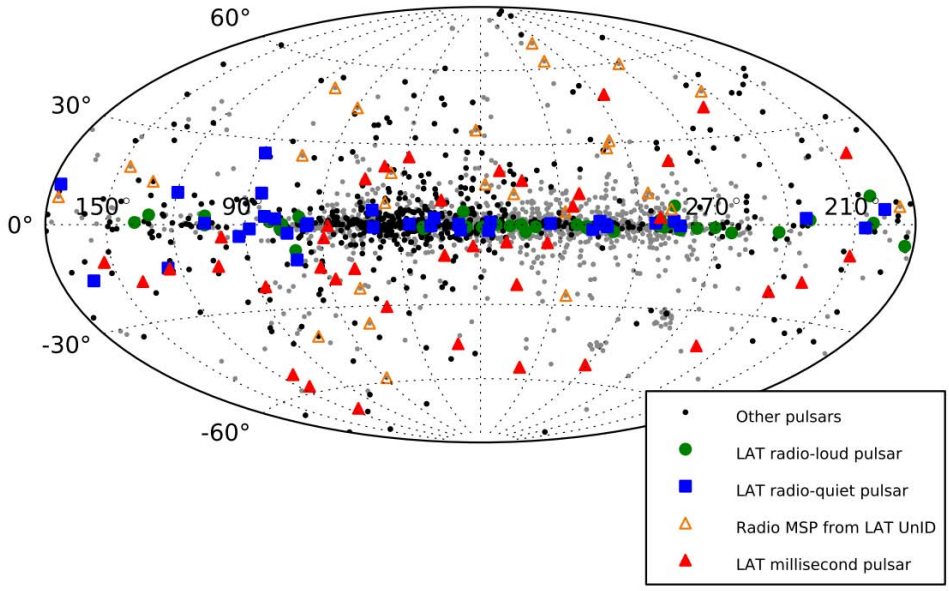

Figure 3.1: Pulsar skymap from the 2nd Fermi Pulsar Catalogue. Taken from [60].

The magnetic field at the surface of these stars can become up to $B \sim 10^{12}$ G strong, the highest magnetic intensities ever detected. We can only comprehend such magnetic field intensities when we consider that the strongest magnetic fields that we are able to produce artificially are of the order of 10 G, so *eleven* orders of magnitude below.

The forces exerted by these extreme magnetic fields dominate by more than 10 orders of magnitude over gravity. Thus, they are able to extract charged particles from the NS surface and to inject them into the magnetosphere. This creates two collimated particle and radiation flows aligned with the magnetic poles of the star. This is valid for radio wavelengths but not for the γ-ray emission, where emission is suspected to be produced from regions further out in the magnetosphere. We still do not have a complete theory of the magnetosphere of the pulsar but there are several candidate models which we will describe latter in this section.

The magnetosphere of a pulsar is far from empty: being the magnetic forces at its surface much stronger than the gravitational ones, a continuous flow of charged particles is injected in the surrounding medium. The magnetosphere ends up filled with a dense co-rotating plasma: charged particles rotate rigidly at the same angular speed of the pulsar up to a certain distance known as the

light cylinder radius (hereafter, we will use the notation LC when there is no ambiguity). The LC is the geometrical region of the magnetosphere defined by a cylinder coaxial with $\mathbf{\Omega}$, and whose radius such that particles need to travel at the speed of light to remain co-rotating with the pulsar. Therefore, $R_{\rm LC} = c \cdot T/2\pi = c/\Omega$, which typically lies between 10^3 km and 10^7 km.

The simplest way to study the pulsar magnetosphere is to model it as a magnetic dipole rotating in vacuum: magnetic field lines emerge from the magnetic north pole and end at the magnetic south pole but it is an oblique rotator. This means that, in general, their magnetic axis $\mathbf{m}$ and rotational axis $\mathbf{\Omega}$ are not aligned (see schematic view in figure 3.8). Note that some magnetic field lines are closed within the radius of the LC and others are considered "open", although they really close in a region far away from the LC. This fact allows us to define two regions within the magnetosphere: the **open zone** and the **closed zone**. The last closed magnetic field line is tangent to the LC and lines emerging closer to the north pole are therefore open lines.

Charged particles can scape the LC moving along these open lines and forming an intense **pulsar wind**. Close to the pulsar this wind is dominated by the radiative component, but at distances bigger than the LC, the wind becomes kinetic-dominated, transforming the pulsar magnetosphere in an outwards flowing plasma.

A pulsar is not a homogenous object but it has an spherical, multilayered structure. The outermost material layer is a tiny hidrogen atmosphere: the extreme gravitational field compresses it down to only ~ 10 cm of thickness, even though its extreme temperature of 10^6 K. The next layer is a solid crust of heavy elements like iron that, according to the **starquake model** [61], periodically suffers fractures due to gravitational stress, releasing at least 10^{32} erg in the process. Underneath the crust, there is a superfluid sea composed of neutrons, protons and electrons. The inner core is formed only by neutrons, probably in an exotic superfluid state.

A simple calculation can help us understand how pulsars end up having such tiny rotation periods. The conservation angular momentum, L, between the time right *before* the SN explosion, marked with a subindex b, and very long

after the explosion, marked with a, reads

$$L = I \cdot \Omega \sim M\frac{R^2}{T} = \text{const.} \Rightarrow T_a = T_b \left(\frac{R_a}{R_b}\right)^2 \tag{3.1.1}$$

Since the radius of the original star gets reduced in the SN explosion from $R_b \sim 10^8$ m to $R_a \sim 10^4$ m, the rotational period also decreases from $T_b \sim 10^6$ s to $T_a \sim 10^{-2}$ s, which is of the order of the observed periods: pulsars are spinning with a period between 1 ms and 10 s and they get an oblate shape because of those extreme spinning velocities.

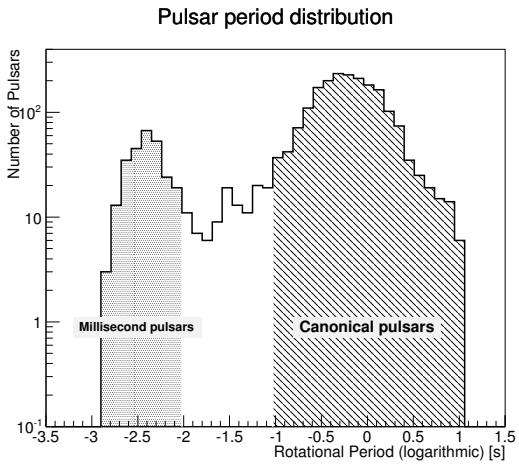

Figure 3.2: Distribution of pulsar periods obtained from the ATNF pulsar catalogue. Two clear populations can be seen, millisecond and canonical pulsars.

Moreover, their extreme density produces a high stability in the emission of the pulsed signal. In fact, pulsar timing is one of the most precise processes ever seen in nature: they get a delay of 1 s every 1 Myr (1 part in 10^{12}). Their internal clock mechanism is so stable that they are used to perform high precision timing experiments. Looking at figures **??** two populations can be clearly differentiated according to their rotational period:

- **Canonical pulsars** have periods of more than $T \gtrsim 0.1$ s, the highest period increase rates $\dot{T}$ and show broader pulses.
- **Millisecond pulsars** have periods of less than $T \lesssim 0.01$ s, much lower period derivatives $\dot{T}$ and their peaks are narrow.

The source of such a difference comes from the pulsar environment: the first kind are located within binary systems where a companion star accreted material onto the pulsar for some time, increasing its angular momentum in the process and reducing its periods to approximately the same values they have today; whereas the second category is composed by isolated NS, created after the

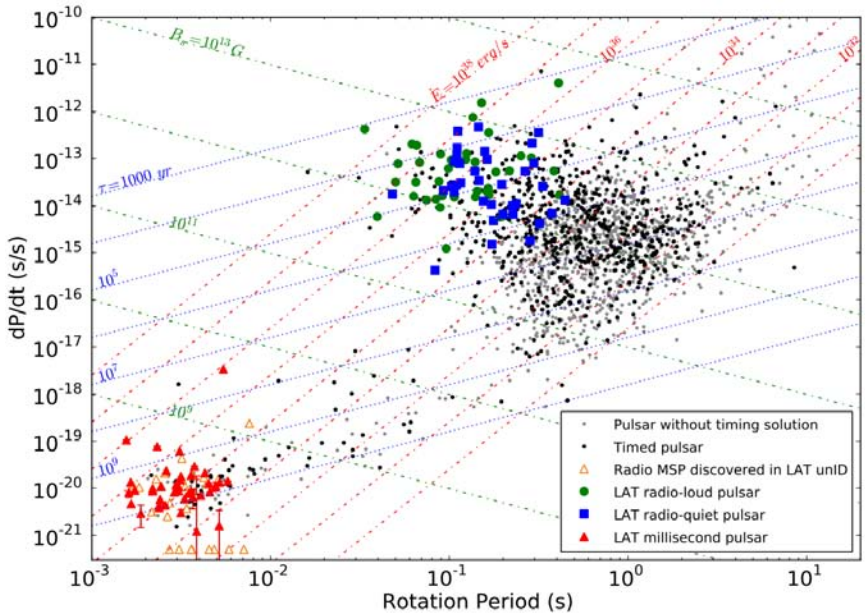

Figure 3.3: Correlation between pulsar spin-down rate and rotational period. Two populations can be seen, where the fastest-spinning pulsars are those with the smaller period derivatives. Note that there are almost 10 orders of magnitude between the spin-down rates for the most extreme cases. Taken from [60].

progenitor expelled all the outer layers and the inner material collapsed under gravity pressure. The first kind of pulsars is also known as *accretion-powered pulsars* and the second kind is known as *rotation-powered pulsars*.

There are several contributions to the slowing down of the rotation of an isolated pulsar: the dissipated energy is carried away by the emitted radiation, the energy and angular momentum losses due to particle emission and also due to magnetic braking and gravitational waves emission. Both the emitted photons and high energy particles form the pulsar wind, which it is dominated by the particle component at long distances from the pulsar.

As we said, pulsars are very precise clocks in short time scales. But, if we compare the pulse arrival times with an ideal clock and we subtract the variations due to spin-down, certain differences are left. These differences are small and look like random variations of the rotational phase, which are characteristic of each pulsar like a signature. It is what is known as the pulsar **timing noise**. Moreover, pulsars undergo sudden shifts in their pulsation a few times per decade, degrading their precision as clocks in the long term. These unannounced events are known as **glitches** and they are probably produced by starquakes, i.e. sudden stress releases and breaks in the pulsar crust.

The measured values of $\dot{T}$ give us a lot of direct information on the energy

emission of the pulsar and the main one is their estimated emitted power. Since their EM emission is highly non-isotropic, their overall luminosity can not be induced by spheric integration. Instead, only an energy loss rate from its spin down can be deduced: the rotational energy variation, $\dot{E}_{\rm rot}$, that is also known as **spin-down luminosity**. We can see the relation between T and $\dot{E}_{\rm rot}$ by means of their inertial momentum I and its rotational frequency $\Omega = 2\pi/T$:

$$E_{\rm rot} = \frac{1}{2} I \Omega^2 = 2\pi^2 \frac{I}{T^2} \tag{3.1.2}$$

Thus,

$$\dot{E}_{\rm rot} = 2\pi^2 I \frac{-2}{T^3} \frac{dT}{dt} = -4\pi^2 I \frac{\dot{T}}{T^3} \tag{3.1.3}$$

If we consider the pulsar as a solid sphere, we can approximate it momentum of inertia as $I = \frac{2}{5} M R^2$, hence

$$\dot{E}_{\rm rot} \approx -\frac{8\pi^2}{5T^2} M R^2 \frac{\dot{T}}{T} \tag{3.1.4}$$

Besides, one can model in a general way the spin-down rate with the use of a power-law:

$$\dot{\Omega} = -C \cdot \Omega^n \tag{3.1.5}$$

where n is the so-called the *braking index* and it is equal to 3 for pure magnetic dipole emission. We can derive the above expression to isolate the braking index as

$$n = \ddot{\Omega}\Omega / \dot{\Omega}^2 \tag{3.1.6}$$

in case the value of $\ddot{\Omega}$ can be measured with sufficient accuracy, which requires a long term monitoring of the pulsar. It has been found that for most pulsars the braking index $n < 3$. For instance, for the Crab pulsar, $n = 2.51$ whereas for the Vela pulsar, $n = 1.4$ [62].

Also a **characteristic age**, τ_c, is often computed out of pulsar period measurements as

$$\tau_c = \frac{T}{2\dot{T}} \tag{3.1.7}$$

This equation is obtained by direct integration of equation 3.1.5 but it re-

quires that we make two assumptions, which are rarely fulfilled: that the pulsar is a perfect magnetic dipole (so $n = 3$) and that its initial rotation was much faster when it was formed than it is now. As a consequence, the actual ages does not often coincide with the characteristic age, as in the case of pulsars associated with an observed SN, whose real age can be estimated with high precision. However, it is a useful parameter to understand how far such objects have evolved since their formation.

The ultrarelativistic charged particles forming the pulsar wind end up interacting with the nebula material around the pulsar. The shockwave of this interaction, where particle velocities are randomized, form a special type of nebula powered by the energy injected by the pulsar through this wind, known as **pulsar wind nebula** (hereafter, PWN), of which the Crab is a perfect example. For young pulsars, the nebula is partially obscured by the shell of stellar material that forms the SNR but this is not the case for older pulsars, whose associated SNR has already been dissolved into space and only the PWN is left.

Pulsars are also very suitable candidates of gravitational wave emitters. This is especially true for those pulsars within systems with a high quadrupole mass momentum, i.e pulsars within binary systems. The first binary pulsar that was discovered, PSR 1913+16 [63], was also used to extract indirect evidence of the existence of gravitational waves for the first time [64]. It was derived from the spin down of the binary system: as gravitational waves reduce the energy of the binary system, the distance between the two bodies steadily decreases, and so does the orbital period which can be directly measured. This energy loss rate was perfectly adjusted by the predictions of GR, as shown in figure 3.4. This discovery triggered a race to open a new observational window, *gravitational wave astronomy*. But, despite of all the scientific efforts during the last 35 years, no other evidence has been found so far about the existence of these oscillatory perturbations of the spacetime fabric.

3.2 The Crab Pulsar

Among the currently known pulsars, the one located at the center of the Crab nebula (RA $05^{\mathrm{h}}34^{\mathrm{m}}31.94^{\mathrm{s}}$, DEC: $+22^{\circ}0'52.12''$, figure 3.5 *left*) is a unique pulsar for several reasons. It lies at the center of the **Crab nebula** or NGC

1952, located in the Taurus constellation and is the brightest steady source in the high-energy domain of the γ-ray sky. It is also the first object of the Messier catalogue, M1, and it has been used as the stellar candle for this band of the EM spectrum to calibrate the performance of IACTs. This nebula is the remnant of the supernova explosion SN 1054 from July 4th 1054 a.C., located at 2.2 kpc from Earth. Several historical records have been found referring to this event [66]: for instance, Chinese and arabic astronomers reported the rise of a new bright star in the night sky that lasted for about 22 months.

The inner region of the Crab nebula where the pulsar is located is very dynamical and there are several detected sub-structures: a torus-shaped region is visible, together with the jets emerging from the pulsar poles. The flow of ultrarelativistic charged particles in the pulsar wind is radiationless or *cold* until it begins to interact with the surrounding medium at the termination surface and up to the inner ring. These interactions produce the so-called **wisps**, i.e. concentrical rings of increased emission which move away from the pulsar, extending into the inner part of the nebula shell [67]. They are clearly visible in X-rays, as well as in other wavelengths (see figure 3.5, *right*) and they are though to be shockwaves moving at speeds between 3% 50% of the speed of light. Besides, a perturbation region called **sprite** and a bright spot or inner knot very close to the pulsar have also been discovered. These sub-structures are known to be rapidly variable, in time-scales between months down to a few hours.

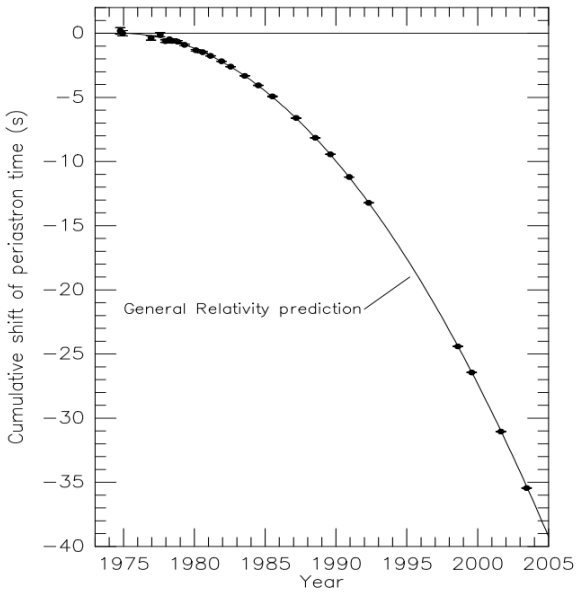

Figure 3.4: The orbital decay of the binary system containing pulsar PSR 1913+16 during 30 years. The solid line represents the GR prediction for gravitational wave emitter. The agreement is of the order of 0.2%. Taken from [65].

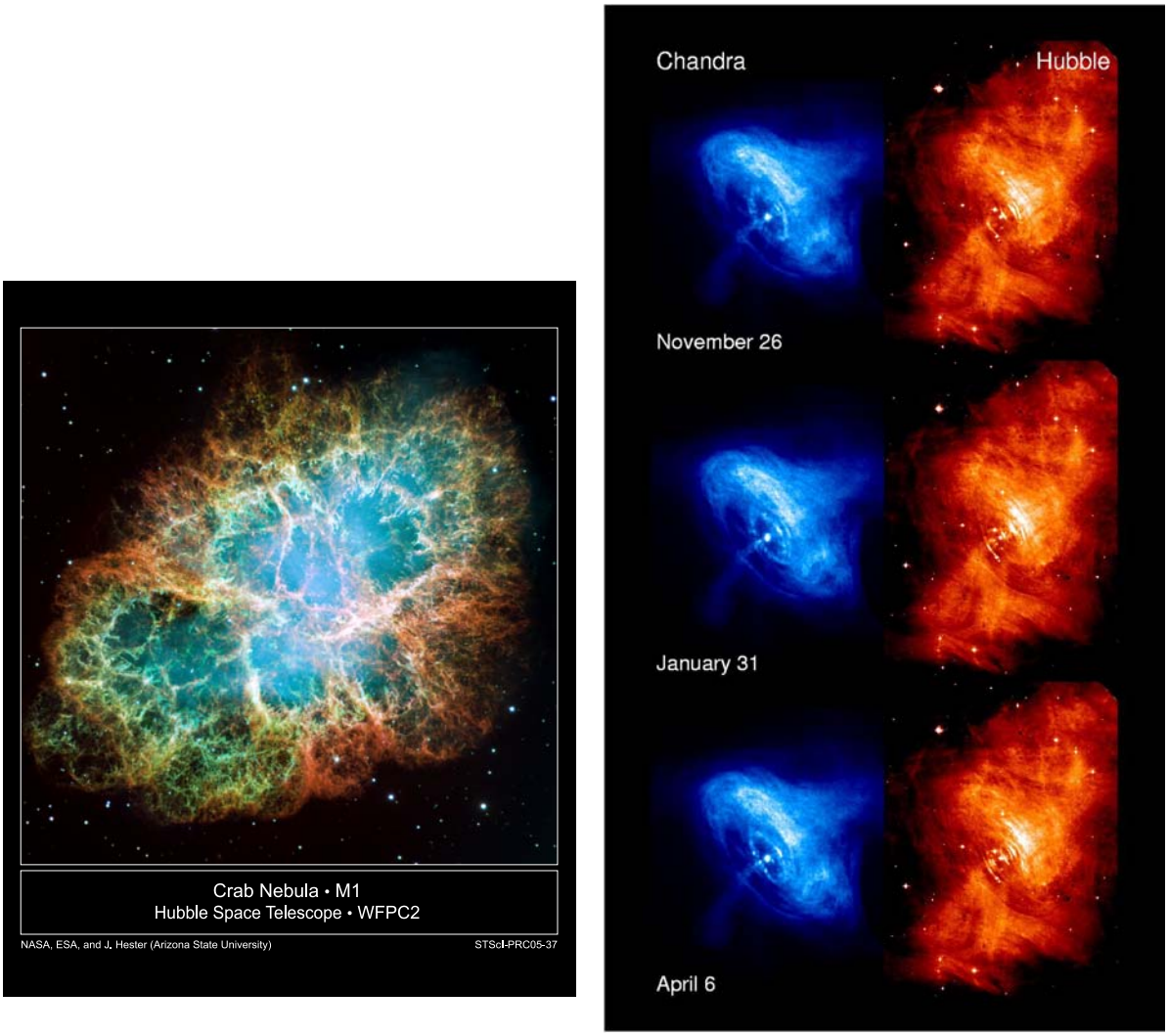

Figure 3.5: *Left)* Mosaic image of the Crab nebula, composed of 24 individual pictures from the Hubble telescope. Neutral and ionized oxygen filaments are colored in blue and red respectively, whereas green represents ionized sulfur. The Crab pulsar lies at the center of this 6 ly wide structure. Image credit: NASA, ESA, J. Hester and A. Loll (Arizona State University). Taken from `http://hubblesite.org/newscenter/archive/releases/2005/37/image/a/`. *Right)* Time evolution of the pulsar environment in optical (*left column*) and X-rays (*right column*) as seen by HST and Chandra, respetively. Image credit: NASA/HST/ASU/CXC/ J. Hester et. al. Taken from `http://hubblesite.org/newscenter/archive/releases/2002/24/image/b/`

The pulsar that lies at the center of the Crab nebula , PSR B0531+21, is therefore about 960 years old, so it is among the youngest pulsars ever observed. It is the remaining core of the progenitor star, now a NS with a mass of $1.4M_{\odot}$ and just 10 km radius. It can be observed along the entire EM spectrum, from radio to VHE γ-rays. Measurements show that we are observing it from an angle of about 60° from its rotation axis $\mathbf{\Omega}$ and a 45° angle is the measured separation between $\mathbf{\Omega}$ and $\mathbf{m}$, the magnetic axis.

It is also the most powerful pulsar detected in the Milky Way: with a rotational frequency of about 30 times per second ($T = 33.6$ ms), a period derivative or spin-down rate of $\dot{T} = 4.2 \cdot 10^{-13}$ and, thus, a characteristic age of $\tau = T/2\dot{T} \approx 1.2\cdot$ kyr, its spin-down luminosity can be estimated using in equation 3.1.4:

$$\dot{E}_{\rm rot} \approx (-4 \cdot 10^{42}\ \mathrm{W \cdot s}) \times (1.3 \cdot 10^{-11}\ \mathrm{s^{-1}}) \approx -5.2 \cdot 10^{31}\ \mathrm{W} \qquad (3.2.1)$$

which is of the order of 10^5 times the luminosity of the Sun but it is thought that only about 1% of this energy output is in the form of EM radiation [68]. One should take into account that the observed luminosity of the entire Crab nebula surrounding the pulsar is approximately 10^{31} W.

The emission of the Crab pulsar is located during three phases along the pulsar rotation: the **main pulse (P1)** located at phase $\phi \approx 0$, dominant at long wavelengths and used to define the initial starting of the pulsar rotation; the secondary pulse or **interpulse (P2)**, located at about $\phi \approx 0.4$ and dominant at the high-end of the spectrum; and the **bridge**, which is the region found between P1 and P2 (see figure 3.9). Their widths and relative height varies for different energy bands.

Its radiation is complex, and several components can be identified (see figure 3.6): a thermal component peaking at X-ray energies is produced close to the surface of the pulsar; multiple non-thermal components like the coherent radio emission are emitted by relativistic particles via synchrotron and curvature radiation mechanisms (see §1.1); a secondary X-ray component is produced by synchrotron emission in the magnetosphere with a power-law spectral distribution; there are just a handful of pulsars detected at optical wavelengths, and its feeble emission has also a non-thermal origin; HE γ-rays are thought

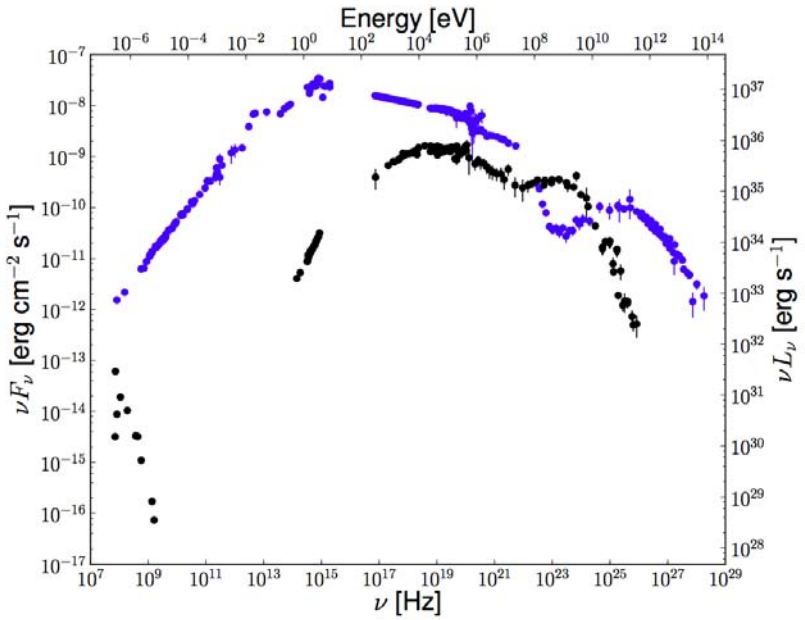

Figure 3.6: Spectral energy distribution of the Crab nebula (*blue*) and phase-averaged pulsar (*black*). Three components are clearly visible for the Crab pulsar emission: one at radio wavelength, a second one peaking at X-ray energies and the last one dominating the pulsar emission at γ-ray energies. Also the IC peak is clearly visible in the spectrum of the nebula at energies of a few GeV. Taken from [68].

to be produced by ultra-relativisitic electrons and positron via curvature radiation; whereas at VHE, IC scattering is believed to be the dominant emission mechanism. The pulse profiles at both ends of the EM spectrum usually differ: the main pulse dominates at radio frequencies whereas the interpulse dominates at γ-ray energies. This suggests that these photons are produced in different regions.

The Crab pulsar has a long record of observations since its discovery at radio wavelengths and its high energy emission was discovered soon after. Several unfruitful attempts were made by WHIPPLE and HEGRA but it was thanks to the LE threshold of MAGIC sum-trigger observations that it was finally detected above 25 GeV by IACTs [37]. A power-law spectrum with an exponential cut-off at energies of 19 ± 3 GeV could be fitted. Later, Fermi-LAT precise measurement estimated that the cut-off position should be around a few GeV [69] and significantly deviating from MAGIC results (see figure 3.7). This contradiction was solved by the the discovery of pulsed emission up to of 400 GeV by VERITAS [70] and MAGIC [71] observations, which could only be fitted a continuous power-law spectrum for the pulsar up to unpredicted energies and discarding the previous claims of the existence of a LE cut-off (see figure 3.7). The latests MAGIC measurements have also discovered bridge emission between 50 and 400 GeV [72].

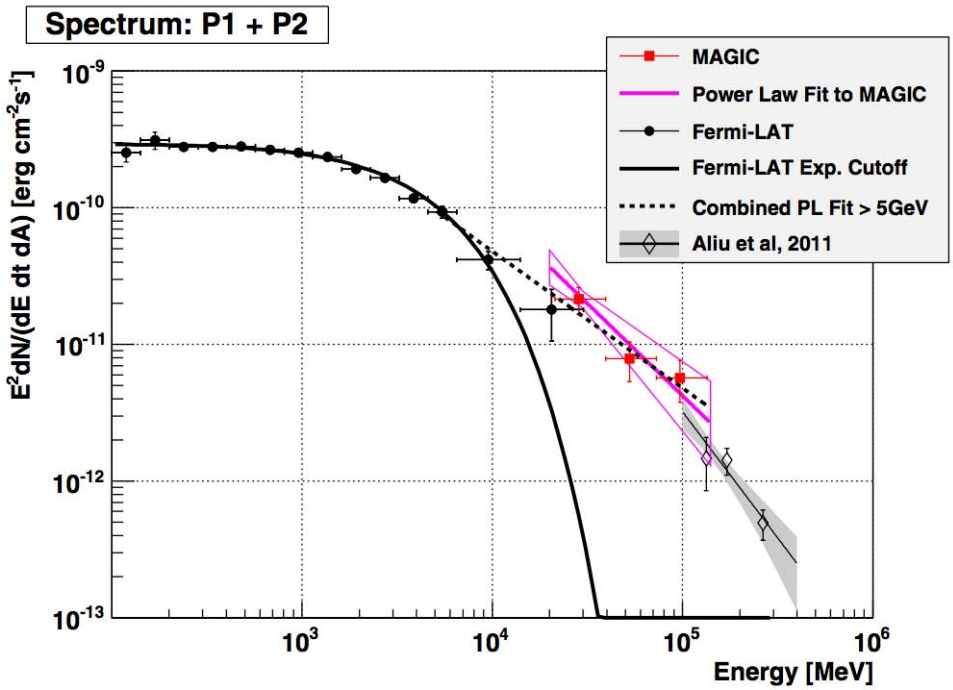

Figure 3.7: Phase averaged spectrum of the Crab pulsar combining measurements from Fermi-LAT (*black circles*), MAGIC using sum-trigger mono (*red squares*) and VERITAS (*empty diamonds*). The exponential cut-off fitted by Fermi is shown as a thick, solid line, single power-law where fitted by MAGIC (*pink line*) and VERITAS (*thin line*) and a power-law fit of the combination of the Fermi-LAT and MAGIC points is displayed as a dotted line. Taken from [73].

3.3 Current emission models

Pulsars are the perfect test-bench for our current physical theories due to their extreme conditions regarding magnetic field intensity, rotation speed or matter density. The Crab pulsar complies with all these characteristics and it is a unique member of this family of sources, mainly due to its youth and to its extremely wide emission spectrum. Several models have been proposed to explain them since its discovery, and each new finding has allowed us to discard some of them and to improve the remaining ones. In this section we describe current models that can be used to understand Crab pulsar observations and we also highlight those predictions where they differ from one another.

The first thing to note about Crab pulsar models is that, in all of them, pulsar rotation is the source of power for the particle or radiation emissions we detect. There is a theoretical basis underlying all current pulsar emission models that describe its inner magnetosphere: the so-called **Goldreich-Julian model** or force-free magnetosphere [74]. In this mode, positive and negative charged particles are surrounding the pulsar, which can be described by a particle density

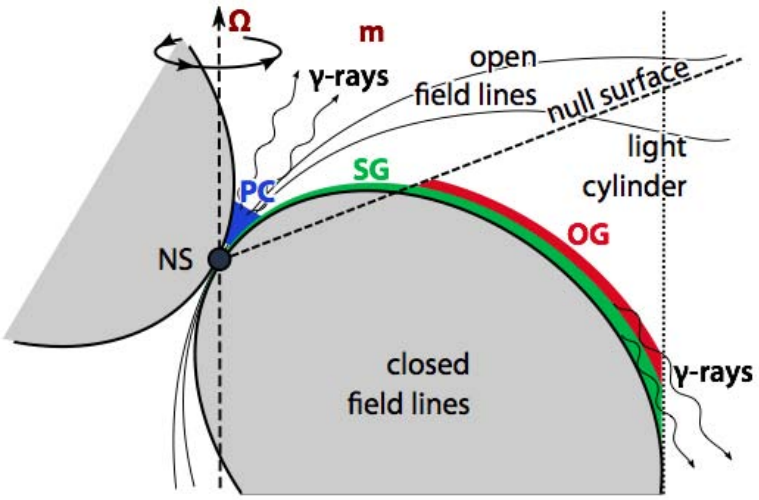

Figure 3.8: Schematic view of the regions within the inner pulsar magnetosphere, as well as the proposed γ-ray emission regions according to current models. The region separating positive from negative charges, where the charge density equals $\rho_{\rm GJ}$, is shown as a dashed line. Taken from [41].

$n_+(r,\theta)$ and $n_-(r,\theta)$, respectively[2], and they distribute in such a way that the ideal magneto-hydrodynamic (MHD) condition $\mathbf{E}\cdot\mathbf{B}=0$ is fulfilled [75].

It is useful to consider the electric field as the sum of two components, parallel and perpendicular to the magnetic field, respectively: $\mathbf{E}=\mathbf{E}_\parallel+\mathbf{E}_\perp$. Under the MHD condition, only a perpendicular electric field can exist, $E_\perp\neq 0$, but then no particle acceleration is allowed beyond a centripetal one, under which particles gain no net energy. According to this model, particles move along quasi-equipotential magnetic field lines $\mathbf{B}$ and only in certain regions where a component $E_\parallel\neq 0$ exists, particle acceleration can occur.

Besides, a certain distribution of the charged particles is induced as a direct consequence of the Poisson equation for such particles, ruling the dynamics of this system:

$$\nabla\cdot\mathbf{E}_\parallel=4\pi(\rho-\rho_{\rm GJ}) \tag{3.3.1}$$

where $\rho=e(n_+-n_-)$ is the total charge density and $\rho_{\rm GJ}\equiv\frac{1}{2\pi}\nabla\cdot\mathbf{E}_\perp$ is the so-called the *Goldreich-Julian charge density*. Within the LC, the second term can be computed as

$$\rho_{\rm GJ}\approx-\frac{1}{2\pi c}\frac{\mathbf{\Omega}\cdot\mathbf{B}}{1-\left(\frac{r}{R_{\rm LC}}\right)^2\sin^2\theta} \tag{3.3.2}$$

[2]Here we are using polar coordinates, where r and θ are the distance to the pulsar and magnetic latitude, respectively.

whereas for the wind region beyond the LC we have that

$$\rho_{\rm GJ} \approx -\frac{1}{2\pi c}\frac{\mathbf{\Omega}\cdot\mathbf{B}}{1-\frac{r}{R_{\rm LC}}\beta_t \sin\theta} \tag{3.3.3}$$

where β_t is the toroidal component of the particle velocity.

In most regions of a pulsar magnetosphere we have that $\rho = \rho_{\rm GJ}$, what we call the force-free configuration. Note that there is a conic geometrical region of space around the pulsar and coaxial with Ω, where $\mathbf{\Omega} \perp \mathbf{B}$ and so $\rho_{\rm GJ} = 0$. This is the so-called *null surface* displayed as a dashed line in figure 3.8, and the Goldreich-Julian charge density changes its sign in there: positive charges are located within the cone and negative charges occupy the space outside it.

The so-called **gaps** are regions where the charge distribution differs from the Goldreich-Julian charge density. This can happen if there is insufficient charge supply, so an efficient acceleration of charged particles can take place in such regions. Gaps can only be located within the open zone described in §3.1, since any $E_\parallel \neq 0$ in the closed zone would be screened by the dense plasmas located there. Several models propose different location of the gap, which allows us to classify them between those where the gap is found in the inner magnetosphere (the polar cap model) and those with the gap in the outer magnetosphere (the outer gap and slot gap models). Other models locate the emission in the wind zone using a different approach [76].

The place where the last open lines emerge from the NS surface define the north and south polar cap regions, respectively. The **polar cap model** [77] proposed that the high energy photons were produced near the magnetic poles, between the stellar surface and several stellar radii away (blue-shaded region in figure 3.8) and at the same location as radio photons. It predicted a narrow radiation beam, so the wide separation observed between the two peaks could only be retrieved from the model if strong constraints were imposed on the orientation and the observer viewing angles. However, pulsar population studies have shown that these angles are typically bigger than those values. The existence of non-thermal optical emission also favor outer magnetospheric models, and it could not account for the VHE-γ-ray pulse profiles. The polar cap model was effectively discarded to explain the Crab pulsar γ-ray emission but it is still valid to model the radio and γ-ray emission of other pulsars [78].

In the **outer gap model** was originally proposed by Cheng [79] and it has been modified later on [80, 81]. It has been one of the most successful models to account for γ-ray emission from pulsars. According to it, emission occurs at high altitudes of about 100 times the stellar radius but still within the LC, in the red-shaded region in figure 3.8. A nearly constant, non-zero $E_{\parallel}$ component appears there and a fan-shaped γ-ray emission region is created. Its leading and a trailing sides can explain the double-peak structure in the lightcurve, as well as the different spectral properties for P1 and P2 regions. Its predicted HE cut-off was ruled out by IACTs observations [70] but it can account for the strong bridge emission recently detected at VHE [72]. It also shows that the shape and separation of primary and secondary peaks in the pulse profile is highly dependent on the magnetic inclination and on the viewing angle [82, 83].

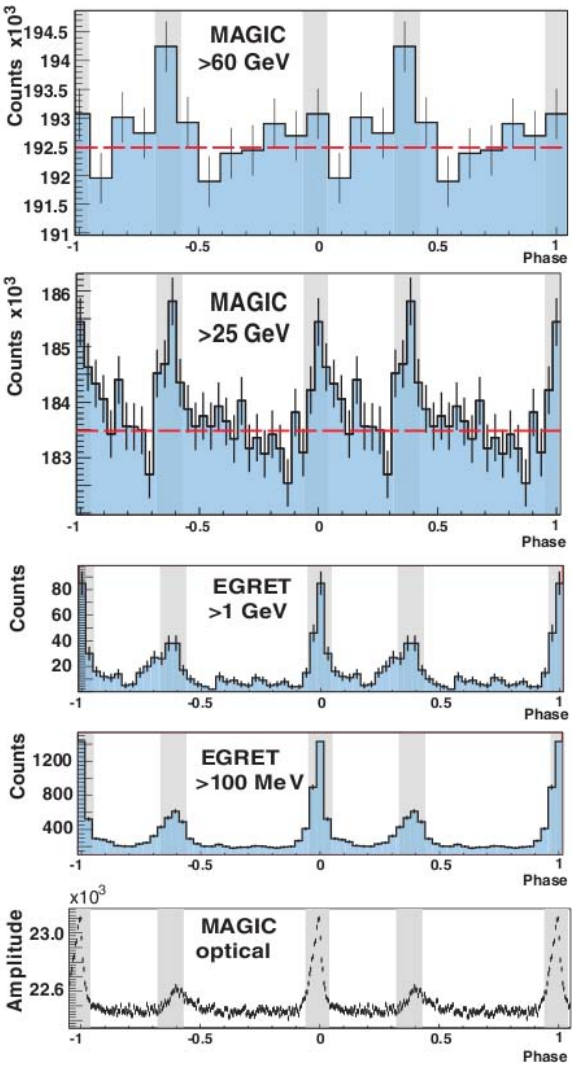

Figure 3.9: Crab pulsar phaseogram or phase-folded lightcurve, in different energy bands from radio to γ-rays. Its characteristic double-peak structure can be observed virtually for all wavelengths. However, at lower energies P1 is the dominant peak, whereas P2 becomes dominant at γ-ray energies. Taken from [37].

The **slot gap model** places the γ-ray emission very close to last open field line, which extends from the star surface up to the LC (green-shaded area in

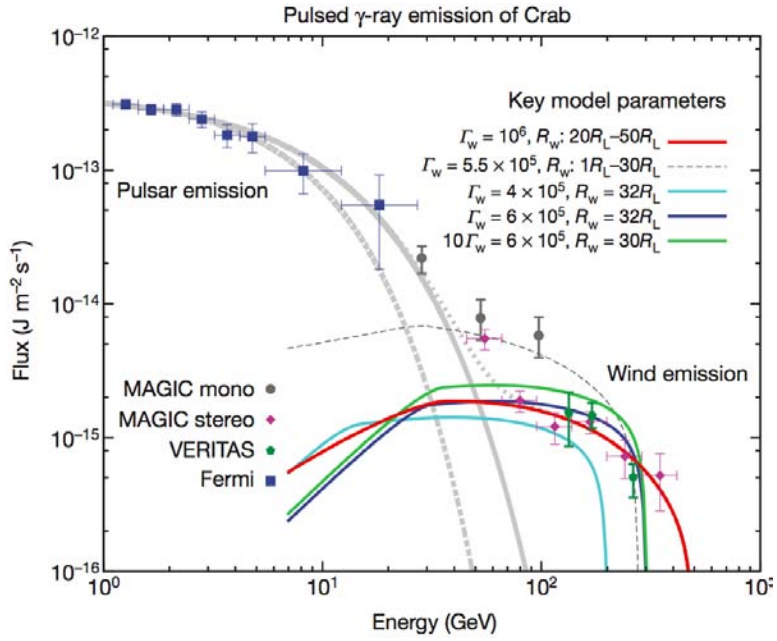

Figure 3.10: Different pulsar spectra as predicted by the wind zone model using several combinations of input parameters. The Crab nebula measurements by Fermi and pulsar measurements by several IACTs are displayed. Taken from [76].

figure 3.8). Numerical simulations showed that the electrons emitted from the trailing side of the poles travel along the last open field line and they form certain superposition patterns and caustics. According to this model, the $E_{\parallel}$ component tends to a constant value at high altitudes, where charged particles can accelerate. Here, the main emitters of γ-rays are electrons via curvature radiation, but there is also an important contribution of emission by secondary particles via synchrotron radiation [84]. The double-peak structure is well predicted, as well as the observed pulsar spectrum up to energies of a few hundred GeV [85].

Using a different approach from the gap modes, **wind zone emission model** places the production of γ-rays beyond the LC, at $\sim 10^4$km distance and before the termination shock[76]. This model proposes that pulsar wind particles can up-scatter X-ray photons into γ-rays via the IC mechanism. This would require a sudden acceleration of the wind up to Lorentz factors of $\sim 10^6$ in a region from the pulsar within approximately 30 to 50 times of LC radii. This model was able to account for the pulsed signal at VHE detected by IACTs, as shown in figure 3.10, and it predicts a sharp spectral cut-off at energies around 500 GeV. However, it fails to reproduce the observed narrowing of the pulses at the highest energies.

Chapter 4

Analysis of the Crab pulsar

The Crab nebula, together with the pulsar that lies within it, is considered a standard candle for ground-based VHE astronomy due to its unique properties (see section 3.2). Hundreds of observation hours are devoted to this source every year: since the first light of the MAGIC telescopes the Crab nebula has been observed for about 1.000 hours in both on-source and wobble observation modes, during each of the different hardware configurations and under every possible observation condition. This chapter deals with an extended effort to analyze all available Crab pulsar data taken since the first light of the MAGIC telescopes in 2005.

This is an unprecedentedly large data set for any IACT experiment in the history of γ-ray astronomy. All of these data have already been analyzed within individual projects and limited results were reported for each observation campaigns or, at most, stacking just a few observation periods together. Hints of pulsated emission were consistently found above the 400 GeV for some of them thus, more data were needed to increase the statistics and turn this hint into a detection of a significant signal at unprecedentedly high energies for pulsars.

The approach to achieve this goal was to analyze all available Crab data taken with the MAGIC telescope. This was the first successful attempt of the MAGIC collaboration to combine such a massive amount of data to produce a single scientific result. Re-analyzing old data which was considered fully-exploited and was stored for years, finally proved to be worthy, as we will see from the obtained results. The discussion about their implications regarding the pulsar environment and the current models for the Crab will be given at the end

of this chapter.

Due to the large amount of observational data and its complex analysis, a work division was required. Two teams were formed to work in parallel: one was responsible for the single telescope data and the other one analyzed data taken with the stereo system. Once both groups provided their individual results, they were merged into a single scientific output.

The author was part of the so-called "mono team" and the details of the performed analysis will be shown here. After it, a short overview of the stereo data analysis will be given in order to put in context the global results of this group effort.

4.1 Classifying the data

The MAGIC telescopes operated in stand-alone mode (hereafter, mono mode) until the second telescope was commissioned and stereo operations started in 2009 until today. During these 10 years, several major hardware changes were carried out, along with minor changes in the optical PSF. Virtually all of them affect the telescope performance but the main distinction consists of data taken with different readout electronics: each system needs a dedicated signal extraction method, they use different signal windows, sampling rates, stored number of memory slices and so on. Many other technical features of the used electronic components are critical for the detection and recording of the shower signal and even if one intends to detect a millisecond pulsation such as that from the Crab: a high-precision timing system is also required, such as the GPS + rubidium clock that was installed in MAGIC to provide for a robust absolute timestamp for each event.

The total amount of available Crab nebula observational time until mid 2014 was of the order of 1000 h, out of which half was taken during the mono era. Among the mono observations there are about 50 h taken using the sum-trigger system. A reduced energy threshold was achieved with this system, which was crucial discover the LE γ-ray emission of the Crab pulsar above 40GeV [37]. However, since we were interested in discovering if any pulsed emission existed at VHE, these data were considered a low priority by the analysis team. A sum-up with the available Crab observation time for all the different hardware configurations can be found in table 4.1.

From 2004 until March 2006, a specific kind of 8-bit, 300 Msample/s FADC units known as "Siegen FACDs" were used to digitize the camera signal. Later on, a set of new FADCs operating at 2 Gsamples/s were installed but their signals were split between the old and the new system, such that consistency could be checked between both. Signal splitting was used for half a year, and all the observations that were performed before and during this period belong to the first "cycle" of MAGIC observations, the so-called **cycle I**. In December 2006 the new MUX system, described in §2.4.5, started operating in stand-alone mode. This new readout configuration was used for more than five years, even after the second telescope started operating. So, data cycles II, III and IV were taken using the MUX system.The MUX readout system was substituted in April 2012 by DRS4 chips, identical to the ones used by then in M2. These data, which belong to cycles V to IX, were analyzed by the stereo team and a thorough description falls beyond the scope of this thesis. Only the necessary details to understand the combined results will given later in §4.9.

Data taken using the Siegen and Siegen+splitters readout systems are stored in a database in Würzburg, Germany. These data needed to be processed with a special version of the MAGIC analysis software. Furthermore, at the beginning of MAGIC operations and as the members of the collaboration learned how to operate the telescopes, several of hardware and software problems were spotted. Therefore, a fraction of the Crab nebula data taken during this first cycle is affected by multiple problems, which are hardly logged.

Even though the original intention was to analyze all the Crab nebula data that were ever taken with MAGIC in mono mode, this ambitious goal was reduced in order to achieve meaningful results. Part of the reasoning behind this decision was the considerably worse sensitivity of the telescopes at the time and the unreliability of the timestamp. We concluded that, if even after analyzing the rest of the much more easily available data, a significant detection of the Crab pulsar at VHE was not achieved, we would focus on processing the oldest data to extend our analysis.

Within each hardware epoch, the MAGIC focusing capabilities varied night by night, mainly due problems related to the mirrors or to the AMC system or due to major weather events like storms or snow. The influence of all these

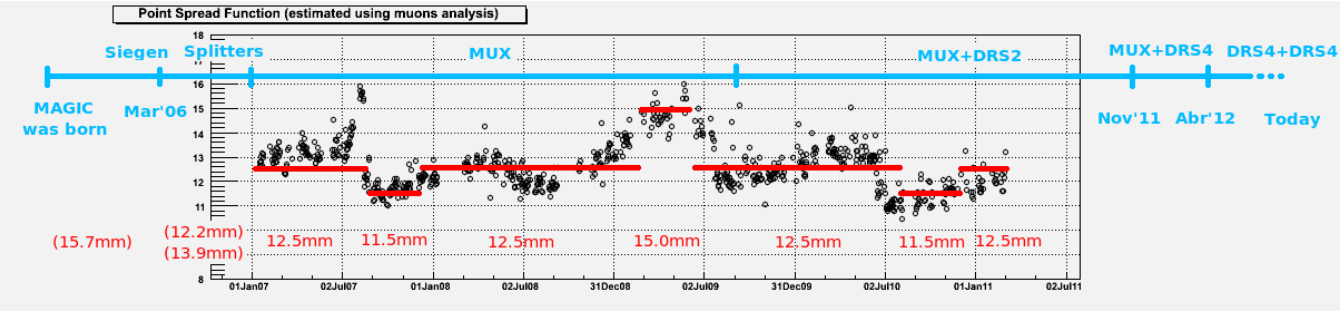

Figure 4.2: Measured PSF values for each observation night while the MUX hardware was used, as well as the first 2 yr of stereo data.

issues could be spotted by measuring the telescope PSF nightly, as shown in figure 4.2 for our period of interest. The analyzed data were subdivided in three different subsets according to the measured average PSFs: 10.6 mm, 9.2 mm and 13.0 mm. These values are the input parameters used in the MC production software, and they are linearly related to the measured values (figure 4.1), 12.5 mm, 11.5 mm and 15.0 mm respectively.

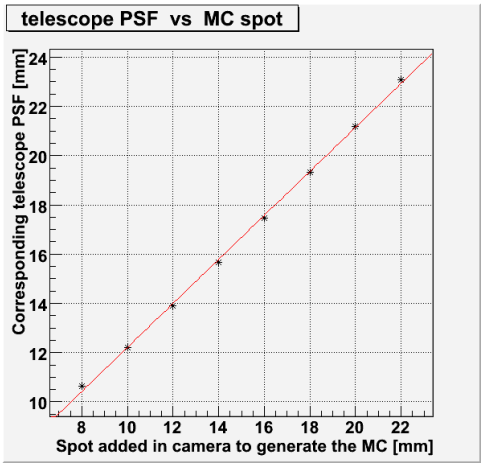

Figure 4.1: Measured PSF spot size vs simulated PSF in the MC at camera software level. A fixed value of 7 mm has to be added in quadrature to the simulated value to obtain the corresponding measured value.

Notice that, even with the hundreds of observation hours, we estimated that the Crab pulsar significance at such high energies would end up being very close to the noise, mainly due to its strong nebula-dominated background and its steep spectrum. The strategy we decided to follow for our analysis was to optimize the data selection such that we could reduce the amount of discarded hours to the minimum and, at the same time, maximizing the statistics of our analysis.

The MAGIC collaboration provides the data for a standard analysis at `star` level, after the cleaning of the shower images with a set of pre-defined cleaning levels. The approach we used was rather different: we wanted to apply lower cleaning thresholds in order to maximize the statistics at the lowest energies by decreasing the result-

Hardware epoch	PSF (mm)	Obs. mode	Obs. time [h]		
Siegen Siegen+splitters	(multiple)	Wobble & On	290		
MUX	10.6	Wobble	119	236	297
		On	117		
	13.0	Wobble	22		
	9.2	Wobble	21	39	
		On	18		
Stereo	(multiple)	Wobble & On	400		

Table 4.1: Amount of observation hours taken with each hardware configuration. Details on the fraction of data for each PSF value and observation mode are given only for the data sample whose analysis is explained in this thesis.

ing energy threshold of our analysis. To do so, the calibrated data files needed to be downloaded and processed manually.

Such decision had two implications. First, the complexity of the analysis was increased, since an additional analysis step was required: Star software on the calibrated data, which required to understand and find the proper input parameters. Second, heavy calibrated files needed to be downloaded, stored and processed. This imposed major constraints for the computing server where these file were downloaded, as well as a considerable amount of additional CPU-time needed to run the jobs using `star` software. A total amount of more 4.5 TB of low-level data files were downloaded from the databases.

Also all the data labelled as Crab-SUM was downloaded, almost 1 TB of disk space. These data were taken using the SUM trigger but those files also contain events that were triggered by the standard L1 trigger. My intention was to use only the latter events in my analysis and those that *only* fulfilled the SUM-trigger condition were discarded. In this way, we increased the total available observation time that was included in the analysis, ending with a total sample composed of ~ 23k Crab nebula data files. The amount of observation hours contained in them will be explained later on in this chapter.

4.2 Cleaning the data

The image cleaning was performed using both the standard cleaning method and the new dynamic cleaning. Time cleaning was applied using both standard and dynamic methods and Sum-cleaning was also used. The cleaning levels for

the standard cleaning were 4-2 for the charge threshold of core and boundary pixels and a 4.5-1.5 for the time differences. This is a much lower cleaning level than the 6-3 charge values used in the standard processing of MUX data, whereas the time cleaning was not modified. Some basic Hillas parameters, like for instance the mean number of islands, were checked to make sure that we were not increasing the amount of surviving events by adding only noise events to our data sample.

Faulty Crab nebula data was discarded like data taken during the commissioning of the MUX system (about the first month and a half after installation), data affected by some kind of wrong settings, data which had some important data branches missing and data affected by some other basic problem. We were able to successfully run Star on most of the remaining selection using the cleaning levels described above: only in a tiny fraction of (less than 100 files) the number of spurious islands in the images after the cleaning process was higher than the standard 20% limit. Therefore, higher threshold was then required: a 5-3 level was enough in those cases to have a satisfactory cleaning of the shower images.

4.3 Training the RF

The next step was to assign an estimated energy, a hadronness and a `disp` value to each event in the data. To do so, specific RFs for each data sub-sample were trained (see §2.5.5). A minimum size cut of 50 phe was also applied to get rid of faint events where Hillas parameters are estimated with bigger uncertainties.

Once each RF classification tree was produced, the separation power of each variable was measured by means of its associated Gini index and the overall achieved sensitivity of our instrument was checked. This was done in the following way: a small but particularly stable sub sample of the data which only included the month of January 2008 was further processed. Since the spectrum of the Crab nebula is well-known and can be easily measured, we used it to check the efficiency of the training variables and to spot any problem occurred during this step of the analysis. We also computed the sensitivity of the telescopes, $S_{5\sigma}$, defined as the weakest source that we can detect in 50 h of perfect observation conditions with a significance of 5σ, and which is usually measured in crab units (C.U.) or in *millicrabs* (10^{-3} C.U.).

PSF [mm]	Source	Zenith angle range [°]
13.0	PKS1717+177	11-30
	MS1050.7+494	20-35
	PKS1424+240	5-20,30-45
	Segue	13-28
	3c279	35-45
9.2	0851+202	9-32
	S5-0716+714	43-45,50-55
	WR-147	12-28
	3c66A	15-20
	1ES0158+003	30-35
	1H1722+119	22-30
	BLLac	14-31
	Cyg-X1	20-50
10.6	Her-X1	8-38
	MGR-HHS	10-32
	MGR2019+37	9-17
	M87	40-55
	1ES1011+496	39
	1ES2344+514	31-43
	Cyg-X3	10-32,51-54
	2E-1415+2557	28-30
	HB89-1553+11	56-58
	M82	38-46

Table 4.2: List of undetected or weak sources whose data were used as off samples for the RF training with `osteria` and for the background estimation in `fluxlc`.

PSF [mm]	Obs. mode	Applied cuts
All	All	Size < 50 phe
10.6	All	Zenith $< 58^\circ$
13.0	wobble	Zenith $< 45^\circ$
9.2	wobble	Zenith $< 53^\circ$

Table 4.3: Data cuts applied during the training of the RF and also for all the following steps of the analysis chain.

An extra limiting factor for the training of the RF was the availability of appropriate MC and off-data samples that matched the characteristics of the data samples we intended to analyze. The most relevant properties to match were the simulated PSF and the zenith angle range, which should be at least as wide as the distribution of real data shown in figure 4.3. In order to be consistent, both the MC and the off-data sample also needed to be processed by Star using the same custom configuration that was used for the on-data themselves. MC files containing almost 10M simulated γ-ray events were retrieved from the MAGIC database and processed from Star level. The off-data were carefully picked from undetected or weak sources that were observed during the same cycle as the on-data, so the telescope response was as similar as possible both for the on and off observations. About 0.1 TB were used, corresponding to 25 different off sources and listed in table 4.2.

These data needed to cover the whole zenith angle distribution of the Crab observations. The zenith angle distribution for the Crab nebula data as well as for the used MC and off samples is shown in figure 4.3. However, the MC production that reproduced the 9.2 mm PSF period observations in on-source mode was no longer available. Since a dedicated RF could not be trained for this subset of the data, and considering the small amount of observation hours contained in this subsample, we decided to use the most similar MC available, the one with 10.6 mm simulated PSF, instead. Some parameters have already been found to efficiently distinguish between hadrons and γ-ray, in the case of hadronness-specific RF for instance. A summary of the used variables can be found in table 4.4. Apart from those, we wanted to see if we were able to improve the separation power of the RF method by adding the new dynamic variables, together with their classic counterparts.

RF with dynamic variables

A small study was performed with the goal of estimating the efficiency of the newly-defined dynamic variables to boost background discrimination when included as test variables for the RF training. Five combinations of variables and

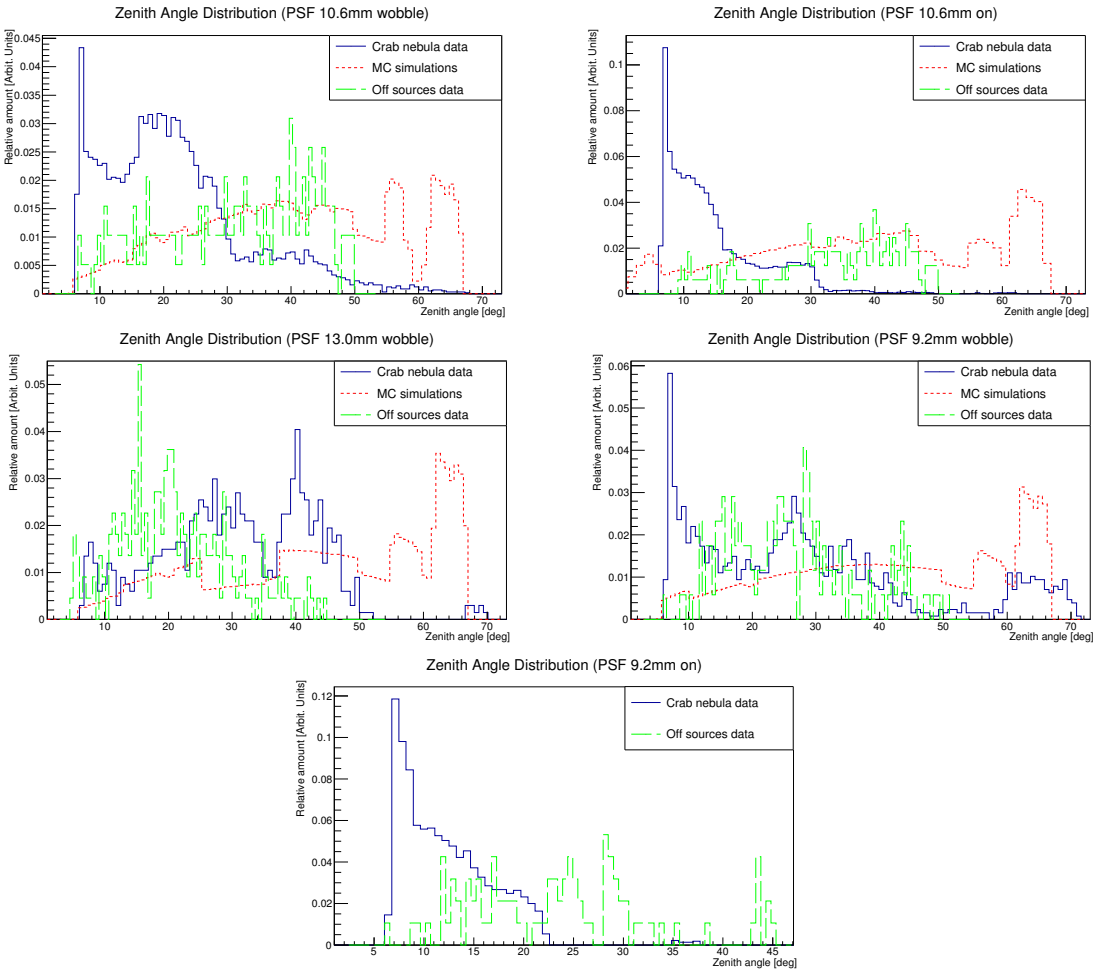

Figure 4.3: Distribution of zenith angles for the Crab nebula observations under study (*solid, black line*) as well as for the MC simulations (*red, dotted line*) and off data samples (*green, dashed line*) needed to analyze it. The different telescope PSFs and observation modes are represented in individual plots. Only these zenith angle ranges, where data, MC and off sources were available, could be simulated. Therefore some data, especially at high zenith angles, could not be analyzed due to lack of contemporaneous off sources, imposing the zenith angle limits listed in table 4.3. Data taken with 9.2 mm PSF in on-source mode (bottom plot) had to be analyzed with MC corresponding to 10.6 mm PSF instead.

cuts were used for the RF training. All of them contained the regular (non-dynamic) Hillas parameter and variables listed in table 4.4.

Set A, the first combination, consisted of the standard variables recommended by the MAGIC collaboration, that have a good performance for a wide range of energies. A cut in `size` WAS also included: any event with a total charge of less than 80 phe was automatically discarded to avoid the fluctuations close to the telescope detection threshold.

Set B included the same variables in set A together with its dynamic counterparts, as well as a reduced `size` cut at 50 phe. The next sets also included this reduced `size` cut.

Set C included set A variables and the dynamic versions of `width`, `length`, `dist` and `RMStime`.

Set D was a copy of set C but without the variable `RMStime` and the dynamic `RMStime`.

Set E was a copy of the previous one but without any dynamic variable: only the standard variables listed in table 4.4 except for `RMStime` plus a reduced `size` cut at 50 phe.

Hadronness	**Energy**	**Disp**
	`Size`	
	`Width`	
	`Length`	
	$\frac{\texttt{Size}}{(\texttt{Width}\times\texttt{Length})}$	
	`Conc`	$\frac{\texttt{Length}}{\texttt{Width}}$
	`Dist`	
	`P1Grad`	
`M3long`	`Leakage1`	$\|\texttt{Asym}\|$
	`Zenith`	

Table 4.4: Variables used in the RF training for γ-hadron separation, energy or disp estimation.

The same procedure used before was applied to measure the improvement in the separation power of each combination with respect to to the standard ones: the Crab nebula spectrum and the telescope sensitivity were computed with the small, good quality data subsample from January 2008. The obtained spectrums and sensitivity plots are shown in figures 4.4 and 4.5. For set A (standard variables and 100 phe cut), a sensitivity of $S_{5\sigma} = 4.4 \pm 0.2\%$ C.U. was reached. However, when set B was used, the sensitivity went down to $S_{5\sigma} = 1.8 \pm 0.1\%$ C.U., an improvement of more than 50%. However, the spectrum was significantly underestimated for the lowest energies and overestimated for the highest energies. After applying the RF trained with set C ($S_{5\sigma} = 1.9 \pm 0.1\%$ C.U.) the flux estimation for the highest energies slightly improved without changing the overall sensitivity. Using set D ($S_{5\sigma} = 1.9 \pm 0.1\%$ C.U.) we managed to partially correct for the wrong

spectrum estimation at low energies an, moreover, the separation power of the Hillas parameters `width`, `length` and `dist` was increased between a 20% and a 50% (as measured by the Gini index of both the standard and dynamic variables combined). In the last case (set E), the spectrum was properly estimated for all the energy range, although the sensitivity got slightly worse than for the previous three cases ($S_{5\sigma} = 2.0 \pm 0.1\%$ C.U.). The separation power improved by set D was lost when the dynamic variables were removed in set E but no way could be found to obtain a correct Crab nebula spectrum with the inclusion of the dynamic variables within this limited study.

We concluded that a further investigation was required to properly include these new dynamic variables in the training process of the RF. Since this was beyond the aim of our research, we decided to use set E, i.e. standard variables without `RMStime` and a reduced `size` cut at 50 phe.

4.4 Selecting the data

Only good quality data was used in the final analysis. The selection was done based the following two criteria. First of all, a loose selection cut was applied regarding two Hillas parameters: any day whose mean `width` and `length` values was beyond 1.5 standard deviations away from the mean of the complete data subsample was discarded.

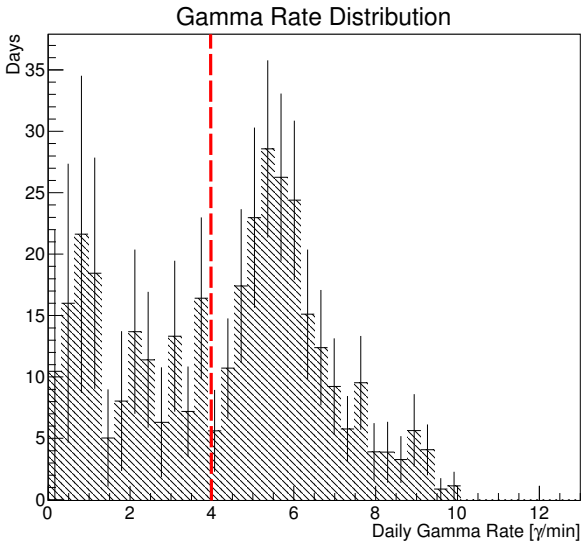

Figure 4.6: Distribution of estimated gamma rates above 280 GeV for the data in the sample below 33° in zenith angle. The quality selection cut is displayed with a red, dashed line.

Second, a cut on the daily γ-rate above 280 GeV, computed as explained in §2.5.8 for two zenith angle bins: low zenith, from 0° to 33°, and

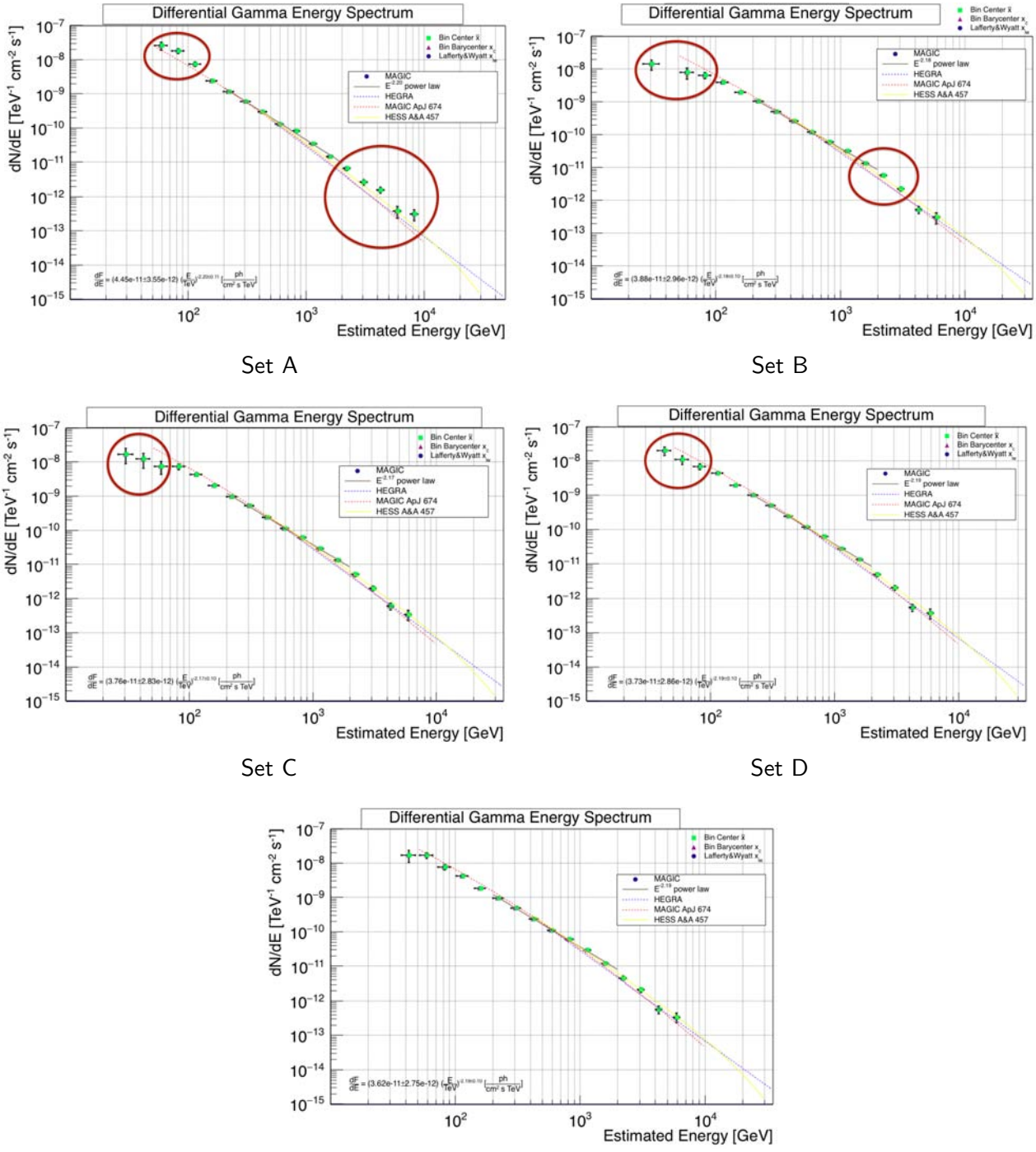

Figure 4.4: Crab Nebula spectrum obtained after applying the RFs trained with different sets of variables, as explained in §4.3. Miscalculations for each combination of training variables are marked with red circles. The curved power-law fits published by different IACTs are shown as a reference.

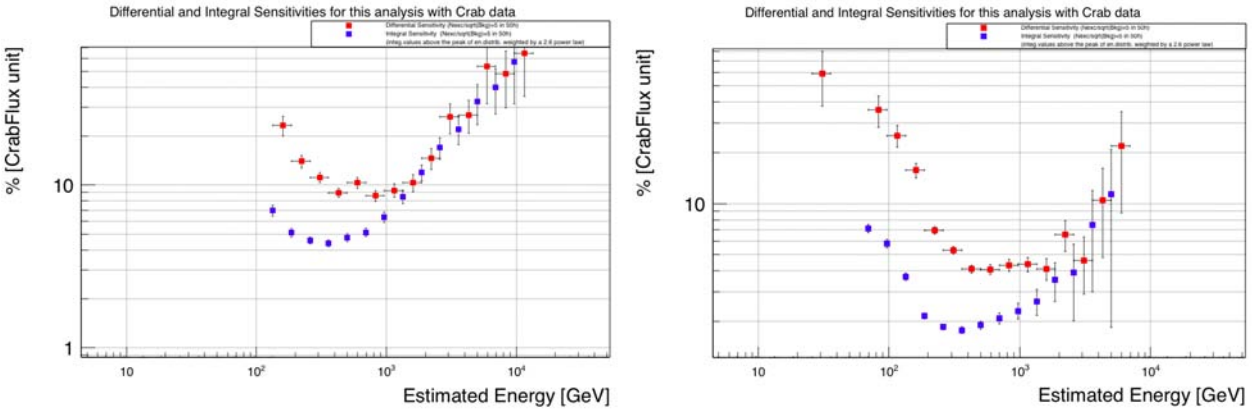

Set A

Set B

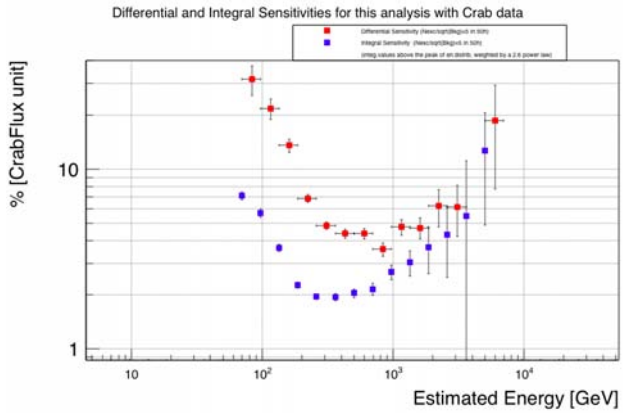

Set C

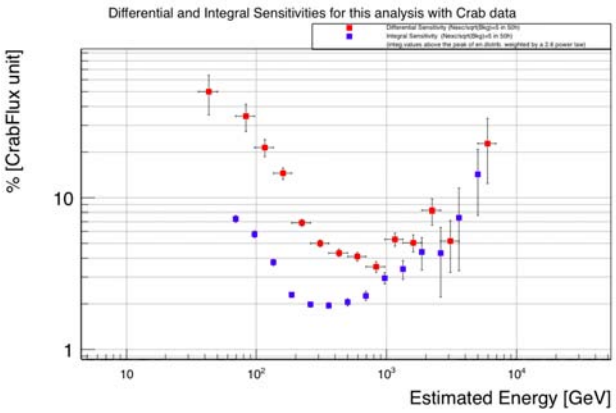

Set D

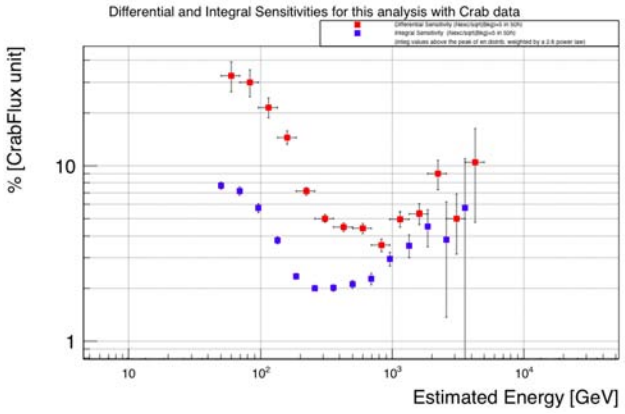

Set E

Figure 4.5: MAGIC differential (*red*) and integral sensitivity (*blue*) obtained after applying the RFs trained with the different sets of variables, as described in §4.3.

high zenith, from 33° to 48°. Two basic hadronness and α cuts were applied to the data and to the MC, at values 0.5 and 10° respectively. The obtained daily γ-rates, shown in figures 4.6, 4.7, B.1 and B.2 had a mean value of about 4.3 γ/min and an RMS of 2.4 γ/min. All the observation days where the γ-rate fall below 4 γ/min were discarded.

The selection of the value for the γ-rate cut was done in a similar manner as for the selection of the RF training variables, as explained in §**??**: the Crab nebula spectrum was computed for each tested value, as well as the source lightcurve. Three combinations were tested: a single, lower cut at 4 γ/min; a lower and upper cut at 4 and 8 γ/min respectively; and no cut at all. In the last case, the obtained mean flux obtained from the lightcurve was well below the expected value but the spectrum showed features that were inconsistent with a single or a curved power-law, even if starting at energies as low as ~ 40 GeV. Adding a lower cut increased the energy threshold so the lowest energy point obtained in the lightcurve was ~ 60 GeV. However, the spectrum was now was fully compatible with a power-law for almost two orders of magnitude. The addition of an upper cut removed the highest flux points in the lightcurve and worsened the sensitivity at high energies, so it was finally discarded.

From the 212 observation days we retrieved from the data base at PIC, 156 days (73.6%) survived the quality cuts. The subsamples with a highest rate of discarded dates were whose with the lowest PSF (9.2 mm), with only 66.7% and 63.2% of remaining days after quality selection for wobble and on observation modes, respectively. Subsample with a PSF of 10.6 mm were those with the highest rates of good quality days: 72.5% and 80.3% for wobble and on modes, respectively. A summary of these figures is shown in table 4.5.

4.5 Optimizing the cuts

Once we have assigned a hadronness value to each event with the use of the RF, one has to select those cuts in hadronness and α (θ^2 in case of stereo observations) that will maximize the significance of the signal of the analyzed source. We are only interested in the detection of the signal from the pulsar but we are observing, at the same time, the γ-rays coming from the nebula, which is actually a very special situation in γ-ray astronomy. We can take advantage of it by using the γ-ray background from the nebula as reference signal to optimize our cuts without biasing the significance of the later pulsar detection!

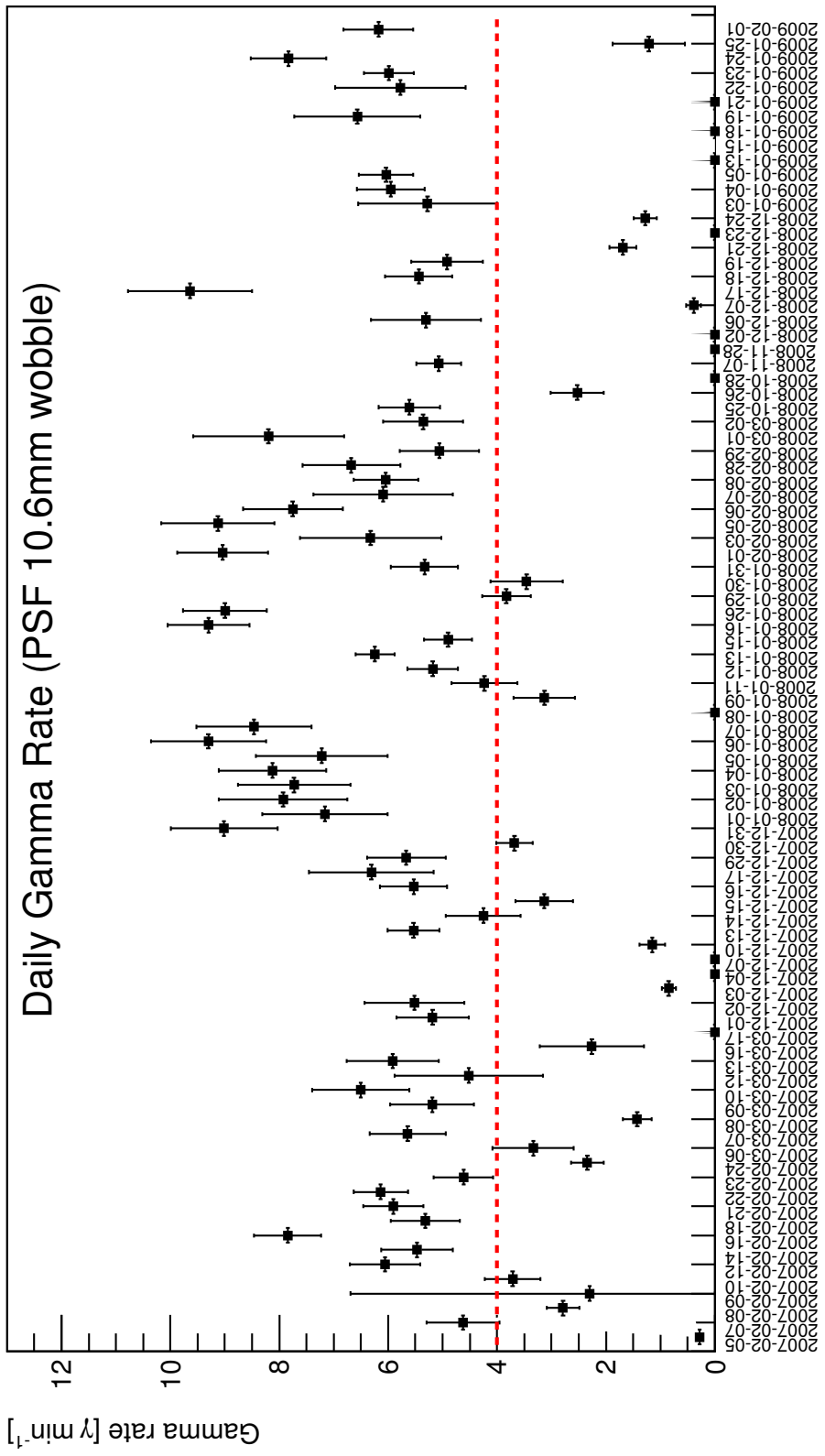

Figure 4.7: Mean daily estimated gamma rates for the observation nights within the 10.6 mm PSF subsample and wobble observation mode included in the presented analysis. With the applied quality selection cut, all nights with gamma rates below 4γ/min were discarded, as shown by the red dashed line. The plot for the rest of the PSF values and observation modes can be found in §B

PSF [mm]	Observation mode	Number of days before cuts	after cuts	Quality Rate [%]
10.6	wobble	91	66	72.5
	on	71	57	80.3
13.0	wobble	19	13	68.4
9.2	wobble	12	8	66.7
	on	19	12	63.2
	TOTAL:	212	156	73.6

Table 4.5: Summary with the number of observation days before and after quality selection in the complete mono data sample. These figures are specified for each subsample according to its PSF and observation mode and its average is also shown in the last row.

To do so, we scan the parameter space of hadronness and α cuts for every pair of values for each energy bin. We then perform the computation of significance of the pulses,excluding the on-region of the phaseogram. Instead, we assume that the previously measured pulsar spectra can be extended to higher energies and we estimate the number of expected pulsed events with those cuts. The expected significance, computed using the off-region signal extracted from the data is plotted as a function of hadronness and α cuts. An optimized set of cuts for each energy bin is extracted and fitted. The fit function will provide the optimized cuts that will be applied to the final analysis. Only in this last step, the signal in the on-region of the phaseogram is unlocked and measured directly from the data.

The data were divided in a certain number of logarithmic bins in estimated energy. Usually one applies between 20 and 30 bins to the energy range between 5 GeV and 50 TeV. For the pulsar analysis, the analysis team decided to use 30 bins in these energy band, whose edge values can be found in table 4.6. Then, two sets of cuts were defined. On the one hand, the **basic cuts** consist of two fixed thresholds on the *number of islands* and on the *leakage1* parameter (see §2.5.2). Dedicated studies within the collaboration have shown that these cuts eliminate events with non gamma-like artifacts, either from hadronic cascades, background light or events affected by to hardware problems in the camera. The first cut eliminates most of the hadronic showers that contain more than one island of triggering pixels and it is especially efficient at high energies,

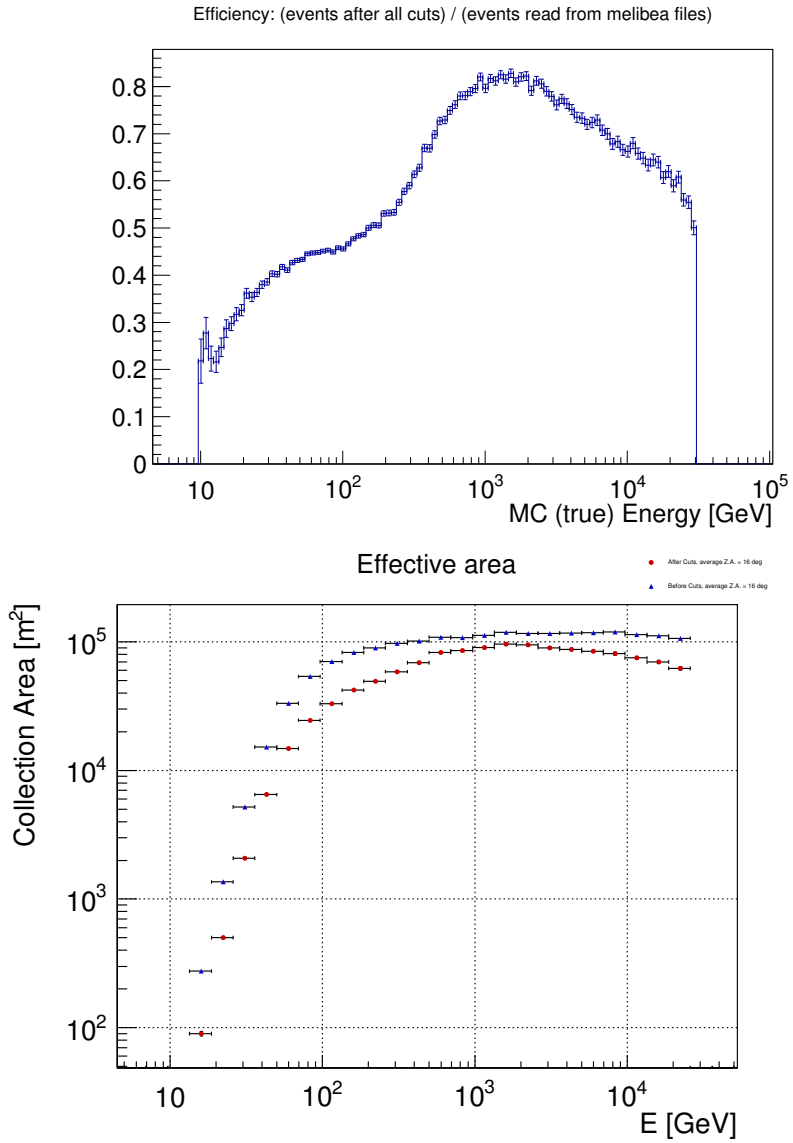

Figure 4.8: *Top)* Efficiency of the analysis cuts that were applied to the biggest data subsample (10.6 mm PSF in on mode), as a function of the true energy, as estimated from the MC simulations. *Bottom)* Effective collection area of the telescopes before (*blue triangles*) and after (*red circles*) the application of the analysis cuts for the biggest data subsample.

Bin	Min. E [GeV]	Max. E [GeV]	Bin	Min. E [GeV]	Max. E [GeV]
1	5.0	6.8	16	500.0	679.7
2	6.8	9.2	17	679.7	923.9
3	9.2	12.6	18	923.9	1255.9
4	12.6	17.1	19	1255.9	1707.3
5	17.1	23.2	20	1707.3	2320.8
6	23.2	31.5	21	2320.8	3154.8
7	31.5	42.9	22	3154.8	4288.5
8	42.9	58.3	23	4288.5	5829.6
9	58.3	79.2	24	5829.6	7924.5
10	79.2	107.7	25	7924.5	10772.2
11	107.7	146.4	26	10772.2	14643.2
12	146.4	199.1	27	14643.2	19905.4
13	199.1	270.6	28	19905.4	27058.5
14	270.6	367.8	29	27058.5	36782.1
15	367.8	500.0	30	36782.1	50000.0

Table 4.6: Definition of the 30 estimated energy bins used in the Crab pulsar analysis. These definitions were used for both the mono and the stereo analysis teams.

where wide hadronic showers are clearly different from the more compact γ-ray showers. The second cut removes images ranging out of the FoV of the camera. The used cut values were:

`MImagePar.fNumIslands` < 2

`MNewImagePar.fLeakage1` < 0.2

The **analysis cuts** are more constraining than the basic cuts since the latter are included in the former, together with a variable selection with respect to two parameters: a maximum hadronness h and an absolute maximum in the orientation angle of the shower, α:

`MHadronness.fHadronness` $< h$

`|MHillasSrc.fAlpha|` $< \alpha$

The actual values of h and α were carefully selected to maximize the chances of detection of the pulsar signal. To determine them, we established the following procedure:

- 50 values of h for the hadronness cut were tested, between 0,02 (the

minimum cut) and 1,00 (no cut at all). For the α cut, 27 values were tested, between 3° and 30°.

- The number of events $N_{\rm off}(h, \alpha|E_i)$ in a given energy bin E_i that survive the analysis cuts and whose phase lies within the off-phase region were computed.

- The number of background events in the on-region was computed as $\mu \cdot N_{\rm off}$, where $\mu = \frac{\Delta\phi_{\rm on}}{\Delta\phi_{\rm off}} \approx 0.1286$ is the ratio between the on and the off-region widths of the phaseogram.

- The efficiency of the analysis cuts, $\epsilon(h, \alpha|E_i)$, must be computed in order to derive the expected number of pulsed events. It is estimated from the MC simulations as the number of events surviving the analysis cuts divided by the number of events surviving the basic cuts. An example of such efficiency for the biggest data subsample can be seen in the top plot of figure 4.8.

- The number of pulsed events, $N_P(h, \alpha|E_i)$, in this energy bin was derived from a theoretical calculation. We assumed an extension above 400 GeV of the previously measured power-law spectrum for the P2 on-region (the dominant peak at HE), $\frac{dN_{P2}}{dEdAdt} = \Gamma_0 \left(\frac{E}{E_0}\right)^{-a}$, where $\Gamma_0 = \Gamma(E_0) = 3.9 \cdot 10^{-8}$ γ/GeV s m^2 is the flux at $E_0 = 40$ GeV and $a = 3.4$. We then multiplied it by the observation time for that subsample, $T_{\rm obs}$, the energy bin width, ΔE_i, the effective collection area after the basic cuts, $A_{\rm coll}(E_i)$ (bottom plot in figure 4.8), and the efficiency, $\epsilon(h, \alpha|E_i)$. Thus, the number of expected events in the on-region was

$$\begin{aligned} N_{on}(h, \alpha|\Delta E_i) &= N_P(h, \alpha|E_i) + \mu \cdot N_{off}(h, \alpha|E_i) \\ &= \frac{dN_{P2}}{dEdAdt} \cdot \Delta E_i \cdot T_{\rm obs} \cdot A_{\rm coll}(E_i) \cdot \epsilon(h, \alpha|E_i) + \mu \cdot N_{off}(h, \alpha|E_i) \end{aligned} \tag{4.5.1}$$

- The significance of those expected pulsed events was computed with the Li&Ma formula (equation 2.5.2).

- The obtained significance was plotted in the hadronness-α parameter space for each energy bin and for each data subsample individually. An example can be found in figure 4.9 whereas the rest of the obtained plots are shown in the appendix (figures C.5, C.6, C.7 and C.8).

- The maximum of this simulated significance scan was found (marked as an empty triangle in the figure). The hadronness cut was then loosened until the significance reaches 95% of the maximum (solid star in the figure), in order to increase the number of surviving events and to improve the statistics of our analysis. The horizontally and vertically projected values of these points as as a function of the estimated energy can be seen in the left and right plots within figure 4.10, respectively, for the biggest mono sub-sample. The rest of the plots are shown in figures **??**, **??**, **??** and **??**.

- These points were fitted with an exponential that becomes constant after reaching the minimum value:

$$f(x) = \begin{cases} A \cdot e^{B \cdot (\log(x) - C)} & \text{, if } x < C \\ A & \text{, if } x > C \end{cases} \tag{4.5.2}$$

  where x is the reconstructed energy and A_i are the minimum cut values: $A = 8^\circ$ for the α cut and $A = 0.2$ for the hadronness cut. The obtained functions are plotted with a red solid line in figures 4.10, **??**, **??**, **??** and **??**. The values of the fitting parameters A, B and C for each of them are summarized in table 4.7.

- The values of these functions at the center of the estimated energy bin were the finally applied cut values in the analysis of the Crab pulsar data, which are marked with a cross in figures 4.10, **??**, **??**, **??** and **??**. In this case, the significance of the pulsed signal could be computed from the actual number of events in the on-region of the phaseogram.

4.6 Building the pulsar LC

Once the hadronness and α cuts were optimized for pulsar detection and applied to our data, we assigned a pulsar phase to each event according to its arrival time measured by the MAGIC timing system. event had been computed, we produced a specific macro to build the set of needed phaseograms (see §2.5.8) with all the events that survived the analysis process. These phaseograms were binned in 51 regularly-spaced bins between phases $\phi = 0.0$ and $\phi = 1.0$. The phase boundaries for the P1 and P2 pulses and for the background region had to be defined a priori, such that we do not introduce a bias by selecting the on

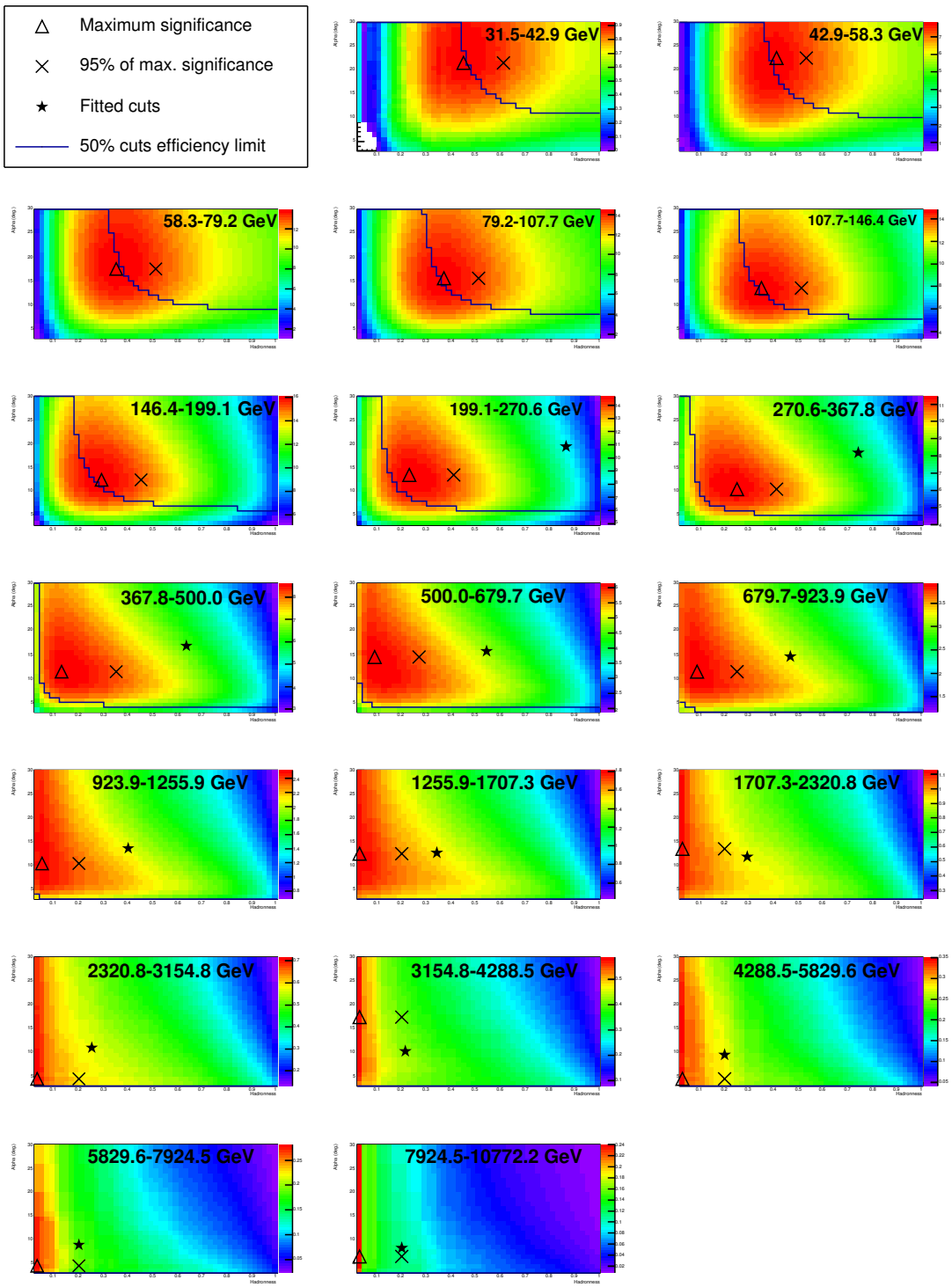

Figure 4.9: Optimization of the α and hadronness cuts to maximize the pulsar significance, for the case of mono data, with 10.6 mm PSF and wobble observation mode. The solid black line shows the 50% limit in the survival rate of events: tighter cuts would remove more than half of the events, reducing the statistics of the analysis. Thus, cuts are always chosen to be looser than that limit. The legend for each symbol can be seen in the top left corner and the optimization plots for the rest of the data subsamples can be found in §C.

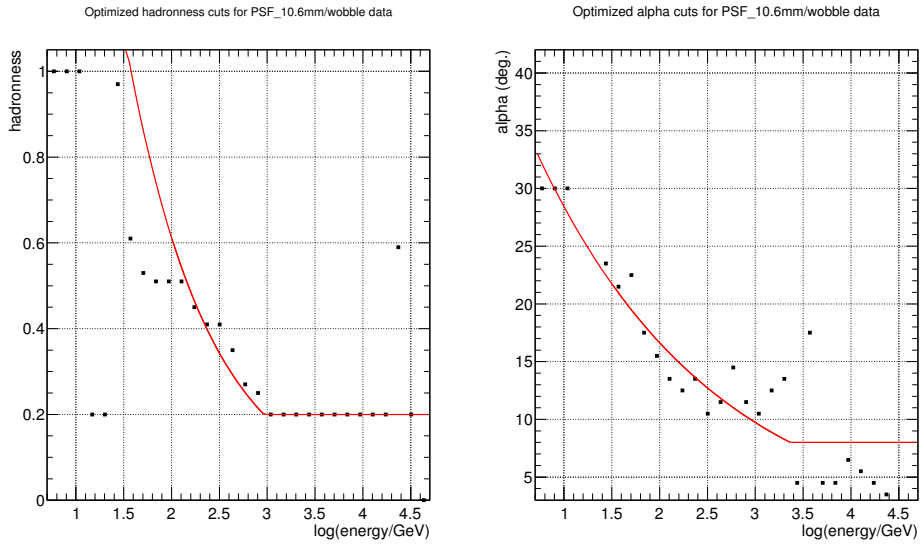

Figure 4.10: Optimized cut values for hadronness and α as a function of the estimated energy for the case of wobble data with a 10.6 mm PSF (the rest of the cases can be found in §C). The black squares represent the point where a loosening of the hadronness cut reaches down to 95% of the maximum in the significance scan. These points are then fitted with the function defined in equation 4.5.2, displayed here with a red, solid line. The values of the fitting parameters can be found in table 4.7.

Data subsample		**α cut fit**		**Hadronness cut fit**	
PSF [mm]	**Observation mode**	B [GeV^{-1}]	C [GeV]	B [GeV^{-1}]	C [GeV]
10.6	wobble	-0.54	2344	-1.16	933
	on	-0.74	676	-0.90	1698
13.0	wobble	-0.54	2344	-0.93	933
9.2	wobble	-0.51	1259	-0.60	1698
	on	-0.92	501	-1.15	297

Table 4.7: Fit parameters of the optimized cut in hadronness and α for each mono data subsample.

and off intervals. The definition of the off-region used throughout this thesis is extracted from the Fermi definition [69]. The on regions for P1 and P2 are taken from [41], where an independent analysis of a subset of the stereo data was performed. The on intervals were defined as centered in the mean value of these gaussians and a width of 2 standard deviations.

This definition may introduce a small bias to the calculated significances in the analysis of the complete dataset, since it is based on information extracted from a subset of the same data that the stereo team was analyzing. However, the resulting on-regions are narrower than most of the alternative definitions, resulting in a lower fraction of background in the signal region. The definitions of the phase regions read then as:

$$\begin{aligned} \text{P1}: &\quad \phi \in [0.983, 0.026] \\ \text{P2}: &\quad \phi \in [0.377, 0.422] \\ \text{OFF}: &\quad \phi \in [0.520, 0.870] \end{aligned} \tag{4.6.1}$$

In this way we obtain the number $N_{\rm on}$ of on events and the number of off events, $N_{\rm off}$. The value of the on-off ratio μ depends on whether the analysis is focused on pulsation coming from either P1, P2 or from both signal regions. This results in 0.1229, 0.1286 or 0.2514 as values for μ, respectively.

The first set of phaseograms that was created was composed by individual phaseograms for each of the 5 data subsamples and for each estimated energy bin were analyzed and are listed in table 4.6, as well as phaseograms with all the data samples stacked together. Phaseograms for several interesting energy ranges where built, both for individual data subsamples as well as for all the samples stacked together. These were the full (FR), the low energy (LE) and the high energy (HE) ranges, with energies between 30 and 1700 GeV, between 30 and 400 GeV and between 400 and 1700 GeV. Lastly, stacked phaseograms for each of those energy ranges were built with an inverted α cut. By doing this we checked that the pulsed signal was a real measurement from the source and not an artifact of our analysis.

A special MARS class was used for this task: the `MHPhase` class. This C++ object contains the necessary tools to compute the statistical significance of the pulsed signal using all the test statistics that were explained in §2.5.7.

Estimating the ephemeris uncertainty

A sub-task that was performed regarding the estimation of the event phases was the computation of the ephemeris uncertainty, $\sigma_{\rm eph}$, a quantity that will be important latter. To estimate it, we will make use of the reported error in the measurement of each ephemeris for all the months when Crab was observed by MAGIC, which were included in this analysis. This makes a total of 39 months, which are listed in table 4.8. In this table, also the errors in the arrival time of each pulsar at the beginning of each month is shown, as reported by the Jodrell Bank ephemeris [53].

As we can see, the estimated value of $\sigma_{\rm eph} \approx 0.00012 \approx 4\ \mu$s is the dominant contribution to the uncertainty in the time estimation of the pulsar events, since it is a factor 4 bigger than the uncertainty of the MAGIC timing subsystem (see §2.4.7), which should be added in quadrature.

4.7 Computing flux and spectra

Once all the previous analysis step were completed, we also estimated the gamma rate per unit area and time, namely the DES of our source (see §2.5.8) using Fluxlc software within the MARS suite. Since we are actually observing two sources at the same time, the Crab nebula and the central pulsar, we were also able to estimate both spectra independently. To do so, Fluxlc had to be executed in two different ways: the standard mode, where off data is taken from the off sample for on data or from a different region of our FoV for wobble data; and the pulsar mode, where the off events are taken from the specified off-region of the phaseogram (see definition of regions in §4.6).

When this process was finished we obtained one DES for the nebula and one for the pulsar for every subsample of our dataset. But this spectra are computed as a function of the estimated energy of the events, which means that the effects the intrinsic sensitivity of our detector were still not taken into account. This includes the non-zero energy bias and limited energy resolution of the MAGIC telescopes, as well as a energy-dependent detection efficiency.

One must correct for this artificial modifications of the spectrum, which are intrinsic to any detector, with the so-called **unfolding procedure**. This final step of the analysis also allows us to combine the different spectra obtained

Month	Year	Uncertainty	Month	Year	Uncertainty
Feb	2007	0.8	Sep	2010	0.7
Mar	2007	1.0	Oct	2010	0.5
Oct	2007	0.7	Nov	2010	0.9
Nov	2007	0.5	Dec	2010	0.6
Dec	2007	0.5	Jan	2011	1.1
Jan	2008	0.5	Feb	2011	1.1
Feb	2008	0.4	Mar	2011	1.0
Oct	2008	0.3	Feb	2012	0.4
Nov	2008	0.6	Mar	2012	0.4
Dec	2008	0.5	Nov	2012	0.6
Jan	2009	0.7	Dec	2012	1.2
Feb	2009	0.5	Jan	2013	0.7
Mar	2009	0.7	Feb	2013	0.5
Sep	2009	0.7	Mar	2013	0.6
Oct	2009	0.6	Nov	2013	0.5
Nov	2009	1.2	Dec	2013	0.6
Jan	2010	1.0	Jan	2014	0.7
Feb	2010	0.8	Feb	2014	0.7
Mar	2010	1.3	Mar	2014	0.3
Apr	2010	2.4			

Table 4.8: 1σ uncertainties of the used Crab ephemeris in units of milliphases, as reported by the Jodrell Bank for each of the months when MAGIC observations were included in combined analysis (mono and stereo). The global uncertainty of the ephemeris is computed as $\sigma_{\rm eph} = \frac{\text{Mean(Uncertainty)}}{\sqrt{N}} = 0.12$ milliphase.

for each data subsample into a single total spectrum. The unfolding can be seen intuitively as the inversion of the energy migration matrix: it is needed to transform functions like the DES, a function of the estimated energy, into a function of the true energy of the γ-rays. This inversion can be a tricky procedure and, if we want to avoid obtaining divergent terms, it usually requires a parametrization of your data, which is known as **regularization**. There are several ways to perform this regularization but a detailed description of them falls out of the scope of these thesis. We will only list the ones that are implemented within the MARS software, which are those we have used to unfold the spectrum of the Crab nebula and pulsar. Namely, these are the forward unfolding, the Bertero method, the Tikonov method and the Schmelling unfolding. None of them is particularly better that the other, so one must check that the obtained spectra are compatible with each other. The results of the unfolding process will be shown in the next chapter.

4.8 Mono analysis results

The analysis of the Crab pulsar data taken in stand-alone mode with the MAGIC telescopes produced a series of scientific outputs that we describe here. After the analysis of the mono observation we were left with a dataset composed of 12.0M surviving events. Most of them (10.3M) belong to the 10.6 mm PSF subsample, 30% on which were taken in on mode and 70% were taken in wobble mode. The remaining ones came from the 9.2 mm PSF subsample (1.4M events, 71% and 29% from on and wobble modes, respectively) and 0.2M events belonged to the 13.0 mm PSF, wobble subsample.

With them we built the pulsar phaseogram for each data subsample in three different energy intervals: **full range** (hereafter FR), extending from 30 GeV to 1.7 TeV in reconstructed energy, and **low** and **high energy ranges**, which divide the former asymmetrically into two parts: below 400 GeV (LE) and above 400 GeV (HE). These phaseograms can be seen in §D, whereas the number of excess events in the P2 signal region for each case, together with the signal significance computed with the Li&Ma formula (equation 2.5.2), are listed in table 4.9. The significance that was obtained using the other test statistics we described in §2.5.7 is shown in the box at the top-right corner of each phaseogram plot (figures D.1, D.2, D.3, D.4 and D.5). They are all consistent with the Li&Ma value, considering the low statistics of the result.

PSF [mm]	Observ. mode	Energy range	Excess Events	Li&Ma signif.
10.6	wobble	FR	524 ± 395	1.3σ
		LE	468 ± 33	1.2σ
		HE	56 ± 42	1.3σ
	on	FR	2379 ± 608	3.9σ
		LE	2322 ± 606	3.8σ
		HE	57 ± 46	1.2σ
13.0	wobble	FR	125 ± 102	1.3σ
		LE	112 ± 100	1.1σ
		HE	13 ± 16	0.8σ
9.2	wobble	FR	361 ± 151	2.4σ
		LE	345 ± 149	2.3σ
		HE	17 ± 19	0.9σ
	on	FR	444 ± 231	1.9σ
		LE	427 ± 230	1.9σ
		HE	17 ± 17	1.0σ
TOTAL		FR	3833 ± 782	4.9σ
		LE	3673 ± 779	4.7σ
		HE	160 ± 70	2.3σ

Table 4.9: Summary of number of excess in the P2 phase region, as well as the obtained signal significance according to Li&Ma (equation 2.5.2) for the mono data analysis. Three energy ranges are analyzed: the full-range (FR) expands between 31 GeV and 1.7 TeV, and the other two divide the FR in two regions, low (LE) and high energy (HE), below and above 400 GeV, respectfully.

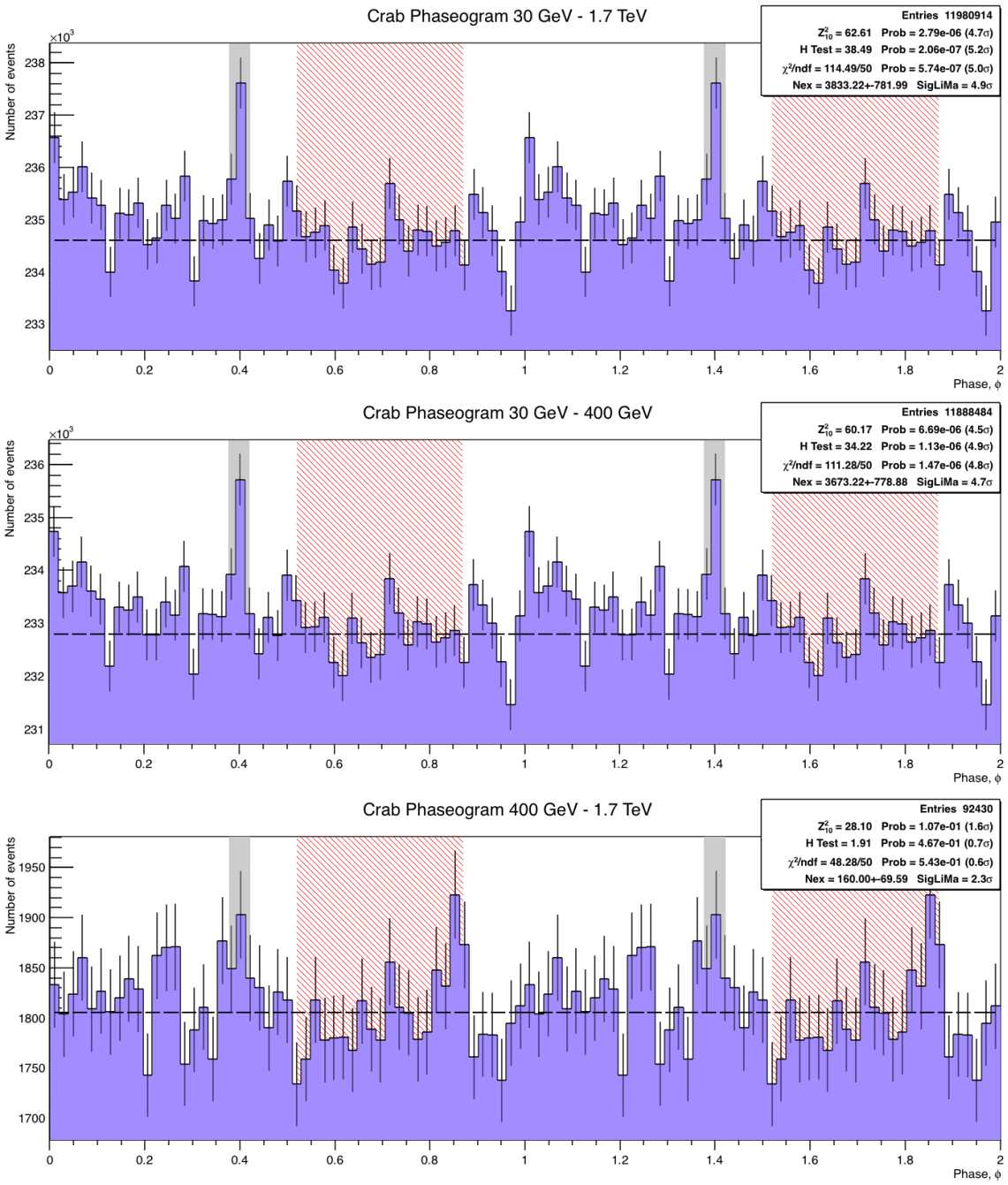

Figure 4.11: Crab phaseogram, i.e. the number of events as a function of the pulsar phase, obtained from the mono data analysis for the full (*top*), low (*mid*) and high (*bottom*) energy ranges. Two full rotations are displayed ($0 < \phi 2$) for an easier interpretation. The on and off regions are marked with the solid-grey and diagonal-red-lined areas respectively, as well as the background level estimated from the off region (dashed, horizontal, black line).

The maximum significance is obtained from the largest data subsample (PSF 106.mm on) for the FR, which is close to the 4σ level. Most of the excess events come from the LE interval and only 2.4% of them are measured above 400 GeV. Moreover, a similar amount of excess at HE is obtained from the 10.6 mm PSF subsample taken in wobble mode, which is remarkable given that it contains less than half of the events in the on sample. For the rest of the samples the statistics are poorer and the signal significance is also worse, especially for the HE range, but none of them shows a negative excess.

Energy	**Excess Events**		**Li&Ma Signif.**	
range	**P1**	**P1+P2**	**P1**	**P1+P2**
FR	1806 ± 758	5938 ± 1150	2.4σ	5.2σ
LE	1756 ± 755	5749 ± 1146	2.3σ	5.0σ
HE	50 ± 70	189 ± 102	0.7σ	1.9σ

Table 4.10: Summary of the total number of excess events in P1 region and for the joining of P1 and P2 signal regions, together with their correspoinding Li&Ma signal significance (equation 2.5.2). These values were obtained from the mono analysis presented in this thesis and three energy ranges are used, namely FR (31-1700 GeV), LE (31-368 GeV) and HE (368-1700 GeV).

The next step was to stack together all the LCs for individual subsamples to produce the overall pulsar phaseogram for the entire mono dataset. The same three energy ranges were used. These LCs are shown on figure 4.11, whereas the number of excess events can be also found in table 4.9. In the FR energy interval (top plot in figure 4.11), 3833 ± 782 excess events were found in the P2 region (marked by a grey shadow) with respect to the off region (marked with a red-shaded area). This represents a clear pulsed signal with a statistical significance of almost 5σ. The output of the rest of periodicity tests described in §2.5.7 were applied and are also consistent with this result, as one can see in the top-right corner of the plots in figure 4.11.

Notice that there is also an excess in the P1 region of this phaseogram (around $\phi_{P1} = 0$ and $\phi = 1$), although not as intense as that in P2: at LE we find an excess of 1756 ± 755 (2.3σ) but the signal vanishes for the HE range, where no significant excess is found (50 ± 70, 0.7σ). With such limited statistics, it is hard to compute a proper spectrum for the P1 region only using mono data. If we define the on region as the combination of both P1+P2 signal regions,

the significance of the detection improves, as one can see in table 4.10. But this is not the case for the HE band, where the addition of the P1 signal region weakens our detection of the Crab pulsar above 400 GeV. The situation can change latter in this chapter when the stereo sample is included in the analysis but it also confirms that the intermediate pulse becomes dominant over the main pulse at γ-ray energies.

When one plots the phaseogram for the LE range, the result is almost the same as for the FR. The reason for that is clear: since our source has a steep power-law spectra, most of the events are in the LE band. In fact, of a total of almost 12M events, 99.2% of them have energies below 400GeV and, the rest, only 92k event lie above this threshold. The number of excess events in P2 for the LE is 3673 ± 779, a significant pulsed signal as any of the used test statistics tell us. For comparison with previous results by MAGIC and other IACTs, we report a 4.7σ significance as computed with the Li&Ma formula. We can therefore confirm of the emission of the Crab pulsar at P2 below 400 GeV from the analysis of the mono data sample alone.

The Crab phaseogram for the HE range does not show a periodic signal as strong as in the previous cases. As expected, the number of excess events in the P2 regions much smaller, 160 ± 70, which corresponds to 2.3σ significance according to Li&Ma. The other test statistics gives diverse values but lower than Li&Ma. The interpretation of this plot is not as straight-forward as the previous ones.

Even though a significance a little above 2σ is not enough to claim a discovery, we have to consider the fact that emission up to 400 GeV has already beed detected by MAGIC and VERITAS [70, 71]. Out intention here is to detect this emission to energies above 400 GeV so we can extend the spectrum of the Crab pulsar. The low statistics of the signal obtained from the mono data analysis would not be enough to claim a discovery but it is enough for a spectral extension of an already known source. This means that it is not compulsory to have a signal in each energy bin with more than 5σ significance because this is the threshold to claim a discovery of a new source. Our analysis of the mono data allows us to compute this additional point of the Crab spectrum, as we show later in this chapter. In addition, we must to take into account that was obtained with only a fraction of the overall Crab pulsar analysis, which included only mono data. The inclusion of the stereo observations, with much improved

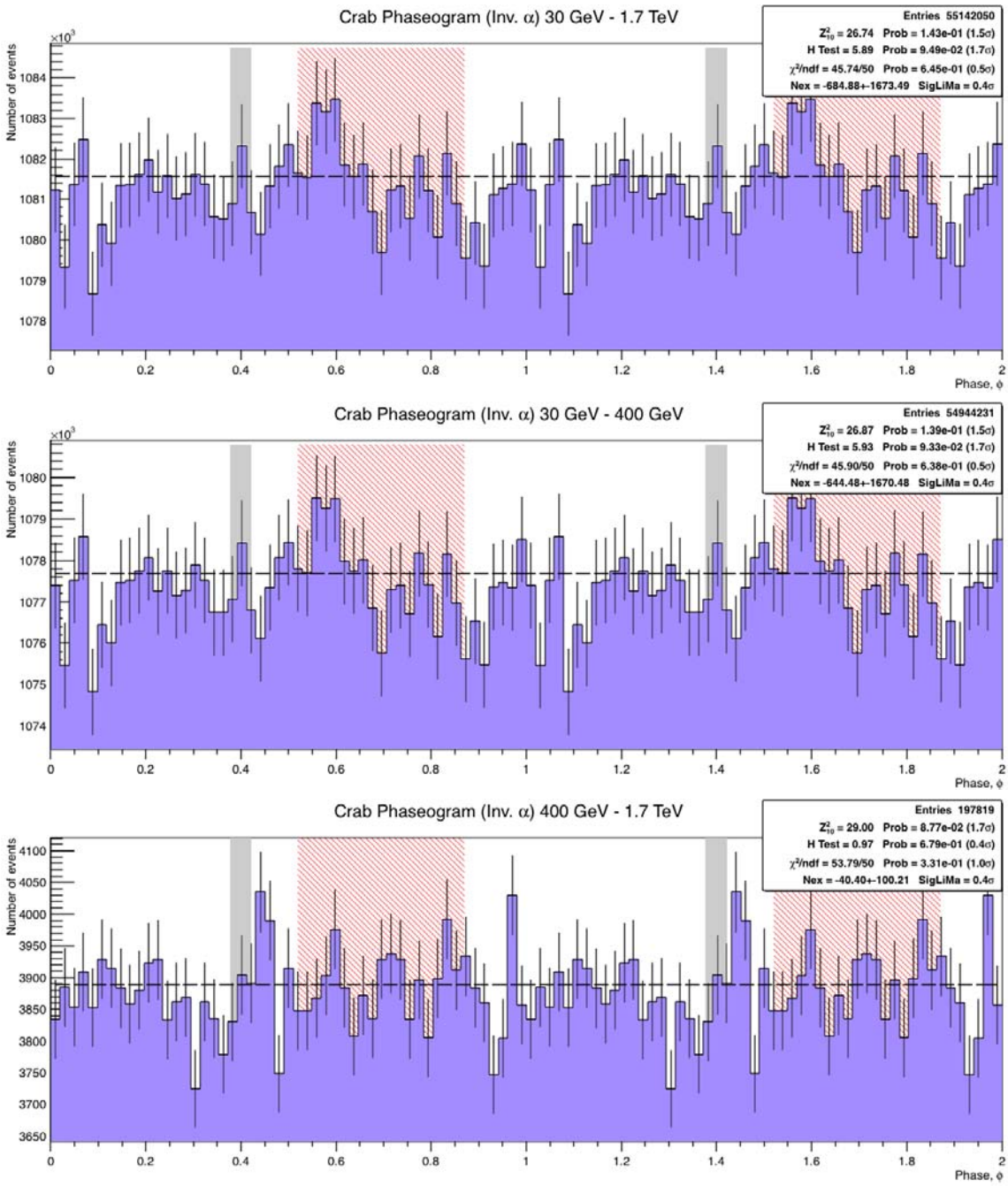

Figure 4.12: Crab phaseogram after the inversion of the α-cut obtained from the mono data analysis for the full (*top*), low (*mid*) and high (*bottom*) energy ranges. Two full rotations are displayed and the on and off regions are highlighted with solid-grey and diagonal-red-lined areas respectively. The background level for each energy range is marked with a dashed, horizontal, black line. These distributions are completely flat within statistical fluctuations.

sensitivity, to the phaseogram will raise the number of excess events, in the same way the stacking of different mono-subsamples improved the significance of the pulsation detection for P2 in every energy range.

One might wonder about the peak at around phase $\phi \approx 0.85$ in the HE phaseogram (figure 4.11, *bottom*), so a short comment is in order. This increase in the number of events in one phase bin, located in the off region, is actually higher than the signal measured in the on region. One could think that, considering the height of this bin to the background level with respect to the size of its error bar, this peak has a significance of about 3σ. However, we are making an *ad-hoc* redefinition of the Crab pulsar signal region when we arbitrarily select one bin as on region *after* examining its content. Hence, to know the significance of such measurement we must first apply a trial factor to account for the possibility that such excess could have been found in *any* of the other 50 phase bins. Once this correction is taken into account, the significance of this peak drops down to 1.5σ. This peak (off-region in the bottom plot on figure 4.11) can therefore be safely considered an statistical fluctuation and further interpretations should be avoided.

In order to check the robustness of these results, two independent tests were performed, which are very common in the particle physics field but rather unusual within the astronomy community. The first one was to plot the phaseogram after applying the same analysis steps but with an inverted alpha cut, which excludes all events from the Crab sky region. In this situation, the periodic signal disappears, as shown in figure 4.12, which proves that the pulsation we found is intrinsic to the observed source region and was not faked by any source of noise, intrinsic to our instrumentation. If it was, events coming from the rest of the FoV should also exhibit such behavior, which is not the case. This test is also a sanity check in order to make sure that there is no obvious problem regarding the computation of the phase of each event.

The second test allows us to check that the pulsed signal is not a simple statistical fluctuation but a real signal from the observed source. It consists in plotting the number of excess events as a function of the number of processed events or, equivalently, as a function of the observation days. If there is a signal in our data (even for a weak one like in our case), the excess should slowly pile up as we add more and more observation time. And this is exactly what we can

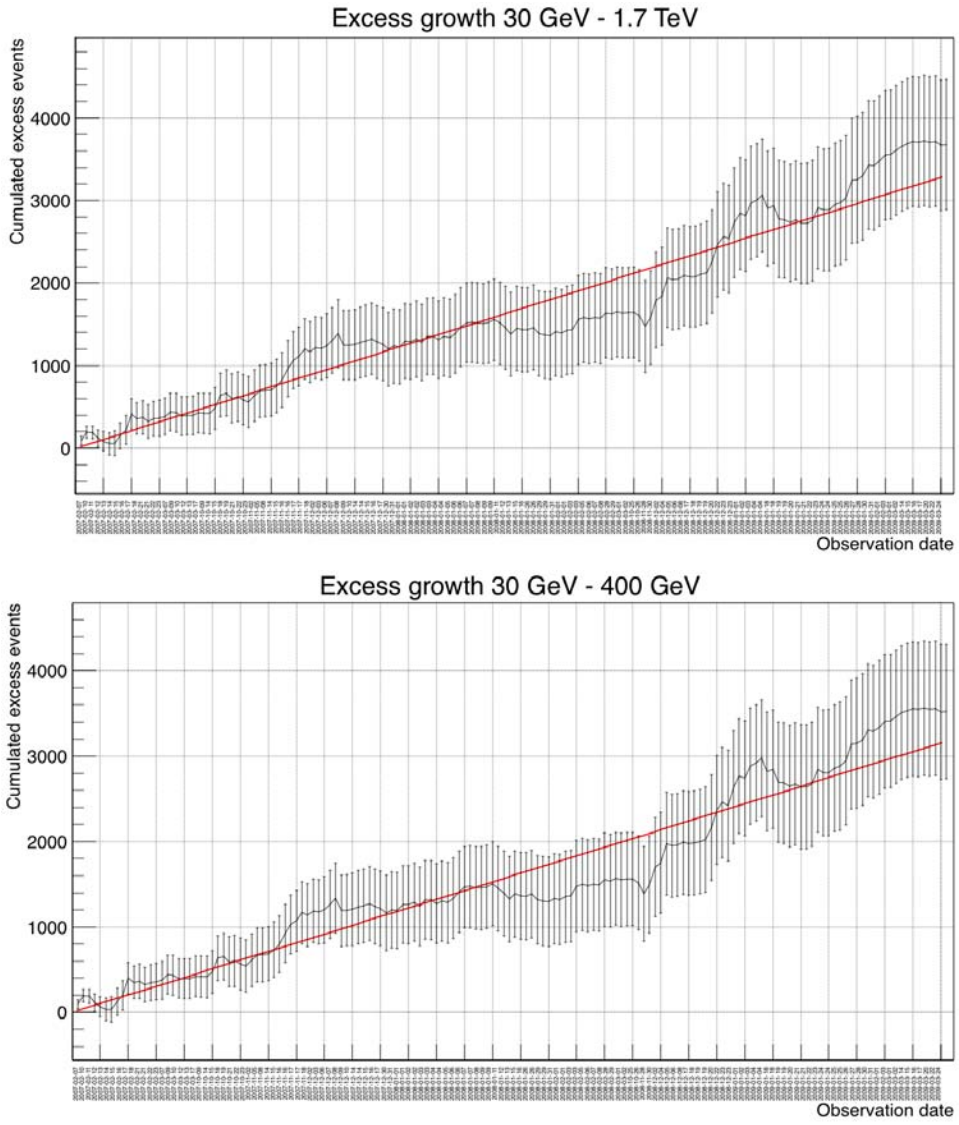

Figure 4.13: Cumulated number of excess events from the Crab pulsar obtained from the mono data analysis as a function of the observation date and for the full (*top*) and low (*bottom*) energy ranges. The case for HE events is shown in figure 4.14. Such a growing behavior is a solid test about the presence of a signal and helps us discard the possibility that the observed signal is a simple statistical upwards fluctuation. A linear fit (*red line*) is also plotted to stress this tendency.

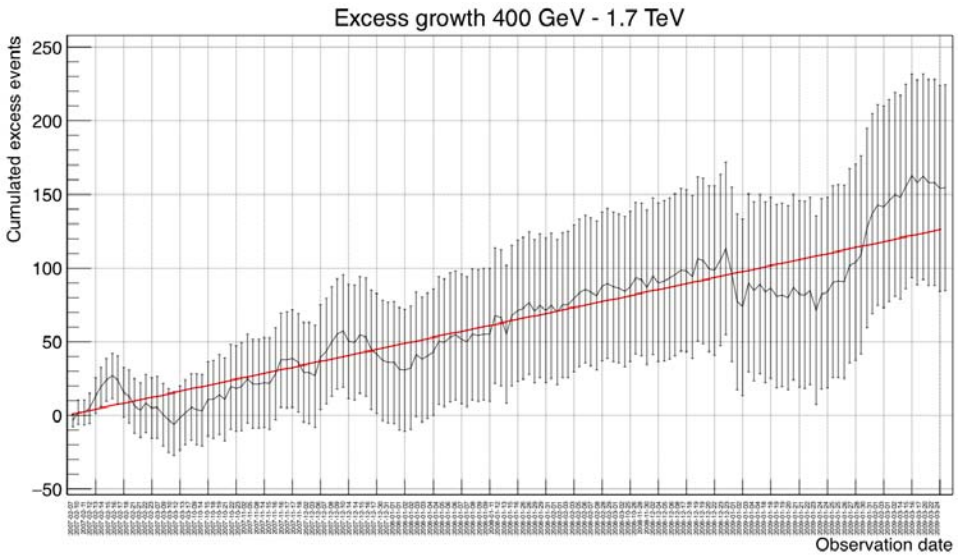

Figure 4.14: Cumulated number of excess events from the Crab pulsar interpulse (P2), obtained from the mono data analysis as a function of the observation date for the high energy range. Such a growing behavior is a solid test about the presence of a signal and allows us to discard the possibility that the observed signal is a simple statistical upwards fluctuation. A linear fit (*red line*) is also plotted to stress this tendency.

see in figures 4.13 and 4.14 for the FR and LE energy intervals, and for the HE energy range, respectively: the number of excess events in the interpulse grows steadily as we add more data to the analysis. There are short periods when this growth is slower and even some short periods when it becomes negative. These might be due to non-optimal observation nights that even though survived our quality selection or, more likely, simple statistical fluctuations. A clear growing tendency can be stablished and it is highlighted in these plots by a linear fit (*red line*), which we forced to cross the origin of coordinates.

In the case of the HE range fluctuations are stronger because excess events are scarcer. They reach down to negative signals for the first month of observations, but there is a clear growing tendency that we also stress with the linear fit (*red line*). One should note that the cumulative number of excess events never departs significantly from this straight line.

In order to compute the spectrum of our source, the processing of wobble and on-source data had to be done separately. These data cover a wide range of zenith angles, so some sub-sampling of the data between low, medium and high zenith angle had also to be applied. Later on, these individual outputs were combined into a single spectrum and, at the same time, several unfolding methods were applied to correct for the instrumental energy resolution and bias. The resulting spectra and SEDs for both the Crab nebula and the P2 region of the Crab pulsar are shown in figure 4.15 and 4.16, respectively. The former

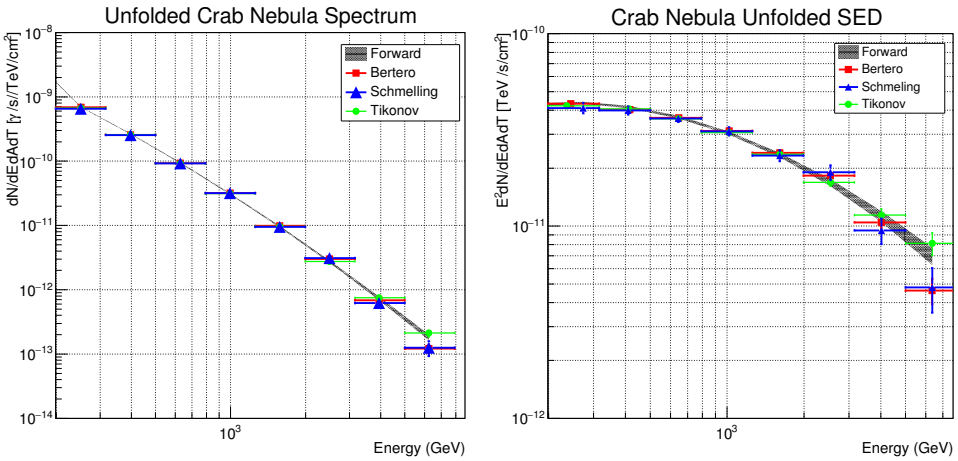

Figure 4.15: Differential energy spectrum (*left*) and SED (*right*) of the Crab nebula, obtained from the analyzed mono data using different unfolding methods. These results are stable and well described by a curved power-law. The fitting values, shown in table 4.11 are all compatible among them, with the exception of some outlier points at energies close to the threshold and can be interpreted as a boundary artifact.

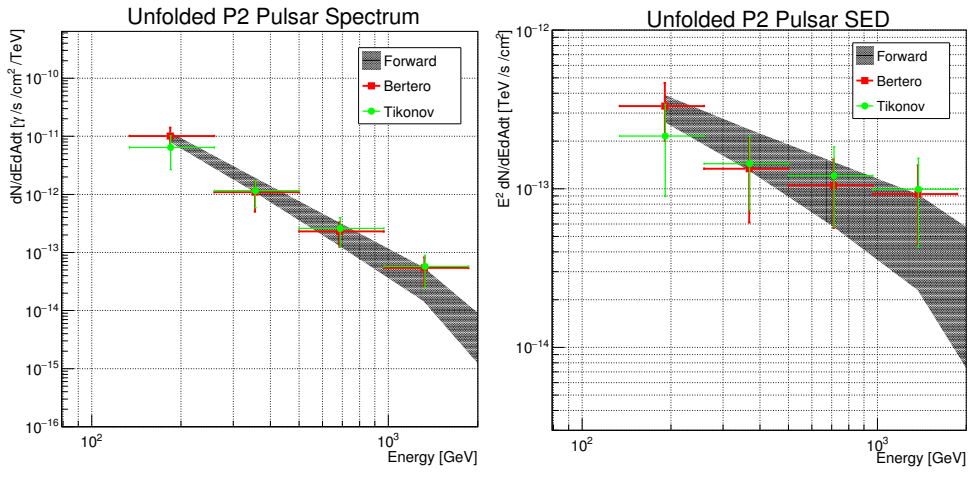

Figure 4.16: Differential energy spectrum (*left*) and spectral energy distribution (*right*) for the interpulse region (P2) of the Crab pulsar phaseogram, as obtained after the analysis of the mono dataset and applying different unfolding methods. These results are well fitted by a single power-law extending up to energies of 1.7 TeV (see fitting parameters in table 4.11).

	Parameter value	Unfolding method Forward	Bertero	Tikonov	Schmelling
Nebula	F_0	3.38 ± 0.06	3.31 ± 0.05	3.05 ± 0.15	3.28 ± 0.12
	a	-2.39 ± 0.02	-2.45 ± 0.02	-2.38 ± 0.02	-2.40 ± 0.02
	b	-0.43 ± 0.04	-0.31 ± 0.04	-0.46 ± 0.05	-0.40 ± 0.04
	χ^2/NDF	$68.34/12$	$2.53/5$	$3.8/6$	$1.49/6$
Pulsar	f_0	2.43 ± 0.73	2.36 ± 0.71	1.9 ± 0.80	-
	a	-2.88 ± 0.33	-2.78 ± 0.46	-2.53 ± 0.47	-
	χ^2/NDF	$3.89/6$	$1.64/3$	$1.06/3$	-

Table 4.11: Fitting parameters of the unfolded Crab nebula and pulsar spectrums, as obtained from the mono data analysis presented in this thesis for each unfolding method. The functions that were used for these fits are defined in equation 4.8.1. Parameter units are $[F_0] = 10^{-11}\gamma/\text{GeV}/\text{m}^2/\text{s}$, $[f_0] = 10^{-13}\gamma/\text{GeV}/\text{m}^2/\text{s}$, $[b] = \text{GeV}^{-1}$ and $[a] = 1$ (adimensional).

was used to check whether the well-established nebula spectrum was retrieved. These two SEDs were fitted to a single and curved power-laws, respectively:

$$\begin{aligned} F(E) &= F_0 \cdot \left(\frac{E}{1\ \text{TeV}}\right)^{-a+b\log(E)} \\ F(E) &= f_0 \cdot \left(\frac{E}{300\ \text{GeV}}\right)^{-a} \end{aligned} \tag{4.8.1}$$

and the values of these parameters can be seen in table 4.11 for each of the unfolding methods that were tested. As we explained in §4.7, in general, none of these regularizations is significantly better than the others, so we can only check that the obtained parameters were approximately compatible among them, in order to have a stable unfolded spectrum.

The pulsar spectrum for the interpeak could be obtained up to energies of 1.7 TeV and fitted to a $\sim -2.8 \pm 0.5_{\text{stat}}$ power-law. The Schmelling regularization, which was used for the unfolding of the nebula spectrum, did not converge in the case of the pulsar. However, too few excess events were found in the main pulse to be able to compute a proper spectrum using only the mono data sample.

4.9 Combined analysis results

In the previous section we reported the results of our analysis of the mono Crab pulsar data and we tested the consistency of the analysis by checking the emission properties of the surrounding nebula. This work was part of a major effort of the MAGIC collaboration whose goal was to analyze all the MAGIC Crab data available in the archives, including the observations that were made in stereoscopic mode, which represent the major fraction of these data. The author of this thesis was not directly involved in the analysis of that dataset, so we will not give an extensive explanation about it, which will be reported elsewhere. However, we briefly describe here the basic characteristics of the stereo dataset, as well as the most important telescope performance parameters, which will be needed later on. Finally, we also report here about the results obtained from the combination of the mono and stereo samples.

Energy	**Excess Events**		**Li&Ma Signif.**	
[GeV]	**P1**	**P2**	**P1**	**P2**
100-400	1252 ± 442	2537 ± 454	2.8σ	5.6σ
> 400	188 ± 88	544 ± 92	2.2σ	6.0σ

Table 4.12: Summary of the total number of excess events in P1+P2 region and only in P2 region, as obtained from the combined analysis (mono and stereo together). The signal significance according to Li&Ma (equation2.5.2) is also shown for two energy ranges, LE (below 400 GeV) and HE (above 400 GeV).

Extensive MAGIC observations of the Crab nebula in stereoscopic mode since the second telescope started operating. A total amount of 220 h of good quality data were analyzed, taken between mid 2009 to April 2014 and corresponding to observation campaigns or cycles from V to IX. During these extended time period, the MAGIC telescopes underwent a major hardware upgrade, as explained in §2.4. This upgrade was quite extensive, since it started in 2012 and finished in mid 2014. Therefore, data had to be divided in 5 different subsamples for each intermediate hardware configuration, where the telescopes performance was significantly altered. We will refer to these subsamples as C56, C56-on (the only fraction of stereo data taken in on-source mode), C7, C8 and C9.

Each sample was analyzed independently, so specific off-sources were selected to train of specific RFs for each of them and also specific MCs had to be

applied so the correct performance of the telescope during each cycle could be properly reproduced. The performance of the telescopes regarding the energy estimation of the events is characterized by its migration matrix, obtained after applying the analysis cuts to a set of MC events, where the true energy of the events is obviously known. An example of such migration matrix for the C7 subsample is shown in figure 4.18.

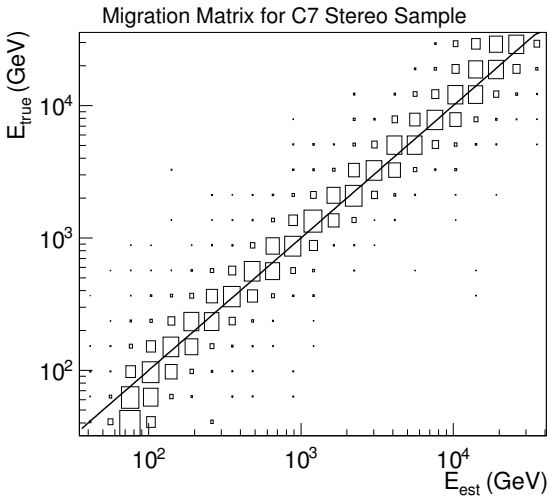

Figure 4.17: Example of the energy migration matrix for the C7 stereo subsample. The size of the box shows the probability if a value of estimated energy $E_{\rm est}$ to be assign to a event with a given true energy, $E_{\rm true}$. The black solid line indicates the perfect energy estimation region where $E_{\rm est} = E_{\rm true}$.

Several independent analysis were carried out by different member of the stereo analysis team within the MAGIC collaboration. They were found to be compatible among them so one of them was selected to produce the plots presented here, and the rest of them were considered as the necessary cross-checks that any result obtained with the use of MAGIC observations needs to have. The same occurred with the analysis of stand-alone observations: three different analysis were performed independently and the obtained results in each of them was compatible with the others, within statistical uncertainties. The selected version of the mono analysis that was finally combined with the stereo sample was not the one presented in this thesis, which was then considered as a cross-check of the former. That analysis followed a different approach compared to that detailed in §4. a different quality selection was used, no hadronness cut was applied for the low energies whereas that the α-cut was based on an efficiency criteria, as opposed to the optimized cuts we applied in our analysis. For the high energy interval, a cut optimization was designed and applied to the data, in a similar way as our optimization described in §4.5. Anyway, as we said, the obtained results for the mono analysis

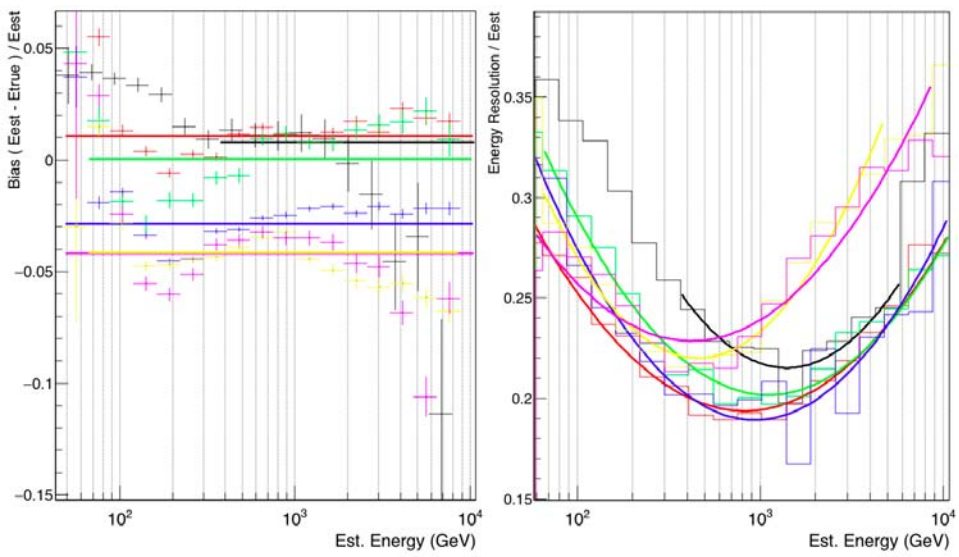

Figure 4.18: MAGIC relative energy bias (*left*) and resolution (*right*) as a function of the estimated energy for each of the performance periods. A constant and a parabolic function in units of $\log(E')$ are fitted in each case, respectively, and the results are shown as thick, colored lines. Each color correspond to a certain subsample of the data: mono (*black*), C56 (*red*), C56-On (*green*), C7 (*blue*), C8 (*yellow*), C9 (*pink*).

were compatible with those reported in this thesis.

We must also explain how the energetic performance of the telescopes was estimated and parameterized, because it will be needed to extract limits to the violation of the Lorentz invariance later on (see chapter 6). The procedure that we describe here is not directly related with the data analysis that was carried out to measure the Crab pulsar emission above 400 GeV. However, it will also be useful to see how different each of the subsamples can be. The description that we provide in the next paragraph applies only to the telescope performance under the analysis cuts optimized for the pulsar detection. One should remember that these are not the same cuts used by `fluxlc` or `flute` softwares to compute the source spectrum, lightcurve as well as other related quantities (see §2.5.8).

From each one of these matrixes, we extracted the distributions correspond-

Fitting parameter	**Pulsar region SED** P1	P2
F_0	$1.0 \pm 0.5_{\rm stat} \pm 0.2_{\rm sys}$	$2.2 \pm 0.4_{\rm stat} \pm 0.4_{\rm sys}$
a	$-3.5 \pm 0.4_{\rm stat} \pm 0.3_{\rm sys}$	$-3.1 \pm 0.2_{\rm stat} \pm 0.3_{\rm sys}$

Table 4.13: Values of the parameters for the joint fitting of the Crab pulsar SED shown in figure 4.21. A single power-law was used as fitting function $F(E) = F_0 \cdot \left(\frac{E}{300\ \text{GeV}}\right)^{-a}$, where parameter units are $[F_0] = 10^{-13}\gamma/\text{GeV}/\text{m}^2/\text{s}$ and the spectral index is adimensional $[a] = 1$.

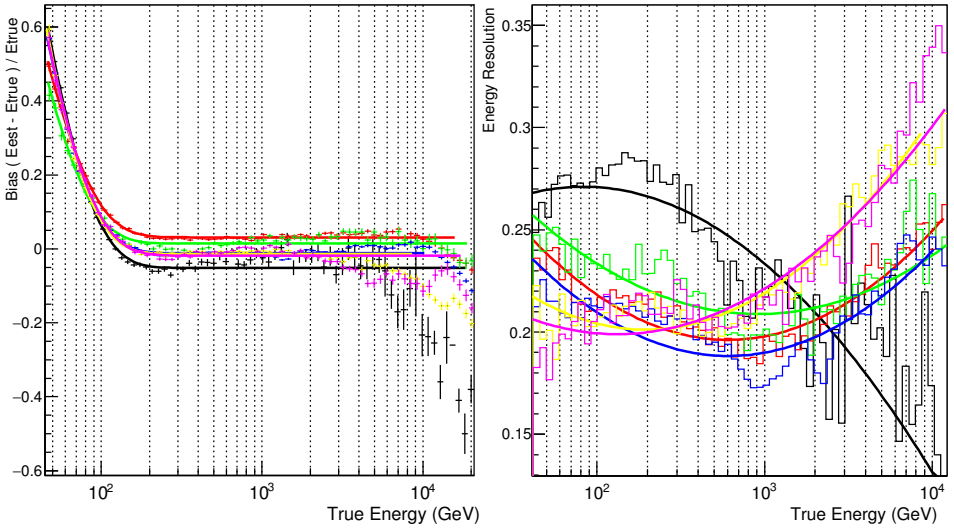

Figure 4.19: MAGIC relative energy bias (*left*) and resolution (*right*) as a function of the true energy for each of the performance periods. An exponential decay plus constant fit and a parabolic fit as a function of $\log(E')$ were applied in each case, respectively, and shown as thick colored lines. Each color correspond to a certain subsample of the data, namely: mono (*black*), C56 (*red*), C56 On (*green*), C7 (*blue*), C8 (*yellow*), C9 (*pink*).

ing to each slice along the horizontal axis (for a given logarithmic bin in estimated energy) and also along the vertical axis (for each true energy bin). All these distributions were approximately gaussian and we fitted with such functions to obtain the positions μ_k and widths σ_k, where k stands for each of the performance periods listed above. The mono data was also analyzed in a similar way.

Once a value for each one of these variables was obtained for every bin in true energy (E_i) and in estimated energy (E_i'), the relative energetic bias and resolution of the MAGIC telescopes could be computed for each period. Those distribution are shown in figures 4.19 and 4.18. Each of them was fitted to a function that described them approximately, so a smooth estimation of the performance parameters could be used later on.

The background-subtracted pulsar LC or phaseogram that is obtained using the complete MAGIC dataset, with mono and stereo combined, can be seen in figure 4.20, both for LE (*top*) and HE ranges (*bottom*). Note that the size of the binning used in the signal regions P1 and P2 was reduced to emphasize the sharpness of the peaks. The found signal for the interpulse is very clear in both energy intervals and the number of excess events and its Li&Ma significance are shown in table 4.12, together with the values associated with the main peak. The weak pulsed signal that we saw above 400 GeV with the use of mono data now becomes a much more intense signal, at the level of 6.0σ. This is not the

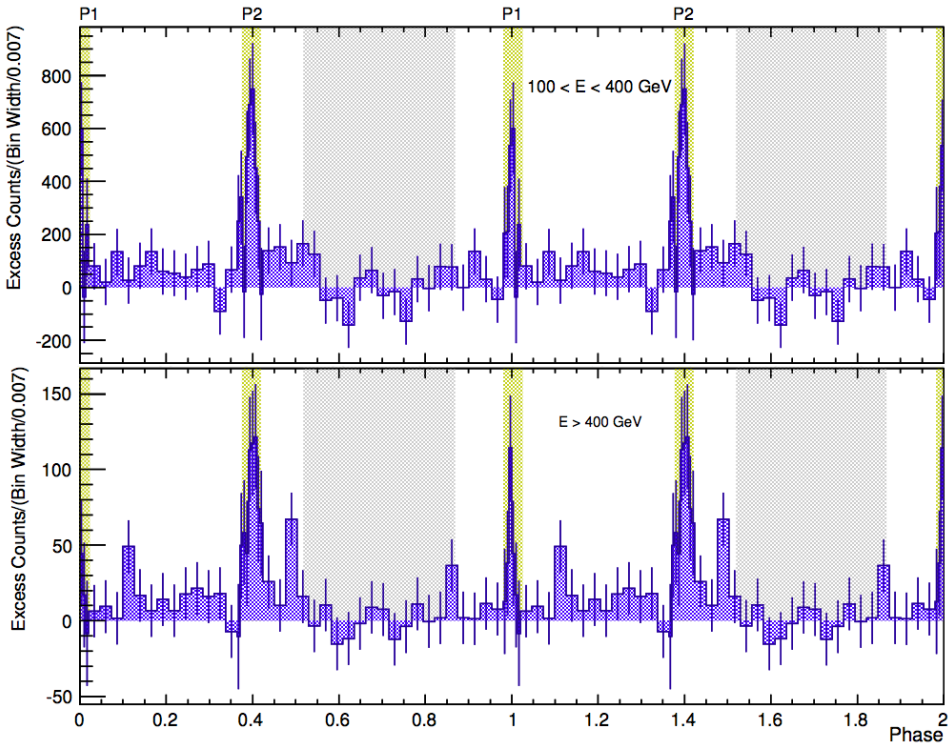

Figure 4.20: Crab pulsar phaseograms for low (100-400 GeV, *top*) and high (> 400 GeV, *bottom*) energies, obtained with the complete data set, i.e. mono and stereo data combined. The on and off phase regions are highlighted with yellow- and grey-shaded areas, respectively, and, for the sake of clarity, two pulses are shown ($0 < \phi < 2$). The number of events in each phase bin is background-subtracted and a finer binning is used within the P1 and P2 pulse regions to stress the sharpness of the peaks.

case for the main pulsar peak, P1: only 2.2σ were obtained.

The spectral energy density of the Crab pulsar was also compute using the complete dataset. The unfolded, phase-resolved SED is shown in figure 4.21. Power-laws could be fitted to P1 and P2 spectra independently. The main pulse could only be detected up to 500 GeV and upper limits of the order of 10^{13} TeV^{-1}cm^{-2} s^{-1} could be established to limit the emission at P1 beyond that energy. However, the spectrum for the interpulse (P2) could be extended well-beyond the previous limit of 400 GeV: two additional spectral points could be derived and the pulsar emission in that phase region could be measured up to 1.7 TeV. The implications of these results regarding physical emission mechanisms and current pulsar models will be discussed in §4.10.

4.10 Discussion

The last section in this chapter is devoted to discuss the implications of the discovery of TeV emission from the Crab pulsar that we exposed here. The general result can be summarized in the following way: the pulsed emission could be detected both for energies below and above 400 GeV. An significant

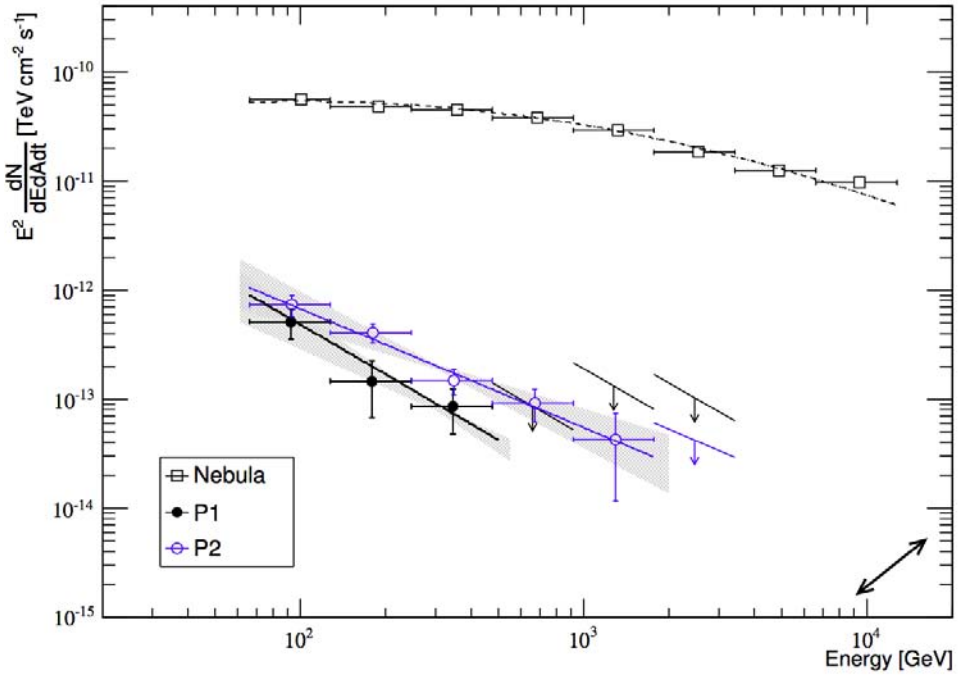

Figure 4.21: Unfolded and phase-resolved Crab pulsar SED for the main peak P1 (black) and for the interpulse P2 (blue) obtained from the combined data analysis. The results presented in this thesis are shown as filled circles, whereas Fermi measurements are represented by the empty circles. The fit to simple power-law for the MAGIC measurements are displayed with solid lines and the power-law with a cut-off used to fit Fermi data is plotted as dashed lines. Some upper limits are extracted from MAGIC measurements for the highest energy bins.

extension of the Crab pulsar spectrum at the interpulse (P2) could be achieved: emission was detected up to energies of 1.7 TeV and the spectrum could be fit with a power-law with a -3.1 spectral index, which is compatible with Fermi-LAT observations at lower energies. For the main pulse or P1, a 2.3σ hint was obtained in the LE range and no signal could be detected above 400 GeV from the mono data analysis alone.

These results are important because of two different reasons. First, from a technical point of view, mono data has been considered for a long time as not-worth analyzing by most members of the MAGIC collaborations due to its technical complexity. However, we have bee able to confirm the discovery made by MAGIC [37] with the use of these data. Our factor ~ 2 higher energy threshold was expected since a special trigger called sum-trigger (§2.4.4), together with a dedicated analysis, was used to lower the energy threshold as much as possible for that discovery, and our goal was precisely the opposite, i.e. the improvement our sensitivity for the highest energies. The LE discovery was done analyzing a different dataset than the one we analyze here but, more importantly, the observations whose analysis is reported here were performed mainly *before* the sum-trigger started operation (although a small fraction of it

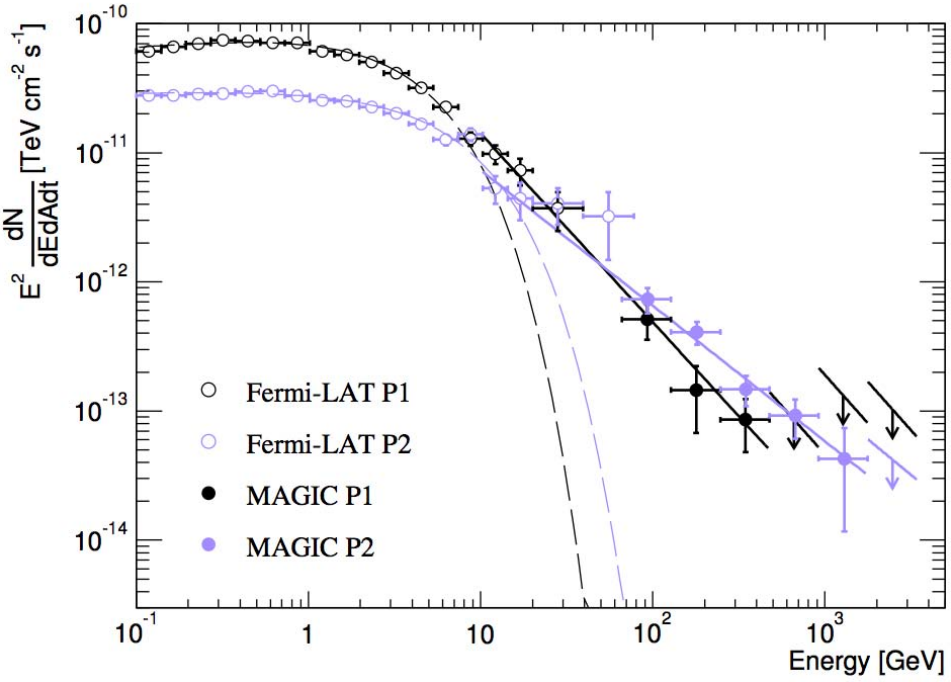

Figure 4.22: Unfolded and phase-resolved Crab pulsar SED for the main peak P1 (black) and for the interpulse P2 (blue) obtained from the combined data analysis. The results presented in this thesis are shown as filled circles, whereas Fermi measurements are represented by the empty circles. The fit to simple power-law for the MAGIC measurements are displayed with solid lines and the power-law with a cut-off used to fit Fermi data is plotted as dashed lines. Some upper limits are extracted from MAGIC measurements for the highest energy bins.

was taken simultaneously). These MAGIC data was already available in 2009 and could have been used to claim the discovery of the Crab pulsar up to 400 GeV about *4 years* before the discovery claim of HE pulsation.

The second reason we think the obtained results are relevant is that the analyzed data were collected in order to study the Crab nebula surrounding the pulsar, the standard candle for VHE γ-rays detectors, and not the pulsar that lies within it. Our result proves that data produced with to achieve a certain goal, which has already been analyzed and is now considered fully-exploited, can actually be useful to make discoveries that were not foreseen when the observations where carried out. Sometimes even new sources can be discovered if we observed a crowded FoV. A high potential for discovery of new sources remains hidden in the thousands of observation hours current γ-ray telescopes have stored in their archives.

The statistics of the analysis results where further improved when mono and stereo samples were combined. The overall data analysis comprised about 320 h of good quality data in more than a dozen different hardware configurations and the MAGIC collaboration has been able to join them together to produce a single

scientific output. This is a major success and the results are detailed in §4.9. In short, using seven years of MAGIC observations the phased-resolved Crab spectrum could be measured more precisely and the following parametrization was used for the power-law spectral fit:

$$F(E) = F_0 \cdot \left(\frac{E}{300 \text{ GeV}} \right)^{-a} \tag{4.10.1}$$

A spectral index of $a = -3.1 \pm 0.2$ was obtained for P2 and a steeper spectrum with $a = -3.5 \pm 0.4$ was found for P1. Due to this difference, the P1 pulse could be detected up to 600 GeV but not for higher energies, which is a factor ~ 3 lower that the maximum energy where P2 could be measured but is still a factor 3 higher than previous measurements. Even when we are reporting the results of the biggest data analysis in any IACT experiment up to date, the emission of the pulsar reaches the limit of our sensitivity for such a weak and extremely background-dominated source.

If also include the LE pulsar emission detected by the LAT instrument onboard of the Fermi satellite (see figure 4.22), the spectral index of those power-laws can be determined with a higher precision, as shown in table 4.14. They differ by about 0.4 ± 0.1 units, so we can confirm that the P1 spectra is significantly softer that for P2.

It is important to notice that the obtained extension of the Crab pulsar spectrum for energies above 400 GeV was not predicted by the current models for this source (see §3.3). Moreover, the fact that a single power-law can properly fit the spectrum from ~ 10 GeV up to TeV energies implies that a single mechanism is responsible for the emission of these photons. A mechanism can be confidently discarded as responsible for such HE photon emission: synchro-curvature radiation, which could only account for it if the radius of curvature of $\mathbf{B}$ in the pulsar magnetosphere was larger than 5 to $20 R_{\rm LC}$, which is one order of magnitude bigger than the typical values that can be reasonably conceived.

Thus, our measurements of pulsed emission up to 1.7 TeV clearly favor IC of LE photons by ultrarelativistic electron as the primary production mechanism of these γ-rays. This process would be then the underlying mechanism that produces the new component in the spectrum of the Crab pulsar above a few tens of GeV. The involved electrons need to have extremely high Lorentz factors of about $\Gamma \sim 10^6$ or higher, which is only achievable if they undergo strong

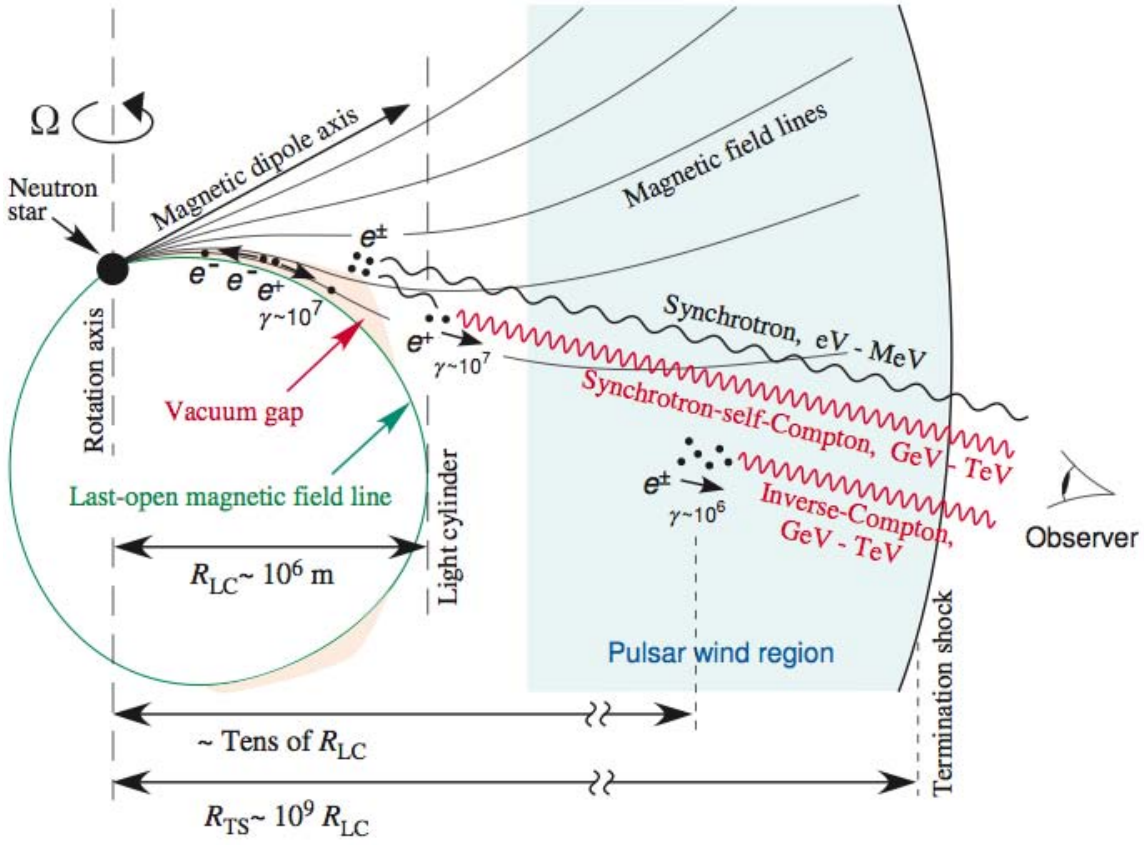

Figure 4.23: Schematic view of the pulsar magnetosphere as well as the pulsar wind region up to the termination shock. The possible locations where IC scattering can take place are shown, which is the only physical emission process that can account for the unpredicted VHE emission reported in this thesis within realistic values of its parameters.

accelerations beyond the light cylinder.

These measurements can only be explained by current models if strong constraints are imposed to the proposed physical scenarios. We now provide with some preliminary implications of the reported observations for the models that have been used so far to explain the γ-ray emission of the Crab pulsar. We have to consider that the Crab is a particularly unique pulsar, so models that explain the emission of the few detected γ-ray pulsars may not be able to explain the Crab TeV pulsation we have detected. After thorough discussions between the Crab analysis team and some of the authors of these models, only two of them

have been able to accommodate within their framework the IC mechanism that our observations imply: the SSC model extension of the outer magnetospheric gap and the IC model within the pulsar wind region (see §3.3), which place the emission in a different region of the pulsar magnetosphere. An schematic view of the emission regions under consideration by these two models can be seen in figure 4.23.

In one hand, in the outer gap model electrons are accelerated in the open-zone, within the thin region where the charge density differs from the Goldreich-Julian density, $\rho_{\rm GJ}$. These electrons up-scatter soft seed photons up to TeV energies but they are quickly absorbed by the dense plasma surrounding the pulsar via pair-creation. This triggers a magnetospheric cascade, in a similar way EAS are produced when γ-rays interact with molecules on the Earth atmosphere (§2.2). The electron-positron pairs produced in the cascade can again emit γ-rays, so the process is repeated. However, these higher generations of charged particles are located further away from NS surface, where photon and particle density quickly drops. Hence, γ-rays are less absorbed there and some can eventually scape from the pulsar magnetosphere and finally reach us.

Fitting	**Pulsar SED**	
parameter	**P1**	**P2**
F_0	1.1 ± 0.4	2.3 ± 0.4
a	-3.5 ± 0.1	-3.1 ± 0.1
χ^2/NDF	$1.73/4$	$5.31/7$

Table 4.14: Values of the parameters for the joint fitting of the Crab pulsar SED shown in figure 4.21, which includes the Fermi-LAT measurements above 10 GeV as well as the MAGIC points obtained from the combined analysis. A single power-law was used as fitting function (see equation 4.10.1), where parameter units are $[F_0] = 10^{-13}\gamma/\text{GeV}/\text{m}^2/\text{s}$ and $[a] = 1$.

This interpretation is able to explain the existence of pulsed photons up to the observed energies but it is not lacking some difficulties. For instance, the emission region of GeV photons would be far away from the emission region of the TeV photons. Since the distance between the GeV and the TeV emission regions in this model would then be of the order of $\sim 10^3$ km, this implies that the positions of the peaks in these two energy ranges phase would differ by about ~ 0.1 phases. This is about a factor 20 higher that the hint of delay between LE and HE pulses we have seen in §6.2. In conclusion, the pulses at GeV and TeV energies should not be as synchronous as we actually measure

them, an issue that this model would need to address.

On the other hand, the pulsar wind model could account for the emission of pulsed TeV photons if they were produced by IC scattering of lower energy radiation (up to MeV X-rays) by the relativistic electrons and positrons that form the cold pulsar wind. As we explained before, those charged particles would be required to have extremely large Lorentz factors. We know that the pulsar wind is dominated by its radiation component near the LC and also that it becomes a kinetically-dominated wind towards the nebula region. This conversion should take place in a relatively narrow, cylindrical region according to this model, which was estimated to be located somewhere between 20 and $50R_{\rm LC}$ from the NS surface.

However, the emission region must extend at least up to $\sim 70R_{\rm LC}$ so $e^+ - e^-$ have enough time to accelerate up to the Lorentz factors $\Gamma \sim 10^6$ implied by the observations reported in this thesis. The acceleration region proposed by this model is far to small to reach such ultrarelativistic speeds. In this case, the pulsar wind model would still have serious difficulties to reproduce the shape of the spectrum below energies of ~ 100 GeV. An additional complication would be to obtain the observed narrowness of the peaks at TeV energies from this model, as well as the ratio between main and secondary peaks.

In conclusion, the IC scattering of seed photons into γ-rays must occur at distances of the NS surface of the order of the light cylinder or larger. Both the outer gap and the pulsar wind models can account for the VHE Crab pulsar observations reported in this thesis. However, neither of them predicted pulsed emission at such high energy bands and some of the physical parameters need to be extrapolated to extreme values to explain for our observations. Furthermore, both models present problems trying to reproduce all the features of the pulsar lightcurve and/or the phase-resolved spectra. Revisions of these models are needed to understand how the observed TeV pulsar photons are able to escape its magnetosphere and still be precisely and synchronized with their low energy counterparts.

Chapter 5

The quest for Quantum Gravity

Although through the 20th century most of the fundamental forces of Nature have been integrated in a single theory, namely quantum-electrodynamics within the Standard Model, gravity has remained separate from the rest. This long-standing problem, the search for a Theory of Everything (ToE), that accounts for every basic interaction using only a single explanation, was already spotted by Einstein and he devoted his last 20 years of scientific research trying to solve it, unsuccessfully. To date, gravity is the only force in Nature that remains intrinsically non-quantic, both from a theoretical and from an experimental point of view.

Dozens of theories have been proposed and physicists are attacking the issue from any possible angle. In this chapter we will address this topic, starting with the historical, scientific and philosophical motivations for such a quest. Then, we will continue with a short introduction to the main proposed theories trying to quantize gravity, their achievements but also their major deficiencies. Next, we shortly review some of the multiple experimental tests proposed by these theories in order to experimentally confirm or discard them as a valid explanation of physical reality. Finally, we will provide for a detailed description of the approach followed throughout this thesis to test quantum gravity theories (from now on QG), based on the measurements of time-of-flight of photons arriving from astrophysical sources. We will finish this chapter listing the state-of-the-art limits on the energy scale of the LIV that different astronomical facilities around the world have been able to set.

5.1 The need for a quantum gravity theory

Since the first natural philosophers started to wonder about the very existence of the Universe and which are the rules that govern the world we live in, simplicity has always been preferred over complexity, as well as symmetry over amorphism. The desire of Mankind to understand Nature became embedded with the search of beauty in the way we explain the world around us. An aesthetic mind, combined with any measure of logical thinking, cannot tolerate a complex explanation whenever a simpler one is at reach. Complexity must emerge out of necessity, because simpler theories cannot account for an observed physical phenomenon, but never out of the wanderings of an idle, sharp mind.

This does not imply that physical theories are always simple: Nature is nothing but a complex system, so our ways of explaining its behavior will always end up being intricate. However, the scientific method requires that we check every small assertion before claiming a bigger one, so we are always building on safe ground, i.e. on previously confirmed ideas. If these knowledge elements or "science bricks" are complex from the start, we will have a hard time looking for the faulty parts. One could say that science starts from simple concepts to finally build a complex explanation of reality so Occam's razor always applies [86]:

Pluralitas non est ponenda sine necessitate[1]

Because of this, a single explanation of a set of phenomena is always preferred over several. A lot of efforts have been made throughout history of science to merge distinct theories, that explained certain phenomena, into a single one that can account for as many observations as possible. This approach proved to be very successful in most of the main scientific milestones.

The paradigmatic case would be the unification of the electric, magnetic and optics theories. James Clerk Maxwell realized that all the previously reported observations and experiments that involved either electric and magnetic forces could be explained and better understood as the observational effects of a single field, what we have come to know as **electromagnetic force** (EM), governed by the famous four Maxwell equations.

[1] Latin for "plurality should not be posited without necessity".

Two other cases of application of this simplicity principle that are relevant for the topic of this thesis were the proposals of the **Unification** (UT) and **Grand Unification Theories** (GUTs). With the former, it was proposed that at an energy scale of $\sim 10^2$ GeV, EM force was indistinguishable from the weak force, responsible for radioactive β-decay, becoming then just a single interaction: the so-called *electroweak force*. This was later confirmed in 1983 at CERN with the discovery of its force carriers, the W^+, W^- and Z^0 bosons. With GUT theories, the electroweak force was merged with the strong force, responsible for binding atomic nucleus together, at an energy scale of $\sim 10^{15}$ GeV. There are dozens of GUT candidates but none of their predictions has yet been confirmed. Nevertheless, the fact that such a unifying theory exists is already a big theoretical achievement.

This series of successful merging of theories fueled the search for the definite theory to unite all known forces into a single one, merging the (so-far classical) gravity with the other (quantum) forces. But there are crucial differences between them regarding the mathematical frameworks those theories work with.

On the one hand, gravity is currently described by General Relativity, a theory embedded in a classical framework, where physical properties like position and velocity of particles can always be determined with infinite precision, if the proper instruments are available. The current cosmological model cold dark matter + cosmological constant Λ (hereafter ΛCDM) is based on GR theory but still need some extra assumptions to explain our observations, for instance inflation. GR theory introduced the concept of *generally covariant equations*, i.e. equations written only with tensors in a form that is independent of the reference system we wish to calculate the terms in.

On the other hand, the other interactions between elementary particles operate within the quantum field theory framework (QFT), where physical properties are described in terms of probability and where the uncertainty principle always applies. Besides, QFT is not written in a generally covariant form: it relies on a fixed, flat spacetime described by the Minkowski metric, so we say QFT is not **background independent**.

However, Nature is a unique entity. As it was beautifully expressed by Lee Smolin,

A pen is made of atoms and it falls in the Earth's gravitational field.

A pen exists within a size and an energy scales where there is no obvious contradiction between gravity and quantum mechanics. But, there are certain extreme scenarios that require both theories to be applied at the same time. For instance, during the formation of a black-hole or during the first instants of existence of the Universe.

The search for ToE that can account for every interaction in the Universe is the holy grail of modern physics for the 21st century. Unfortunately, gravity and quantum mechanics can not be coupled easily. The gravitation field has resisted for decades all the attempts to being quantized because it is an intrinsically non-renormalizable field: if one uses a perturbative approach on gravitation, as it was successfully done to quantize EM, weak and strong field forces, it leads to an infinite number of free parameters, forbidding any concrete predictions and losing any of its scientific value [87].

We can try, instead, using a curved background within QFT but then this theory becomes much more complicated to formulate. But if we do not fix the metric at all and we treat it as a free dynamical entity (as it is done in GR), then QFT completely collapses. No way has been found in more than 70 years to formulate a consistent QFT with a dynamic background metric [88]. Thus, there is the need of a new theory that merges together the current models of GR for gravitation and SM for quantum mechanics. But a completely new way of attacking this problem is required. We will review the two main candidates in §5.2.

A last remark about this topic is that, so far, **there is no experimental need for a QG theory**, in the sense that there are no observed but unexplained phenomena which explicitly require the use of a fully-functional QG framework. New experimental results are being accounted for by models that use the current theories and no observations, to my knowledge, have been left unexplained just waiting for a working formulation of QG. The lack of observations demanding a QG theory might be a crucial point in this quest for a ToE or it may be totally insignificant: either there is no way to merge the two current physical theories or we have not observed any QG phenomenology because it is likely related to extreme astrophysical and cosmological scenarios, unavailable to us with present day technology. But, if we finally succeed in this quest, history tells us we should expect the unexpected: some observed and partly-unexplained phenomena, which are not seen as related to the QG research field, will be the key to

unlock this new theory and they will open the door to a whole new understanding of the Universe we live in.

As a motivation for such a quest, we would like to state my personal opinion on this topic, once and for all throughout this thesis. We think that this theory-driven scientific exploration is of capital importance because it will take human knowledge farther away than any currently-at-reach experimental evidence allows us for. A complete QG theory should elucidate what is the true nature of spacetime at the smallest scales; how blackholes form, evolve and eventually disappear; how the Universe begin and where does its original state comes from in order to produce what we have come to know as Big Bang, among other topics. Related phenomenology will emerge when a solid version of the theory is achieved and completely new effects will be predicted against which we will be able to test it.

But, more importantly, new and completely unimaginable applications of the theory will infallibly arise, in the same way previously-unimaginable technologies like the global positioning system (GPS) was possible once GR theory was successfully formulated. Comprehension of the very nature of spacetime itself will enable us to create new technologies that are, hard to predict today. However, human imagination is always one step ahead. It is not hard to imagine that classical, science-fiction topics like time-traveling, superluminal communications or transportation and quantum teleportation are areas where this new QG theory should shed a light on. And these possibilities are what makes this topic so thrilling. What we personally like about this ToE is that it has the potential to take our species a huge step forward into the space exploration, paving the road for the next centuries to come.

5.2 Quantum gravity candidate theories

GR was established in 1915 by Albert Einstein and quantum mechanics was founded soon after (1926). However, the problem of combining their fundamental principles was already noted by Einstein a decade earlier, in 1916 [89]. To perform this task, two main lines of research were developed during the 20th century: on the one hand, the *covariant theory*, which later on lead to the **String Theory** we know today, is based on an extension of the SM, where the GR metric tensor is included in a perturbative fashion but assuming a Minkowski

flat spacetime as zero or background state for the spacetime fabric; on the other hand we had the *canonical theory*, which lead to **Loop Quantum Gravity** (from now on LQG), based on applying spacetime measures within a Hilbert space but in a background-independent way, i.e. assuming no background metric. Other ideas have also been explored, like sum-over-histories approach, twistor theory, doubly special relativity or non-commutative geometry, but these theories have not reached the critical mass the other three have today. For the sake of shortness, they will not be described in this thesis.

In general, we can say every research line that has ever been followed can be classified into two main categories: the particle-physics perspective, leading to string theory, and the GR perspective, leading to LQG. Work by experts with a particle physics profile or with a relativity and cosmology background were usually contributing to develop either the first or the second approaches, respectively. But all of those theories have many common ideas and during their development they all have intersected each other quite often, so their mutual influence can not be overlooked. For a short historical review on the topic one could read [87].

5.2.1 String theory

From a point of view of a particle physicist, the natural approach to QG is to treat the gravitational field as a perturbative quantum interaction and derive the properties of its associated force carrier, the so-called *graviton*. The role the spacetime geometry plays in this process is just that of a given background where all the interactions take place, which can be described as a classical Riemannian manifold in the same way Einstein did within his GR theory. But string theory includes many major changes in the description of particles, fields and interactions beyond the SM. The most fundamental change is introduced by the concept of *string* as a substitute of point-like particle species. Strings can be opened or closed, their size is of the order of the Planck length, $l_P \sim 10^{-33}$ cm, and their vibration modes define them as photons, electrons or even gravitons.

Another important characteristic of String theory is that it requires several extra hypothesis and mathematical structures in order to be consistent. The first one is that String theory needs 10 dimensions to be a functional theory, 6 spatial dimensions more than usual 4 that we observe. So, how do we accommodate

such a revolutionary hypothesis with every observation ever made? The solution lies in the *size* of these dimensions: they are proposed to be very small, of the order of the Planck length, far too small to be observed with current technology. A compactification is achieved through the use of 6-dimensional Calabi-Yau manifolds in standard string theory, resulting in an effective 4-dimensional theory in the low energy regime where we have done every experimental tests up to now. However, new proposals of bigger but still microscopic dimensions could be incorporated to string theory.

The last major assumption made by string theory is a new physical symmetry called *supersymmetry* or SUSY. This new symmetry is introduced as an elegant solution to many problems of the SM and the ΛCDM cosmological model. It states that, for every particle with an integer spin (a boson), there must exist a supersymmetric companion or superpartner that has the exact same properties but whose spin differs in one half (a fermion), and vice versa. A direct consequence of SUSY breaking at low energies, a list of new particles is proposed to exist, one SUSY companion or superpartner for every particle described by the current SM. Up to now, all of them remain undiscovered by any particle accelerator or astroparticle detectors. However, the energy at which the SUSY is broken may be beyond what current instrumentation allows us to test.

After the so-called "first string revolution", 5 different versions of the string theory were defined, namely type I, type IIA, type IIB and the two so-called heterotic types: SO(32) and E_8xE_8. Later on, equivalence relations were discovered to exist between some of the previously mentioned versions of the theory. Several other discoveries enabled string theorists to see every version of the string theory just as particular cases of a unique, background-independent theory, the so-called **M-theory**. It is expected to operate in a 11-dimensional Universe but is still under construction [90, 91].

5.2.2 Loop quantum gravity

LQG is a QG candidate that started developing in the early 1980's by Lee Smolin and Tod Jacobson as an attempt to combine together both the principles of QFT and the axioms of GR using a new formulation of GR [92]. It is a non-perturbative, background-independent theory for quantum spacetime but, currently, it is not a candidate for a GUT, since the rest of the interactions

are not yet included. And, instead of using differential equations to describe the evolution of spacetime, its basic mathematical tools are finite differences equations. As every mature QG candidate, it has succeeded in solving several theoretical problems [93]:

- The exact black-hole entropy has been obtained for the static, rotating, charged and neutral cases [94].
- Discretization of spacetime into "atoms" of volume (surface) of the order of the cubic (squared) Planck length, $l_P^3 = \left(\hbar G/c^3\right)^{3/2} \sim 10^{-99}$ cm^3 ($l_P^2 \sim 10^{-66}$ cm^3) [95]. Actually, this seems to be a model-independent feature of QG [96] but here those values are obtained as the spectrum of eigenvalues of the volume (surface) operators [97]. Besides, they evolve in discrete time steps of the order of the *Planck time*, $t_P \equiv \sqrt{\hbar G/c^5} \sim 10^{-43}$ s.
- Spacetime is seen as a flat continuum where the Minkowsky metric is valid only at the largest scales. At the shortest scales, even in vacuum, the fine structure of spacetime is foamy and quickly changing, far away from the flat metric that it is assumed by GR. This is a unique feature of LQG, since no background metric is assumed and spacetime evolves freely within certain boundary conditions.
- Singularities do not appear in extreme gravitational fields, neither close to blackholes nor at the Big Bang time [98].
- In some models of LQG, gravity becomes repulsive at densities of the order of $10^{12} M_\odot$ inside the volume of a proton. According to them, there was never a Big Bang but a *Big Bounce* because the previous Universe was contracting until gravity flipped sign. However, no information from the previous Universe was conserved in this process. There is no need for an inflation hypothesis since it arises naturally from repulsive gravity [99]. Besides, dark energy can be also obtained.
- Newtonian gravity has been proved to be a special limit of LQG, when one imposes the proper boundary conditions [100].

LQG theory has gained much momentum during last decade, so tens of new scientists are devoting their efforts solving different aspects of the theory. However,it still has some important challenges ahead: there are big areas where no

one has yet extracted solid conclusions and, in some cases, the proper mathematical tools to be used are still unclear. Some of the points in the above list are derived from certain branches of LQG and, in the near future, these different versions of LQG should be somehow merged into a unique theoretical framework. But we can already see that LQG predicts a very different Cosmology, especially for the very first fractions of seconds in the history of the Universe [101]. At the same time, it manages to agree with the well-established features of blackholes thermodynamics or expansion and inflation of the Universe.

Moreover, LQG seems to be a promising theory to study regions of the spacetime fabric that have been strictly forbidden to the classical GR theory: singularities emerged in GR even for the simplest cases, like in the Schwarzschild metric, i.e. the exact solution of the Einstein equations for an empty, static space with spherical symmetry. These singularities arise because properties of spacetime at the scales we can directly experience can not be directly extrapolated down to the lowest distances or up to the highest gravitational intensities. The new quantum physics of spacetime seems to get rid of most of these problems. Besides, new features and phenomena will arise in the microscopic scales that can not be predicted from the macroscopic observations, just like the quantum tunnel effect or the uncertainty principle could not be inferred from any experiment at classical scales.

Apart from these theoretical milestones that we have listed, there are also some major drawbacks or missing links in LQG theory. They all need to be addressed before we can positively claim that we have found a definitive ToE.

- A necessary limit that still has to be derived to be consistent is to find GR emerging as a special case of LQG.

- A general description of dynamics is still missing. A sort of "Quantum Einstein Equations" are expected to be formulated, so we are able to describe and predict the evolution of dynamic systems in a similar manner as we did with GR.

- The matter and gravity coupling problem is not solved: we don't know how and how many types of matter can LQG couple to this new quantum gravitational field. Actually, a common criticism to LQG is that there is

no way yet to compute the masses of the particles in the same way the SM does, thus disputing its position as a valid ToE candidate.

- As any other QG theory, few predictions for cosmological measures have been extracted. A huge effort has been done in this direction, in order to find a set of clear predictions of the theory that can be measured with current technology. However, the mathematical formalism used by LQG is so complex that this task becomes almost unmanageable [102].

Notwithstanding the last point in this list, some semi-heuristic approaches have managed to derive observable effects [103]. For instance, the one we are interested in this thesis, the violation of Lorentz symmetry, that we will define formally in next section §5.3.

5.3 Defining Lorentz invariance

The two main candidates to QG theory that we have just presented have been intensely explored in order to derive any phenomena that could be used experimentally to test them. But, since none of those theories is yet complete, the derivation of some of these phenomena is usually through effective theories or other heuristic approximations and simplifications. In this thesis we are interested in one of those effects, probably the one which has received most of the attention from the scientific community since the publication of the seminal paper by Amelino-Camelia [104].

A common approach is to look for cases where of the Lorentz invariance principle from special relativity (hereafter, LI) is violated. We will refer to this hypothetic situation as **Lorentz invariance violation** or, for the sake of shortness, only as **LIV**.

Before getting into details about the state of the art of LIV tests, we should clearly establish what it is and what it is not LIV. To do so, consider the following action S for a scalar field $\psi(x^\alpha)$ ([2]):

$$S = \frac{1}{2}\int d^4x\sqrt{-g}(g^{\mu\nu}\partial_\mu\psi\partial_\nu\psi) \tag{5.3.1}$$

Where the metric is $g^{\mu\nu} = \eta^{\mu\nu} + h^{\mu\nu}$ and $h^{\mu\nu}$ is a small deviation from the Minkowski metric $(\eta^{\mu\nu}) = \text{Diag}(-1, 1, 1, 1)$. Since the action S is defined in

[2]Here, we are using the Einstein notation for contracted indexes: $x^\alpha y_\alpha \equiv \sum_\alpha x^\alpha y_\alpha$

tensorial form, it is therefore a spacetime scalar, i.e. invariant under Lorentz transformations: if you make a coordinate transformation to move to another inertial frame, every tensor in the action, including the background field g, will be modified but the value of S remains unchanged. This is what we know as *passive* or *observer LI* and it implies that we can choose any inertial coordinate system we prefer to perform the computations required by a physical law, as long as this law is expressed in tensorial form. Otherwise, the scalar S would ill-defined, so this is not an acceptable kind of violation of the LI.

In general, when we talk about LIV we refer to the violation of the *active* or *particle* LI, where only the dynamical field ψ is Lorentz-transformed, which means that particles are boosted or rotated. Let's consider now a Lorentz transformation to a new reference system, where magnitudes measured in it are labeled with a prime ($'$). The coordinates in the new reference system (x'^{μ}) are related to the coordinates in the old one (x^{ν}) by the Lorentz transformation matrix $\Lambda^{\mu}_{\nu} = \frac{\partial x'^{\mu}}{\partial x^{\nu}}$ ([3]):

$$x'^{\mu} = \frac{\partial x'^{\mu}}{\partial x^{\nu}} x^{\nu} = \Lambda^{\mu}_{\nu} x^{\nu} \tag{5.3.2}$$

so the scalar field ψ transforms as

$$\psi' = \psi(x'^{\alpha}) = \psi\left(\Lambda^{\alpha}_{\beta} x^{\beta}\right) \tag{5.3.3}$$

whereas its derivatives transform as

$$\partial'_{\mu}\psi' = \frac{\partial \psi(x'^{\alpha})}{\partial x'^{\mu}} = \frac{\partial x^{\nu}}{\partial x'^{\mu}} \frac{\partial \psi(x'^{\alpha})}{\partial x^{\nu}} = (\Lambda^{-1})^{\nu}_{\mu}\, \partial_{\nu}\psi(x'^{\alpha}) \tag{5.3.4}$$

The action in this new reference frame reads

$$\begin{aligned} S' &= \frac{1}{2}\int d^4x\sqrt{-g}\, g^{\mu\nu}\partial'_{\mu}\psi'\partial'_{\nu}\psi' \\ &= \frac{1}{2}\int d^4x\sqrt{-g}(\eta^{\mu\nu} + h^{\mu\nu})\, (\Lambda^{-1})^{\rho}_{\mu}\partial_{\rho}\psi\, (\Lambda^{-1})^{\sigma}_{\nu}\partial_{\sigma}\psi \\ &= \frac{1}{2}\int d^4x\sqrt{-g}\left[\eta^{\rho\sigma} + h^{\mu\nu}(\Lambda^{-1})^{\rho}_{\mu}(\Lambda^{-1})^{\sigma}_{\nu}\right]\, \partial_{\rho}\psi\partial_{\sigma}\psi \end{aligned} \tag{5.3.5}$$

where the Lorentz transformation has left $\eta^{\mu\nu}$ invariant but, in general,

[3] A Lorentz transformation is often defined as the lineal transformation that leaves the flat spacetime metrics $\eta^{\rho\sigma}$ unchanged, i.e. $\eta^{\rho\sigma} = \Lambda^{\rho}_{\mu}\Lambda^{\sigma}_{\nu}\eta^{\mu\nu}$.

$$h^{\mu\nu}(\Lambda^{-1})^{\rho}_{\mu}(\Lambda^{-1})^{\sigma}_{\nu} \neq h^{\rho\sigma}$$

hence it will not leave the action invariant either ($S' \neq S$).

In this case one says that the action *violates LI* and the physics of the system will vary. Whenever in this thesis we refer to LI, we will assume active LIV so the use the labels "active" or "passive" is no longer needed.

The fact that quantum-gravitational effects are expected at energies of the order of the Planck energies sets a preferred scale in the Universe, which can also be seen as defining a special reference frame. In other words: the foamy structures that emerge in LQG at distances of the order of the Planck length define an especial reference system where these tiny structures are at rest. Another case of a special reference frame, an possibly related to the first one, is the cosmic microwave background (from now on, CMB) co-moving frame: in it, the CMB measurements do not show any global dipole moment, so we can say that the CMB is at rest.

This is sometimes interpreted as a contradiction with the LIV principle but this is not the case: LIV principle states any law of physics which is valid in a particular inertial frame must also be valid in every other inertial frame. This does not imply that a reference system that is unique for some reason can not exist. It only implies that any physical law that we confirm within it can be also applied in any other inertial frame as well.

5.4 Lorentz invariance phenomenology

SM describes the behavior and properties of several quantum fields, which are required to describe the fundamental interaction of Nature, except gravity. These fields are the fermion field, the electroweak boson fields, the gluon field and the Higgs field. Besides, SM is a gauge theory because there are extra degrees of freedom in this fields that do not correspond to any change in the description of the physical system. One can incorporate LIV simply by introducing extra, renormalizable, LI-violation tensors in this model, which varies the phenomenology above a certain energy but still predicts the same correct results at low energies. This approach is followed by the Standard Model Extension (SME) theory, sometimes referred to as the minimal Standard Model Extension (mSME).

5.4.1 Test using terrestrial experiments

An expanding set of LIV tests have been performed in the last decades using only terrestrial experiments at low energies. Most of them are limiting LIV terms in the QED sector, a certain subset of the parameters of the SME. We will briefly name some of them but it is not the purpose of this thesis to describe every LI test in detail. Extensive reviews on the topic can be found elsewhere [105].

Clock comparison experiments

Ultra-precise tests have been performed using atomic clocks. These experiments compare the transitions of two different atomic or ionic elements that are located at some different points in space and usually under different orientations. As the clocks rotate together with the Earth and their orientations change, a sidereal drift between the two clocks is accumulated and limits to different components of the Lorentz violating tensors can be set. Since the clock frequencies can be measured over long time periods and with ultra-high precision, the upper limits set on the terms of the SME that break Lorentz symmetry are quite constraining, especially in the neutron sector [106, 107].

Penning traps

These devices allow us to fix the position in space of a charged particle using EM fields. Particles can still oscillate and rotate and the energy levels for these movements are quantized. Transitions between them can be induced via an oscillating magnetic field, which allows measurements of their magnetic moments as well charge-to-mass ratios. Besides, these measurements are useful to set limits to certain Lorentz invariance violating coefficients of the mSME. A second approach is to monitor some of these measurements as the Earth rotates, so the orientation of the experimental arrange varies with respect to preferred reference system, a direct consequence of LIV. If there really is any LIV effect, different values for these measurements should be expected during daytime than during nighttime. The best limits are extracted from high precision measurements of $e^+ - e^-$ pairs and proton-antiproton systems [108].

Cavity experiments

This technique tries to measure any shift in the resonance frequency of a cavity with respect to a fixed frequency, as it changes its orientation in space, [109].

The usual time dilation of GR may also be modified at high energies or using high clock speeds, if LIV is not an exact symmetry of nature. Based on this fact, comparison between Doppler shifts at low and high speed have been performed for lithium ions. These tests are able to limit LIV in the proton and electron sectors of the SME at the level of 10^{-11} GeV [110]. There are other tests on Lorentz violating components within the SME like muon experiments or constrains from the Higgs sector but they are intrinsically harder to do in any current experimental setup [111, 112].

5.4.2 Test using astrophysical source

A natural place to look for the effects of a possible LIV is in the observations of astrophysical sources because physical scenarios usually involve either violent events at extremely high energies (the most energetic particles ever detected are produced here), extreme distances or ultra-fast phenomena, or several of these properties at the same time. Even though QG effects are expected to become dominant at energies far away from the energy of any observed event, the tiny physical effects of the Lorentz symmetry breaking may still pile up along the way from the source towards us, until the effect becomes measurable with our current instrumentation.

The use of astrophysical sources to test LIV was first proposed by the seminal paper by Amelino-Camelia in 1998 [104], after the confirmation that GRBs had very big redshifts ($z \sim 1$ or even more), thus probing their cosmological origin. This paper sets some limits on the energy scale of the violation of LI based on the time-of-flight difference between photons of different energies. We will describe this effect with more detail latter in this section. But other observable effects were also proposed to set limits to LIV. We will now describe some of those predicted phenomena.

Particle thresholds

Different interactions may be modified if LIV is not an exact symmetry. For instance, kinetically forbidden reactions may arise, like photon decay; observed interactions may be suppressed by the appearance of new thresholds; or existing energy thresholds may be shifted, like the GZK cutoff in the UHE CR spectra or like the cutoffs in the spectrum of AGNs [105]. The related phenomenology

is rather complex and a detailed description falls out of the scope of this thesis.

Vacuum birefringence

Different traveling speeds for different photon polarizations, is one of the foreseen phenomenon if there is LIV at some scale. Consider that LIV is not an exact symmetry of nature but an *almost* exact one. Then, one should expect some small modifications, $\Delta_{QG}(p, E) \ll 1$, to the well known **dispersion equation** for massless particles:

$$E^2 = p^2c^2 + \Delta_{QG}(p, E) \tag{5.4.1}$$

Since there is no complete theoretical framework for QG, the usual approach is to perform some pragmatic approximation like in an effective field theory [102]. It is interesting to assume that different polarization states may behave differently

$$E_{\pm}^2 = p^2c^2 + \epsilon_{\pm}\frac{p^3c^2}{E_P} \tag{5.4.2}$$

where $\epsilon_+ = -\epsilon_-$ represents the left and right photon helicity states and E_P is the Planck energy scale, $E_P \equiv \sqrt{\frac{\hbar c^5}{G}} \approx 1.2210^{19}$ GeV, the scale at which such an effect would appear. Photons with different polarization should then travel at different speeds. Linearly polarized radiation would also rotate its polarization angle along the way in a quantity of the order of $\alpha_{\pm} = 2p^2t\frac{\epsilon_{\pm}}{E_P}$, where t is the propagation time between the radiation source and the observer.

Lorentz violating refringence may also remove any linear polarization of the emitted photons as they propagate towards the Earth, so any birefringence measurement from distant source may be able to limit this effect. It has also been proposed that an energy-dependent birefringence may induce correlations between the photon energy, polarization and arrival time. Several cases have been derived and for each of them limits have been set with polarization measurements of GRBs [113, 114], of the order of $|\epsilon_{\pm}| < 1.1 \cdot 10^{-14}$.

Vacuum birefringence can also be tested with the polarization measurements of the CMB radiation. Current theories predict no correlation between the curl-free E-modes and the divergence-free B-modes. However, since these two modes mix under rotation of the polarization direction, a non-zero vacuum birefringence would correlate these two CMB components. A summary of the limits for such

effect have been obtained with different experiments and good reviews can be found elsewhere [115].

Time-of-flight constraints

Modifications to the speed of particle propagation are expected and it may vary with the particle energy. Departure from the conventional value $c \equiv 299,792,458$ m/s can be limited measuring the correlations between particle energy and arrival time. An assumption of simultaneous emission is compulsory if no confirmed model of emission at the source is available but some methods can be used to distinguish source and propagation effect. For instance, if multiple LIV measurements were performed with several kind of sources at varying distances, by combining them we could find clear correlation of those delays with the distance. In such case, we would have detected LIV in a source-independent way. Pulsars can be also used to distinguish between source and propagation effects but we will explain the method later in §5.5.3. In this thesis we will discuss only the case for time-of-flight differences for photons but neutrinos emitted by GRBs can also be use for such tests [116], although no neutrino measurement associated with a GRB event has been detected so far.

Since this thesis is focused on setting constraining limits to LIV by using measurement of time-of-flight (from now on t.o.f.) differences between low and high energy γ-rays, a more detailed explanation of this effect is necessary. We would like to describe the theoretical basis of such effect but, since there is no definitive derivation for it using the whole mathematical formalism of any candidate QG theory, a heuristic modeling will be used. An estimation of the current sensitivity to any LIV-induced time delay will be given for each of the different families of astrophysical sources.

First of all, we shall consider the modified dispersion relation stated above (equation 5.4.1) where now the term Δ_{QG} can be expanded with a Taylor series of the energy

$$p^2c^2 = E^2\left[1 + \sum_{n=1}^{\infty} \xi_n \left(\frac{E}{E_{\mathrm{QG}n}}\right)^n\right] \tag{5.4.3}$$

where c is the standard speed of light, i.e. the speed of photons at low energies, $c = \lim_{E\to 0} v_\gamma(E)$, $E_{\mathrm{QG}n}$ is the energy scale of the LIV for the n-th term and $\xi_n = +1,\ 0$ or -1 represents here the sign of the variation. The modifica-

tions from the standard photon energy dispersion must be small because LI is confirmed in every experimental set-up at low energies until today. This energy scale is expected to be of the order of the energy where quantum gravitational effects start to become dominant, i.e. of the order of the Planck energy E_P.

We can now compute the speed of photons in empty space, v_γ, which is defined as the group velocity of the EM wave. After removing any non-dominant, high order energy term (see appendix §A) we end up with the following equation

$$v_\gamma = \frac{\partial E}{\partial p} \approx c \cdot \left[1 - \sum_{n=1}^{\infty} \xi_n \frac{n+1}{2} \left(\frac{E}{E_{\mathrm{QG}n}}\right)^n\right] \tag{5.4.4}$$

When we look for t.o.f. differences between photons of a certain energy range, we focus on a certain LIV term, i.e. either lineal ($\xi_1 = 1$ whereas $\xi_n = 0$ for every $n > 1$) or quadratic ($\xi_2 = 1$ and the rest are equal to 0).

In general, the t.o.f. of photons emitted from an arbitrary astrophysical source would be

$$t = \frac{\Delta l}{c}\left[1 + \xi_1 \frac{E}{E_{\mathrm{QG1}}} + \xi_2 \frac{3}{2}\left(\frac{E}{E_{\mathrm{QG2}}}\right)^2 + \mathcal{O}(E^3)\right] \tag{5.4.5}$$

where Δl is the co-moving distance to the source. If the source is galactic, then $\Delta l = d$ is directly the distance between us and the source; for extragalactic but close by objects with redshift $z \ll 1$, one can use the Hubble law that reads $\Delta l = z \cdot c/H_0$ where $H_0 \approx 70$ km/s/Mpc is the local Hubble constant [117]; but for the farthest sources the expansion of the Universe has to be properly taken into account, therefore

$$\Delta l = \frac{c}{H_0}\int_0^z dz \frac{(1+z)^n}{\sqrt{\Omega_M (1+z)^3 + \Omega_\Lambda}} \tag{5.4.6}$$

where Ω_M and Ω_Λ are the total matter density of the Universe and the cosmological constant, the standard cosmological parameters of the ΛCDM model.

If we only consider the source under study in this thesis, a galactic source such as the Crab pulsar, we can simplify the computation of this distance to $d = d_P \approx 2.2$ kpc. The difference between the t.o.f. of a photon with low

energy, E_l, and another with high energy, E_h, is then

$$\Delta t = \underbrace{\frac{d}{c}\frac{E_h - E_l}{E_{\mathrm{QG1}}}}_{\Delta t_1} + \underbrace{\frac{d}{c}\frac{3}{2}\frac{E_h^2 - E_l^2}{E_{\mathrm{QG2}}^2}}_{\Delta t_2} + \mathcal{O}(E^3) \tag{5.4.7}$$

If no difference in the t.o.f. between photons is found, we can only claim that, if there is any chromatic effect due to LIV, it can only be below our instrumental sensitivity Δt_{min}. Therefore, for the linear case

$$\Delta t_1 < \Delta t_{\mathrm{min}} \Rightarrow E_{\mathrm{QG1}} > \frac{d}{c}\frac{E_h - E_l}{\Delta t_{\mathrm{min}}} \tag{5.4.8}$$

whereas for the quadratic case

$$\Delta t_2 < \Delta t_{\mathrm{min}} \Rightarrow E_{\mathrm{QG2}} > \sqrt{\frac{3d}{2c}\frac{E_h^2 - E_l^2}{\Delta t_{\mathrm{min}}}} \tag{5.4.9}$$

Since we are usually comparing arrival times of photons whose energy differ by one order of magnitude or even more, we can assume that $E_h \gg E_l$. Thus, we can say that $E_h - E_l \approx E_h$ and it is even safer to claim that $E_h^2 - E_l^2 \approx E_h^2$. Using these approximations, the limits to the energy scale of a linear and a quadratic energy-dependent LIV will be given instead by

$$E_{\mathrm{QG1}} \gtrsim \frac{d}{c}\frac{1}{\Delta t_{\mathrm{min}}} E_h \tag{5.4.10}$$

$$E_{\mathrm{QG2}} \gtrsim \sqrt{\frac{3}{2}\frac{d}{c}\frac{1}{\Delta t_{\mathrm{min}}}} E_h \tag{5.4.11}$$

5.5 Candidates for time-of-flight tests

Among the different families of astrophysical sources, some show the necessary properties to become sensitive to detect hypothetical LIV phenomenology or to set competitive limits if none is detected. For time-of-flight differences between photons of different energies, three characteristics are required for a source to be a good candidate for testing LIV and the reasons for this are self-evident when one looks at the expression for an induced time-of-flight difference, equation 5.4.7. Namely:

- **Far away objects**: great distances allow different photons to integrate

Source family	d [pc]	E [GeV]	δt [s]	Expected limits E_{QG1} [GeV]	E_{QG2} [GeV]
GRB	10^{10}	10^{1}	$10^{0} - 10^{2}$	$10^{17} - 10^{19}$	$10^{9} - 10^{10}$
AGN	10^{8}	10^{4}	$10^{2} - 10^{5}$	$10^{15} - 10^{18}$	$10^{9} - 10^{11}$
Pulsar	10^{3}	10^{2}	$10^{-2} - 10^{-4}$	$10^{17} - 10^{19}$	$10^{10} - 10^{11}$

Table 5.1: Order of magnitude of the main properties of astrophysical candidates to test LIV, as well as expected LIV limit that one could set with them if no energy-dependent delay in their signal was found.

a bigger delay between them up to measurable times. The most distant objects known so far are GRBs, located at cosmological distances of the order of Gpc; thus, they have become a classical candidate for LIV tests.

- **High energy emission**: the effects of LIV are expected to increase with increasing energy, thus the highest the energy of the detected photons the more constraining the limit to the LIV will be. Since LIV limits are extracted from comparing arrival times at low and high energies, emission in a wide energy range is also necessary. However, the sensitivity to any LIV effect depends on the difference, or quadratic difference, in energy between photons. Therefore, when the energy range is more that one order of magnitude, the high energy photon dominates equations 5.4.10 and 5.4.11. A common misunderstanding is to think that comparing radio lightcurves with γ-ray measurements will provide the best sensitivity but there is virtually no difference when we use low energy γ-rays instead of radio data. Concerning the astrophysical sources, AGNs emit the most energetic photons detected so far, up to $\sim 10^4$ GeV.

- **Variable flux**: fast flux changes in a wide energy band allows for a more sensitive testing of LIV effects, since the fine time structure would not be preserved after the smearing effect of the LIV. The sources with the fastest variations of the γ-ray flux are probably millisecond pulsars, whose pulses last less than 10^{-4}s.

In table 5.1 we summarize the properties of the most suitable families of astrophysical γ-ray sources to perform time-of-flight tests to limit LIV.

5.5.1 Active Galactic Nuclei

Galaxies containing an active center are among the most energetic γ-ray emitters in the Universe: typical energies for an AGN with a hard spectrum usually reach tens of TeV. If there was any LIV in the Universe for the highest energy photons those emitted by AGN would be more sensitives to it. Besides, they are often detected in a flaring state, i.e. a period of a few days or even weeks during which their emission gets increased sometime by more than one order of magnitude. The most important parameter of these flares regarding a possible limitation of any LIV is the speed at which the AGN flux varies, that is the steepness of the flare. Typical times for these fluctuations are of the order of hours but some have reported more extreme escenarios where the time scales for 2-fold in the flux are around 5 minutes [118]. If we take also into account the extreme distances of some of these sources we realize that they are a good natural laboratory to test LIV, especially for this violation is quadratically-dependent with the energy of the photon (see expected limits in table 5.1).

The best LIV limit for these kind of source was obtained with the observations of PKS 2155-304, a BL Lac object with a measured redshift of $z \approx 0.116$. This AGN flared on July 28 2006 [119] and for the first hours its lightcurve showed extremely short bursts where its flux increased up to a 10-fold as compared to its usual flux of $\sim 15\%$ of the Crab. These flare was modeled with a series of 5 asymmetric gaussian functions and a likelihood maximization was applied to look for correlations between the list of times and energies of the recorded events. Very competitive limits to LIV could be derived using these data [120]:

$$\begin{aligned} E_{\mathrm{QG1}} &> 2.1 \cdot 10^{18} \text{ GeV (95\% C.L.)} \\ E_{\mathrm{QG2}} &> 6.4 \cdot 10^{10} \text{ GeV (95\% C.L.)} \end{aligned} \tag{5.5.1}$$

The quadratic one was the most constraining limit to LIV for several years until their were improved by a GRB detected by Fermi, as explained in the next section.

5.5.2 Gamma-ray Bursts

As explained in §1.2.2, GRBs are cataclysmic events that occurred at cosmological distances. The photons that were emitted have been traveling towards us for almost as long as the age of the Universe, since these events took place when the Universe was just a few Gyr old. Their duration is usually extremely short: always below a few minutes and with a typical structure of narrow peaks where flux increases occur in a few seconds and typically less than a second. These two facts make GRBs one of the best candidates to test LIV, even if they are not the most energetic sources in the γ-ray sky, with energies typically below a few GeV and down to X-ray energies.

The most constraining limits for LIV are currently derived from GRB 090510. Recorded by the LAT detector onboard of the Fermi satellite on 10 May 2009, the posterior measurement of its afterglow revealed an estimated redshift of $z \approx 0.90$, which can be translated into at a cosmological distance of about 10 Glyr, assuming standard cosmological parameters. The impressive time-of-flights for those photons is combined with high energies: this GRB contained the most energetic photon ever detected for such family of source: a single 31 GeV photon can be seen in the bottom plot of figure 5.1.

In 2009, the most competitive limit so-far for a linear, energy dependent LIV was derived from this event using the unbinned DisCan method [121]: a 95% C.L. lower limit of $1.5 \cdot 10^{19}$ GeV could be established for the most conservative astrophysical scenario [122]. This limit exceeded for the first time the value of the Planck energy, $E_{Pl} = 1.22 \cdot 10^{19}$GeV, the threshold for many quantum gravity models that predicted such LIV effects. Thus, most of those models could be ruled out with this new limits. Furthermore, a posterior analysis of the same GRB event using a new statistical method called PairView managed to increase this limit to the linear term [123]. This new method studies the distribution of the so-called *spectral lags*, a combination of time and energy difference for every possible pair of events in a GRB event. The LIV limit in the linear term obtained using this method improved the previous one by a factor 5, setting the most competitive energy threshold for LIV effects at

$$E_{\mathrm{QG1}} > 9.3 \cdot 10^{19} \text{ GeV (95\% C.L.)} \tag{5.5.2}$$

an energy scale of almost an order of magnitude above the Planck energy.

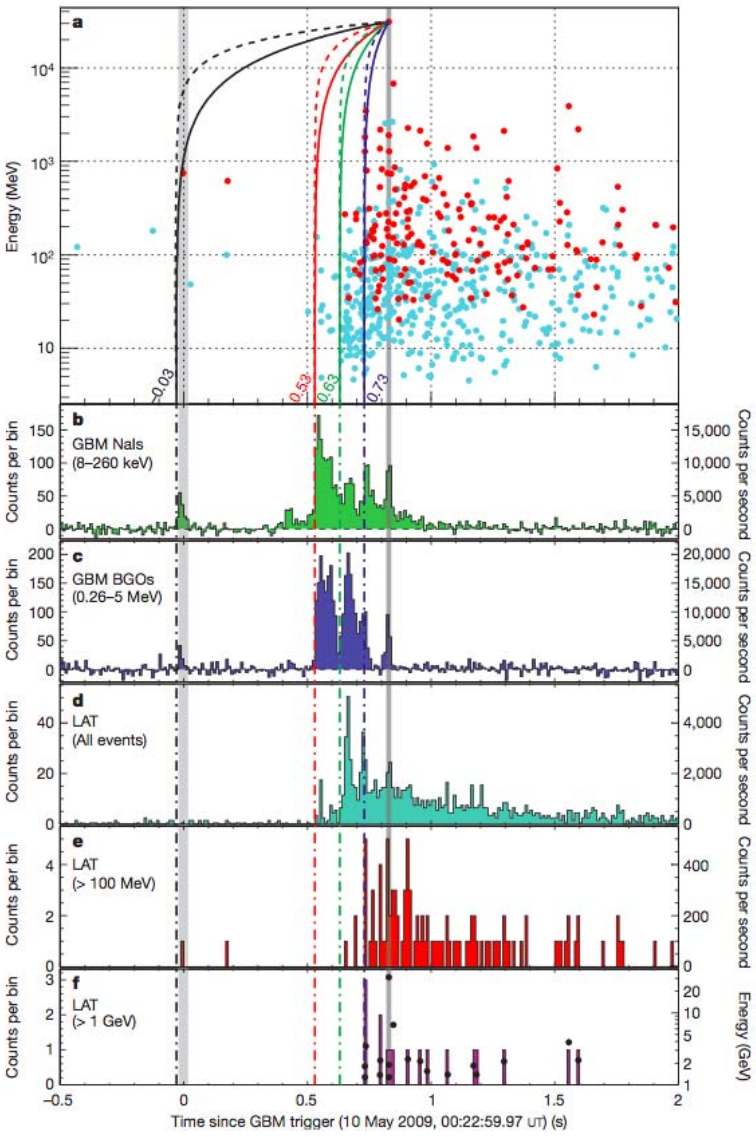

Figure 5.1: Energy and arrival time of the γ-ray events associated with GRB090510, as recorded by the GRM and the LAT instruments onboard of the Fermi satellite. Taken from [122]. The highest energy event (31 GeV) can be seen within the grey-shadowed area at the center of the bottom plot.

Besides, the data of the same GRB were also used to apply the so-called *sharpness maximization method*, which was a modification of the DisCan. The goal of such method is to restore the sharpness of the original lightcurve that any LIV-induced, energy-dependent time delay would have smeared out. By doing so, they managed to improve the previous best LIV limit on the quadratic term by a factor ~ 2:

$$E_{\mathrm{QG2}} > 1.3 \cdot 10^{11} \text{ GeV (95\% C.L.)} \tag{5.5.3}$$

5.5.3 Pulsars

Pulsars are a very special family of candidates for limiting LIV and the reason for this is two-fold. First of all, one does not rely on a serendipitous observation like a GRB or an AGN flare, but instead the limit is based on the statistical integration of years of data. Therefore, the longer the exposure time for a certain pulsar, the better the precision in the pulse phase and a correlation between energy and photon arrival phase is easier to find. The LIV limits extracted from a γ-ray pulsar can be improved just by integrating more data, an unique characteristic to limit LIV that no other source possesses.

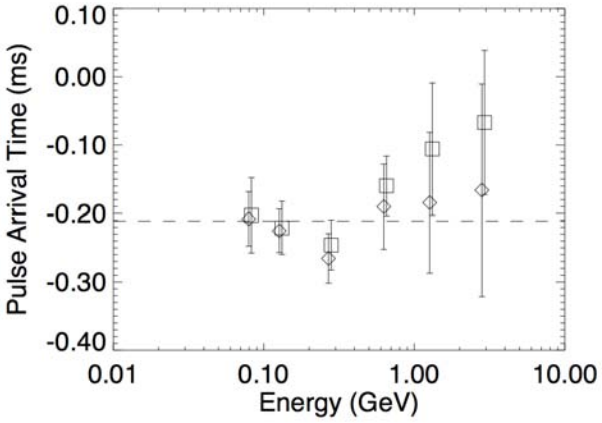

Figure 5.2: Measurement of the Crab pulse arrival time for energies between 70 MeV and 3 GeV by Kaaret using CGRO-EGRET [124].

The second reason, and also a unique feature of pulsars, is that they are able to provide a way to distinguish between source and propagation delays. The basis for this is that a possible LIV-induced delay Δt is a fixed quantity whereas the corresponding, LIV-induced phase delay is not fixed because the pulsar period is slowly increasing with time. Since $T(t) = T(0) + \dot{T} \cdot t$ with $\dot{T} > 0$, we can see that the phase difference between high and low energy photons $\Delta\phi(t) = \Delta t/(T(0) + \dot{T} \cdot t)$ is steadily decreasing with time. If a peak position dependence on energy is found and is caused by LIV, it will be steadily

reduced as the pulsar slows down, a clear evidence that allows us to virtually exclude any source-intrinsic effect.

Comparison of pulsar leak positions in 1999 using CGRO-EGRET data [124]. The peak position was estimated for 6 energy bins between 70 MeV and 3 GeV (figure 5.2). The derived limits to a linear LIV effect, the most constraining at the time, were set to $E_{\mathrm{QG1}} > 1.8 \cdot 10^{15}$ GeV.

Limits to LIV were also derived from Crab pulsar observations by the VERITAS Cherenkov telescopes, thanks to the detection between 120 and 400 GeV[70]. Since the interpulse position at those energies was coincident with the position measured by Fermi within the uncertainties, this LIV limit could be improved to $E_{\mathrm{QG1}} > 3 \cdot 10^{17}$ GeV. Besides, a limit to the quadratic energy dependence could be also set at $E_{\mathrm{QG2}} > 7 \cdot 10^{9}$ GeV [125].

Chapter 6

Lorentz invariance violation tests

Lorentz symmetry breaking or Lorentz invariance violation (LIV) is usually tested in astrophysics with the use of extragalactic sources so time between the emission of photons at the source and the detection by our telescopes, the so-called time-of-flight, is maximized. However, there is a family of sources located in the Milkyway that can also impose strong constraints to LIV due to their high energy emission together with their extremely fast flux variations: γ-ray pulsars, such as the one at the center of the Crab nebula.

In this chapter we want to make use of the discovered VHE emission reported in chapter 4 to derive the best possible limits on possible LIV-induced correlations between energy and arrival time of pulsar photons. We will apply two different methods to do so: first, a simple approach where peak positions at high and low energies are compared; and a second method based on the maximization of the statistical likelihood of our observations to be described and parametrized by certain pulsar and LIV models. This method will be adapted to the unique characteristics of pulsar emission for the first time.

Our ultimate goal is to improve the sensitivity beyond the current best limits on LIV obtained using astrophysical sources[1]. Since we would like to have an unbiased estimator of such LIV effects, we must choose *a priori* whether we intend to measure or to limit the energy scales at which those hypothetic LIV effects become dominant. The already existing limits constrain the existence of

[1]The best limits at the time of writing this thesis were set at $9.3 \cdot 10^{19}$ GeV for the linear term and $1.3 \cdot 10^{11}$ GeV for the quadratic term, both at 95% C.L. [123]. Details can be found in §5.5.2

any LIV effect to very high energy scales, especially for the linear case where this scale has already surpassed the Planck mass. Even in the most favorable case, where the scale of LIV would be right above those limits, a statistically significant measurement using pulsars is not granted, as explained in §5.5.

Based on these two facts, we chose to focus on setting limit on $E_{\mathrm{QG}n}$ using the discovered Crab pulsation at TeV energies. The algorithms created for this thesis were optimized with such goal in mind. After applying them, two situations are possible:

1. No significant correlation between energy and arrival time can be measured so we are able to derive strong constraints on the scale of LIV, which may be of the order of the current best limits.

2. A significant correlation is observed, so the derived limits are less competitive. If we then decide to perform an actual measurement of the LIV scale from the data presented in this thesis, the significance such measurement would be reduced, in order to account for a certain trial factor. This trial factor arises from the fact that, once we have found a correlation, we changed our goal from setting a limit to measuring a value for the LIV energy scale.

As shown in table 5.1, the characteristics of pulsar emission make these kind of sources comparatively more sensitive to the quadratic term of the dispersion relation for photons. Hence, this is the limit we focused on improving. Our chances to improve on the linear term are quite scare.

6.1 Physics case for pulsar emission

First of all, if we want to test if there is any difference in the time-of-flight of the photons from the Crab, certain *a priori* assumption will have to be made. The most important of those is to suppose that the photons were emitted simultaneously at the source. In this way we can look for delays that fit those we expect due to LIV. This assumption is not very risky if we notice that the Crab pulsar lightcurve is well aligned for every energy band where MAGIC is able to detect it, as shown in table 6.1, and also with its low-energy counterparts, such as the detection by Fermi or Chandra.

The only possible scenario where a significant time delay could co-exist with such narrow, synchronized pulsation would be that photons of different energies

where emitted at different times at the source, but that they accumulated the precise delay along the path due to LIV so that all of them finally arrive to the Earth simultaneously. This kind of "LIV conspiracy" will be considered as an highly unlikely situation. However, this possibility could only be completely ruled out if several γ-ray pulsar were discovered to emit TeV radiation. Since they would be located at different distances from us, it is impossible for a single LIV effect to synchronize the signal of each of them at once.

To have a better understanding of the delays that a LIV effect could produce to pulsar photons, the expected phase delays for realistic values of the LIV energy scale were computed. Staring from the LIV-induced time delays of equation 5.4.7), we now divide them by the pulsar period, $T \approx 0.0336$ s, to obtain the corresponding phase delay given LIV energy scale of order n, $E_{\mathrm{QG}n}$:

$$\Delta\phi_n(E|E_{\mathrm{QG}n}) = \frac{1}{T}\Delta t_n(E_{\mathrm{QG}n}) = \xi_n \frac{n+1}{2}\frac{d_P}{c\,T}\left(\frac{E}{E_{\mathrm{QG}n}}\right)^n \tag{6.1.1}$$

There are two possible physical cases that allow for such a delay: either a subluminal case $\xi_n = +1$, where HE photons are delayed with respect to their low-energy counterparts; or a superluminal case, i.e. $\xi_n = -1$, where LE photons are those being delayed with respect to the HE ones. Using this definition, $E_{\mathrm{QG}n}$ is positive-definite and the sign of the photon velocity change is given by the ξ_n parameter.

However, this definition of the LIV energy scale presents two major problems. The first one is that, if we want to test a no-LIV scenario we need to set $E_{\mathrm{QG}n}$ to very high values, virtually to infinity: $E_{\mathrm{QG}n} \longrightarrow \infty$. In order to have a proper fitting parameter, a re-definition is required. Following the recipe proposed in [126], we define the **LIV parameter** as

$$\lambda_n \equiv \frac{\langle E_{\mathrm{QG}n}\rangle}{E_{\mathrm{QG}n}} \tag{6.1.2}$$

where $\langle E_{\mathrm{QG}n}\rangle$ is an arbitrary scaling factor. The actual value of $\langle E_{\mathrm{QG}n}\rangle$ is used to force λ_n to take values close to the unity for the LIV scales we need to consider, which makes numerical computations technically easier. Therefore, we selected the values $\langle E_{\mathrm{QG1}}\rangle = 10^{19}$ GeV for the linear case and $\langle E_{\mathrm{QG2}}\rangle = 10^{12}$ GeV for the quadratic case. These definitions are of the same order as

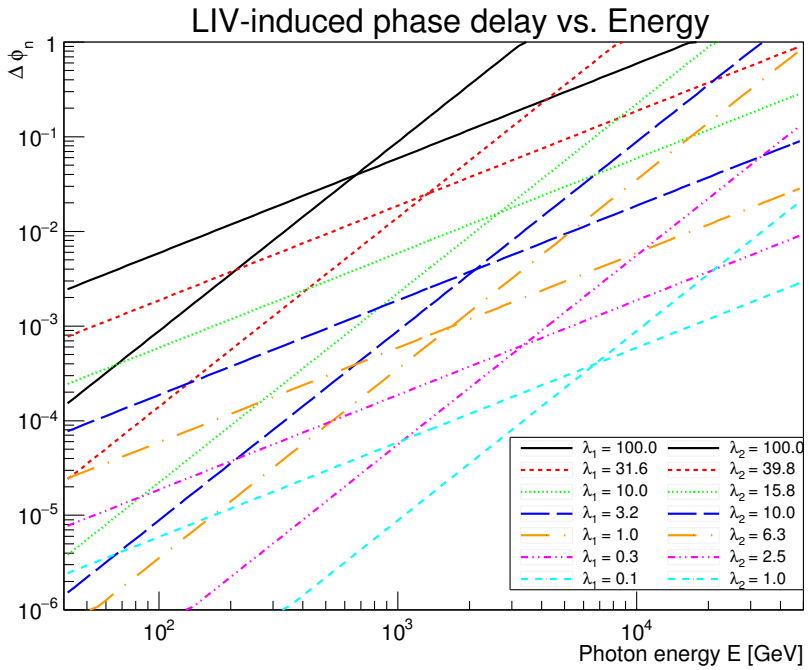

Figure 6.1: LIV-induced phase delay for Crab pulsar photons as a function of their energy. An approximately evenly-spaced selection of LIV parameters is plotted, both for the quadratic (λ_2, steeper lines) and linear (λ_1) cases.

the limits we expect to obtain with the Crab pulsation at $\sim 10^2$ GeV (see table 5.1). As a rule of thumb, a LIV parameter below 10 represents a weak LIV effect, of the same order of magnitude of the best quadratic limits by Fermi. On the contrary, values larger than 10 represent an intense LIV effect, which can be translated into less competitive limits[2]. The situation where absolutely no correlation between energy and arrival time of the photons is found corresponds to a value of the LIV parameter $\lambda_n = 0$, which is what one would expect from a properly-defined fitting parameter.

Using the definition introduced in equation 6.1.2, we can now transform equation 6.1.1 into

$$\begin{aligned} \Delta\phi_1(E|\lambda_1) &\approx 5.91 \cdot 10^{-7} \cdot \xi_1 \, \lambda_1 \left(\frac{E}{\text{GeV}}\right) \\ \Delta\phi_2(E|\lambda_2) &\approx 8.86 \cdot 10^{-12} \cdot \xi_2 \, \lambda_2^2 \left(\frac{E}{\text{GeV}}\right)^2 \end{aligned} \tag{6.1.3}$$

[2]The best LIV limits by Fermi are set at $E_{\text{QG1}} > 9 \cdot 10^{19}$ GeV and $E_{\text{QG2}} > 1.3 \cdot 10^{11}$ GeV by the time of writing this thesis. This corresponds to LIV parameter values of $\lambda_1 \lesssim 10^{-2}$ and $\lambda_2 \lesssim 8$, respectively. The second best for the quadratic case, set by H.E.S.S. at $E_{\text{QG2}} > 6.3 \cdot 10^{10}$ GeV, corresponds to $\lambda_2 \lesssim 16$.

The second problem with the definition of the LIV parameter is related to the inclusion of the sign ξ_n. In order to have consider all the possible situations in our minimization procedure, we decided to implement our ML method including this sign within the LIV parameter itself, so we could explore the entire range $\lambda_n \in (-\infty, \infty)$. This is a trivial change of variables in the case of a linear LIV

$$\xi_1 \lambda_1 \longrightarrow \lambda_1 \tag{6.1.4}$$

where now a negative value of the redefined λ_1 parameter produces advancement of the HE photons, as we would expect in the case of $\xi_1 = -1$.

But it is not so trivial for the quadratic case. One can still redefine the LIV parameter in the same way, namely $\xi_2 \lambda_2 \longrightarrow \lambda_2$ but, since λ_2 is squared in the computation of the LIV delay (equation 6.1.3), the sign of the LIV effect will be lost: $(\lambda_2)^2 > 1$. Thus, the redefinition has to be applied to the square parameter instead:

$$\xi_2 (\lambda_2)^2 = (\xi_2 \lambda_2) \cdot \lambda_2 \longrightarrow \lambda_2 \cdot |\lambda_2| \tag{6.1.5}$$

If we implement this change of variables in equation 6.1.3, a negative value of λ_2 will also produce a negative value of $\lambda_2 \cdot |\lambda_2|$, and an advancement of the HE photons will occur.

For a LIV energy scale $E_{\mathrm{QG}n}$ of the order of the current best limits, the induced phase shift for a 400 GeV photon is of the order of $\Delta\phi_1 \sim 10^{-5}$ and of $\Delta\phi_2 \sim 10^{-4}$ for the linear and the quadratic cases, respectively. For higher energies such as a $E = 2$ TeV photon, we have that $\Delta\phi_1 \sim 10^{-4}$ and $\Delta\phi_2 \sim 10^{-3}$, respectively. This phase delays are comparable with the resolution we have for the estimation of the phases of an event, which is determined by the uncertainty in the Jodrell bank ephemeris, $\sigma_{\mathrm{eph}} \approx 10^{-4}$ (see §4.6). In figure 6.1 one can see the absolute value of the phase delay produced by different values of the LIV parameter for both the linear and quadratic cases.

Now, let us estimate the integrated effect of LIV-induced time-of-flight delays (or advancements) in the phaseogram of a pulsar. The consequence of such delay is a displacement of the phaseogram peak, linearly or quadratically

proportional to the energy E of each photon:

$$\phi_{\rm P2} \longrightarrow \phi_{\rm P2} + \Delta\phi_n(E|\lambda_n) \tag{6.1.6}$$

Since the phaseogram is built in coarse bins of estimated energy, the combination of different peak shifts will produce an asymmetric smearing of the pulse phase profile.

Another point is that, the time profile is a phaseogram in the case of pulsars, and the phase ϕ is a circular variable bound between values of 0 and 1. This implies that an energy-dependent delay can only produce a scrambling events in y the phaseogram, since y events are displaced from their original positions but can not be shifted out of the observation window. For instance, for the case of a delay ($\xi_n = +1$) an event emitted at the interpulse can be shifted by LIV towards the main pulse region. But if LIV is intense enough this shift can take it to regions beyond the lower limit ($\phi < 0$), so it will re-enter the phaseogram from the opposite boundary. Such event may end up being detected in off region or *even back to the interpulse*, if the phase delay is close to an integer value.

This last situation could only happen, in the case of the Crab pulsar, for the highest photon energies ($E > 2$ TeV) and for the most intense LIV scenarios ($\lambda_n \gtrsim 40$). However, such regions of the parameter space are virtually ruled out by previous LIV limits obtained by different experiments and from a variety of astrophysical sources (see §5.4.2). We must be taken into account this special situations when we simulate intense LIV scenarios later in this thesis, for instance to test the performance of our algorithms.

In addition, we saw in equation 6.1.1 the same time delay is transformed into diverse phase delays for different pulsars, the larger the phase shift the shorter the pulsar period P is. Therefore, these extreme phase shifts we described could also take place for pulsars with periods even an order of magnitude smaller than that of the Crab pulsar. If one such pulsars was detected in the future in the VHE γ-ray band, competitive LIV limits could be derived from it and these considerations about the periodicity of the phase must be taken into account.

In conclusion, the existence of pulsed VHE emission, together with its precise synchronization with the lower energy pulses, limits the possibility of any energy-dependent time delay, such as those predicted by some QG models. The phase

delays induced by LIV effect of the order of the best limits so far are at the same level of our phase resolution. The simplest way to test this claim is by direct comparison of the P2 peak positions at different energies. This is the first method we applied and it will be described in the next section, together with the obtained LIV limits. However, these limits are not expected to be competitive with those set by observation of extragalactic sources, so a more complex analysis of the pulsar data will be required.

6.2 Comparison of peak positions

The first method to look for a correlation between the time-of-flight of pulsar photons and their energy is to compare the peaks position for two energy bands. The smaller the distance between them, the stronger the limit on any LIV effect, i.e. the higher the limit on the LIV energy scale $E_{\mathrm{QG}n}$ These procedure was applied to the Crab pulsar LC obtained after the analysis complete MAGIC dataset (see §4.9). Gaussian functions were fitted to the pulsar LC for each of the energy bin where we were able to detect the Crab pulsation. We tested different phaseogram binnings, multiple number of energy bins and diverse energy intervals and we finally obtained the best fit for the following 4 energy bands:

$$\begin{aligned} &E \in [40, 90] \text{ GeV} \\ &E \in [90, 150] \text{ GeV} \\ &E \in [150, 400] \text{ GeV} \\ &E \in [400, 1700] \text{ GeV} \end{aligned} \tag{6.2.1}$$

The corresponding LCs can be seen in figure 6.2, together with a Gaussian fit on top of a flat background. Only P2 region was modeled, since its spectrum reaches higher energies than for P1, and it is for the highest energies where we are more sensitive to LIV delays. The background level was estimated in from the off phase region and the selection of the number and limits of these energy bins is a critical step: if bins were too narrow, the P2 peak was not visible do to statistical fluctuations; but if they were too wide, the energy difference between them would have been reduced, which would had worsened our sensitivity to any hypothetical LIV effect.

The obtained peak position ϕ_{P2} and width σ_{P2} values for each energy bin

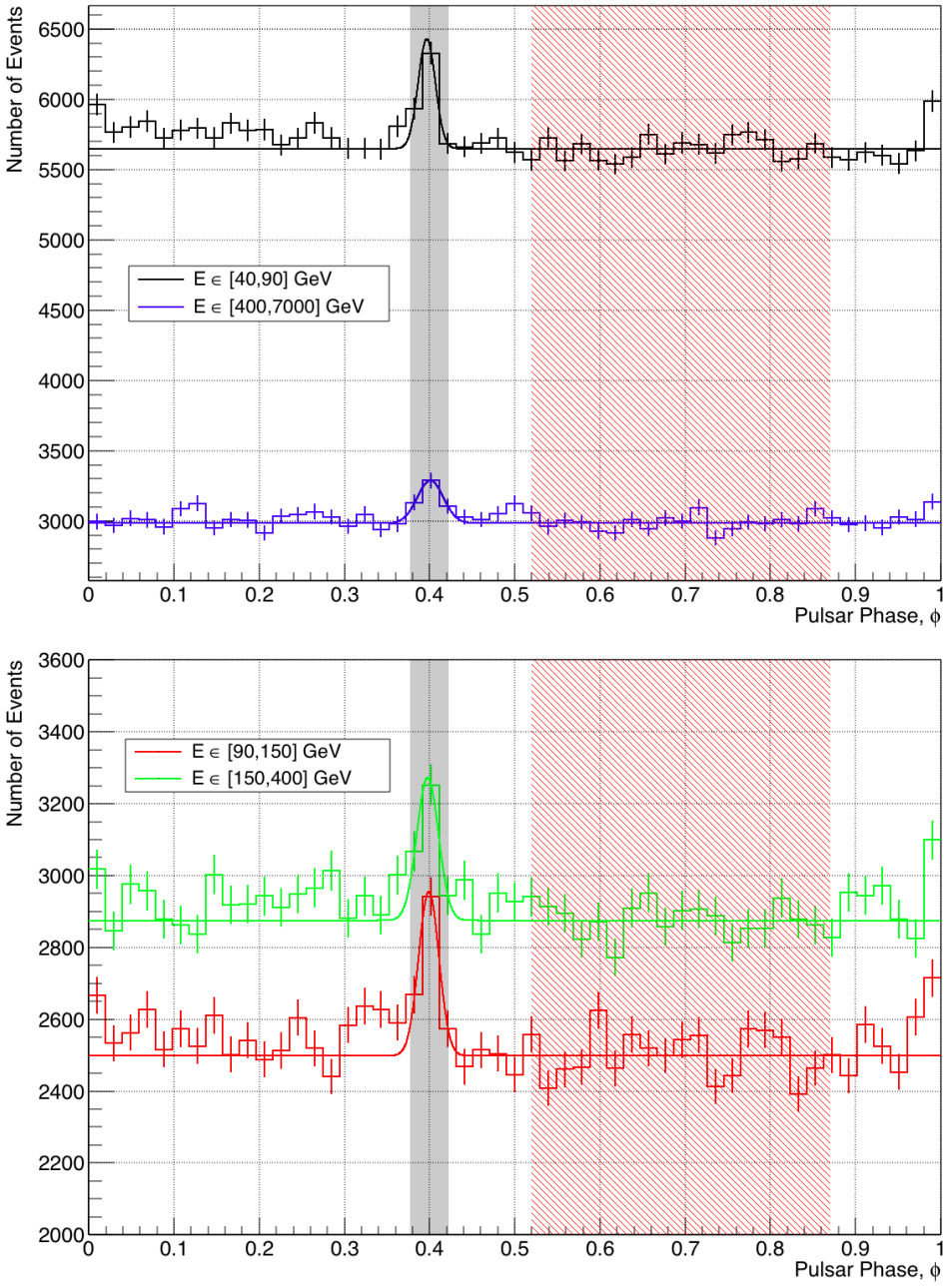

Figure 6.2: Crab pulsar LC obtained with the combined data analysis (mono+stereo) with their corresponding Gaussian fits for the P2 pulse. 51 phase bins are used, as well as the four energy ranges defined in equation 6.2.1: lowest and highest energies on the left plot, intermediate energies on the right plot. The on and off regions, as defined in equation 4.6.1, are highlighted with gray- and red-shaded areas.

were plotted in figure 6.3, left and right plots respectively. To have a complete description of these crucial fit parameters, those points were fitted using the following function:

$$K + B \cdot \log\left(\frac{E}{100\ \text{GeV}}\right) \tag{6.2.2}$$

These fits were done twice: once with a fixed value of $K = 0$, so we obtain a constant fit independent of the energy; and a fit where the K parameter was left free, to obtain a linear function in logarithmic energy units. The obtained values of the fitting parameters can be seen in table 6.2. We can see that the peak position is best fitter with a constant function because the reduced χ^2 value is closer to one in this case. On the contrary, the pulsar width is fitter slightly better with a linearly decreasing function of $\log E$. This is consistent with the known sharpening of the peaks as the energy increases [71].

Energy [GeV]	**Pulsar peak parameter** $\phi_{\mathbf{P2}}$	$\sigma_{\mathbf{P2}}$
$[40, 90]$	0.397 ± 0.003	0.010 ± 0.003
$[90, 150]$	0.399 ± 0.002	0.012 ± 0.002
$[150, 400]$	0.398 ± 0.003	0.013 ± 0.002
$[400, 1700]$	0.403 ± 0.003	0.009 ± 0.003

Table 6.1: Estimated P2 peak position (ϕ_{P2}) and width (σ_{P2}) for the 4 energy ranges defined in equation 6.2.1. These values are plotted in figure 6.3.

One must also take into account that, as explained in §4.9, the events contained in these LCs are the output of one of the multiple, independent analysis of the mono and stereo datasets performed within the MAGIC pulsar working group. The included mono events were not obtained from the analysis described in chapter 4 of this thesis, but from an independent mono analysis that followed different approaches, especially for the lowest energies: no hadronness cut was applied below 400 GeV. In order to simplify the modeling, we decided to build the LCs shown in figure 6.2 using *only* the stereo data sample for the LE range (below 400 GeV) and both mono and stereo datasets for energies above that threshold.

Moreover, the fitting of the phaseogram for the highest energies is shown only for illustrative purposes, since it was not derived in the same way as for the

lower energy bins. Instead, the pulsar LC at the highest energies was carefully studied by other members of the Crab pulsar analysis team and a more sophisticated fit was applied, based on the maximization of the statistical likelihood. In this way, a more precise measurement of the position and width of the pulsar peak was achieved for the emission discovered in this energy band, in comparison the simple gaussian fit that we shown figure 6.2. We will make use of those results but we will not extend on the details, which will be reported elsewhere.

In order to apply this first method to limit LIV energy scales, one needs to estimate the peak position in two energy ranges with the highest precision available. For such comparison, we used the lowest and highest energy bins listed in equation 6.2.1, i.e. below 90 GeV and above 400 GeV. Under the assumption that emission at LE and HE occurs simultaneously at the source, one can compute the LIV energy scale that would produce the observed difference in the position of those peaks in the phaseogram. As shown in table 6.1, the measured P2 peak positions at the highest and lowest energy bins are:

$$\begin{aligned} E \in [40, 90] \text{ GeV} &\Rightarrow \phi_{\mathrm{P2}} = 0.397 \pm 0.003 \text{ }_{\text{stat.}} \\ E \in [400, 1700] \text{ GeV} &\Rightarrow \phi_{\mathrm{P2}} = 0.403 \pm 0.003 \text{ }_{\text{stat.}} \end{aligned} \tag{6.2.3}$$

Notice that only statistical errors are reported here, because any systematical source of error would affect the peak position estimation for both energy bins in the same way. Since we are only interested in the difference between these two peak positions, $\Delta\phi_{\mathrm{P2}}$, the systematic contribution to the error cancels out and we are left only with its statistical uncertainty. The difference in the P2 peak position obtained in this way is then:

$$\Delta\phi_{\mathrm{P2}} = \phi_{\mathrm{P2}}(E > 400\text{GeV}) - \phi_{\mathrm{P2}}(E < 90\text{GeV}) = 0.006 \pm 0.004_{\mathrm{stat}} \tag{6.2.4}$$

This represents a small delay between HE and LE photons but only at a 1.5σ level. Let us now use this measurement to limit the scale of LIV for an energy dependence of order n, $E_{\mathrm{QG}n}$. We will analyze each of the physical scenarios independently, namely the subluminal case ($\xi_n = 1$) and the superluminal case ($\xi_n = -1$).

If one wants to limit the maximum phase delay produced by LIV at the

standard 95% C.L., one needs to look for the one-sided limit where 95% of the area of a Gaussian distribution is contained [127]. This condition is fulfilled at 1.645σ from the mean value, where σ is the width of the Gaussian. Therefore, 95% C.L. limits on the phase delay due to LIV are:

$$\begin{aligned} \Delta\phi_{\mathrm{P2}} &< 0.006 + 1.645 \cdot 0.004 = 0.013 \text{ for } \xi_n = 1 \\ \Delta\phi_{\mathrm{P2}} &> 0.006 - 1.645 \cdot 0.004 = -0.001 \text{ for } \xi_n = -1 \end{aligned} \tag{6.2.5}$$

If isolate the LIV energy scale from equations 6.1.1 we obtain

$$E_{\mathrm{QG}n} > \left(\xi_n \frac{n+1}{2} \, \frac{d_P}{c\,P} \, \frac{E^n}{\Delta\phi_{\mathrm{P2}}} \right)^{\frac{1}{n}} \tag{6.2.6}$$

One wants to compare the phase shift between two energies, E_{max} and E_{min}. As done in equations 5.4.10 and 5.4.11, for the two selected energy ranges we have that $E_{\mathsf{max}} \geq 400$ GeV and $E_{\mathsf{min}} \geq 40$ GeV. Combining these last two expressions with the obtained limits for the phase shift (equation 6.2.5) for $n = 1$ and $n = 2$, we finally get the LIV limits from direct comparison for the linear:

$$\begin{aligned} E_{\mathrm{QG1}} &> 1.8 \cdot 10^{17} \text{ GeV} \quad \text{(subluminal case)} \\ E_{\mathrm{QG1}} &> 2.4 \cdot 10^{18} \text{ GeV} \quad \text{(superluminal case)} \end{aligned} \tag{6.2.7}$$

whereas for the quadratic case these limits are:

$$\begin{aligned} E_{\mathrm{QG2}} &> 1.1 \cdot 10^{10} \text{ GeV} \quad \text{(subluminal case)} \\ E_{\mathrm{QG2}} &> 3.8 \cdot 10^{10} \text{ GeV} \quad \text{(superluminal case)} \end{aligned} \tag{6.2.8}$$

6.3 Maximization of the likelihood

The second method we applied to look for LIV-induced correlations between energy and arrival time of the Crab pulsar photons is the **maximum likelihood method** (from now on, ML). This technique is based based on the construction and maximization of the statistical likelihood of our set of observed photons to be described by a certain emission model at the source, together with the

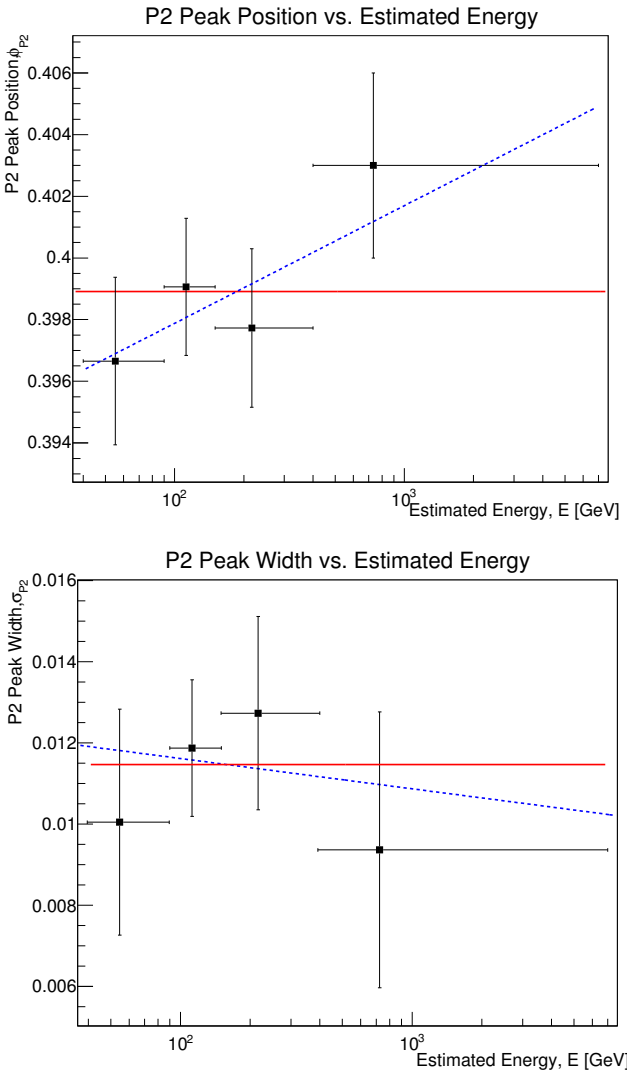

Figure 6.3: Estimated values of ϕ_{P2} (P2 peak position, *left*) and σ_{P2} (width, *right*). They were obtained from the used Gaussian fits in the first 3 energy ranges. The last point in both plots was estimated using a more complex analysis which is not described here. Two fits are shown: a constant fit (*red, solid line*) and a linear one in $\log E$ (*blue, dotted line*). The values of the fitting parameter can be found in table 6.2.

effects if a chosen LIV scenario. An *a priori* assumption is therefore needed regarding the parameterization of the emission, which makes this method model-dependent. Its main advantage with respect to other methods is that it uses the complete list of measurements of each individual event, rather than binned phase or energy distributions. In the later case, we build histograms where photons are grouped according to the selected binning, so some information is lost in the process. However, in the ML method all the available information is used.

The ML method has been used in particle physics experiments for many decades. It is not so common within the astroparticle community but it has

Parameters	**Constant Fit**		**Linear Fit in $\log$E**	
[Phase units]	**Position $\phi_{\mathbf{P2}}$**	**Width $\sigma_{\mathbf{P2}}$**	**Position $\phi_{\mathbf{P2}}$**	**Width $\sigma_{\mathbf{P2}}$**
K	0.399 ± 0.001	0.012 ± 0.001	0.398 ± 0.002	0.012 ± 0.001
$B/10^{-3}$	0	0	3.8 ± 4.3	-0.7 ± 3.0
χ^2/NDF	$\frac{2.7638}{3}$	$\frac{0.9843}{3}$	$\frac{0.5217}{2}$	$\frac{0.9479}{2}$

Table 6.2: Values of the fitting parameters for the interpulse position and width, shown in figure 6.3. They were fitted with the function defined in equation 6.2.2, where the K parameter is fixed to zero for the constant fits and is left as a free parameter to fit the points linearly with $\log E$.

also been successfully applied to extract LIV limits from astrophysical sources in the past. For instance, the MAGIC collaboration used it, among other methods, to find a hint of energy-dependent delays in the arrival times of the photons of the AGN Markarian 501 [128], during the flare recorded in 2006 by the MAGIC collaboration [129]. This hint of delay between high and low energy photons had a statistical significance of 2.5σ, so a discovery could not be claimed, but competitive LIV limits could be derived.

A year later, Martinez and Errando applied the same method to a flare of the AGN PKS2155-304, observed by the H.E.S.S. collaboration in 2007 [119]. They could set the most constraining limit at the time for the quadratic LIV energy scale [126]. It has also been used recently to extract LIV limits from a set of GRB observed by the Fermi-LAT telescope [123]. The ML method is statistically robust and scientifically powerful so we decided to apply it to a periodic signal for the first time.

6.3.1 Description of the method

The goal of the ML method is to find the estimator of the LIV parameter, $\widehat{\lambda}_n$, such that the likelihood function $\mathcal{L}(\widehat{\lambda}_n)$ is maximized:

$$\mathcal{L}(\widehat{\lambda}_n) = \max \mathcal{L}(\lambda_n) \tag{6.3.1}$$

But first, one needs to compute the likelihood of the complete data set of N events for a given value of the LIV parameter, λ_n. This data set is composed of a list of estimated energies and phases for all the events that survived the

analysis process: $\{E'_i\,,\,\phi'_i\}_{i<N}$ ([3]).

If one considers the estimated phase and energy as statistically independent variables, one can build the likelihood function as the product of the individual probability density functions (hereafter, PDF) for each event in our dataset, $f_k(E'_i, \phi'_i|\lambda_n)$:

$$\mathcal{L}(E_{\mathrm{QG}n}) = \prod_{k}^{N_{\mathsf{samples}}} \prod_{i}^{N_k} f_k(E'_i, \phi'_i|\lambda_n) \tag{6.3.2}$$

where N_{samples} is the number of data samples with different telescope performance periods, N_k is the number of events in the k-th data sample and the total number of events is $N = \sum_k^{N_{\mathsf{samples}}} N_k$.

From a computational point of view, the variations of $\mathcal{L}(\lambda_n)$ caused by the LIV energy scale $E_{\mathrm{QG}n}$ are relatively small, considering that we have to evaluate and sum the PDF f_k for several hundreds of thousands of events of a background-dominated source. This problem is further increased when we test the weak LIV effects would expect, given that the λ_n parameter space for is considerably limited by previous experimental constraints, described in §5.5. This creates problems with the maximization software, which expects variations of the order of ~ 1. To avoid these kind of problems, equation 6.3.2 had to be modified.

One should keep in mind that our main interest is to compare how the introduction of LIV-induced delay in the modeling of the pulsar LC changes the value of $\mathcal{L}$. Those changes would be easier to see if we compare that situation with a no-LIV situation or null hypothesis, $\mathcal{L}(0)$, where no delay is introduced. Such comparison is efficiently performed if one defines the **likelihood ratio** as:

$$D(\lambda_n) \equiv -2\log\left[\frac{\mathcal{L}(\lambda_n)}{\mathcal{L}(0)}\right] \tag{6.3.3}$$

where $\mathcal{L}(0)$ is the likelihood of our set of events when the null hypothesis if fulfilled, i.e. when LI is not violated[4]. Our original goal, i.e. the maximization of the likelihood $\mathcal{L}(\lambda_n)$, is then transformed into a **minimization of the likelihood**

[3] We will use the prime symbol ($'$) to refer to the estimated values of a certain physical magnitude.

[4] This is equivalent to set the LIV energy scale to infinity, $E_{\mathrm{QG}n} \to \infty$, according to the definition of the LIV parameter in equation 6.1.2.

ratio $D(\lambda_n)$, which is our new test statistics:

$$D(\widehat{\lambda}_n) = \min D(\lambda_n) \equiv \widehat{D} \tag{6.3.4}$$

In the large data sample limit, the probability distribution of the minimum likelihood ratio, $\widehat{D}$, is approximately equivalent to a chi-squared distribution with a number of degrees of freedom (hereafter, NDF) equal to NDF $= d(\lambda_n) - d(0) = 1 - 0 = 1$, where $d(0) = 0$ and $d(\lambda_n) = 1$ are the NDF of the null-hypothesis and the alternative model, respectively [127].

Another major advantage of this new test statistics is that we can easily measure or limit the values of λ_n at any confidence level (hereafter, C.L.). To perform a measurement of the LIV parameter, one must to be able to exclude a no-LIV scenario with some statistical significance. This means that we have to find the positive and negative error intervals and they should not contain the LIV parameter value $\widehat{\lambda}_2 = 0$. This error intervals, $\Delta^{\pm}_{1\sigma}$, $\Delta^{\pm}_{1\sigma}$, $\Delta^{\pm}_{1\sigma}$ ... for 1σ, 2σ, 3σ ... significance levels, respectively, can be derived from the likelihood ratio as [127]:

$$\begin{aligned} D(\widehat{\lambda}_n \pm \Delta^{\pm}_{1\sigma}) &= \widehat{D} + 1 \text{ , where } \widehat{\lambda}_n \pm \Delta^{\pm}_{1\sigma} \gtrless 0 \\ D(\widehat{\lambda}_n \pm \Delta^{\pm}_{2\sigma}) &= \widehat{D} + 4 \text{ , where } \widehat{\lambda}_n \pm \Delta^{\pm}_{2\sigma} \gtrless 0 \\ D(\widehat{\lambda}_n \pm \Delta^{\pm}_{3\sigma}) &= \widehat{D} + 9 \text{ , where } \widehat{\lambda}_n \pm \Delta^{\pm}_{3\sigma} \gtrless 0 \end{aligned} \tag{6.3.5}$$

However, as explained at the beginning of the present chapter, our goal is not to measure but to limit the LIV energy scale. Therefore, we will not use the significance intervals for measurements defined above. Instead, once the minimum likelihood ratio $\widehat{D}$ has been found at $\widehat{\lambda}_n$, we will look for the intervals $\Delta^{\pm}_{90}$, $\Delta^{\pm}_{90}$, $\Delta^{\pm}_{90}$ ... around the minimum such that the likelihood ratio is increased by the following amounts:

$$\begin{aligned} D(\widehat{\lambda}_n \pm \Delta^{\pm}_{90}) &\approx \widehat{D} + 1.643 \text{ , where } \widehat{\lambda}_n \pm \Delta^{\pm}_{90} \gtrless 0 \\ D(\widehat{\lambda}_n \pm \Delta^{\pm}_{95}) &\approx \widehat{D} + 2.705 \text{ , where } \widehat{\lambda}_n \pm \Delta^{\pm}_{95} \gtrless 0 \\ D(\widehat{\lambda}_n \pm \Delta^{\pm}_{99}) &\approx \widehat{D} + 5.415 \text{ , where } \widehat{\lambda}_n \pm \Delta^{\pm}_{99} \gtrless 0 \end{aligned} \tag{6.3.6}$$

By doing so, we will be able to obtain 90%, 95%, 99% ... C.L. limits on the

LIV parameter, respectively. To make an easy comparison with the limits derived by other experiments, we choose to give LIV limits at a 95% C.L. Thus, if one is able to find a value for Δ^{+}_{95} such that $\widehat{\lambda}_n + \Delta^{+}_{95} > 0$, then a limit on the LIV parameter can be set at a 95% C.L. for the subluminal case; similarly, if we can find a value for Δ^{-}_{95} such that $\widehat{\lambda}_n - \Delta^{-}_{95} < 0$, we can then set a 95% C.L. limit for the superluminal case. In general, if any of the conditions in equation 6.3.6 are met, we can then limits the LIV parameter at the corresponding C.L.:

$$\begin{aligned}
&\lambda_n < \widehat{\lambda}_n + \Delta^{+}_{90} \text{ (for } \xi_n = +1) \text{ and } \lambda_n > \widehat{\lambda}_n - \Delta^{-}_{90} \text{ (for } \xi_n = -1) \text{ at 90\% C.L.} \\
&\lambda_n < \widehat{\lambda}_n + \Delta^{+}_{95} \text{ (for } \xi_n = +1) \text{ and } \lambda_n > \widehat{\lambda}_n - \Delta^{-}_{95} \text{ (for } \xi_n = -1) \text{ at 95\% C.L.} \\
&\lambda_n < \widehat{\lambda}_n + \Delta^{+}_{99} \text{ (for } \xi_n = +1) \text{ and } \lambda_n > \widehat{\lambda}_n - \Delta^{-}_{99} \text{ (for } \xi_n = -1) \text{ at 99\% C.L.}
\end{aligned} \tag{6.3.7}$$

Finally, using the definition of the LIV parameter in equation 6.1.2 and taking into account the additional sign for the negative values of the LIV that we added in equation 6.1.5, we can translate these limits into constraints for the LIV energy scale $E_{\mathrm{QG}n}$ at the same confidence level. We will only write the expression for the 95% C.L., which is the standard C.L. reported by most experiments for LIV tests:

$$\begin{aligned}
E_{\mathrm{QG}n} &> \frac{\langle E_{\mathrm{QG}n} \rangle}{\widehat{\lambda}_n + \Delta^{+}_{95}} \text{ (95\% C.L., } \xi_n = +1) \\
E_{\mathrm{QG}n} &> \frac{\langle E_{\mathrm{QG}n} \rangle}{|\widehat{\lambda}_n - \Delta^{-}_{95}|} \text{ (95\% C.L., } \xi_n = -1)
\end{aligned} \tag{6.3.8}$$

For an easy visualization of the above described procedure, two examples of $D(\lambda_2)$ functions are shown in figure 6.4. They represent the outcome of the application of the ML method for two simulated pulsar LCs with a quadratic LIV effect of $\lambda_2 = 20$. We can see that both likelihood ratio functions $D(\lambda_2)$ are approximately parabolic around their minimum value, $\widehat{D}$. We will now illustrate how one would measure or limit the LIV energy scale using these examples.

On one hand, the function $D(\lambda_2)$ depicted in the top plot of figure 6.4 has a minimum value of $\widehat{D} \approx -8.3$ located at $\widehat{\lambda}_2 \approx 22.1 > 0$. Since we can find increases in the LIV parameter such that $D(\widehat{\lambda}_2 + \Delta^{\pm}_{2\sigma}) = \widehat{D} + 4 \approx -4.3$

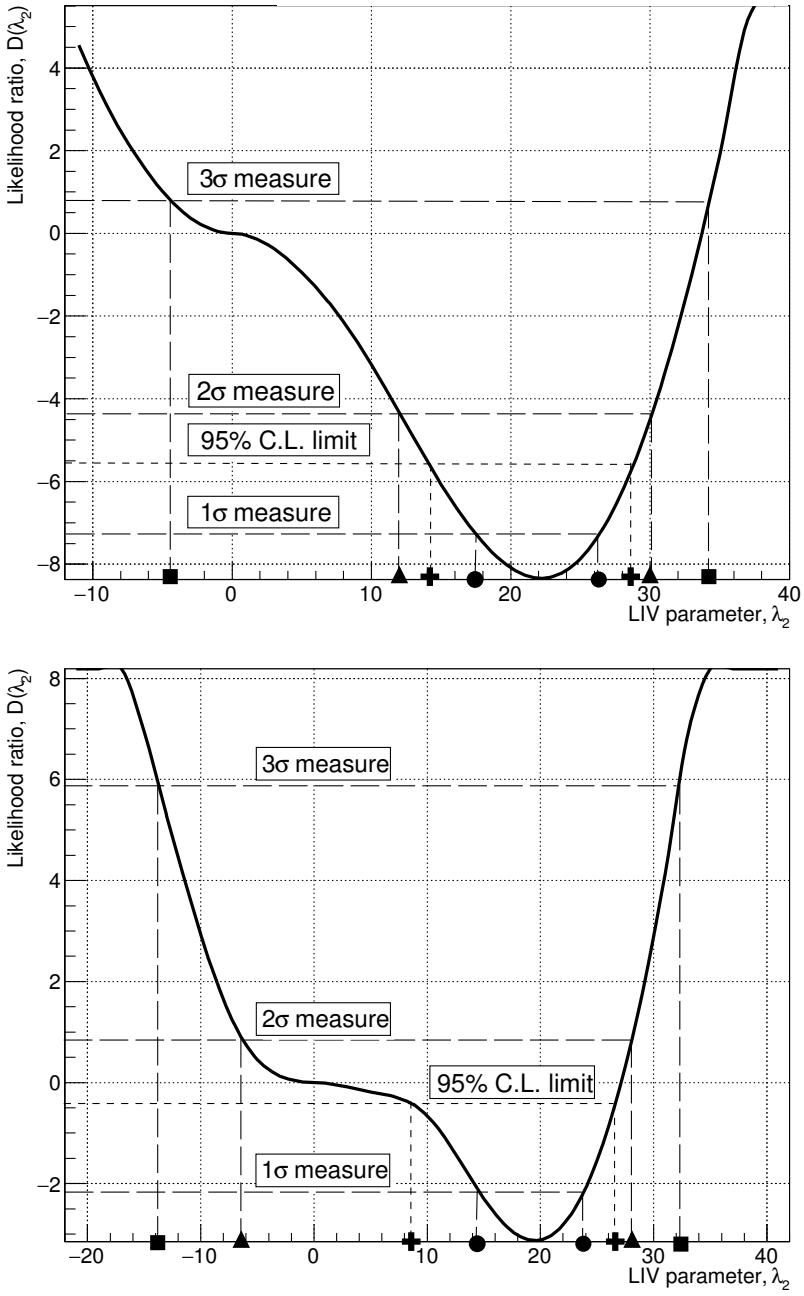

Figure 6.4: Example of two likelihood ratio functions, $D(\lambda_2)$, for a simulated quadratic LIV effect of $\lambda_2 = 20$. The top plot shows a case where a LIV delay can be detected at 1σ and 2σ significance levels but not at 3σ (long-dashed lines). In the example of the bottom plot, no measurement can be achieved beyond a 1σ significance level. The derived 95% C.L. limits are also shown as short-dashed lines and the corresponding crosses on the horizontal axis.

(long-dashed line and associated triangles in the plots), we can say that the ML method is able to exclude a no-LIV scenario with a significance of 2σ. However, we can not exclude it at a 3σ level since the interval $(\widehat{\lambda}_2 - \Delta^-_{3\sigma}, \widehat{\lambda}_2 + \Delta^+_{3\sigma})$, marked withsquares in the horizontal axis, where $D = \widehat{D} + 9 \approx +0.7$ already includes the null LIV parameter: $\widehat{\lambda}_2 + \Delta^-_{3\sigma} \approx -4 < 0$, marked with squares in the horizontal axis.

On the other hand, the bottom plot in figure 6.4 shows a minimum likelihood ratio of $\widehat{D} \approx -2.67$ at $\widehat{\lambda}_2 \approx 16.2$. We would only be able to measure a LIV effect at 1σ level, since the 2σ interval already includes the zero LIV parameter value (left triangle in the plot, $\widehat{\lambda}_2 - \Delta^-_{2\sigma} \approx -11.8 < 0$). But we could set a 95% C.L. to the LIV energy scale if we find the place where $D = \widehat{D} + 2.705 = 0.04$, which occurs at $\lambda_2 = \widehat{\lambda}_2 + \Delta^+_{95} \approx 26.1 > 0$ (marked with crosses on the horizontal axis). Thus, we can say that the LIV parameter is below $\lambda_2 < 26.1$ with a 95% probability, which corresponds to a 95% C.L. limit in the LIV energy scale of $E_{\mathrm{QG2}} > \langle E_{\mathrm{QG2}} \rangle / 26.1 \approx 3.8 \cdot 10^{10}$ GeV for the subluminal case. At the same time, the function also takes the value $D = 0.04$ for $\lambda_2 = \widehat{\lambda}_2 - \Delta^-_{95} \approx -4.1 < 0$. Thus, for the superluminal case we can also assure that the LIV parameter is above $\lambda_2 > -4.1$ with 95% probability, which corresponds to a limit $E_{\mathrm{QG2}} > \langle E_{\mathrm{QG2}} \rangle / |-4.1| \approx 8.5 \cdot 10^{11}$ GeV.

Due to the construction of the likelihood ratio, the function $D(\lambda_n)$ will always cross the coordinates origin:

$$D(0) = \log\left[\frac{\mathcal{L}(0)}{\mathcal{L}(0)}\right] = \log(1) = 0 \tag{6.3.9}$$

Thus, the value of the likelihood ratio at the minimum, $\widehat{D}$, already tells us what is the maximum statistical significance that one could assign to a measurement of the LIV parameter: if $\widehat{D} < -1$, the value $\lambda_n = 0$ can be excluded at 1σ significance level, at least; if $\widehat{D} < -4$, the exclusion of the non-LIV scenario is more constraining, at a 2σ significance level or more; and if $\widehat{D} < -9$, the significance of our measurement would be of 3σ or higher.

The value of $\widehat{D}$ can also tell us something about the best LIV parameter limit we are able to set: if $\widehat{D} > -2.71$, we will be able to set 95% C.L. limits on the LIV energy scale for both the subluminal and superluminal QG scenarios. Otherwise, if $\widehat{D} < -2.71$ is found for $\widehat{\lambda}_n > 0$, we will only be able to set 95% C.L. limit for the subluminal case ($\xi_n = +1$). But, since an

increase of the likelihood function of 2.71 would not occur for $\lambda_n < 0$, we will have to look for a higher increase on the likelihood ratio, such as those needed for 99% C.L. limits, namely $D = \widehat{D} + 5.429$. Thus, stronger limits to the superluminal scenario ($\xi_n = -1$) can be set in this situation. Similarly, if a minimum $\widehat{D} < -2.71$ is found at $\widehat{\lambda}_n < 0$, we would still be able to limit the superluminal case at 95% C.L. but stronger constraints could be provided for the subluminal sceneario.

6.3.2 Building the pulsar PDF

The most critical point of the ML method probably is the construction of the PDF, because it requires some assumptions to be made regarding the source emission model. In general, given an event with estimated energy E' and estimated phase ϕ', recorded in the k-th performance period, its PDF can only be proportional to two contributions: its probability of to be either a P2 pulsar event or a background event. Both probabilities must be computed per unit phase and per unit energy. We are not interested in the contribution of the main peak (P1) because P2 becomes dominant at high energies, that is where any LIV would be stronger. Therefore, we only include the interpulse in our modeling of the pulsar LC and the PDF reads:

$$f_k(E', \phi') \propto \frac{\mathrm{d}N_{\mathrm{off},k}}{\mathrm{d}E'\,\mathrm{d}\phi'} + \frac{\mathrm{d}N_{\mathrm{P2},k}}{\mathrm{d}E'\,\mathrm{d}\phi'} \tag{6.3.10}$$

These two terms must be somehow estimated from the observations. Since the background is flat in ϕ, the first term can be simply obtained by counting the number of events in the off region (defined in 4.6.1) for the k-th performance period, $N_{\mathrm{off},k}$, for a set of reconstructed energy bins and dividing this number by the energy bin width $\Delta E'$ and off region width $\Delta\phi_{\mathrm{off}}$:

$$\frac{\mathrm{d}N_{\mathrm{off},k}}{\mathrm{d}E'\,\mathrm{d}\phi'} = \frac{N_{\mathrm{off},k}}{\Delta E' \Delta\phi_{\mathrm{off}}} = B_k(E') \tag{6.3.11}$$

In this way we have defined the **background spectral distribution**, $B_k(E')$, a smooth function that goes through the points where $\frac{\mathrm{d}N_{\mathrm{off},k}}{\mathrm{d}E'\,\mathrm{d}\phi'}$ is measured and which will be interpolated for intermediate values by means of a spline function. The obtained functions are shown in figure 6.5.

The second term in equation 6.3.10, the P2 pulsar contribution, can be

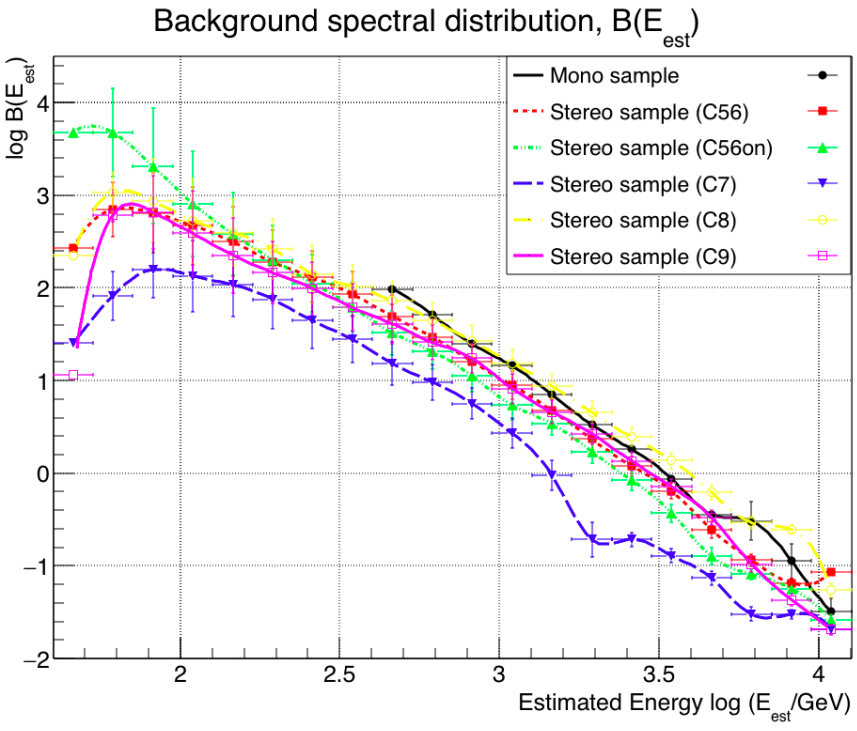

Figure 6.5: Background spectral distributions, $B_k(E')$, estimated from the complete Crab pulsar analysis for each of the data subsamples.

computed in a similar way: we divide the number of events for the k-th performance period in the on region of the phaseogram $N_{\mathrm{on},k}$ by the energy bin width $\Delta E'$ and the on region width $\Delta\phi_{\mathrm{on}}$ and then we subtract the background contribution that was computed before:

$$\frac{\mathrm{d}N_{\mathrm{P2},k}}{\mathrm{d}E'\,\mathrm{d}\phi} = \frac{N_{\mathrm{on}}}{\Delta E'\Delta\phi_{\mathrm{on}}} - \frac{N_{\mathrm{off}}}{\Delta E'\Delta\phi_{\mathrm{off}}} \tag{6.3.12}$$

However, we not use this equation because we must account for the effect of LIV on the likelihood. An alternative way to compuete the pulsar contribution is needed. Note that we will only introduce a LIV-induced delay in our equations for the term that accounts for pulsar photons. Since background photons evenly distributed with respect to the pulsar phase, a LIV delay would just scramble them but no visible change in the pulsar LC would be produced.

Another comment is in order, regarding the distinction between the true and the estimated values of phase and energy of each event. A hypothetic LIV will introduce a delay between high and low energy photons in their *true phase*, which will be proportional to their *true energy*. We will later measure a value of the *estimated phase* and *estimated energies* that may differ from the original values due to the limited time and energy resolution of our instrument. When

we implement such LIV-induced delays, we have to take into account this difference: we only know the value of the estimated energy of an event, E', so we have to consider the LIV delay for all the possible true energies E that could be measured by our telescope as E', and weight each of those values according to the probability of such measurement, i.e. the energy resolution. The same reasoning can be applied to the events phases.

It then follows that, for an event recorded during the k-th performance period with an estimated energy E' and an estimated phase ϕ', we can compute the pulsar contribution to the PDF in the following way:

$$\begin{aligned}\frac{\mathrm{d}^2 N_{\mathrm{P2}}}{\mathrm{d}E'\,\mathrm{d}\phi'} &= \iiint \mathrm{d}t\,\mathrm{d}E\,\mathrm{d}\phi\ \frac{\mathrm{d}^3 N_{\mathrm{P2}}}{\mathrm{d}E(t)\,\mathrm{d}t\,\mathrm{d}A_{\mathrm{eff}}(t)}\frac{\mathrm{d}E}{\mathrm{d}E'}\frac{\mathrm{d}A}{\mathrm{d}E}\frac{\mathrm{d}\phi}{\mathrm{d}\phi'}\frac{\mathrm{d}P}{\mathrm{d}\phi} \\ &= \Delta t_k \int_0^\infty \mathrm{d}E\ \Gamma_{\mathrm{P2}}(E) G_k(E|E') A_{\mathrm{eff},k}(E) \int_0^1 \mathrm{d}\phi\ J_k(\phi|\phi') F_{\mathrm{P2}}(\phi)\end{aligned} \tag{6.3.13}$$

where each term is:

- Δt_k is the **effective observation time** for the k-th performance period.
- $A_{\mathrm{eff},k}(E) = \frac{\mathrm{d}A_k}{\mathrm{d}E}$ is the telescope **effective collection area** after all cuts, derived from MC. This quantity is computed in bins of true energy and a spline is interpolated for intermediate values. A function containing the logarithm of the effective area vs the logarithm of the true energy is created for each performance period, which are shown in figure 6.10.
- $G_k(E|E') = \frac{\mathrm{d}E}{\mathrm{d}E'} = \mathrm{Gaus}(\mu_k(E'), \sigma_k(E'))$ stands for the **energy resolution** of our instrument for a given estimated energy E', during the k-th telescope-performance period. It is built in a two-step computation: first, normalized Gaussian functions are fitted to each slice of the detector migration matrix (see figure 4.17 for an example). The positions $\mu_k(E')$ and widths $\sigma_k(E')$ of those Gaussians for each estimated energy bin are used to compute the telescope energy bias and resolution, which are shown in figure 4.18. Second, these two distributions are fitted with functions (thick lines in this same figure) so we can evaluate the energy bias and resolution in a continuous fashion and not only for those bins in which μ_k and σ_k are measured.

- $J_k(\phi|\phi') = \frac{\mathrm{d}\phi}{\mathrm{d}\phi'} = \mathrm{Gaus}(\phi', \sigma_{\mathrm{eph}})$ is the **phase resolution** of our detector given an estimated phase ϕ'. As estimated in §4.6, we are dominated by the uncertainty in the pulsar ephemerides, which is $\sigma_{\mathrm{eph}} \approx 0.00012$ in phase units. We model it this resolution as a Gaussian function of ϕ centered at ϕ' and whose width is σ_{eph}.

- $\Gamma_{\mathrm{P2}}(E) = \frac{\mathrm{d}^3 N_{\mathrm{P2}}}{\mathrm{d}E\,\mathrm{d}t\,\mathrm{d}A}$ is the **pulsar differential energy spectrum for P2**, modeled by a single power-law with a spectral index -3.1, as reported in §4.9. Since no hint of a cut-off was detected, we assume an extension of this power-law up to 7 TeV and no pulsar emission beyond that energy. We also assume no spectral variability along the extension of the observations.

- $F_{\mathrm{P2}}(\phi) = \frac{\mathrm{d}P}{\mathrm{d}\phi} = \mathrm{Gaus}(\phi_{\mathrm{P2}}, \sigma_{\mathrm{P2}})$ is the **normalized Gaussian model for the Crab pulsar phaseogram**. It is estimated from the LC fit for the lowest energy bin shown in figure 6.2 since any LIV effect there would be negligible in comparison with those at the highest energy bin. Thus, the values of the Gaussian position and width are $\phi_{\mathrm{P2}} \approx 0.397$ and $\sigma_{\mathrm{P2}} \approx 0.010$, respectively (see table 6.1).

In a similar way, we could also include the angular resolution as part of the telescope response. However, the angular resolution of the MAGIC telescopes is larger than the angular size of the Crab nebula, so we are not able to resolve it and the source is perceived as point-like. This additional term is hence not required.

Notice that several Gaussian functions are involved in this computation. Since we are integrating two gaussians with respect to the phase ϕ, namely $J_k(\phi|\phi')$ and $F_{\mathrm{P2}}(\phi)$, the result of this convolution is well-known: another gaussian will be obtained with a width equal to $\sigma = \sqrt{\sigma_{\mathrm{P2}}^2 + \sigma_{\mathrm{eph}}^2} \approx \sigma_{\mathrm{P2}}$, where the previous approximation could be done because $\sigma_{\mathrm{P2}} \approx 0.01 \gg \sigma_{\mathrm{eph}} \approx 0.00012$. This means that our phase resolution is much better than the peak we are trying to resolve. We will end up with only one Gaussian with a peak of the same width as P2, σ_{P2}, so we can safely assume that our true and estimated phases are virtually the same, $\phi' \approx \phi$. We will no longer make any distinction between estimated and true phases and the $'$ symbol will be dropped hereafter. In practical terms, the integral with respect to the phase ϕ in equation 6.3.13 can be eliminated together with the phase resolution term J_k.

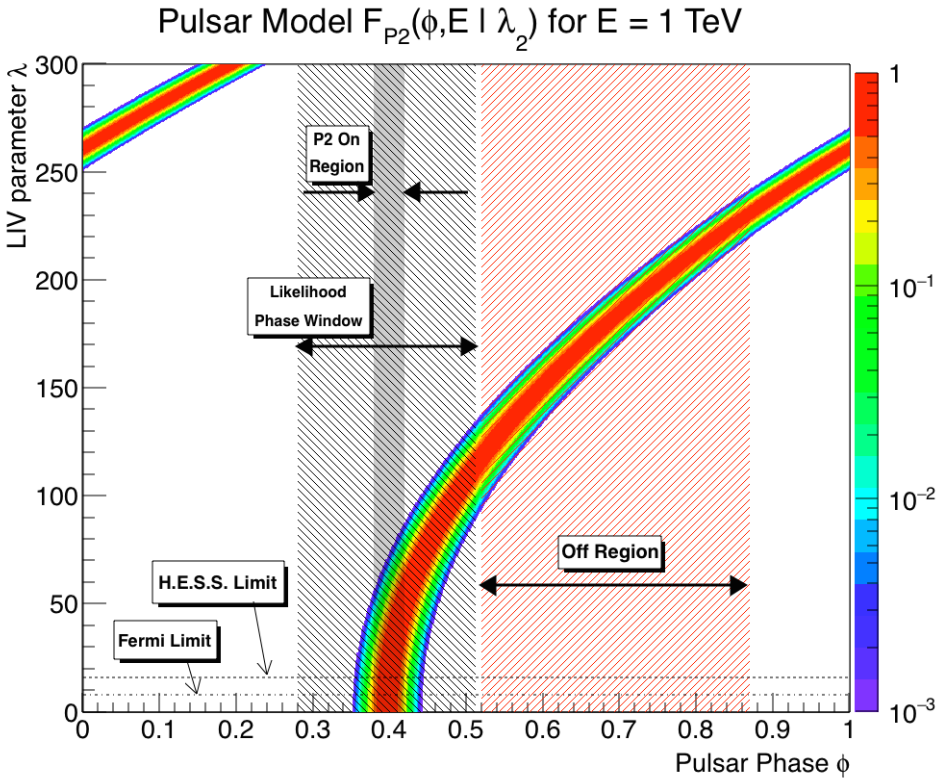

Figure 6.6: Pulsar LC model as a function of the event phase ϕ and the quadratic LIV parameter λ_2 for 1 TeV pulsar photons. The on and off regions of the phaseogram are highlighted using solid, grey area and red, diagonal lines from bottom-left to top-right, respectively. An arbitrary phase window around the interpulse position is shown as an example using black, diagonal lined region, top-left to bottom-right. The best and second best quadratic LIV limits at 95% C.L. are marked using slash-dotted and dotted lines, respectively.

After these considerations, equation 6.3.13 now becomes:

$$\frac{dN_{\rm P2}}{dE' d\phi} = \Delta t_k \int_0^\infty {\rm d}E \; R_k(E|E') \Gamma_{\rm P2}(E) F_{\rm P2}(\phi) \tag{6.3.14}$$

where we have defined the **response function** of the telescope for an event with estimated energy E' recorded in the k-th performance period, $R_k(E|E')$ as the product of the two instrumental terms, i.e. the effective area and the energy resolution, so $R_k(E|E') \equiv A_{{\rm eff},k}(E) \cdot G_k(E|E')$.

Note that the P2 peak model $F_{\rm P2}(\phi)$ is a function of the pulsar phase and does not depend on the energy of the γ-ray at this stage. We introduce the effect of the LIV within this term, as described in §6.1, which adds a dependency on the photon true energy E: the pulsar peak will be shifted accordingly to the delay $\Delta\phi_n(E|\lambda_n)$, calculated with equation 6.1.3 for a given a value for the LIV parameter λ_n:

$$\phi_{\rm P2} \longrightarrow \phi_{\rm P2} + \Delta\phi_n(E|\lambda_n) \tag{6.3.15}$$

And the modeling function for the pulsar phaseogram $F_{\rm P2}$ for a certain energy E will now be centered on this new P2 peak position:

$$F_{\rm P2}(\phi) \longrightarrow F_{\rm P2}(\phi, E|\lambda_n) = \frac{1}{\sqrt{2\pi}\sigma_{\rm P2}} \exp\left[-\frac{1}{2}\left(\frac{\phi - \phi_{\rm P2} - \Delta\phi_n(E|\lambda_n)}{\sigma_{\rm P2}}\right)^2\right] \tag{6.3.16}$$

Here, the energy dependence has been made explicit and this new function is plotted in figure 6.6 for a 1 TeV photon within a wide range of LIV parameters.

Finally, the PDF for the Crab emission reads

$$f_k(E', \phi|\lambda_n) = C_k \cdot \left[B_k(E') + \Delta t_k \int_0^\infty {\rm d}E \; R_k(E|E') \Gamma_{\rm P2}(E) \; F_{\rm P2}(\phi, E|\lambda_n)\right] \tag{6.3.17}$$

where we have included a normalization constant C_k, which is an important parameter for the ML method and is different for each subsample. Besides, it has to be computed in such a way that the integral of f_k in the range of allowed values of E' and ϕ is always equal to 1, no matter the value of the LIV

parameter λ_n. If it is not properly calculated, we can not interpret the values of the function $D(\lambda_n)$ in the same probabilistic terms of a likelihood function. Since the value of the free parameter in the PDF, λ_n, only determines the position of the gaussian pulsar peak in the phaseogram, it does not change the actual value of this integral. This claim was tested using some toy MC, which is described in §6.3.3. The constant C_k was computed for several simulated LIV parameters and the same value was always obtained. For the sake of simplicity, the computation of C_k was hereafter done assuming $\lambda_n = 0$, i.e. no LIV delay.

On top of this, it is important to remember that the starting point of our method is the list of events $\{E'_i\,,\,\phi_i\}_{i<N}$, used for the computation of the likelihood ratio. However, it may be useful to discard some of the events in that list if we know they will not provide us with useful information regarding LIV-induced delays, or at least with *not enough* information to be worth the time it takes to process them with the ML method.

Since any LIV effect will be affecting much more intensely HE photons than LE photons, we will do a first selection of events based on their estimated energy: only events above the threshold $E' \geq 400$ GeV will be considered in the computation of $D(\lambda_n)$. This simple criteria reduces the effective number of events by more than a factor 4, from almost $7.3 \cdot 10^5$ events down to less than $1.6 \cdot 10^5$ events, and reducing our limited computation time proportionally.

We also applied an upper energy cut. The reason for such a cut is that, event if events with the highest energies are most sensitive to any LIV phenomenology, above a certain energy finding a pulsar event becomes more and more unlikely. Eventually, we will be left only with background event, which can not tell us much about LIV delays. Besides, even if a high energy cut discards a much smaller fraction of events, those events are those producing the most extreme phase delays, which could produce some problems with the minimization algorithm.

First, we had to find out what was the maximum energy of the pulsar events that may be contained on the data, even when above 1.7 TeV they are not numerous enough to produce a detectable signal but may be relevant for our LIV studies. The following procedure was applied: toy MCs with no background events were produced, with 544 events above 400 GeV, as detected in the real dataset. Then, the energy distribution of those events was investigated and the event with the maximum energy was found. After 10 trials, the mean of those

maximum energies was found to be about 7 TeV. If we assume that the pulsar power-law emission shows no spectral cut-off up to 7 TeV, we can say that no pulsed events with an energy higher than 7 TeV can be contained in our dataset.

Since the pulsar was detected up to energies of approximately 2 TeV, events above 7 TeV could only be background events and so, they would give us no clue about the existence of any LIV effect and that is the reason why we decided to discard them. Even if we recorded one pulsar event with an energy above 7 TeV, this cut should not hamper the sensitivity of the ML method, since this event would be undistinguishable from the background.

On the other hand, the spectrum of the interpulse P2 is harder than the spectrum of the main pulse P1, which implies that P2 will contain a greater number of VHE events. Thus, we decided to apply the ML method only to events which can be associated to the P2 regions, i.e. those events found inside a certain **phase window** around the P2 position. This window is useful to discard both events from P1 as well as background events. An example of such window can be seen in figure 6.6, represented by the region filled with diagonal black lines.

The width of this phase window is a parameter we have to decide *a priori* so we don't introduce an undesired bias in the derived LIV limits. Several widths were tested using MC simulations, chosen applying with the following criteria: the perfect phase window should include all pulsar events for any LIV-induced delay we want to test while, at the same time, minimize the amount of background included in the likelihood ratio computation. Thus, windows were centered in the position of P2 and extended symmetrically to $\pm 3\sigma_{\mathrm{P2}}$, so 99.7% of the pulsar events were included.

To take into account translation of the events due to LIV, we estimated the maximum expected shift delay for realsitic values of the involved parameters: for 4 TeV P2 photons (a safe assumption given that the pulsar is not detected above 2 TeV energies), four values of λ_2 were used to define these windows. First, we took as reference value the second best quadratic limit so far, equivalent to $\lambda_2 \approx 16$ and the corresponding phase shift is estimated to be $\Delta\phi_2 = 0,0894661$. The window was extended in that amount from both sides symmetricaly, so we can apply the same window for both the subluminal (were events are delayed) and superluminal cases (were events are advanced). The resulting phase window was then $\phi \in [0.2708, 0.5230]$, which was named phase window A.

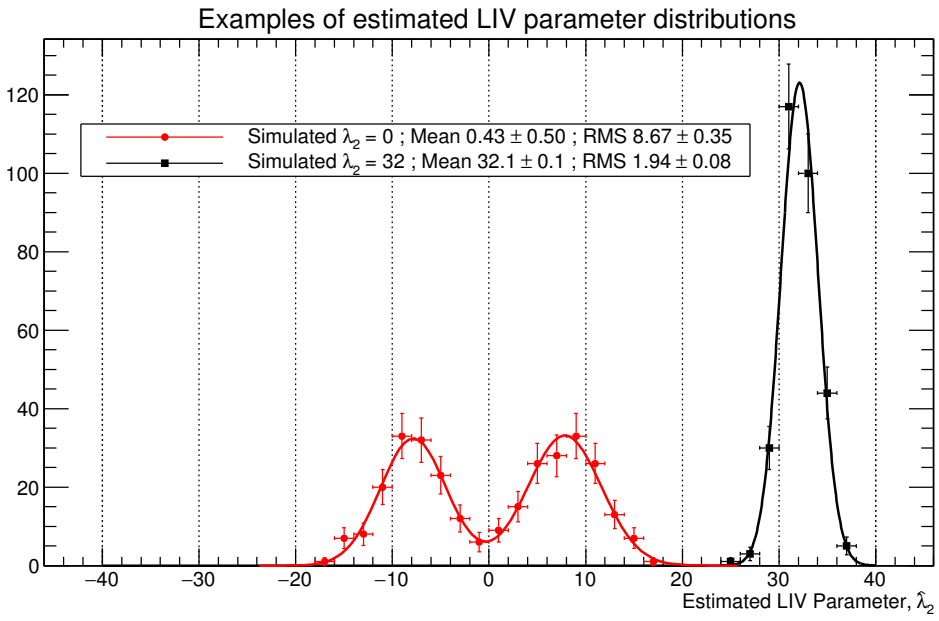

Figure 6.7: Distribution of the estimated LIV parameters $\widehat{\lambda}_2$, i.e. the position where the minimum likelihood ratio $\widehat{D}$ was found. 300 pulsar LCs with a N2S $= 3$ were simulated to produce each one of these two curves, each of them simulating a quadratic LIV parameter of $\lambda_2 = 20$ (*black squares*) and $\lambda_2 = 0$ (*red circles*). Single- and double-Gaussian fits are shown for each distribution, respectively, only for the sake of easier visualization of the shape of these distributions.

The same procedure was also applied using the best quadratic limit by Fermi, set at $\lambda_2 \approx 10$, which would produce a delay of $\Delta\phi \approx 0,01418$ to 4 TeV photons. In this way a narrow phase window (named as C) was defined. Two more LIV parameter values were used: $\lambda = 25$ and $\lambda = 3$. They correspond to a LIV effect stronger than the H.E.S.S. limit (phase window A) and a LIV weaker than the Fermi limit (phase window D), respectively. The four phase windows under test, ordered from looser to tighter, were then:

$$\begin{aligned} &\text{Window A: } \phi \in [0.2708, 0.5230] \\ &\text{Window B: } \phi \in [0.3247, 0.4691] \\ &\text{Window C: } \phi \in [0.3461, 0.4477] \\ &\text{Window D: } \phi \in [0.3589, 0.4349] \end{aligned} \tag{6.3.18}$$

Two tests involving MC simulations were performed to decide which of these windows was optimal to use derive competitive LIV limits. For both of them, 300 simulated pulsar LCs were created, which reproduced the features of real pulsar data, with the exception of the background: in order to reduce the amount of CPU-time required for this test, these simulations were produced with fraction

of the background events, which was parametrized with the so-called **noise-to-signal ratio** or **N2S**, i.e. the number of background events divided by the number of pulsar events in the whole data sample. A value of N2S $= 3$ was used in most tests involving toy MCs, which was approximately 2% of the amount of background present in real data.

As an example of these MC simulations, two distributions of estimated LIV parameters $\widehat{\lambda}_2$ are shown in figure 6.7, obtained for a set of pulsar LCs that were simulated using a LIV parameter $\lambda_2 = 20$ and $\lambda_2 = 0$. A detailed description of the production algorithm for these MC simulations will be given in §6.3.3, whereas an exhaustive characterization of the estimated LIV parameter distributions retrieved from the algorithm will be given in §6.3.4.

Let us just say now that the shape of these distributions strongly depends on the simulated value of λ_2, as we can see in the example: for values typically of $\lambda_2 \gtrsim 10$, such as the one represented by black squares in the example, distributions are compact, Gaussian-shaped, and centered at the simulated value of the LIV parameter, which represents a good performance of the ML method. However, for LIV parameter values of $\lambda_2 \lesssim 10$, such as the example represented by red circles in figure 6.7, the obtained distributions of $\widehat{\lambda}_2$ are similar to a double Gaussian peak, which are wide and always centered in estimated LIV parameters of $\sim \pm 7$. This means that the ML method is not able to properly estimate which LIV intensity we simulated. In order to characterize these distributions consistently along this chapter, we will give the mean, Mean$(\widehat{\lambda}_2)$, and RMS, RMS$(\widehat{\lambda}_2)$ of these distributions.

Coming back to the test of the candidate phase windows, the first check we did was to see which of the above defined windows produced the smallest bias for the estimation of LIV parameters. We think the reduction of the amount of background was a legitimate simplification of the simulation because one only expects the resolution of the ML method to change when the amount background is modified, whereas a significant bias change is considered as less likely. The bias and resolution of the ML method was computed from the characterization of the obtained distributions, such as those showed in the example figure 6.7. For each phase window and for each simulated LIV λ_2 from 0 to 30 in steps of 5, 300 MCs were produced and the distributions of $\widehat{\lambda}_2$ were plotted.

Then, the following quantities could be estimates for each of them:

$$\begin{aligned} \text{Bias} &= \frac{\text{Mean}(\widehat{\lambda}_2) - \lambda_2}{|\lambda_2|} \cdot 100 \\ \text{Resolution} &= \frac{\text{RMS}(\widehat{\lambda}_2)}{|\lambda_2|} \cdot 100 \end{aligned} \tag{6.3.19}$$

The results can be seen in figure 6.8. As we can see in the top plot, the ML method has an almost-constant bias between -15% and +15% for simulated LIV parameters above $|\lambda_2| > 10$. For such region of the parameter space, phase window C is slightly favored, since it produces a bias closer to zero than the rest of them. At the same time, the resolution of the ML method is below 20% and very similar for every window, as we can see in the bottom plot of the same figure.

For weaker LIV effects, i.e. $|\lambda_2| \leq 10$, both the bias and the resolution rise fast, which can be interpreted as the inability of the ML method is not able to properly estimate the simulated LIV parameter.

The last test used what we called the *sensitivity* of the ML method, S_{95}. It was computed for each of the above described MC sets in the following way:

$$S_{95} \equiv \text{Mean}(\widehat{\lambda}_2) - \sqrt{2.705} \cdot \text{RMS}(\widehat{\lambda}_2) \tag{6.3.20}$$

where the value $\sqrt{2.705} \approx 1.645$ is the same as used in equation 6.3.6 to derive 95% C.L. limits. Defined in this way, this quantity intuitively represents the ability of the ML method to resolve a simulated LIV properly. For the simulated LIV parameter where $S_{95} \leq 0$, the $\widehat{\lambda}_2$ distribution is already too wide to measure a significant LIV effect, but meaningful 95% C.L. limits can still be derived. The result of this test is shown in figure 6.9: we can see there that this condition is fulfilled also at $\lambda_2 \lesssim 10$, which confirms our previous interpretation of the abnormal behavior of the bias and resolution.

In conclusion, we have seen that our implementation of the ML method is not sensitive to detect quadratic LIV effects weaker than $\lambda_2 \lesssim 10$. Besides, for more intense LIV scenarios, the phase window C produces the smallest bias, whereas the resolution and sensitivity of the method are not significantly

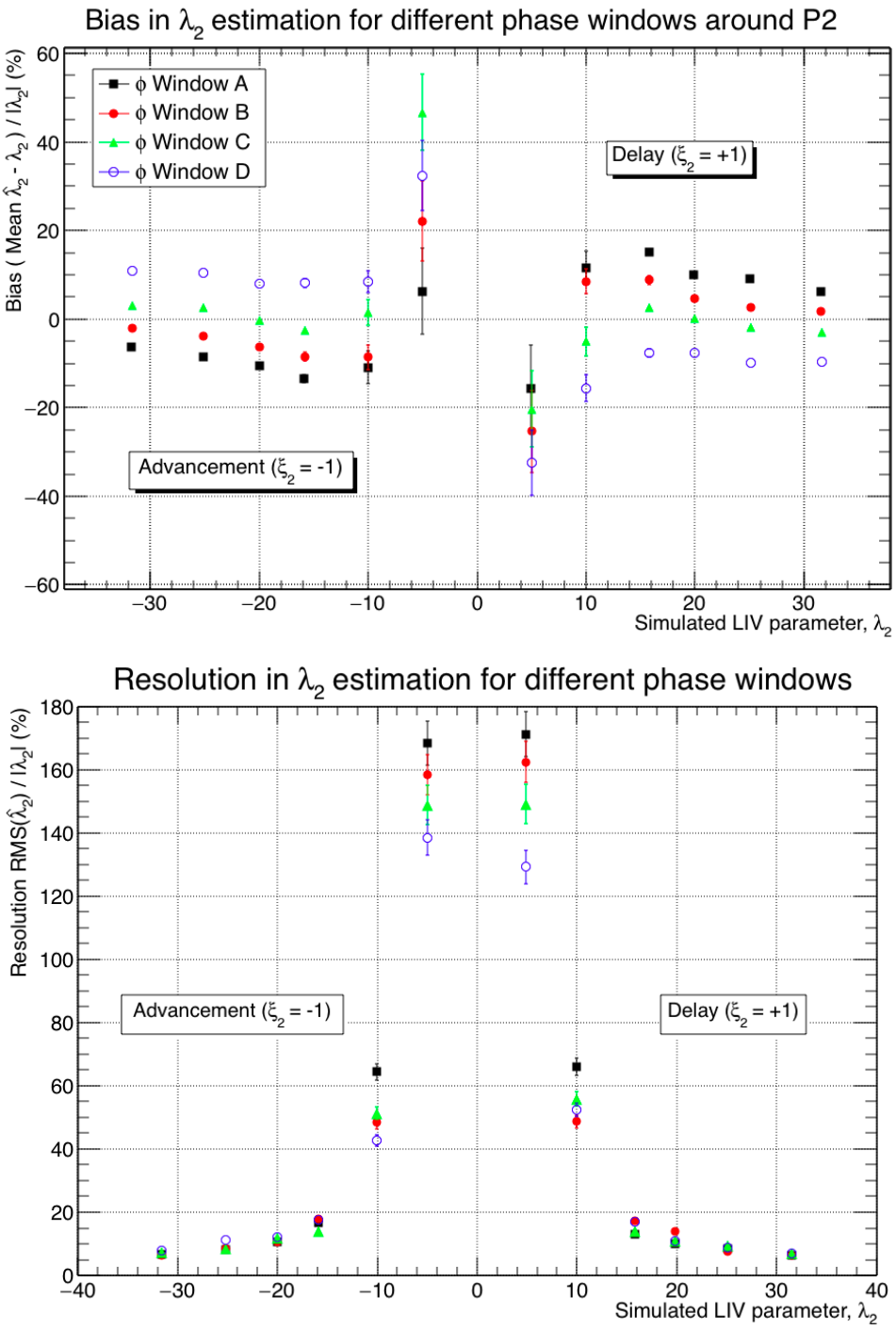

Figure 6.8: Bias (*top*) and resolution (*bottom*) for the estimation of the LIV parameter $\widehat{\lambda}_2$ as a function of the simulated quadratic LIV parameter λ_2. They are computed using the mean and RMS of the $\widehat{\lambda}_2$ distributions obtained using 300 MC simulations with a fixed simulated LIV λ_2 and a N2S ratio of 3. Each term is computed as $\frac{\text{Mean}(\widehat{\lambda}_2)-\lambda_2}{\lambda_2}$ and $\frac{\text{RMS}(\widehat{\lambda}_2)}{\lambda_2}$, respectively. The likelihood ratio D has been computed using the different phase windows shown in the legend, which correspond to the windows A, B, C and D as defined in equation 6.3.18.

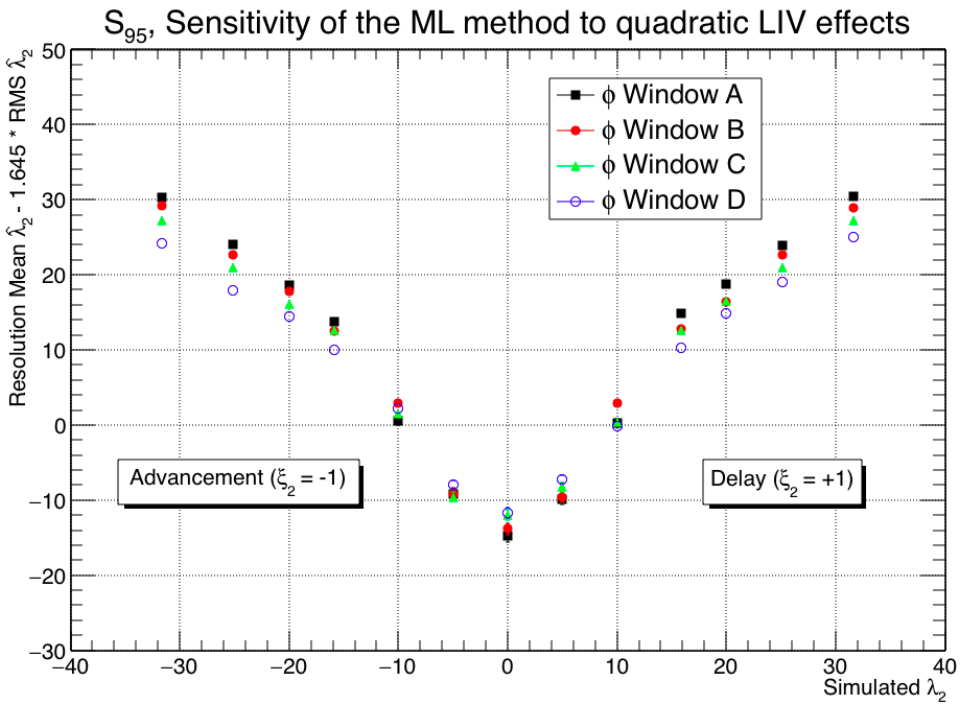

Figure 6.9: Value of $S_{95}(\lambda_2)$ (defined in equation 6.3.20) for the four different windows under test, A, B, C and D, which are marked with black boxes, red circles, green triangles and blue inverted-triangles, respectively. This test was done with 300 MC simulations containing 2% of the real background for the Crab pulsar (N2S $= 3$). The position where S_{95} changes sign allows us to spot the minimum value of λ_2 for which we can distinguish a LIV effect from the null-hypothesis case with a 95% probability.

changed when we apply any other phase window. We therefore select window C as the optimized phase window that allows us to include all the relevant photons for LIV into the likelihood computations, while at the same time minimizing the included amount of background.

6.3.3 Production of MC

To test de performance of the ML method, we needed to produce simulated sets of photons or toy MCs, where we could control the different experimental parameters. The energy and phase distributions of those events was as similar as possible tot the real spectral distribution and LC. Different initializations of a random number generator were used to produce toy MCs were generated. In this way we obtained any amount of independent LCs for any simulated value of λ_n and to which the method could be applied.

Due to statistical fluctuation, the produced simulated LCs and the obtained likelihoods are not easily comparable between each other. For example, the minimum of the likelihood ratio function is not always exactly at the value of the simulated LIV parameters, but located in a region close it. A single toy MC could not be used to study the effect of varying a given experimental

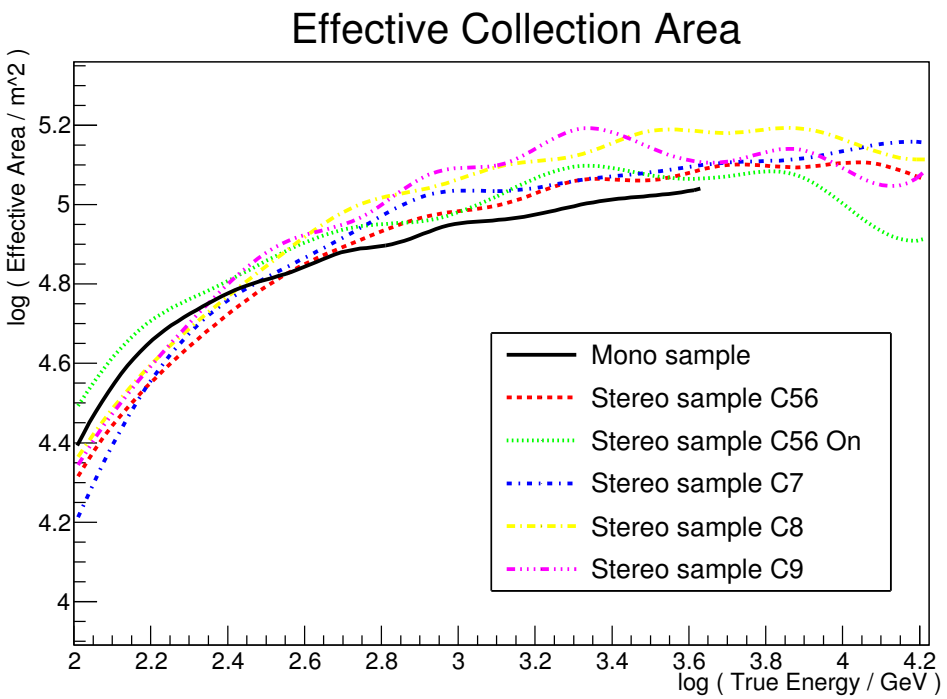

Figure 6.10: Effective area of the MAGIC telescopes after the analysis cuts, optimized for pulsar detection, during the k-th performance period and as a function of the true energy, $A_{\mathrm{eff},k}(E)$.

parameter, so a systematic study had to be done to account for such variations. We decided to test each of the parameters under study producing sets of 300 independent LCs using the same configuration of parameters. Then distributions of a given parameter with 300 entries each could be built, like the estimated LIV parameter $\widehat{\lambda}_n$ (where the minimum likelihood ratio was found) or the position of the positive or negative 95% C.L. limit on λ_n.

In this way the influence of the experimental parameters on the performance of the ML method could be studied in a consistent way. The results of these studies are reported in the next section. First of all, we will describe the details about the MC production.

Our MC always contained the same number of HE Crab pulsar events as measured in the observations reported in this thesis. This is particularly relevant for energies above 400 GeV, since those were the events to which we applied the ML method and, most likely, the main factor limiting its LIV estimation power. From table 4.12 we know that the number of excess events in the complete dataset for the P2 region was 544 ± 92. Their are distributed following a power-law SED with an spectral index $a = -3.1 \pm 0.5$ (see table 4.13). Thus, the

simulated pulsar events in the MC were produced following this energy distribution and only that number of P2 events were simulated: the MC production algorithm stopped once the amount of simulated pulsar photons above 400 GeV reached 544. No pulsar events above energies of 7 TeV were produced in the toy MC.

The toy MC production algorithm required the following ingredients:

- The **effective area**, $A_{\rm eff}(E)$, for each of the k-th data subsamples as a function of the true energy E. The same as those used in equation 6.3.13 and shown in figure 6.10.

- The **energy response** of the telescopes $G(E'|E) = \frac{{\rm d}E'}{{\rm d}E} = {\rm Gaus}(\mu_k(E), \sigma_k(E))$, i.e. the probability that a simulated event with a certain true energy E is detected as an event with an estimated energy E'. This ingredient is similar the energy resolution used the implementation of the ML method, but note that here the variables are inverted in comparison to the expression included in equation 6.3.13. The reason for this is simple: for a given MC event we know the value of the simulated true energy E and we want to know the probability of detecting that event with an estimated energy E'. This is exactly the opposite situation as in real data, where we know the value of E' estimated by our telescope and we are interested in the probability that the true energy of that event was actually E. We also modeled this probability using a normalized Gaussian function of E' centered at $\mu_k(E)$ and with a width $\sigma_k(E)$, which are extracted from the fits of the energy bias and resolution of the MAGIC telescopes as a function of the shower true energy, shown in figure 4.19.

- The **noise to signal ratio, N2S** could be arbitrarily selected to simulate any background level, from a no-background scenario (N2S $= 0$) to a realistic situation, where this ratio was found to be N2S ≈ 150. Several noise levels were used between these two values, in order to test if the method was sensitive enough to extract the correlations predicted by LIV when the signal gets dominated by background. This condition was never applied in previous implementations of this method: it was only used to extract LIV limits from high signal-to-noise sources, like GRBs or AGN flares, which are the brightest sources in the γ-ray sky during the short period they are active.

- The **order and energy scale** of the LIV effect to be simulated. Only a 2nd order LIV effect was tested, so a value of the LIV energy scale E_{QG2} or, equivalently, a LIV parameter value λ_2 was required as an input.

Once we had these elements, algorithm to produce simulated LCs followed this steps:

1. **Background events** were produced using a flat, random number generator between 0 and 1 to assigned their phase ϕ.

2. A performance period k was generated randomly, proportionally to the number events in each period within real data. No LIV-induced delay was applied.

3. Its estimated energy E' was randomly generated according to a PDF equal to the measured background spectral distribution $B_k(E')$.

4. One **pulsar event** was produced every N2S events.

5. Its phase ϕ was randomly generated from a PDF with the same shape of the pulsar LC for the lowest energy bin in equation 6.2.1 (see figure 6.2).

6. The delay $\Delta\phi_n$ was determined from the provided order n and the LIV intensity λ_n. This delay was added to the true phase.

7. The estimated phase ϕ' was randomly extracted from a Gaussian function centered at the delayed phase $\phi+\Delta\phi_n$ and whose width was the ephemeris uncertainty σ_{eph}.

8. The event performance period was selected in the same way applied to background events.

9. The corresponding effective area $A_{\mathrm{eff},k}(E)$ was logarithmically convoluted with a power-law with the parameters reported in 4.9. The event true energy E was randomly derived from the resulting function.

10. A Gaussian function was created, centered at $\mu_k(E)$ (the true energy corrected by the corresponding energy bias) and whose width was derived from the energy resolution in the k-th period, $\sigma_k(E)$. The estimated energy E' was randomly produced using this Gaussian function. If $E' > 7000$ GeV or $E' < 40$ GeV (< 400 GeV for mono events), the event

was discarded and a new true energy value was produced from the same convoluted function described in the previous step.

11. The condition for the algorithm to stop was that 544 pulsar events had been produced.

The computation of the PDF for the MC was done in the same way as we applied it to the data, that is using equation 6.3.14. The values used for the LC parametrization $B_k(E')$ and $R_k(E, E')$ were those extracted from the real Crab pulsar data. However, since the N2S ratio could be arbitrarily selected, the background contribution $B_k(E')$ had to be scaled proportionally. This was done with a simple addition of a scaling factor $B_k(E') \longrightarrow \epsilon \cdot B_k(E')$, where ϵ is the ratio of events in the off region between MC and data above 400 GeV:

$$\epsilon = \left(\frac{N_{\text{off}}^{\text{data}}}{N_{\text{off}}^{\text{MC}}} \right)_{E'>400 \text{ GeV}} \tag{6.3.21}$$

Normalization has to be computed for each MC because the integral of $f_k(E', \phi)$ depends on the actual value of ϵ, i.e. on the level of background included in the LC modeling.

In figure 6.11 we can see two examples of the application of the ML to sets of 300 MC simulations of the pulsar LC using different values for the simulated LIV parameter λ_2 but with only 2% of the background events contained in real data (N2S $= 3$). In the top plot, a subluminal LIV effect is simulated, whereas the bottom plot shows a superluminal LIV situation. In each set, a simulated LIV parameter λ_2 was chosen and the position of the minimum likelihood ratio $\widehat{\lambda}_2$, which we will sometimes refer to as *estimated LIV parameter*, was found and added to a histogram. The resulting distribution of $\widehat{\lambda}$ was drawn, which we will also refer to as estimated LIV parameter distribution.

These distributions were narrow and centered around the simulated λ_2 value, which shows that the ML method is able to find the proper LIV scale when this LIV effect is intense: $\lambda_2 \gtrsim 10$. In those cases, the distributions can be properly described a Gaussian function and fits are shown in figure 6.11 with thick, color lines. However, this simple distributions start to become more complex when we simulate weaker LIVs scenarios. For instance, we can see that for a simulated LIV parameter of $\lambda \approx 10$ (yellow, empty circles in the top plot of the same figure), a tail of distribution towards negative LIV parameters starts to appear.

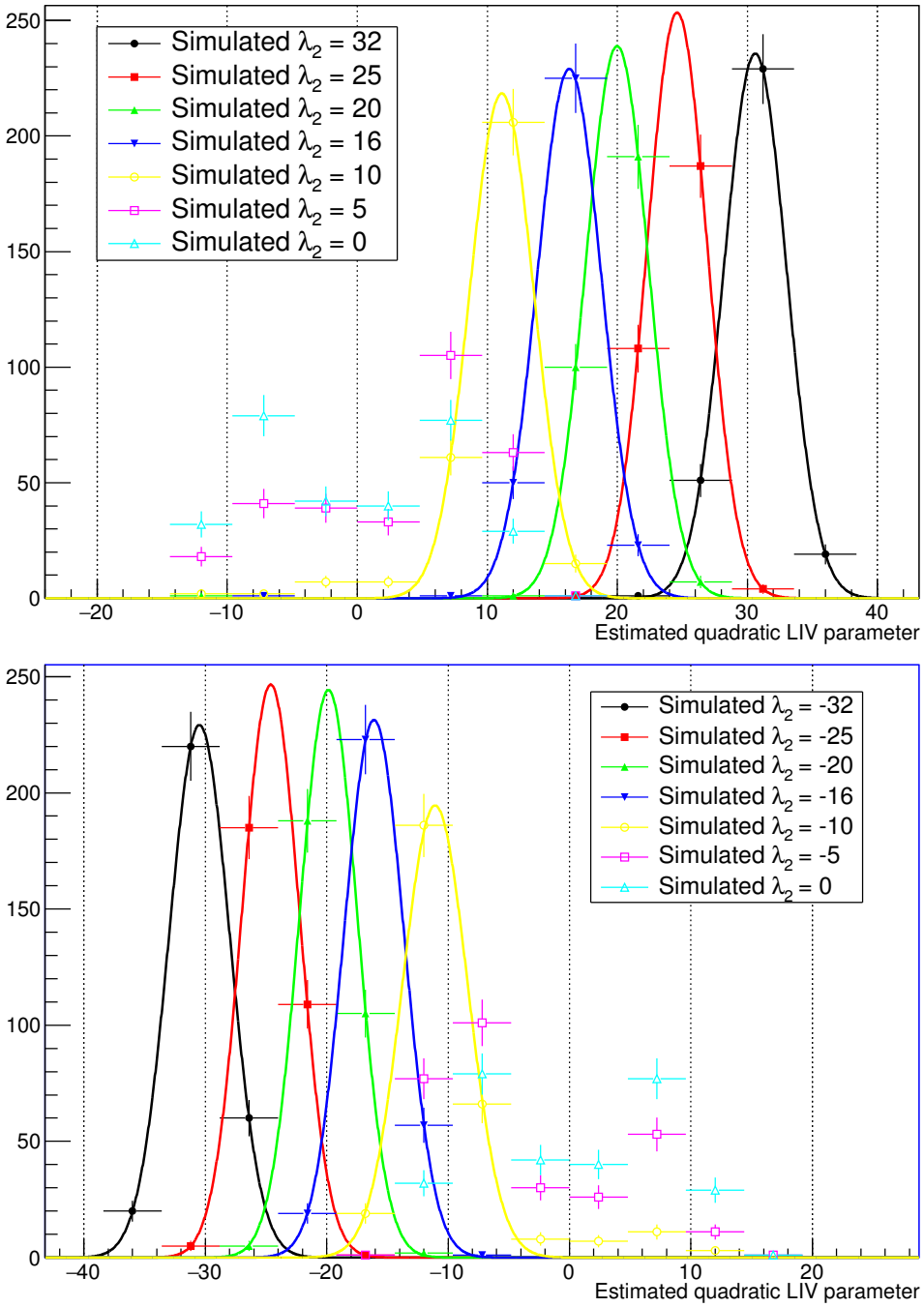

Figure 6.11: Estimated LIV parameter distributions ($\widehat{\lambda}_2$) obtained for 300 MC simulations with the simulated LIV parameter λ_2 showed in the legend and a N2S $= 3$. Subluminal (*top*) and superluminal (*bottom*) LIV cases are plotted independently. Gaussian fits are shown only for the regular-shaped distributions.

For an even weaker LIV such as the one represented by the pink empty squares ($\lambda \approx 5$), the obtained $\widehat{\lambda}_2$ distribution is far from Gaussian: it is peaked around $\widehat{\lambda}_2 \approx 7$ and also a secondary peak start to grow at the symmetric position $\lambda_2 \approx -7$. We call this effect the **phantom peak**, since the ML method is estimating LIV scenarios that we have not used in our simulation. We get very similar distributions if we simulate intermediate values of the LIV parameter such as $\lambda_n = 1$ or 3, which are not shown here.

Besides, the same occurs is we simulate negative LIVs (where HE photons arrive earlier than the LE ones) such $\lambda_2 = -1$, -3 or -5: we get distributions of estimated LIV parameters with a main peak at $\widehat{\lambda}_2 \approx -7$ and a secondary, phantom peak appear around values of $\widehat{\lambda}_2 \approx 7$, and it becomes more important as we simulate weaker and weaker LIV effects.

In principle, when we apply the ML method to a set of simulated pulsar LCs with no LIV effect, i.e. with $\lambda_2 = 0$, we would expect to retrieve a narrow and approximately gaussian $\widehat{\lambda}_2$ distribution centered at zero. But, as we can see from the blue empty triangles in figure 6.11, the obtained distribution is wide ($-14 \lesssim \widehat{\lambda}_2 \lesssim 14$), has only a few MCs with a zero estimated LIV parameter and it also shows two phantom peaks, one at $\widehat{\lambda}_2 \approx +7$ (subluminal) and another $\widehat{\lambda}_2 \approx -7$ (superluminal).

These phantom peaks appear even for the lowest N2S ratios, they are robust and have resisted many checks of our the code where we implemented the ML method. Moreover, they have also been obtained by the independent application of the method by a second member of the MAGIC collaboration. All these facts, together with their perfects symmetry, lead us to the following interpretation of the phantom peaks: **the ML method is not able to resolve LIV parameters lower than ~ 10**, which is of the order of the best quadratic LIV limit by Fermi GRB observations. This result was also confirmed by further testing done using MC simulations and described in §6.3.4.

6.3.4 Characterization of the ML algorithm

In order to check that the ML method was properly implemented, a series of tests were performed with the use of extensive MC simulations. Their goal was to estimate the performance and precision of the ML method, as well as to find out the sources of systematic errors in the estimation of the limits to the LIV energy scales.

Stability

We check the stability of our implementation of the ML method with respect to the variations of experimental parameters. To do so, a set of 300 MC simulations was produced where we applied variations to each one of these parameters at a time, such as assuming different source properties or diverse analysis cuts. The obtained results where compared with the standard situation, i.e. simulations with the real values of these experimental parameters.

First, the effect of the **background level** was tested. To do so, we produced 300 MCs where pulsar photons were delayed according to a simulated LIV of $\lambda_2 = 20$, a LIV effect twice as intense as the current best quadratic limit by Fermi. The chosen N2S values were 0, 3, 15, 75 and 150, which correspond to a 3%, 10%, 25%, 50% and 100% of the background level contained in the real Crab pulsar data. The distribution of estimated LIV parameters can be seen in figure 6.13 (*top*), where the optimized phase window (window C) was used.

We can see that the distribution is properly centered around the simulated LIV parameter value for the lowest background level N2S $= 3$. However, it quickly shifts towards lower estimated values as the background contribution increases, until reaching a minimum at $\widehat{\lambda}_2 \approx 7$. In the top plot of figure 6.13, Gaussian fits are shown for the right-hand-side of the distribution to highlight this tendency. The double peak or phantom peak at negative LIV parameters $\widehat{\lambda}_2 \approx -7$ also starts to appear for the highest background levels, similarly to the case where no LIV effect is included in the simulations, which is shown in figure 6.12 (*top*). This means that the ML method is hardly able to distinguish the simulated LIV effect from a no-LIV situation when background events dominate our sample.

However, this is no longer the case when we loosen the phase cuts that we apply to the events included in the likelihood ratio computation. In the bottom plot of figure 6.13 we can see how well the ML method performed with the same simulated LIV of $\lambda_2 = 20$ and same background levels but after applying the looser phase window A, as defined in equation 6.3.18. Now, the estimation of the LIV effect is significantly improved, even for the highest background levels. A significant bias is produced in those cases: for instance, with a realistic N2S ratio, the estimated LIV parameter distribution is peaked at $\widehat{\lambda}_2 \approx 16$. Moreover, a phantom peak also starts to appear in a symmetric position $\widehat{\lambda}_2 \approx -16$, which is

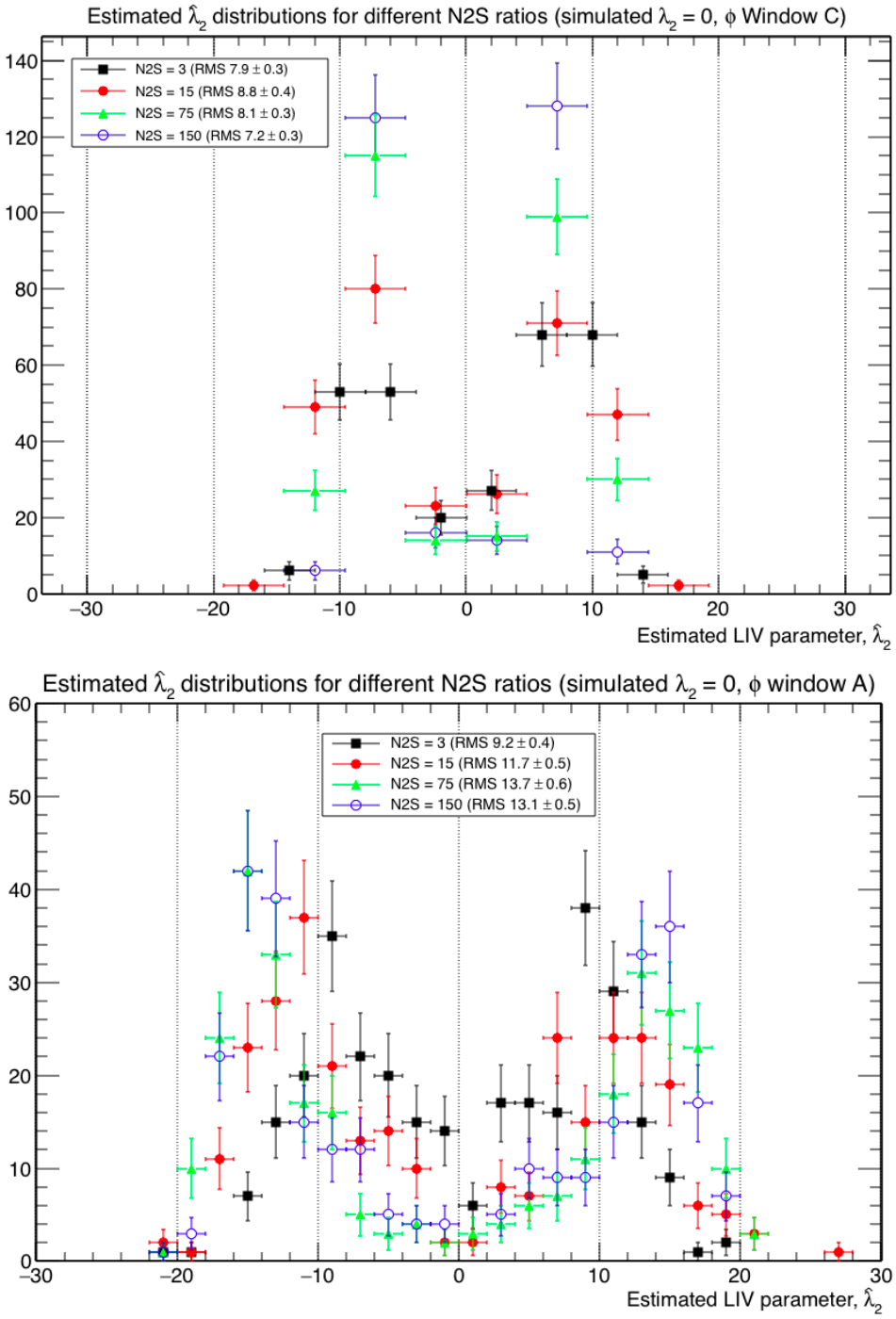

Figure 6.12: Distribution of estimated LIV parameters $\widehat{\lambda}_2$ for no simulated LIV effect of ($\lambda_2 = 0$) using loose phase cuts (phase window C, *bottom*) and using tight phase cuts (phase window A, *top*), for 4 different N2S ratios: namely, N2S $= 3$ (black squares), 15 (red circles), 75 (green triangles) and 150 (blue, empty circles), which correspond to a 3%, 10%, 50% and 100% of the real background in the Crab pulsar data, respectively. The mean and RMS of each distribution is also shown inside the legend.

not the case for the low-background simulations such as N2S ≤ 15. This means that when the background level is high, we have a non-zero probability of estimating a LIV effect with the opposite sign of what we have actually simulated.

Thus, two effects are playing a role here: if the LIV effect is weak, a tight window is enough for the ML method to properly infer the simulated LIV value. However, if we have a more intense LIV, HE photons will be shifted farther away from their original positions and, eventually, they will be moved out of the phase window. In this case, the ML method will not consider them for the calculation of $D(\lambda_n)$, so the method becomes less and less effective reconstructing the simulated LIV effect. With a higher background level, this efficiency is drastically reduced and the estimated LIV parameter distribution gets more and more similar to that obtained for a no-LIV scenario.

As an example, we can compare the distributions for realistic background ratios of N2S $= 150$ in the top plot of figures 6.12 and 6.13, marked as blue, empty circles. In these distributions, phase window C was used, where photons are only used if their phase is within $\phi \in [0.3461, 0.4477]$. It is hard for the ML method to tell between those two distributions, even when in the first one, no phase delay was included whereas in the second one, a $\lambda_2 = 20$ LIV effect was simulated. Thus, in the case that an intense LIV effect is not discarded, we need to increase the phase window, so the photons which have suffer a bigger delay are also taken into account. This what we did in the bottom plot of figure 6.13: now a looser window is used (window A, $\phi \in [0.2708, 0.5230]$) and now we are able to recover the simulated LIV parameter in most of the cases. However, note that a phantom peak for negative λ_2 values is starting to appear, much sooner than in the simulations with lower background levels, where we needed to reach values of the LIV parameter as low as $\lambda_2 \sim 5$ to start seeing this phantom peak.

In our case, since many experiments have already set strong constraints to a LIV effect, we do not expect to find an intense and so, the above described scenario does not apply. Due to this, we think that tight phase window can be safely used. However, if we were this was the first ever attempt in measuring or limiting such a LIV effect and we had no clue of what the possible values of the LIV energy scale were, we would need to use a looser phase window, to make sure we are considering the event the most delayed pulsar events.

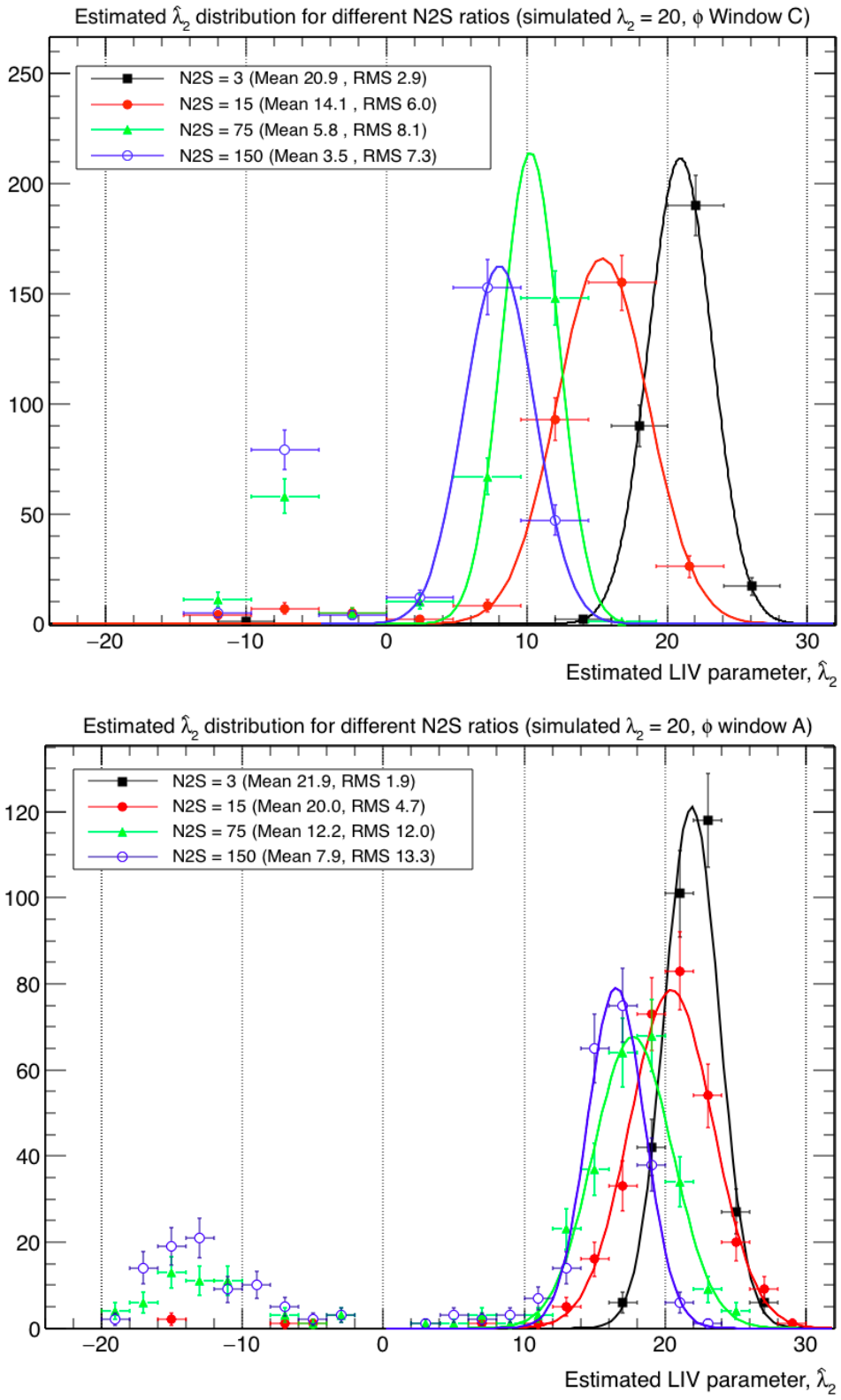

Figure 6.13: Distribution of estimated LIV parameters $\widehat{\lambda}_2$ for no simulated LIV effect of ($\lambda_2 = 0$) using loose phase cuts (phase window C, *bottom*) and using tight phase cuts (phase window A, *top*), for 4 different N2S ratios: namely, N2S $= 3$ (black squares), 15 (red circles), 75 (green triangles) and 150 (blue, empty circles), which correspond to a 3%, 10%, 50% and 100% of the real background in the Crab pulsar data, respectively. The mean and RMS of each distribution is also shown inside the legend.

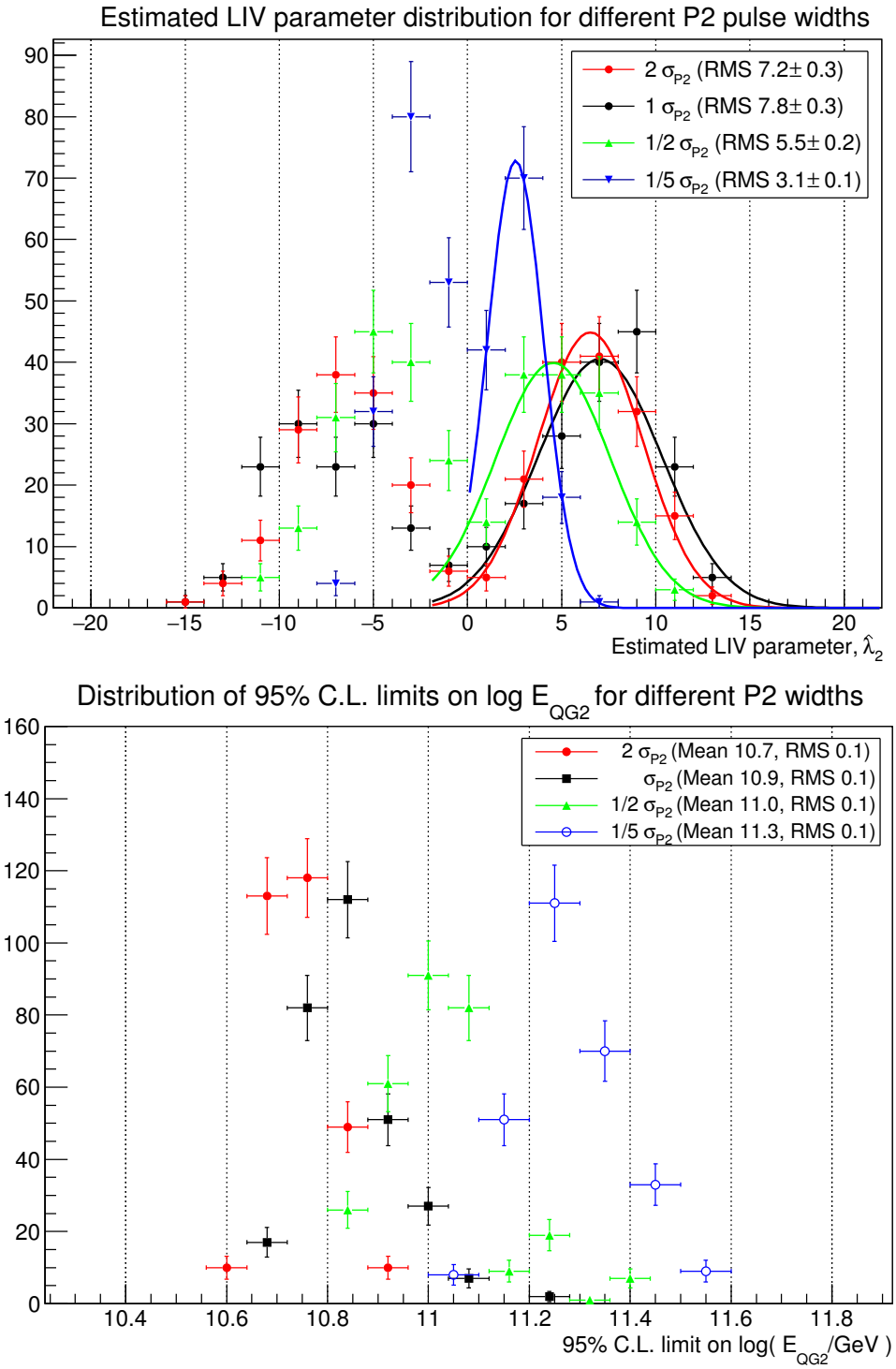

Figure 6.14: Distribution of estimated LIV parameters (*top*) and 95% C.L. LIV scale limits (*bottom*) for simulated pulsar LCs with no LIV effect and 4 different P2 widths, corresponding to 20%, 50%, 100% and 200% of the measured value. For an easier visualization, Gaussian fits are shown in the top plot using thick, solid lines

The second text consisted in simulating Crab pulsar LCs with **different widths of the P2 peak**, together a quadratic LIV of $\lambda = 20$. The chosen values of $\sigma_{\rm P2}$ where a factor 10 better and worse than the value of this parameter as measured in real data, respectively. Its effect on the estimated LIV parameter were measured with the use of the $\widehat{\lambda}_n$ distributions shown in figure 6.14.

For wider P2 peak, it is hard to see much difference between the position of the minimum of the likelihood function (top plot): the black and red points and curves are compatible, as well as the RMS of the associated distributions within the reported errors (in the legend). But we can see that the derived limits (bottom plot) are significantly worse when the pulsar emission region P2 increases by a factor 2.

This tendency is confirmed when a sharper P2 peak is simulated: the green and blue points, corresponding to 50% and 20% smaller $\sigma_{\rm P2}$ respectively, show two phantom peaks closer to zero and a significantly smaller RMS of those distributions. The 95% C.L. limits shown in the bottom plot are also significantly better that in the standard case.

Thus, the width of the emission region has an important effect on the sensitivity of our method: the sharper the peak, the better the limits to LIV that we are able to derive. In the limit where the peak is infinitely narrow, any LIV delay would smear it out so such an effect would be much easier to detect and, consequently, much stronger we would be able to set the constraints.

Third, pulsar LCs were simulated with no LIV effect ($\lambda = 0$) and using **different interpulse spectral slopes**. The measured -3.1 slope case was compared with a harder -2.0 and a softer -4.0 spectrum, which represent spectral indexes $\sim 2\sigma$ away from the measured slope. Its effect on the estimated LIV parameter can be seen in figure 6.15, where we show the obtained $\widehat{\lambda}_n$ distributions (*top*) as well as the distribution of limits on the LIV energy scale $E_{\rm QG2}$ at 95% C.L. (*bottom*).

As we can see, the spectral slope has a critical influence in the position of the phantom peak. It is clear that the steeper the spectrum, the wider the $\widehat{\lambda}_2$ distributions and the larger the value of the LIV parameter where we find the phantom peak: as we said, these peaks are located at $\widehat{\lambda}_2 \approx \pm 7$ in the standard case, whereas they move in for a harder spectrum ($\widehat{\lambda}_2 \approx \pm 3$) and out for a softer one ($\widehat{\lambda}_2 \approx \pm 12$). It seem clear that the higher the fraction of HE events in our dataset, the more accurately the ML method is able to estimate any

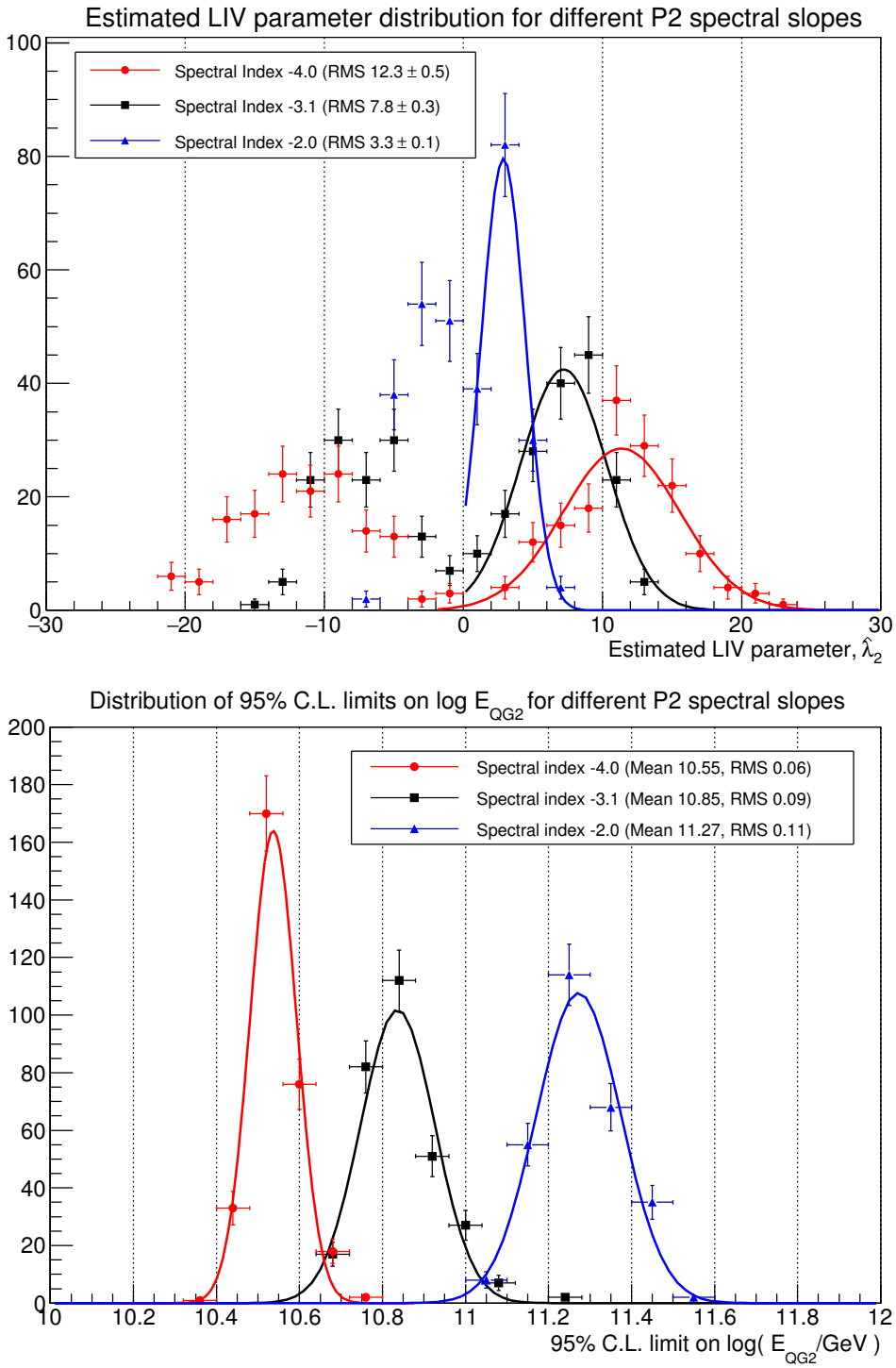

Figure 6.15: Distribution of estimated LIV parameters (*top*) and 95% C.L. LIV scale limits (*bottom*) for simulated pulsar LCs with no LIV effect and varying P2 spectral slope. For an easier visualization of the distributions, Gaussian fits are shown as thick, solid lines.

possible LIV effect.

In other words, for the harder spectrum there is a bigger amount of events at the VHE tail. Remember that the MC production was designed in such a way that there is always about 544 pulsar events above 400 GeV in our event list, the same amount as was found in the real Crab data. However, the closer the phantom peaks are to zero, the harder they are to resolve given the resolution of the ML method, so the estimated LIV parameter distribution becomes more similar to what we expect from a no-LIV situation: a compact, symmetric distribution with a single peak at $\widehat{\lambda}_2 = 0$. However, softer spectrum, where most of the photons are found at lower energies, the efficiency of the ML method is reduced and the position and width of the phantom peaks is increased. Very similar conclusions can be extracted from the plot of the limits on the LIV energy scale shown in the bottom plot of figure 6.15: more constraining LIV limits can be derived the bigger the fraction of VHE events contained in our datasample. These results confirm our previous claim that the VHE energy events are the most relevant ones regarding the testing of any LIV effect.

In a fourth test, the ML method was applied to a set of 300 MC simulations with a simulated quadratic LIV of $\lambda = 20$ but we now applied **different energy cuts** to the event list we used for the likelihood ratio computation, $D(\lambda_2)$. Three cases were tested: $E' \in [400, 7000]$ GeV (standard case), $E' \in [600, 7000]$ GeV and $E' \in [400, 1700]$ GeV. The result in the distribution of $\widehat{\lambda}_n$ can be seen in the top plot of figure 6.16. The derived limits on the LIV energy scale only get significantly worse when the VHE photons are left out of the construction of $D(\lambda_2)$, as we can see in the bottom plot of figure 6.16. Besides, if a LIV effect is simulated, applying such a HE cut produces a higher bias and a worse resolution in the determination of $\widehat{\lambda}_2$. This test also confirms our claim about the importance of VHE photons in the estimation of LIV effects, since their sensitivity to it along their path is much greater than that of LE photons.

Moreover, the lower plot in figure 6.16 tells us that it does not matter much the selected value for the LE cut, but it is better to apply looser cuts for the highest energies in order to derive constraining limits to LIV. This may seem contradictory with the fact that the P2 spectrum could only be computed up to energies of 1.7 TeV. But that plot shows us that it is useful to include events whose energy is above that value to test a LIV effect: if there is only background events above that threshold, correcting for LIV delays will only produce a very

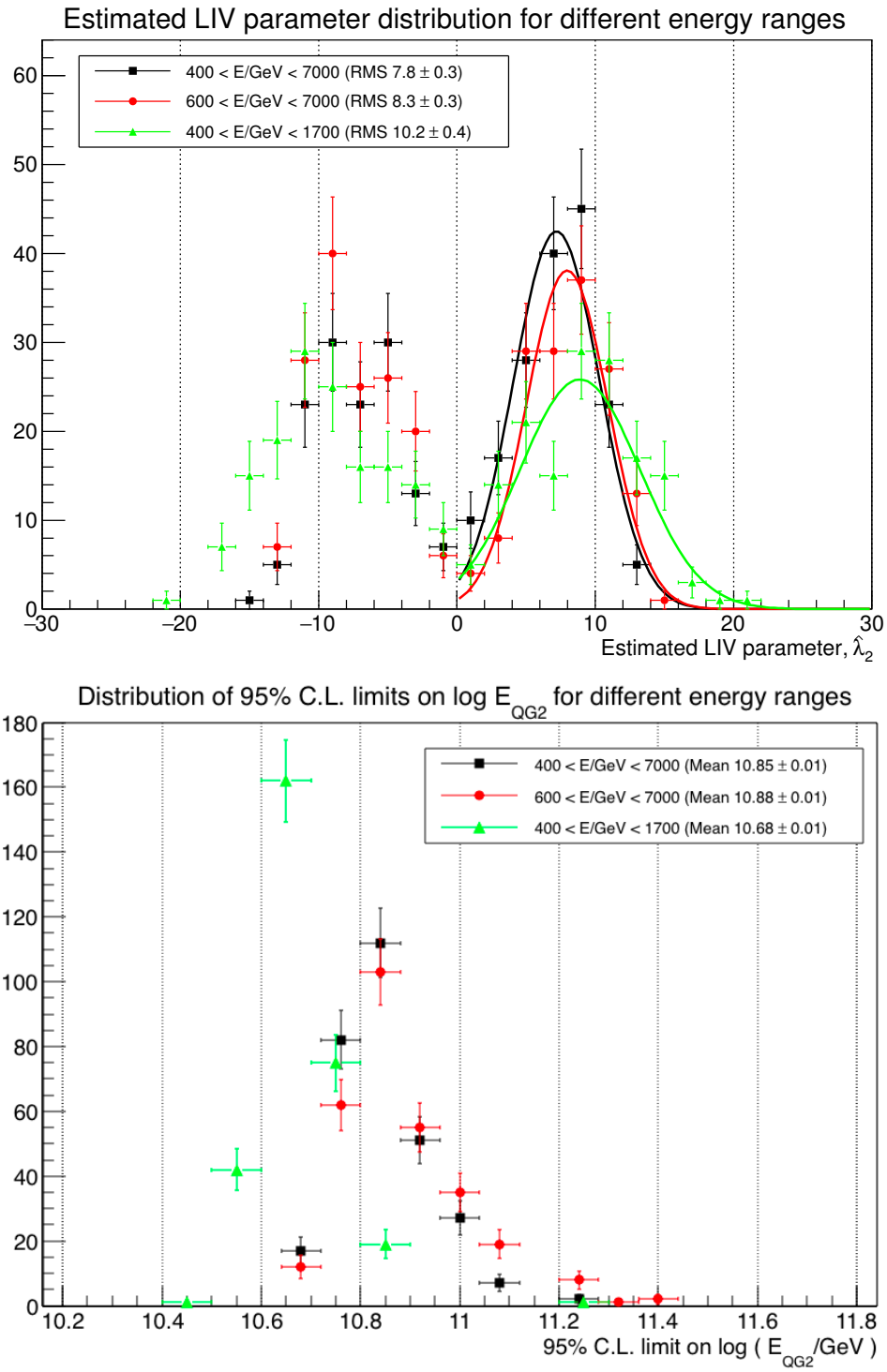

Figure 6.16: Distribution of estimated LIV parameter (*top*) and limits on $\log(E_{\mathrm{QG2}})$ (*bottom*) for a simulated pulsar LC with no LIV effect ($\lambda_2 = 0$) using 3 sets of energy cuts for the computation of $D(\lambda_2)$.

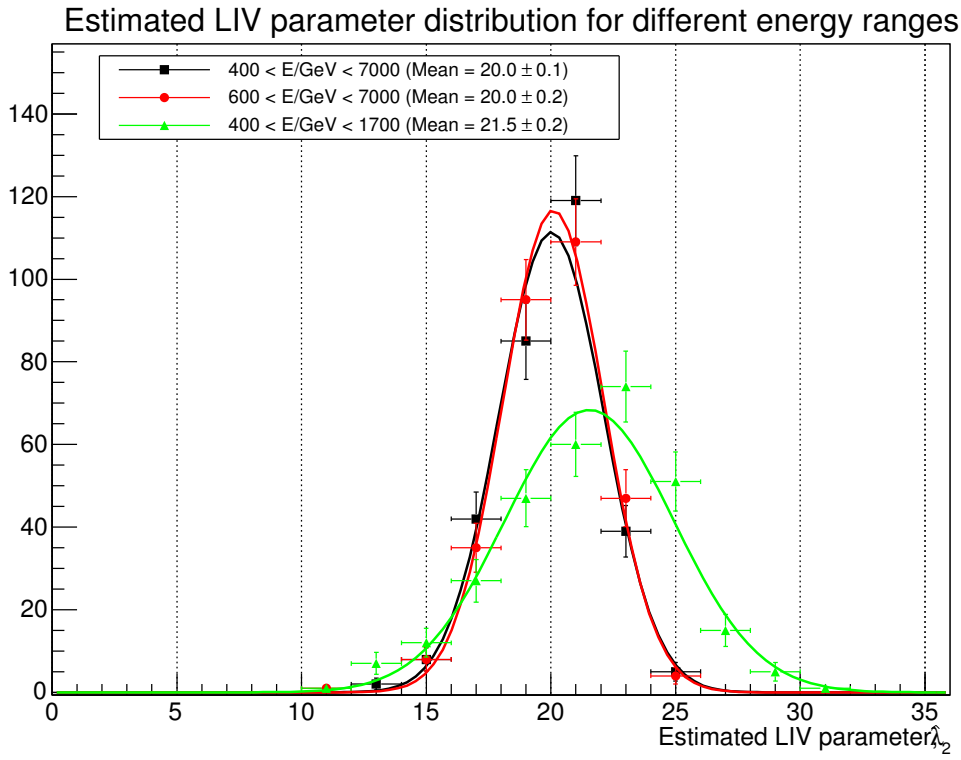

Figure 6.17: Distribution of estimated LIV parameter for a simulated pulsar LC with simulated LIV effect of $\lambda_2 = 20$ using three sets of energy cuts for the computation of $D(\lambda_2)$.

similar flat distribution of event phases. However, if there was a LIV effect that smeared out the P2 peak at the highest energies, correcting for the LIV delays may rebuild the original pulsar peak in that energy range. The likelihood function is telling us that this is not the case: VHE photons do not pile up at phases around $\phi_{\rm P2}$ when the account for possible LIV delays, so the ML method is able to set much stronger constraints when those VHE events are included.

Finally, we estimated the effects of the pulsar spin-down on the possible phase shifts of the recorded events. As stated in §3.1, the rotational period of the pulsar slowly increases with time. However, equations 6.1.1 and 6.1.3 tell us that the variations in the event phases depend on the inverse of the pulsar period, which is not absolutely constant in time. Since our entire Crab data sample spans for more than seven years, we had to make sure that the period variations were small enough as to consider them irrelevant for our purposes.

According to the Jodrell Bank ephemeris, the pulsar period changed during our observations from $T_0 = 0,0335997$ s at the beginning of 2007 to $T_1 = 0,0336915$ s and at the beginning of 2014. This represents a maximum change of $\frac{\Delta T}{T_0} = 0,27\%$ relative increase. The maximum change in the LIV-induced

phase delay, i.e. between a 2007 photon and a 2014 photon would then be

$$\phi_1 \propto \frac{1}{T_1} = \frac{1}{T_0}\frac{1}{1+\frac{\Delta T}{T_0}} \approx \frac{1}{T_0}\left(1-\frac{\Delta T}{T_0}\right) \propto \phi_0\left(1+\frac{\Delta T}{T_0}\right) \qquad (6.3.22)$$

Thus, the variation in the pulsar phase do to slow-down is approximately $\Delta\phi \approx -\frac{\Delta P}{P_0} \approx -0.27\%$. This of the order of the delays produced by LIV in some regions of the parameter space. However, this phase shift is completely independent of the energy of the events, so it can not fool the ML method, which look for very specific dependencies of this delay with the energy. For simplicity, we assume that the pulsar period is $P = P_0 = 33,5997$ ms is constant throughout the whole data sample and we will include the 0.27% variation as a part of the systematics of our implementation of the ML method.

Robustness

An important characterization of the ML method consist in estimating its robustness when the telescope response wrongly estimated. To do so, several sets of MC simulations were produced using the measured telescope response R_k but this term in equation 6.3.14 for the ML method was substituted by a wrong response function $\tilde{R}_k$. For each of these test, only one of the following instrumental parameters was modified: energy bias, energy resolution and effective area.

A a factor 2 and 5 bigger **energy bias** than it is shown in figure 4.19 was used as a response function $\tilde{R}_k$ for the ML method. This is equivalent to assuming that our instrumental energy bias lies between 2% and 10% and between 5% and 25%, respectively, with respect to the measured bias, which lies approximately below 5%. The obtained distribution of $\widehat{\lambda}_2$ parameters after simulating 300 MCs with $\lambda_2 = 0$ and $\lambda_2 = 20$ are shown in figure 6.18 (top and bottom plots, respectively).

In the first case, the distributions are hard to distinguish. The double phantom peak at $\widehat{\lambda}_2 \approx \pm 7$ is reproduced but we get a 6-8% bigger bias in the estimation of the LIV parameter. The obtained limits on the LIV energy scale are approximately equivalent in the three situations. In the second case, the effect is also small and we can only see a slight worsening in the bias of the estimated LIV parameter for the most extreme case of a 5 times bigger energy bias.

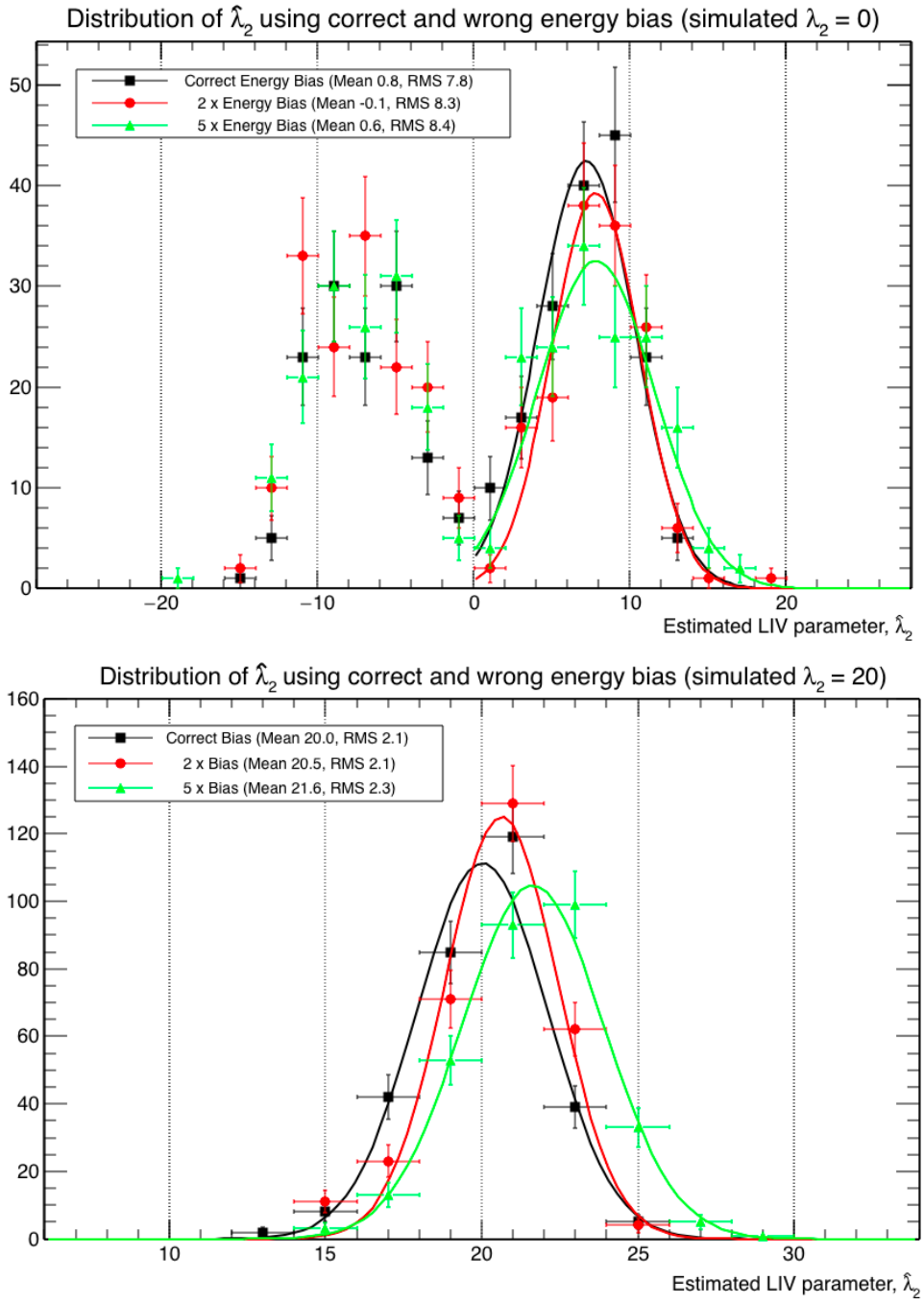

Figure 6.18: Distribution of estimated LIV parameters $\widehat{\lambda}_2$ for the case where the assumed energy bias is estimated to be twice (red circles) and 5 times (green triangles) stronger than it actually is, as compared to the proper estimation of the bias (black squares). Two scenarios were tested: a no-LIV situation (*top*) and a $\lambda = 20$ LIV situation (*bottom*). Gaussian fits for the positive-hand-side of the distributions are shown for an easier interpretation.

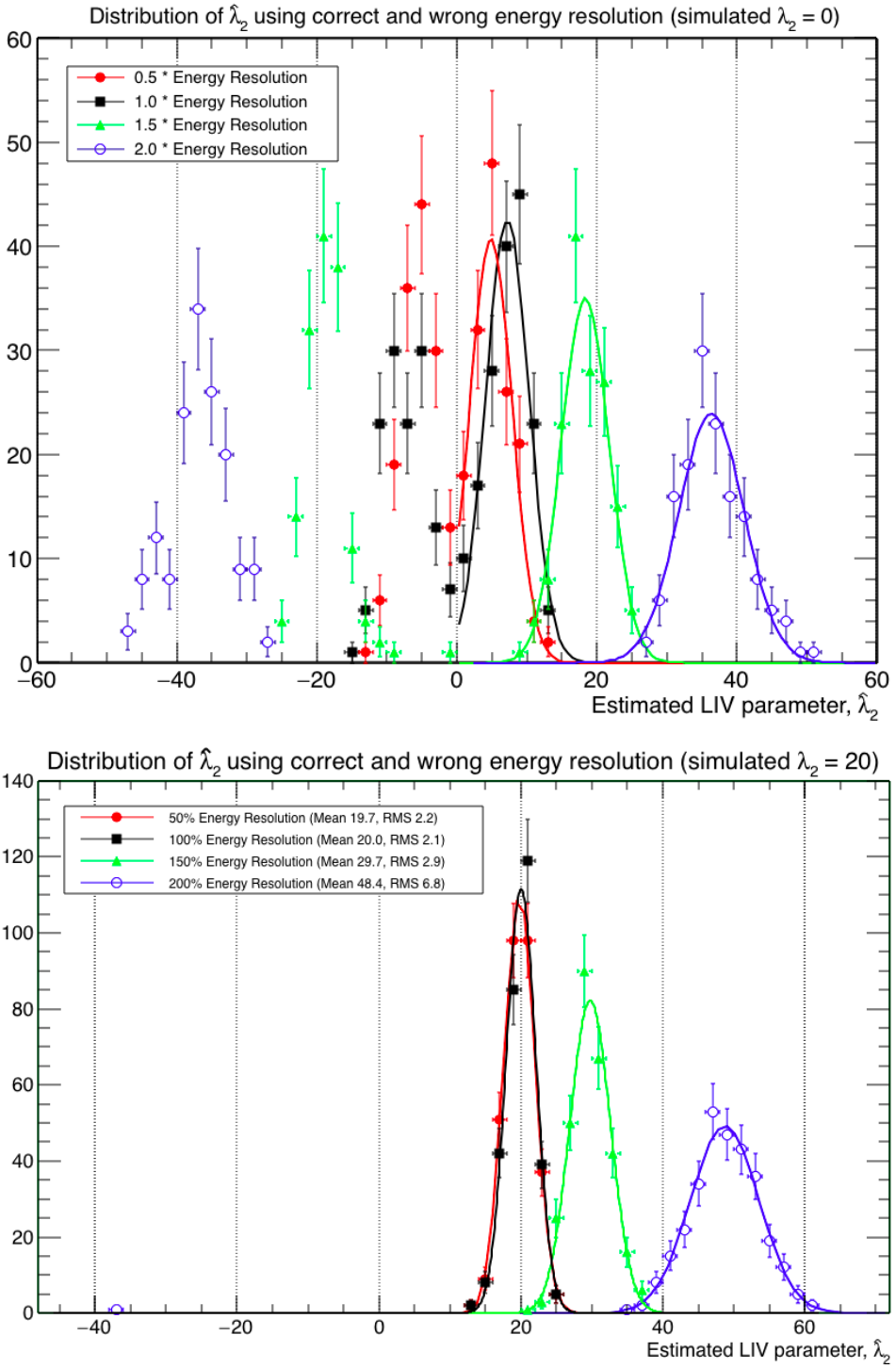

Figure 6.19: Distribution of LIV parameter where the minimum likelihood ratio was found for the case where the assumed energy resolution is estimated to be 5 times worse than the actually simulated value. Gaussian fits for the positive-hand-side of the distributions are shown for an easier interpretation.

A 50% better and a 50% and 100% worse **energy resolution** was used in the response function $\tilde{R}_k$. This means that, instead of the actual 20% to 35% energy resolution of the MAGIC telescope we would estimate that this resolution was, in each case respectively, between 10% and 18%, between 30% and 43% and between 40% and 70%.

The estimated LIV parameter distribution is shown in figure 6.19. Again, we have tested the effect of this misestimation in two sets of toy MCs, with and without a simulated LIV effect. On one hand, in the bottom plot of this figure we can see the case where pulsar events are shifted according to a $\lambda_2 = 20$ LIV effect. The distribution of estimated LIV parameters is centered around the simulated value for the cases of correct (*black*) and 50% better energy resolution (*red*) but not for the cases were the energy resolution is assumed to be 50% (*green*) and 100% worse (*blue*) that its real value. In these two last situations, a 50% and 150% bias is introduced for each case, respectively. Besides, we can see that the resolution of the ML method is also worse, since the RMS of these last two distributions is increased by a factor approximately 40% and 220%, respectively.

On the other hand, in the top plot we can see the effect of the misestimation of the instrumental energy resolution on a set of MC with zero LIV delay. The double peak structure is always present but its position and width proves to be highly dependent on these parameter: it is located at $\widehat{\lambda}_2 \approx \pm 19$ and $\widehat{\lambda}_2 \approx \pm 38$ for the two cases with an estimated energy resolution larger than the real value, and at $\widehat{\lambda}_2 \approx \pm 5$ for the opposite situation, where the energy resolution is estimated to be better than it actually is. Note that for one of the toy MC for the case of 200% energy resolution, the LIV parameter was estimated to have the absolute value similar to the other MCs (close to $\widehat{\lambda}_2 \approx 40$) but with the opposite sign: event were found to be better described with an intense phase advancement than with an intense phase delay. Is is interesting that this occurs for the worse estimation of the energy resolution but not for the rest of the simulated cases. However, there is only a single event where this occurs, so it is hard to extract any conclusions out of it.

To conclude, we have seen that the effect of a wrongly estimated energy resolution is critical to the detection of a LIV effect. The phantom peak feature is found to be highly-dependent of this instrumental parameter and a clear non-linear correlation has been found between energy resolution and bias and

resolution of the ML method.

Finally, the effect of a wrongly estimated **effective area** was tested. First, a mild shift of 50 GeV on the effective area was applied $\tilde{A}_{\rm eff}(E) = A_{\rm eff}(E + 50\ {\rm GeV})$ with respect to its measured value $A_{\rm eff}(E)$. This means that we are wrongly evaluating the telescopes effective area associated with an event of a certain energy with the effective area that corresponds to a 50 GeV more energetic event. It is a common error for IACTs, often committed when observations are performed under hazy atmospheric conditions and no correction is applied during the analysis process. The same procedure was also executed simulating an stronger effective area misestimation, using an 150 GeV energy shift instead.

The obtained distributions of $\widehat{\lambda}_2$ are shown in figure 6.20 for two cases: no simulated LIV effect (*top*) and a LIV of $\lambda_2 = 20$ (*bottom*). In both cases, we can see that the estimated LIV parameters are virtually the same: the double phantom peak is reproduced at the same position and with the same width, approximately, for both the weak and the intense effective area misestimation the obtained LIV limits are also equivalent. There is only a small variation of the LIV parameter estimation bias (-0.2 and $+0.3$, respectively) but this effect is hardly significant once we take into account that the error of the distribution mean is slightly larger than 0.1.

6.3.5 The obtained LIV limits

Once the method has been properly described and characterized, the application to the complete Crab pulsar data set and the obtained results will be reported here. As summary, only events between estimated energies of 400 and 7000 GeV and inside the optimized phaseogram phase window was used, namely phase window C, was used to build the likelihood ratio function $D(\lambda_2)$. Two cases were tested: a LIV delay linearly dependent with the energy ($\Delta\phi_1$) and a quadratic LIV delay, $\Delta\phi_2$.

We did not expect the linear limits to be competitive with the extremely high values derived by Fermi-LAT from GRB observations but, once the ML method was implemented and the algorithm was tested, it was free to extract those limits so the results are reported here. The likelihood ratio plot for such case and using the narrow phase window C can be seen in figure 6.21. As we can see, the minimum $\widehat{D} = -0.508$ is found at $\widehat{\lambda}_1 \approx 8.3 \pm 1.7$ and an increase of $\Delta D \approx 2.71$, corresponding to a 95% C.L. limit, was found at $\widehat{\lambda}_1 \approx 26.2 \pm 0.3$

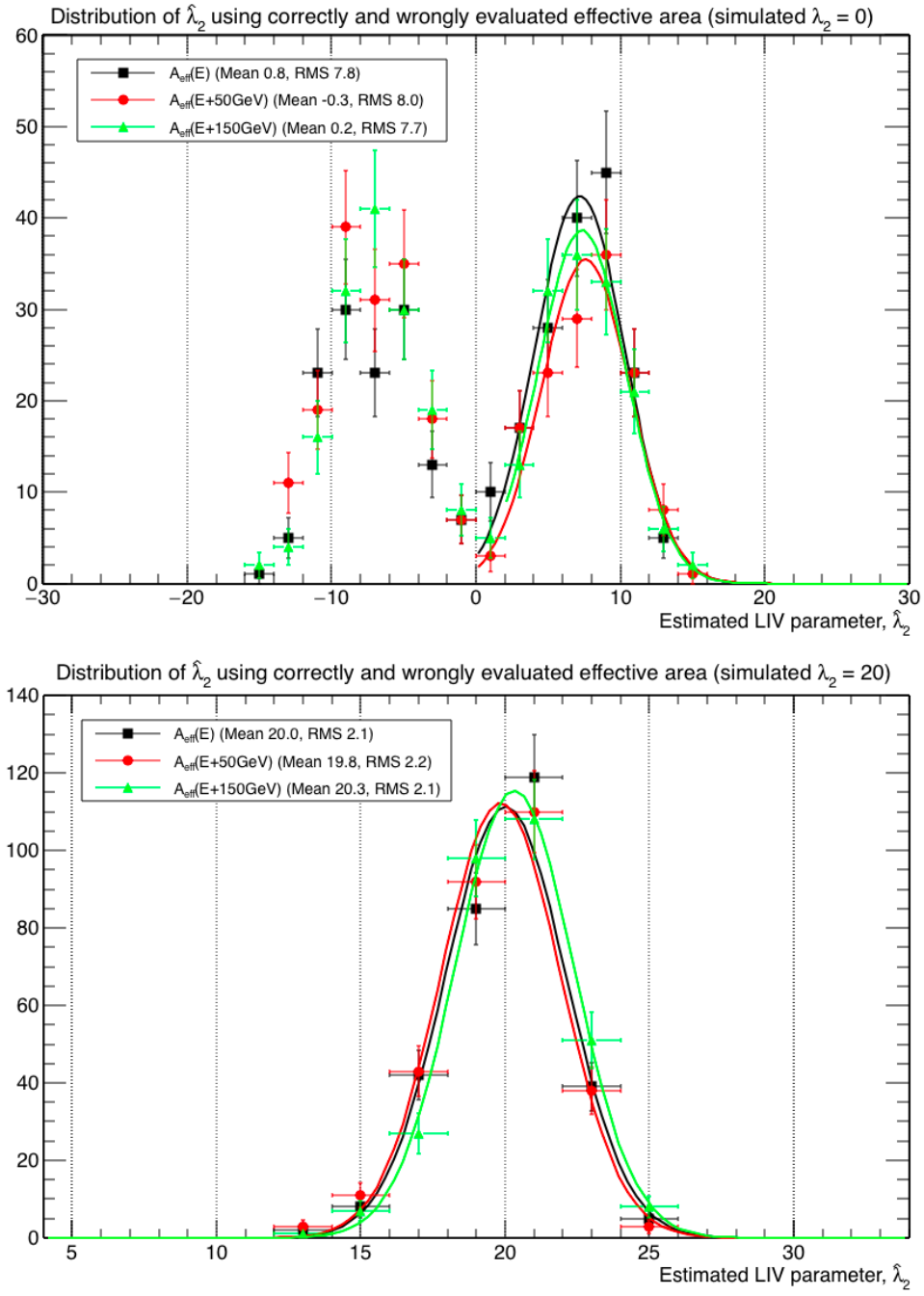

Figure 6.20: Distribution of estimated LIV parameter $\widehat{\lambda}_2$ when the properly ($A_{\rm eff}(E)$, black squares) and wrongly estimated effective areas ($\tilde{A}_{\rm eff}$) = $A_{\rm eff}(E + 50$ GeV), red circles and $\tilde{A}_{\rm eff}$) = $A_{\rm eff}(E + 150$ GeV, $greentriangles$), red circles) are used in the ML method. Two scenarios where simulated with 300 MCs each: pulsar LCs with no LIV delay ($\lambda_2 = 0$, *top* plot) and a subluminal LIV with $\lambda_2 = 20$ (*bottom*). Gaussian fits for the positive-hand-side of the distributions are shown for an easier interpretation.

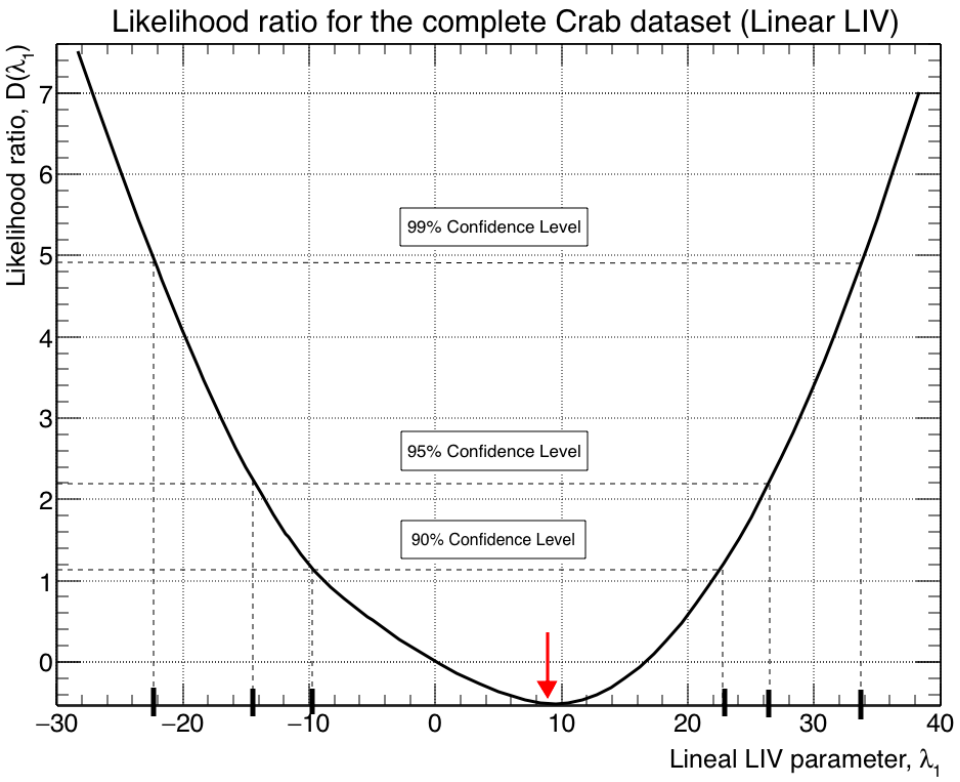

Figure 6.21: Evaluation of the likelihood ratio function $D(\lambda_1)$ for the complete Crab pulsar data set for a quadratic LIV effect. Only events with estimated energy between 400 GeV and 7 TeV were included in the computation and whose phase where within phase window C. The minimum is found at $\widehat{\lambda}_1 \approx 8.3 \pm 1.7$ where $\widehat{D} \approx -0.508$ and the derived limits to first order LIV can be found in equation 6.3.23.

and $\widehat{\lambda}_1 \approx -14.2 \pm 0.5$ for the subluminal and superluminal cases, respectively. From them, we can derive the following limits for the linear energy scale where QG effect start to dominate:

$$\begin{aligned} E_{\mathrm{QG1}} &> (3.8 \pm 0.1) \cdot 10^{17} \text{ GeV (95\% C.L. , } \xi_1 = +1) \\ E_{\mathrm{QG1}} &> (7.0 \pm 0.1) \cdot 10^{17} \text{ GeV (95\% C.L. , } \xi_1 = -1) \end{aligned} \tag{6.3.23}$$

As we expected, these limits are several orders of magnitude below the linear LIV limits derived from farther away sources such as GRBs. This confirms our prediction that pulsars are not the most suitable candidates to limit the linear component of a LIV delay. We also have to take into account that all the testing, characterization and optimization of the ML method has been done always trying to improve the obtained limits for the *quadratic* LIV term, and not for the linear one. For instance, the phase window that was used to produce these linear limits was phase window C, that was optimized only considering quadratic LIV parameters.

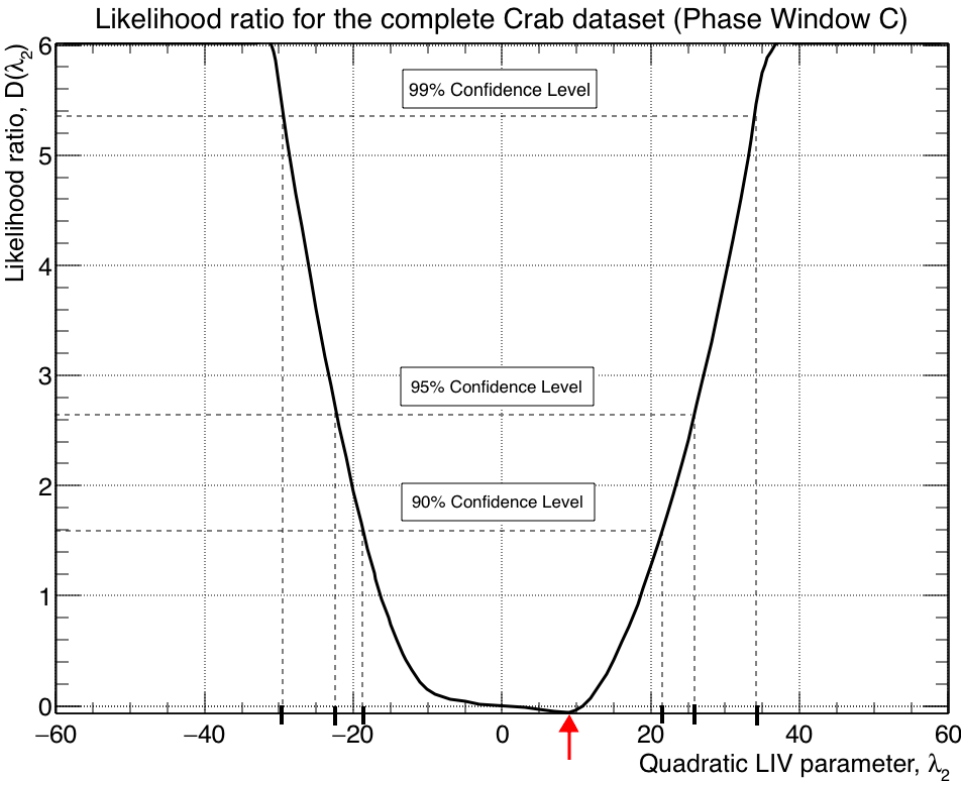

Figure 6.22: Evaluation of the likelihood ratio function $D(\lambda_2)$ for the complete Crab pulsar data set for a linear LIV effect. The optimized phase window C is used ($\phi \in [0.3461, 0.4477]$) and only events with estimated energy between 400 GeV and 7 TeV are included in the computation. The minimum is found at $\widehat{\lambda}_2 \approx 8.4$ where $\widehat{D} \approx -0.058$ and the derived limits to LIV can be found in equation 6.3.24.

The result for the quadratic LIV delay is shown in figure 6.22. As we can see, its minimum value, $\widehat{D} = -0.058$, was found at $\widehat{\lambda}_2 = 9.0 \pm 1.0$. A 95% C.L. limit can be extracted at the LIV parameter value where $D = \widehat{D} + 2.705$ (horizontal dashed lines in the figure), which in our case is $\lambda_2 < 25.7 \pm 0.3$ for the subluminal case and at $\lambda_2 < -22.5 \pm 0.4$ for the superluminal case. These limits are equivalent to the following limits on the quadratic LIV scale, according to equation 6.3.8:

$$\begin{aligned} E_{\mathrm{QG2}} &> (3.9 \pm 0.1) \cdot 10^{10} \text{ GeV (95\% C.L. , } \xi_2 = +1) \\ E_{\mathrm{QG2}} &> (4.6 \pm 0.1) \cdot 10^{10} \text{ GeV (95\% C.L. , } \xi_2 = -1) \end{aligned} \tag{6.3.24}$$

To check result, an independent implementation of the ML method was performed by another member of the MAGIC collaboration. Even though a slightly different approach was followed there, the obtained result is of the same order of magnitude and it was obtained using the same dataset: $E_{\mathrm{QG2}} > 4 \cdot 10^{10}$ GeV, which is compatible with our result.

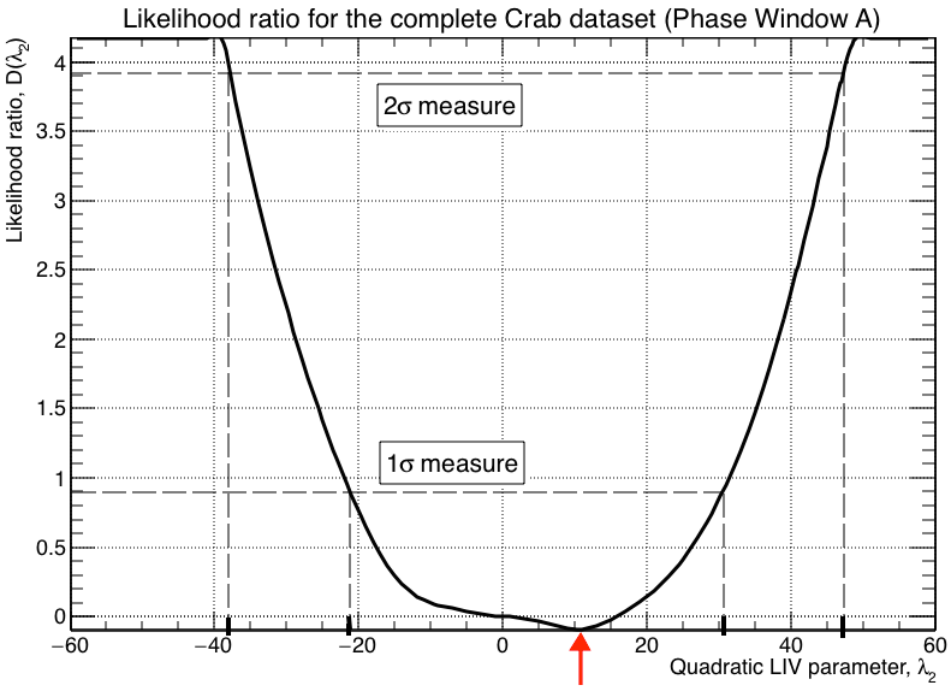

Figure 6.23: Evaluation of the likelihood ratio function $D(\lambda_n)$ for the complete Crab pulsar data set using a wide phase window (window A, see equation 6.3.18) to check that no delay between low and high energy events was present. Only events with estimated energy between 400 GeV and 7 TeV are included in the computation. The minimum is found at $\widehat{\lambda}_2 \approx 11.0$ where $\widehat{D} \approx -0.092$, perfectly compatible with zero.

In the previous section we have seen that the use of a narrow phase window limits the ability of the ML method to resolve intense LIV effects when the background level is high (see §6.3.4 and figures 6.12 and 6.13). Even though we do not expect to find any measurable delay in our data due to LIV (previous limits already constrain the values of E_{QG2} beyond the parameter space where the ML method we implemented is effective), we also made sure that nodealy could be measured with the use of a loose phase selection (window A). The results can be seen in figure 6.23. A minimum likelihood function of $\widehat{D} \approx -0.092$ at $\widehat{\lambda}_2 \approx 11.0$, which is compatible with no delay, as we can see by the error intervals marked in the figure with the dashed lines.

Since the Crab pulsar data does not contain any measurable delay, we can safely use a narrow phase window to set an unbiased estimation of a LIV limit at for a quadratic energy dependence of the speed of light, which confirms that the limits we set before using the optimized phase window was unbiased or, at least, its bias was small.

6.4 Discussion

In chapter 6 we explained how one can use our set of Crab nebula events to limit the violation of the Lorentz invariance. Due to the distance of this source to the Earth, its emission spectrum and its typical flux variability timescales, we estimated that pulsars are suitable candidates to derive competitive limits to the quadratic scale of this LIV effect, and not so much for the linear term.

When we simply compared the position of the P2 peak below 90 GeV and above 400 GeV, we were able to set limits to the LIV energy scale of the order of $2 \cdot 10^{17}$ GeV for the subluminal scenarios and $2 \cdot 10^{18}$ GeV for the superluminal scenarios. Regarding the limits for the quadratic energy scale, E_{QG2}, they are of the order of $1 \cdot 10^{10}$ GeV and $4 \cdot 10^{10}$ GeV for each scenario, respectively.

Thanks to the reported detection of the Crab pulsar at TeV energies reported in this thesis, these limits already improve those that were derived previously from the same source by VERITAS [125] by a factor 2 and 5 for the quadratic cases, respectively, and a factor 8 for the subluminal limit in the linear case. However, these last limit in the superluminal scenario is 40% weaker than those previously derived. We think this situation occurs because we are actually measuring a delay, although not statistically significant. Hence, the LIV scenarios where HE photons are advanced with respect to the LE ones can be tightly constrained, whereas those constrains are looser in the scenarios where those photons get delayed instead.

If we compare with LIV limits derived from other families of astrophysical sources, the linear one is almost three orders of magnitude below the best limit by Fermi (see §5.5.2). However, the quadratic limit is only one order of magnitude below the best lower limit and a factor ~ 6 below the second best (§5.5). This fact confirms our previous estimation that pulsars are candidates best suited to limit a quadratic correlation between energy dependence and arrival time, rather than a linear one.

The maximization of the likelihood function of our dataset to be described by a certain LIV scenario is a more complex method to perform one such test. We adapted it for the first time to the features of a periodic, background dominated source and it was optimized to derive quadratic limits to LIV from the Crab pulsar (§6.3). Its application on the discovered VHE emission reported in this thesis shows that no significant correlation between the photons arrival time

and their energy can be found (figure 6.22).

We do not expect the linear limits derived with the ML method to be much more constraining than those obtained by peak comparison, since our implementation of the ML method has been optimized to derive the best quadratic limits to LIV. The linear term can be obtained for free once the macro is created and we report our findings here for the sake of completeness. A limit at a C.L. of 95% could be set at the level of $E_{\rm QG1} > 4 \pm \cdot 10^{17}$ GeV for the subluminal case ($\xi_1 = +1$), 2-fold improvement with respect those by peak comparison. The limit for the superluminal case ($\xi_1 = -1$), $E_{\rm QG1} > 7 \cdot 10^{17}$ GeV, is however a factor 3 worse than the simple limit.

Regarding the quadratic dependence of photons delay with the energy, a limit at a C.L. of 95% could be set at the level of $E_{\rm QG2} > 4 \pm \cdot 10^{10}$ GeV for the subluminal case ($\xi_2 = +1$), which represents a factor 4 improvement with respect to one obtained by simple peak comparison. The limit for the superluminal case ($\xi_2 = -1$), $E_{\rm QG2} > 5 \cdot 10^{10}$ GeV, is however a only 20% better than the simple one.

If we compare it with those limits extracted from other astrophysical sources in a subluminal LIV scenario, we see that ours is less than one order of magnitude below the current best quadratic limit obtained by Fermi, and very close behind the second best limit set by H.E.S.S. (see §5.5.1).

Even though we could not improve the current best limit, we think our result is important because of three reasons. First, we managed to obtain competitive LIV limits from a very small number of excess events, only 544 above 400 GeV. Second, this is the first ever application of the ML method to limit LIV with the periodic signal of a γ-ray pulsar, which required certain modifications to be made with respect to its application to serendipitous events such as AGN flares of GRBs. Third, we have also proved that the ML method can be applied to background-dominated sources, a non-trivial hypothesis since previously, it had only been used to derive LIV limits from astrophysical sources with a extremely low signal-to-noise ratio and, in some cases, the background could even be completely ignored in the modeling of the PDF.

The reported limits using the ML method were derived using an optimized phase window to build the dataset likelihood. In §6.3.4 we have shown that such window would not be suitable to estimate an intense LIV effect. In order to be fully consistent, a wider phase window was tested on the same Crab pulsar

data and we could confirm that no quadratic, LIV-compatible phase delay is contained in our data (figure 6.23). However, one may consider that building the likelihood function using a different, wider phase window is actually a second trial regarding the determination of the LIV effect. In other words, the result of this last test could have an strong influence in the validity of the limit that we set in equation 6.3.24, because if a significant delay of HE photons would have been found, then the use of a narrow phase window would have blinded us from detecting it.

Following this line of thought, it may be justified to correct the required increase in the likelihood ratio $D(\lambda_2)$ to obtain a limit at the same C.L. of 95% as we intended to do. In this case, the one-sided limit for two trials would be found where an increase of $D = \widehat{D} + 3.80$ occurs within figure 6.22, which happens to be both at $\widehat{\lambda}_2 \approx -25.5 \pm 0.3$ and $\widehat{\lambda}_2 \approx 29.9 \pm 0.2$, for the superluminal and subluminal cases respectively. The 95% C.L. limits on the quadratic LIV energy scale would then be $E_{\mathrm{QG2}} > (3.3 \pm 0.1) \cdot 10^{10}$ GeV ($\xi_2 = +1$) and $E_{\mathrm{QG2}} > (3.9 \pm 0.1) \cdot 10^{10}$ GeV ($\xi_2 = -1$), which are about 10% and 15% worse, respectively, than those previously derived using only one trial.

In the opinion of the author, previous limits on the LIV scale derived from astrophysical sources by other telescopes are enough to justify the use of a narrow phase window and so, the plotting of the likelihood ratio $D(\lambda_2)$ using a wide phase window A is not necessary. Such plot only confirmed what other experiments have claimed before, i.e. that if there is any quadratic LIV effect in Nature, it must start to dominate at energy scales higher than $\sim 10^{11}$ GeV, which is beyond our current sensitivity (see §6.3.4). However, we understand that others may have a different opinion on this matter, hence we leave this question open to the interpretation of the reader.

Chapter 7

Conclusions and outlook

The first goal of this thesis was to detect the Crab pulsar at the highest energies ever observed by any astronomical facility. This means measuring its spectrum above To reach this goal, we had to analyze virtually all the Crab nebula observations performed by MAGIC during 7 years of operations. More than 300 hours of good quality data, which is the largest data analysis in any IACT experiment, so far. Such a massive workload required the formation of a dedicated team within the MAGIC collaboration, whose only mission was the analysis of the massive amount of Crab nebula data stored within the MAGIC archives.

Whithin these huge dataset, two different periods could be clearly differentiated: the observations performed with a single telescope, i.e. mono data, and the stereo data period, after the second MAGIC telescope began its operations. Since the analysis procedure was significantly different in those two cases, the Crab analysis team was split in two subgroups. Within each task-force, several analyzers would run the complete MAGIC data analysis pipeline independently (described in §2.5), so their results could be used as independent cross-checks. The author was part of the mono analysis team.

A non-standard low-level analysis was performed: custom cleaning levels and quality selection criteria were used, the optimal variables for the training of the γ-hadron separation RF were determined, and the applied analysis cuts were specifically optimized for the detection at the Crab pulsar at the highest energies, under the assumption that its power-law spectrum extended up to TeV energies. Since by previous measurements found no sign of a cut-off and a pure spectrum power-law fit was favored, this hypothesis described the most likely

scenario.

From the mono dataset alone, Crab pulsar emission below 400 GeV could be confirmed and the spectrum for the intermediate could be extended up to energies of 1.7 TeV, more than a factor 6 above previous detections. It is important to note that these data were recorded years before the detection of the Crab pulsar by VERITAS and MAGIC in 2011, and we did not use any of the MAGIC data that was used for that discovery. This means that the Crab pulsar emission could have been discovered years before if archival data, recorded to measure the properties of the surrounding nebula, would have been reanalyzed.

The results of the global effort are also reported in this thesis, which combined the results of the mono and stereo data analysis into a single Crab pulsar spectrum. The interpulse spectrum could be characterized more precisely and also the main pulse could be detected up to energies of 500 GeV, but with a steeper spectrum. This is in direct contradiction with the theoretical models, which predict a spectral cut-off for this source at energies of a few hundreds of GeV.

This unpredicted emission at TeV energies can only be understood as a new component in the pulsar spectrum, produced by inverse-Compton scattering of soft-photons by ultrarelativistic electrons and protons. Extreme particle velocities are required, of the order $\Gamma \sim 10^6$, which could only be achieved if charges are accelerated at regions well-beyond the light-cylinder. This discovery was not predicted by and imposes strong constrains to the current Crab pulsar models.

Some of this models may be able to include such emission mechanism within their theoretical frameworks. For instance, the outer gap model could account for TeV emission from the pulsar via magnetospheric cascades induced by accelerated charges interacting with low energy pulsar photons along the gap. Also the pulsar cold wind model may accommodate the up-scattering of pulsar photons by wind electrons, which should get accelerated in a region of the pulsar magnetosphere of about tens of times the light cylinder radius. However, both models have problems reproducing all the lightcurve and spectrum features, hence revisions will be required.

The second goal of this thesis was to make use of the discovered VHE emission of the Crab pulsar to test one of the phenomena that is predicted by some Quantum Gravity candidate theories: the breaking of Lorentz symmetry, one of the best-established physical symmetries. If LIV occurs at some energy

scale, the speed of photons may depend on their energy so high energy γ-rays emitted by astrophysical sources would be advanced or delayed with respect their lower energy counterparts. Comparing the arrival times photons with different energies we can set limits to the differences between their time-of-flight, and hence also place a limit on the energy scale of a possible LIV effect. So far, such an effect has never been measured.

The Crab pulse arrival times should vary if Lorentz symmetry was broken, so the precisely synchronized photons at low and high energies from the Crab pulsar allow us to set competitive limits to LIV. We test such an effect using two different methodologies.

First, the peak position at the lowest and highest energies were precisely estimated and we can compare those positions to get a phase distance of $\Delta\phi_{\rm P2} = 0.006 \pm 0.004$ between the peak below 90 GeV and above 400 GeV. This represents a positive deviation from zero but only at a 1.5σ significance level. We could set a 95% C.L. limit on a LIV effect with a linear energy dependence at $E_{\rm QG2} > 2 \cdot 10^{18}$ GeV for the superluminal case. This is a factor 8 improvement with respect to previous limits derived from γ-ray observations of the Crab pulsar but, as expected, still several orders of magnitude below the current best limit by Fermi GRB observations. A limit for the subluminal case was set to $E_{\rm QG1} > 2 \cdot 10^{17}$ GeV, which is not so constraining due to the fact that the position difference that was found is consistent with the delay expected in that scenario. For a quadratic-energy dependence, these limits are $E_{\rm QG2} > 1 \cdot 10^{10}$ GeV and $E_{\rm QG2} > 4 \cdot 10^{10}$ GeV, for the subluminal and superluminal cases, which represent a 50% and an factor 6 improvement, respectively, as compared with previous Crab pulsar limits to LIV. These limits are one order of magnitude below the current best quadratic LIV limit.

The second method reported in this thesis is the maximization of the likelihood of our dataset to be described by a Gaussian pulse model whose position depends on the LIV energy scale. This is first time such technique has been implemented to test LIV on a periodic, background-dominated source, which required the introduction modifications in its computation and a dedicated optimization of the method to boost its sensitivity for quadratic LIV delay detection. No significant correlation between arrival time and energy of the photons was found, which allowed us to set quadratic limits on LIV at $E_{\rm QG2} > 4 \cdot 10^{10}$ GeV and $5 \cdot 10^{10}$ GeV for the subluminal and superluminal cases, respectively. They are only a factor 2 lower than the current best limits by Fermi for this term, and

very close behind the second best limits by the H.E.S.S. collaboration. Linear limits were also derived, of the order of $E_{\mathrm{QG1}} > 4 \cdot 10^{17}$ GeV and $7 \cdot 10^{17}$ GeV for the subluminal and superluminal cases, respectively, which represent a factor 2 improvement and a factor 3 worsening with respect to the limits derived by peak comparison.

We were able to set strong constrains on the possibility of LIV. The obtained limits prove that γ-ray pulsars are useful sources to test a spontaneous breaking of the Lorentz symmetry whose intensity depends quadratically on the energy of the radiation, even though they are galactic source, many orders of magnitude closer to the Earth than the the usual astrophysical sources used for LIV tests. Any Quantum Gravity candidate theory predicting such an effect must take into account the limits reported here, which will be improved over time just integrating more observational time.

Future prospects

Several minor tasks within the Crab pulsar analysis had to be postponed for a future study and we would like to list them here. The main one was the analysis of the mono data taken prior to the MUX hardware period (see §4.1): several hundreds of hours stored in a database in Würzburg (Germany) remain unexploited and could improve the amount of pulsar excess events we have found. However, we would have needed to perform an even more custom analysis than the one reported in this thesis, which would have consumed most of the time that was actually used for the LIV studies. Other tasks include the investigation of the correlations between the cumulative excess shown in figures 4.13 and 4.14 and the atmospheric conditions at the time.

Similarly, during the development of the LIV tests presented in this thesis, several tasks had to be left for posterior studies. the most important of which may be to perform an exhaustive study of the systematics of this method. Some hints on this matter were given in §6.3.4, where we have discovered, in a first order approximation, which are the most relevant sources of systematic uncertainties: the estimation of the spectral index of the source, the telescope energy resolution, the width of the pulsar peak. The energy range of the events that are included in the computation of the likelihood is also a critical factor to extract competitive limits, and we have learned in that the best approach is

to apply the cuts for the highest energy events as loose as possible, or none at all, whereas the low energy cut show little influence in the results of the ML method for LIV.

Nevertheless, we should note that these kind of studies are usually long and complex. For instance, the MAGIC software board has a specific taskforce dedicated to the study of the systematics of our instrument. Therefore, a detailed characterization of all of them for the case of LIV testing would require years of additional work and this falls out of the scope of this thesis.

Other pending tasks would be: to use diverse pulse models $F_{P2}(\phi, E'|\lambda_n)$ different from the Gaussian shaped that was used here; other statistical metrics and methods could have been applied to estimate the energy and time correlation, like the DisCan method [121], the Kolmogorov distance [130] or the PairView method [123]; a varying pulsar period could have also been taken into account within our implementation of the ML method, for a more precise estimation of the LIV energy scale, and we think it should be considered any similar LIV test, expanding along several years of observations; after the maximization of the likelihood, the data and the likelihood ratio function could have been binned in energy and phase, and the goodness of this fit could be calculated from the reduced χ^2 value; the production of bootstrap replicas of our dataset could have been used to actually test the probabilistic interpretation of our result; or the inclusion of the P2 peak position and width as a nuisance parameter within the ML method.

In addition, the result reported regarding LIV limits here are a first step towards the systematic application of the ML method to γ-ray sources observed by the MAGIC collaboration. This tool could be adapted to extract limits from other sources, mainly AGN flares, and its implementation is already being discussed within the collaboration. But if one wants to improve the limits presented here using Crab pulsar observations by the MAGIC telescopes, we think the following requirements would have to be met:

- Include more statistics: considering the amount of observation hours we have today, we would need 300 hours more to improve the number of excess by a factor 2. This amount of observational time could be collected by the next generation of IACTs, the Cherenkov Telescope Array, with its foreseen sensitivity in only ~ 30 hours of observations. In such case, an extensive study of the systematics of the instruments and of the ML method would be compulsory. A dedicated team of scientists with the

CTA collaboration would have to perform thorough investigation on the matter for several years, which is a task that is already been considered. Besides, since systematics may change over time, this team would also have to consider to do a dedicated follow up of the already known sources of error as well as any new source that could appear along the decades of operation of CTA.

- Improve the characterization of the telescope response (from now on, CTA), especially regarding its energetic response, would allow us to increase the ML method sensitivity to LIV. A more precise description of the associated energy resolution of each event could include the zenith angle at which it was observed. An increase of a few factors in the energy resolution of the telescope at the highest energies (from the current $\sim 20 - 30\%$ to 10-15% would also help us increase our lower limits to LIV, but this goal is hard to achieve since the response of the telescopes has already been optimized.

- Detection of the pulsar signal at higher energies: if the power-law spectrum extends beyond the 1.7 TeV energies where we have been able to measure it, the limits on any LIV effect could be easily improved. Besides, if the P2 narrowing trend also continues up to higher energies, the power of the ML method to limit LIV would be increased even further, since using narrower peaks significantly improves the method sensitivity on weak LIV effects.

- Better timing could be achieved by improving the precision of the current pulsar ephemeris.

Appendices

Appendix A

Speed of light in a LIV escenario

To compute the group velocity of the photons traveling from the Crab pulsar to the Earth, one must start with the definition of this magnitude, which is given by

$$v_\gamma = \frac{\partial E}{\partial p} \tag{A.0.1}$$

We can then derive both sides of equation 5.4.1 by the energy E:

$$2p\frac{\partial p}{\partial E}c^2 = 2E\left(1+\sum_n \xi_n \frac{E^n}{E^n_{\mathrm{QG}n}}\right) + E^2\left(0+\sum_n \xi_n n \frac{E^{n-1}}{E^n_{\mathrm{QG}n}}\right) \tag{A.0.2}$$

and after dividing for $2E$ we get

$$\begin{aligned}\frac{pc}{E}\frac{\partial p}{\partial E}c &= 1+\sum_n \xi_n \frac{E^n}{E^n_{\mathrm{QG}n}} + \sum_n \xi_n \frac{n}{2}\frac{E^n}{E^n_{\mathrm{QG}n}} \\ &= 1+\sum_n \xi_n \left(1+\frac{n}{2}\right)\frac{E^n}{E^n_{\mathrm{QG}n}}\end{aligned} \tag{A.0.3}$$

Now we can introduce equation 5.4.3 to obtain

$$\frac{\partial E}{\partial p} = c\frac{\sqrt{1+\sum_n \xi_n \frac{E^n}{E^n_{\mathrm{QG}n}}}}{1+\sum_n \xi_n \left(1+\frac{n}{2}\right)\frac{E^n}{E^n_{\mathrm{QG}n}}} \tag{A.0.4}$$

We can apply a Taylor expansion for

$$\begin{aligned}(1+x)^{1/2} &\approx 1+\frac{1}{2}x \\ (1+y)^{-1} &\approx 1-y\end{aligned} \tag{A.0.5}$$

where we can identify the variables x and y as

$$\begin{aligned}x &= \sum_n \xi_n \frac{E^n}{E^n_{\mathrm{QG}n}} \ll 1 \\ y &= \sum_n \xi_n \left(1+\frac{n}{2}\right)\frac{E^n}{E^n_{\mathrm{QG}n}} \ll 1\end{aligned} \tag{A.0.6}$$

These two inequalities can be safely applied because the correction to the thoroughly-tested energy dispersion relation must be small. Thus, we can approximate equation A.0.4 to

$$\begin{aligned}\frac{\partial E}{\partial p} &\approx c\left[1+\frac{1}{2}\sum_n \xi_n \frac{E^n}{E^n_{\mathrm{QG}n}}\right]\left[1-\sum_m \xi_m\left(1+\frac{m}{2}\right)\frac{E^m}{E^m_{\mathrm{QG}m}}\right] \\ &= c\left[1+\frac{1}{2}\sum_n \xi_n \frac{E^n}{E^n_{\mathrm{QG}n}} - \sum_m \xi_m\left(1+\frac{m}{2}\right)\frac{E^m}{E^m_{\mathrm{QG}m}} + \sum_{n,m}\mathcal{O}(E^{n+m})\right]\end{aligned} \tag{A.0.7}$$

After removing the non-dominant terms of order $n+m$, we are left with

$$v_\gamma = \frac{\partial E}{\partial p} \approx c\cdot\left[1-\sum_{n=1}^{\infty}\xi_n\frac{n+1}{2}\left(\frac{E}{E_{\mathrm{QG}n}}\right)^n\right] \tag{A.0.8}$$

Appendix B

Crab pulsar data quality selection

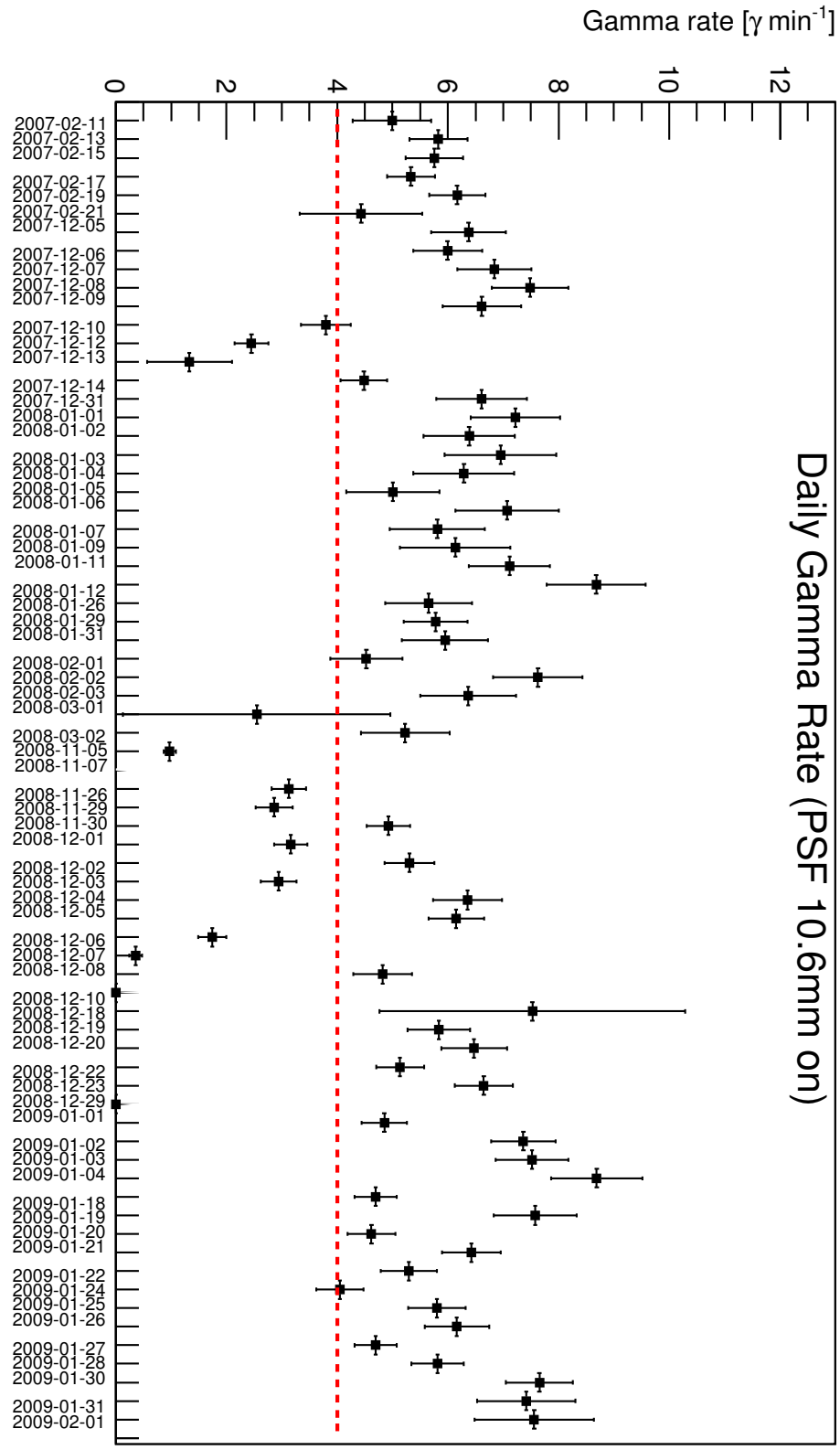

Figure B.1: Mean daily estimated gamma rates for the included observation nights for the the 10.6 mm PSF in on observation mode subsample. A quality selection cut discarded all nights where gamma rate was below 4γ/min, as shown by the red, dashed line.

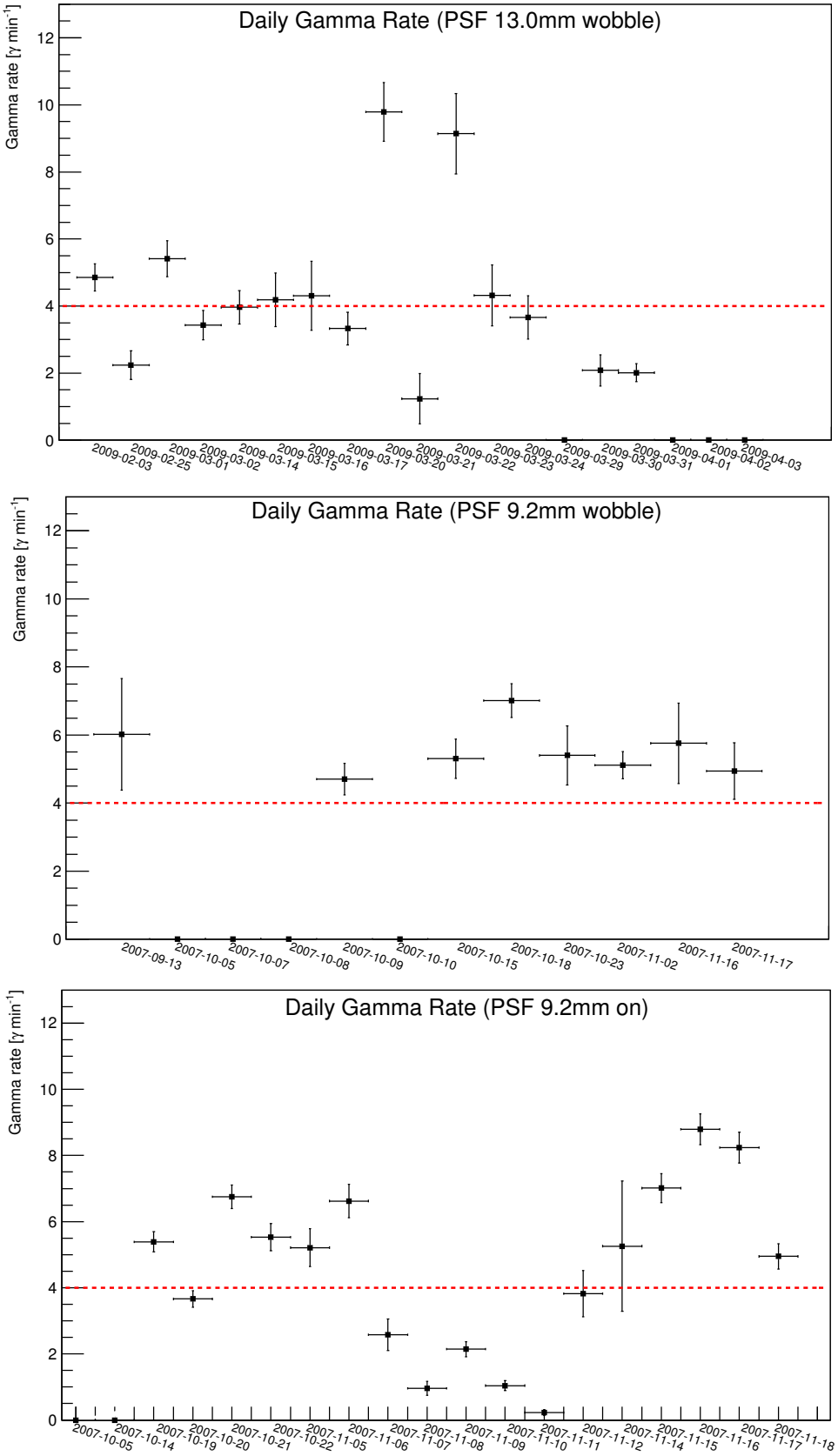

Figure B.2: Mean daily estimated gamma rates for the observation nights within the 9.2 mm and 13.0 mm PSF subsamples included in the presented analysis. Wobble and on observation modes are shown in the *top* and *bottom* plots respectively. A quality selection cut discarded all nights where gamma rate was below 4γ/min, as shown by the red, dashed line.

Appendix C

Cut optimization

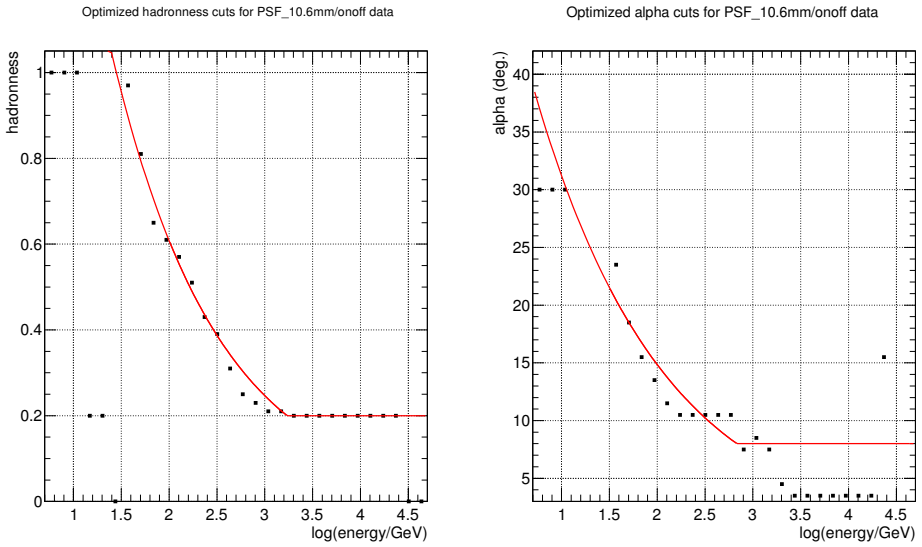

Figure C.1: Optimized cut values for hadronness and α as a function of the estimated energy for the case of on data with a 10.6 mm PSF. The black squares represent the point where a loosening of the hadronness cut reaches down to 95% of the maximum in the significance scan. These points are fitted with the function defined in equation 4.5.2, displayed here with a red, solid line. The values of the fitting parameters can be found in table 4.7.

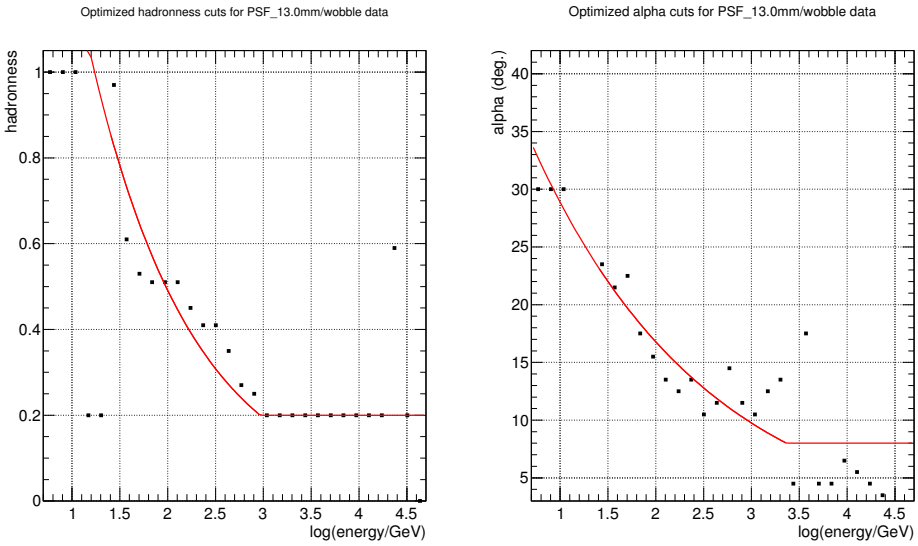

Figure C.2: Optimized cut values for hadronness and α as a function of the estimated energy for the case of wobble data with a 13.0 mm PSF. The black squares represent the point where a loosening of the hadronness cut reaches down to 95% of the maximum in the significance scan. These points are fitted with the function defined in equation 4.5.2, displayed here with a red, solid line. The values of the fitting parameters can be found in table 4.7.

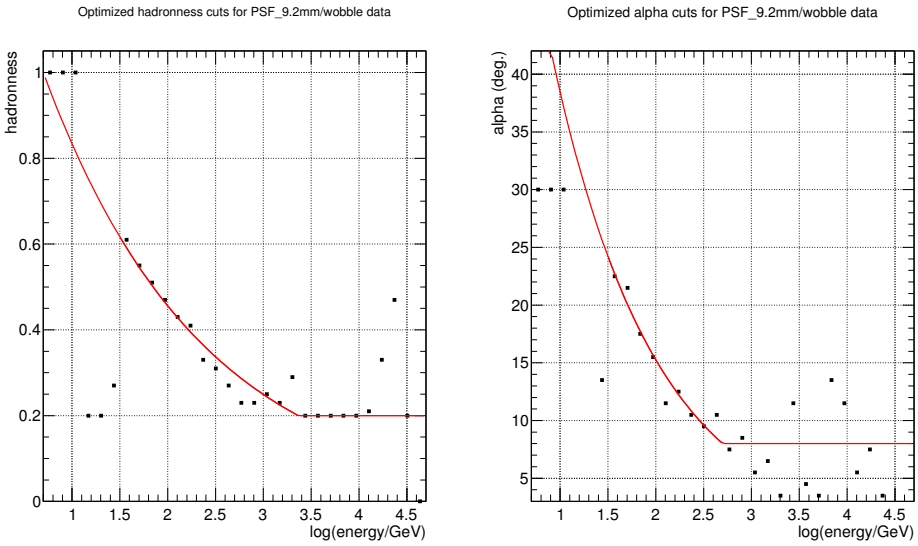

Figure C.3: Optimized cut values for hadronness and α as a function of the estimated energy for the case of wobble data with a 9.2 mm PSF. The black squares represent the point where a loosening of the hadronness cut reaches down to 95% of the maximum in the significance scan. These points are fitted with the function defined in equation 4.5.2, displayed here with a red, solid line. The values of the fitting parameters can be found in table 4.7.

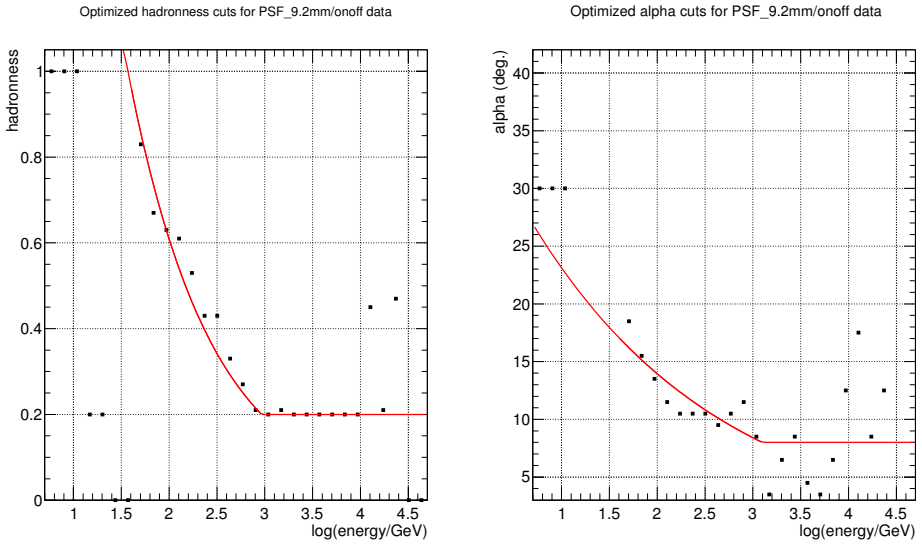

Figure C.4: Optimized cut values for hadronness and α as a function of the estimated energy for the case of on data with a 9.2 mm PSF. The black squares represent the point where a loosening of the hadronness cut reaches down to 95% of the maximum in the significance scan. These points are fitted with the function defined in equation 4.5.2, displayed here with a red, solid line. The values of the fitting parameters can be found in table 4.7.

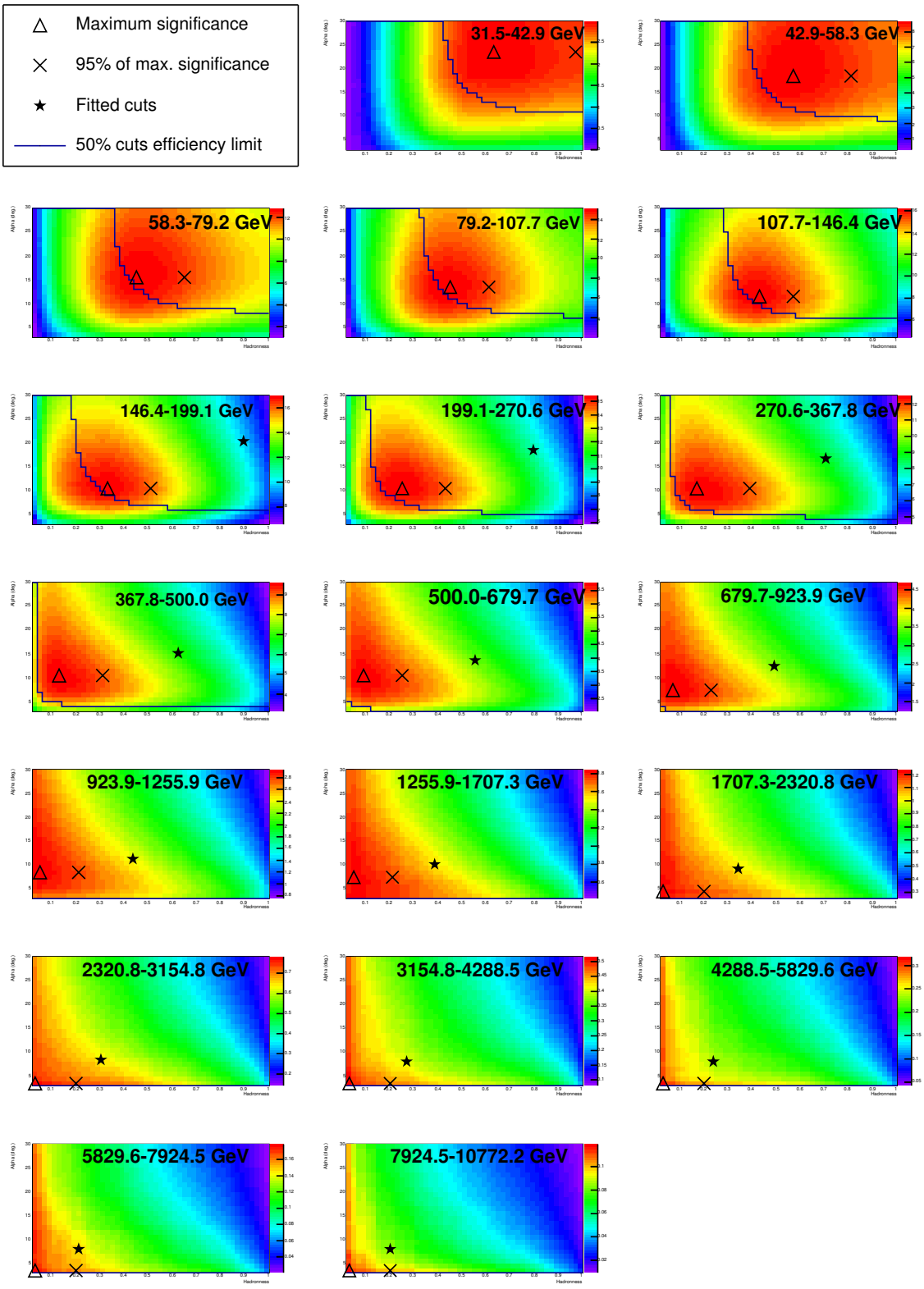

Figure C.5: Optimization of the α and hadronness plots to maximize the pulsar significance, for the case of mono data, with 10.6 mm PSF and on observation mode.

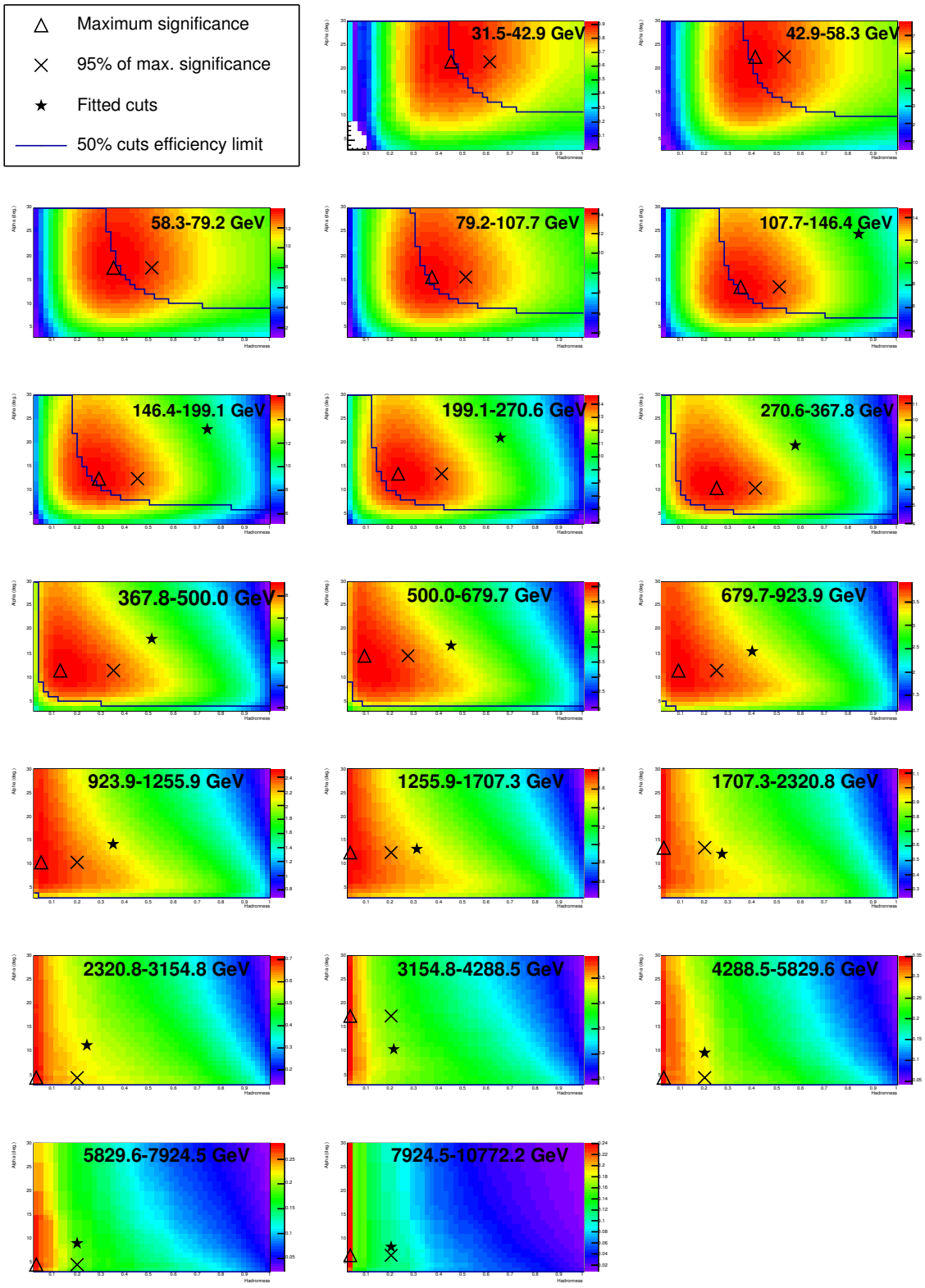

Figure C.6: Optimization of the α and hadronness plots to maximize the pulsar significance, for the case of mono data, with 13.0 mm PSF and wobble observation mode.

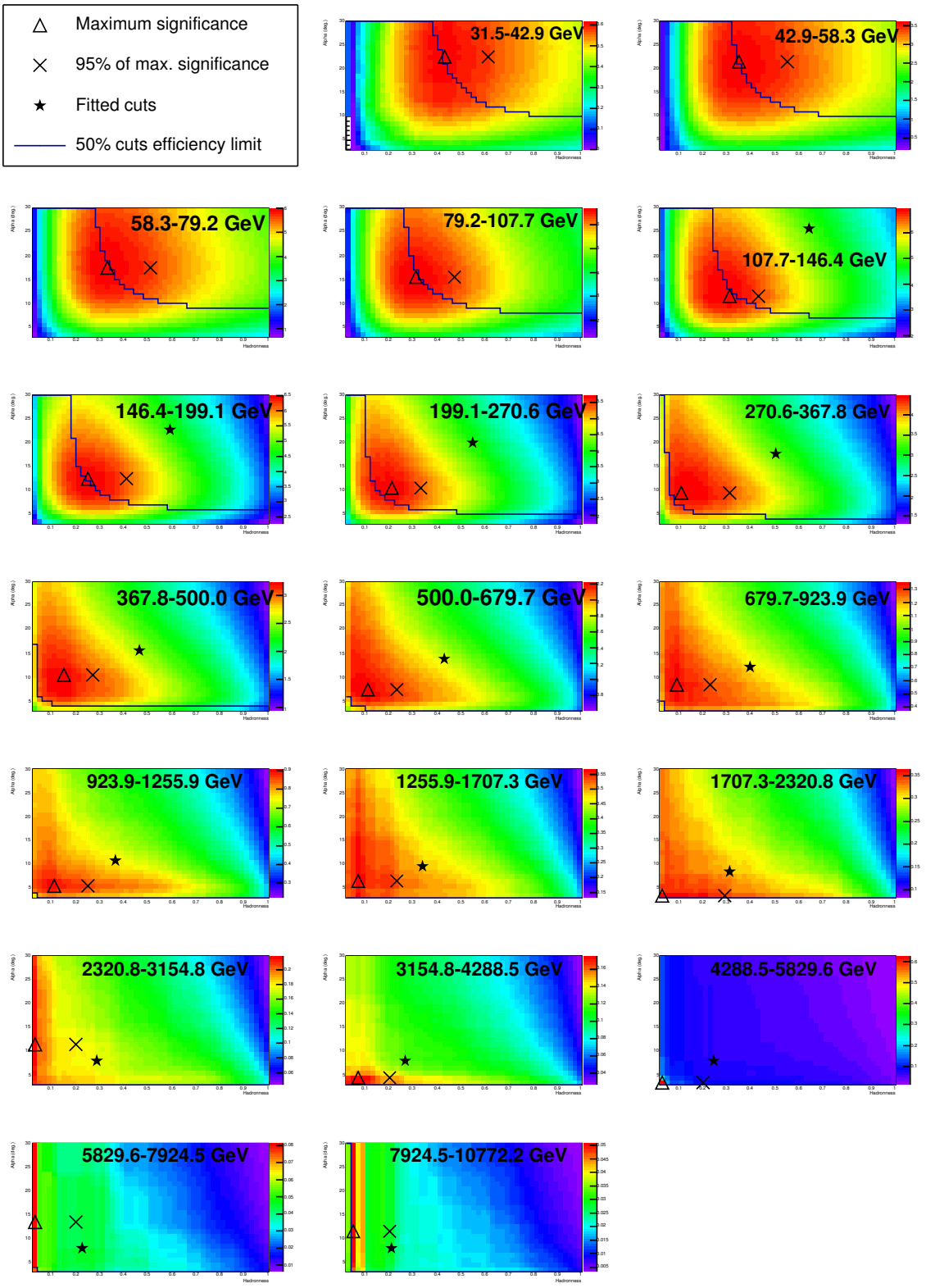

Figure C.7: Optimization of the α and hadronness plots to maximize the pulsar significance, for the case of mono data, with 9.2 mm PSF and wobble observation mode.

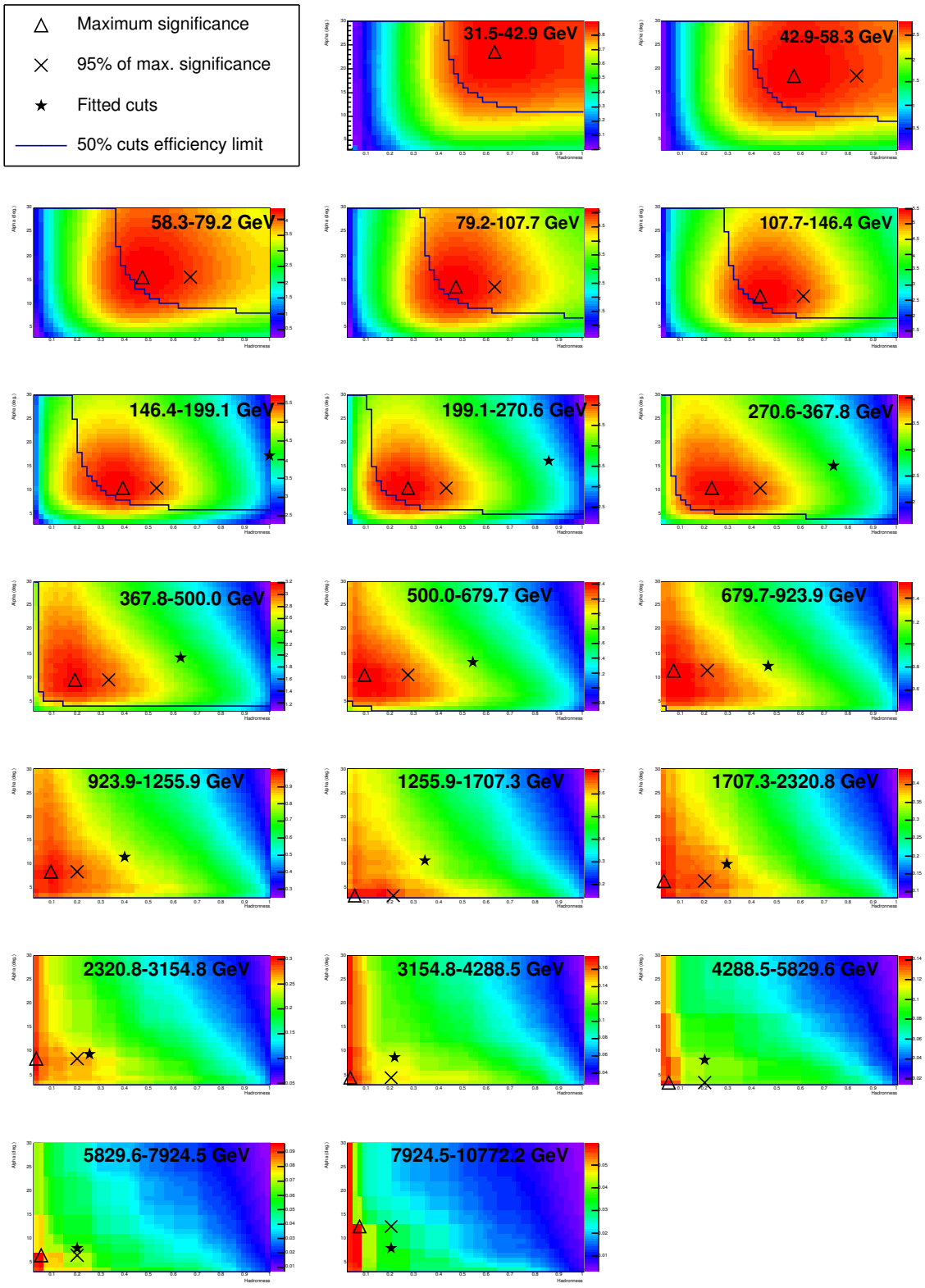

Figure C.8: Optimization of the α and hadronness plots to maximize the pulsar significance, for the case of mono data, with 9.2 mm PSF and on observation mode.

Appendix D

Pulsar phaseograms

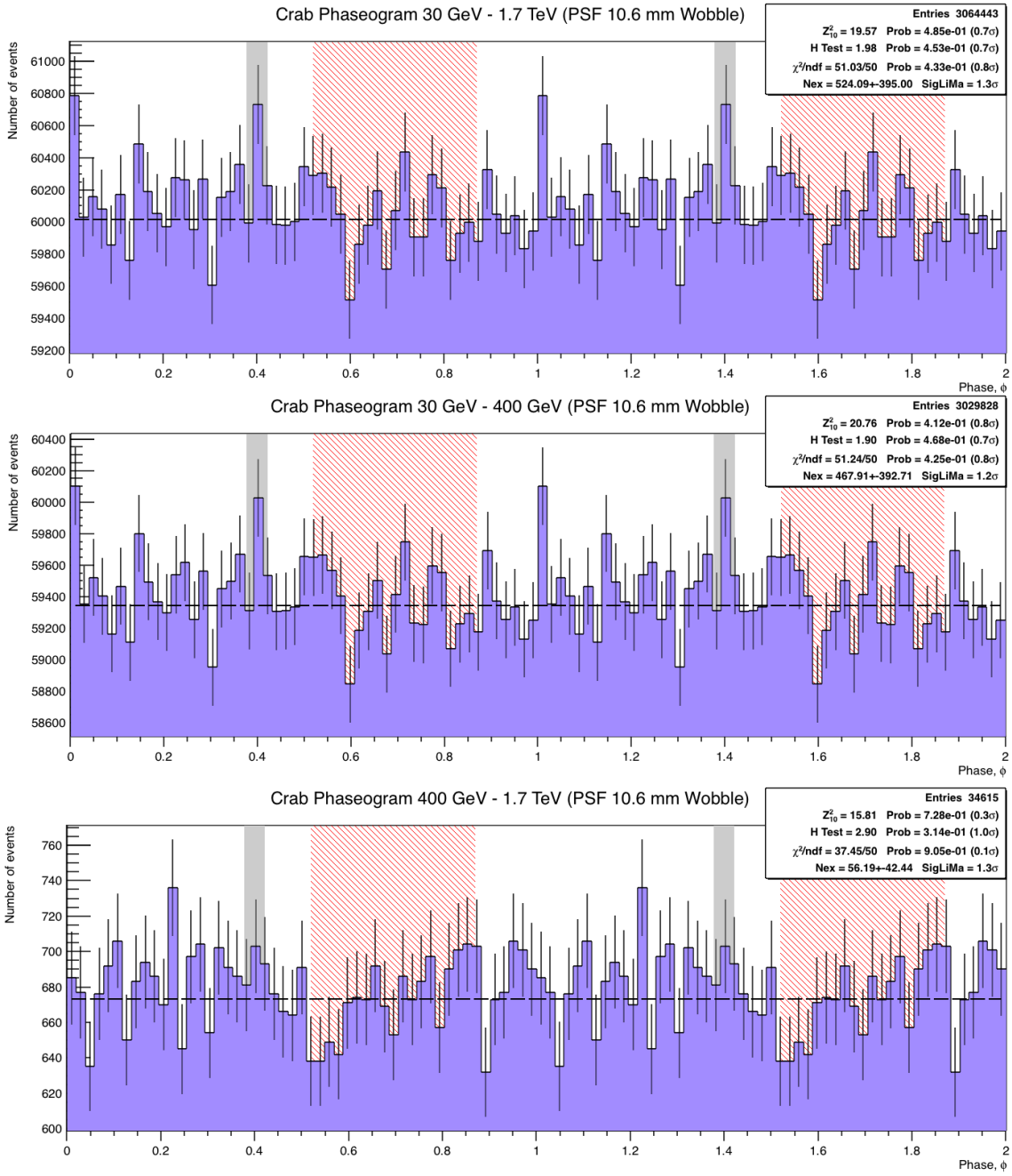

Figure D.1: Crab pulsar phaseogram obtained with the observations in wobble mode with a 10.6 mm PSF. The full (*top*), low (*mid*) and high (*bottom*) energy ranges are shown and two full rotations are displayed for an easier interpretation ($0 < \phi < 2$). The on and off regions are marked with the solid-grey and diagonal-red-lined areas respectively, as well as the background level estimated from the off region (dashed black line). The number of excesses in the signal region and its significance, as measured by each of the test statistics explained in §2.5.7, are shown in the top-right box within each plot.

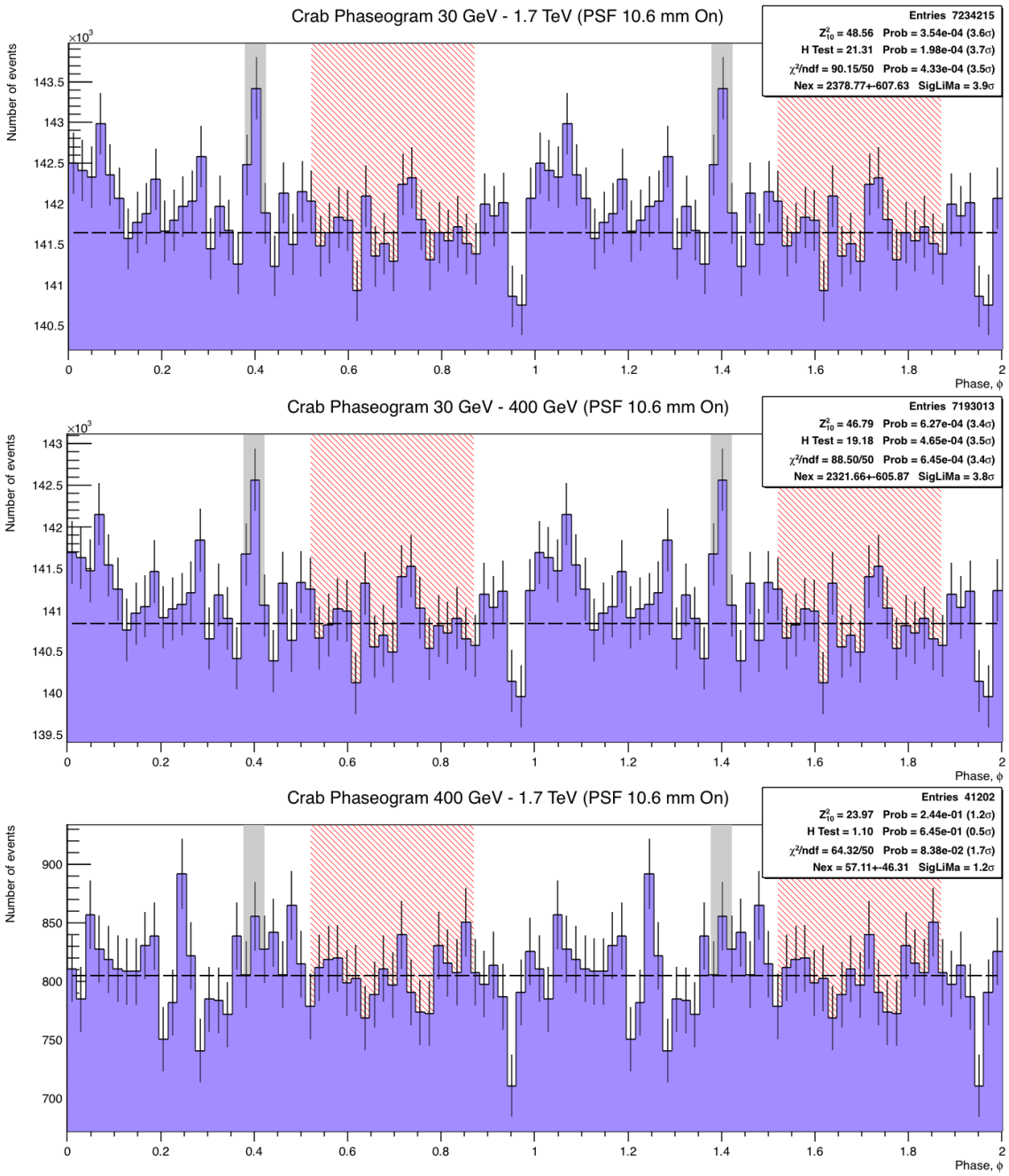

Figure D.2: Crab pulsar phaseogram obtained with the observations in on mode with a 10.6 mm PSF. The full (*top*), low (*mid*) and high (*bottom*) energy ranges are shown and two full rotations are displayed for an easier interpretation ($0 < \phi < 2$). The on and off regions are marked with the solid-grey and diagonal-red-lined areas respectively, as well as the background level estimated from the off region (dashed black line). The number of excesses in the signal region and its significance, as measured by each of the test statistics explained in §2.5.7, are shown in the top-right box within each plot.

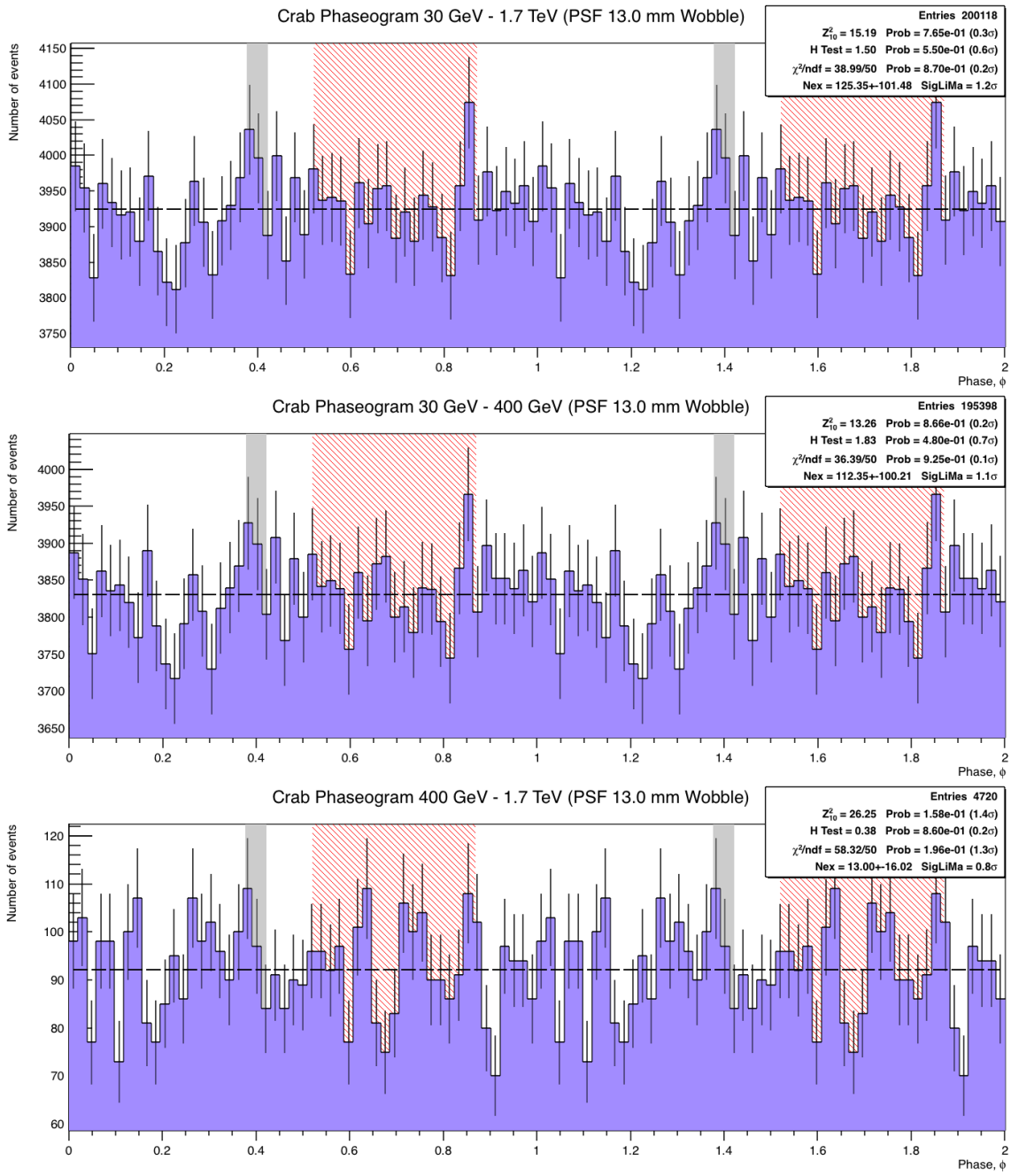

Figure D.3: Crab phaseogram obtained with the observations in wobble mode with a 13.0 mm PSF. The full (*top*), low (*mid*) and high (*bottom*) energy ranges are shown and two full rotations are displayed for an easier interpretation ($0 < \phi < 2$). The on and off regions are marked with the solid-grey and diagonal-red-lined areas respectively, as well as the background level estimated from the off region (dashed black line). The number of excesses in the signal region and its significance, as measured by each of the test statistics explained in §2.5.7, are shown in the top-right box within each plot.

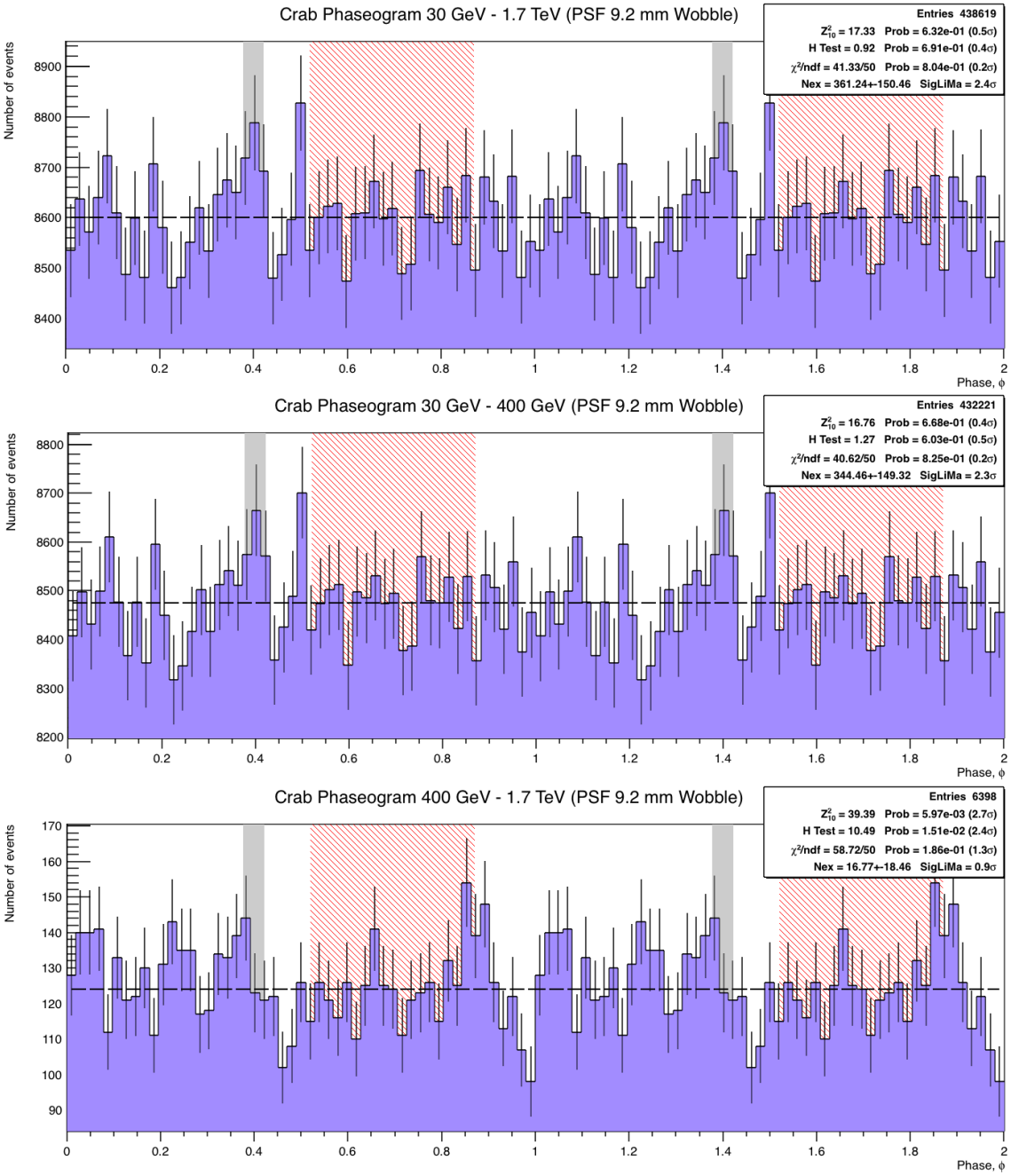

Figure D.4: Crab phaseogram obtained with the observations in wobble mode with a 9.2 mm PSF. The full (*top*), low (*mid*) and high (*bottom*) energy ranges are shown and two full rotations are displayed for an easier interpretation ($0 < \phi < 2$). The on and off regions are marked with the solid-grey and diagonal-red-lined areas respectively, as well as the background level estimated from the off region (dashed black line). The number of excesses in the signal region and its significance, as measured by each of the test statistics explained in §2.5.7, are shown in the top-right box within each plot.

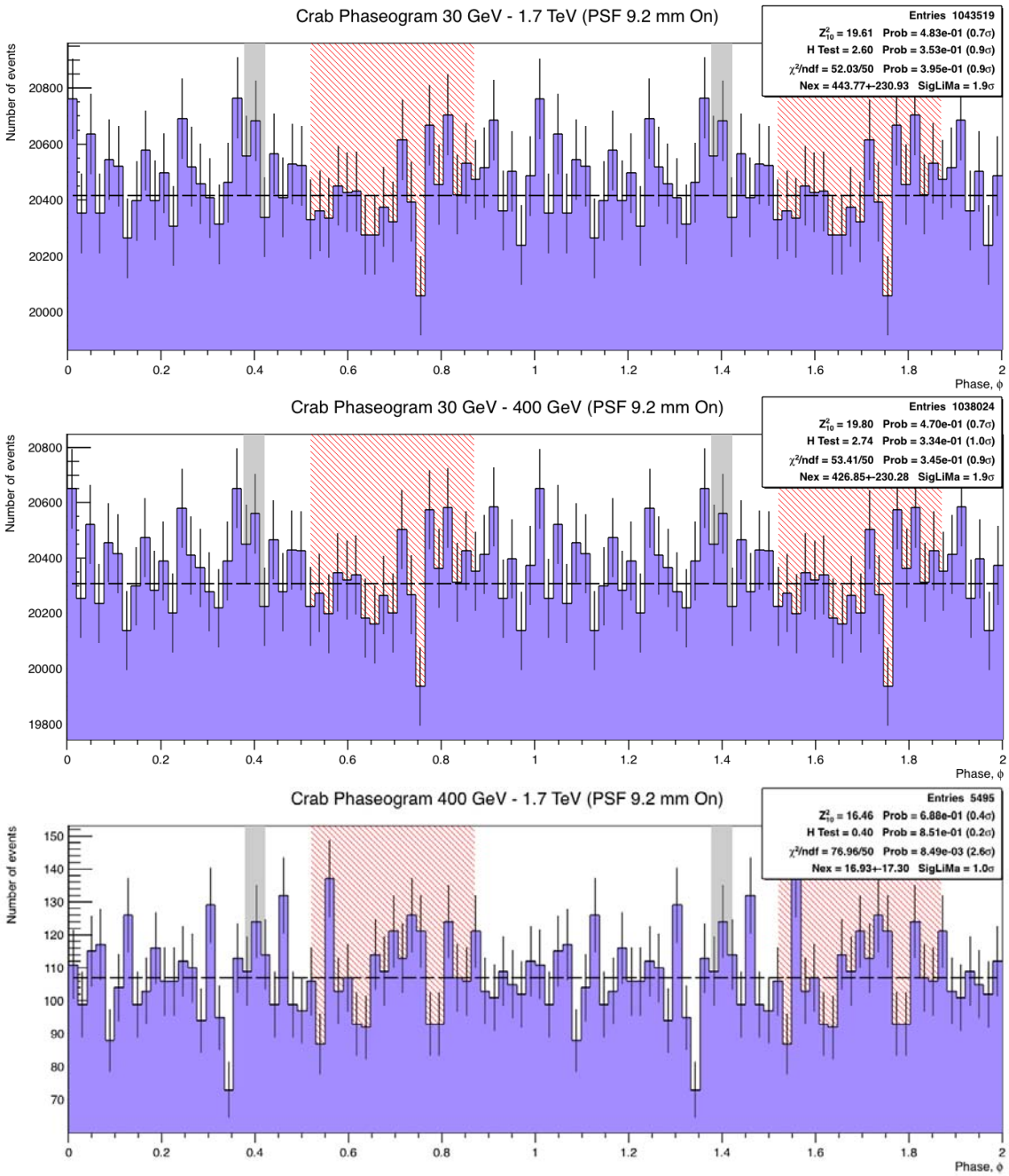

Figure D.5: Crab phaseogram obtained with the observations in on mode with a 9.2 mm PSF. The full (*top*), low (*mid*) and high (*bottom*) energy ranges are shown and two full rotations are displayed for an easier interpretation ($0 < \phi < 2$). The on and off regions are marked with the solid-grey and diagonal-red-lined areas respectively, as well as the background level estimated from the off region (dashed black line). The number of excesses in the signal region and its significance, as measured by each of the test statistics explained in §2.5.7, are shown in the top-right box within each plot.

Agradecimientos/Acknowledgements

This work has been founded by the Formación de Profesorado Universitario grant AP2010-3687, by Ministerio de Educación, Cultura y Deportes of Gobernment of Spain. Thanks to the IAC for the excellent working conditions at the Roque de los Muchachos observatory, as well as to the MAGIC collaboration for such a stimulating and friendly environment.

Este trabajo ha sido financiado pero la beca Formación de Profesorado Universitario número AP2010-3687 del Ministerio de Educación, Cultura y Deportes del Gobierno de España.

Abbreviatures and Acronyms

a.s.l.	above sea level
AMC	Active Mirror Control
AUI	Associated Universities, Inc.
BMFB	*Bundesministerium für Forschung und Bildung*
Callisto	CALibrate LIght Signals and Time Offsets
CANGAROO	Collaboration of Australia and Nippon (Japan) for a GAmma Ray Observatory in the Outback
CCD	Charge-Coupled Device
CoG	Center of Gravity
CR	Cosmic Ray
CTA	Cherenkov Telescope Array
DAQ	Data AQuisition system
DRS4	Domino Ring Sampler version 4
e^-/e^+	electron/positron
EAS	Electromagnetic Air Shower
EM	ElectroMagnetic
FADC	Fast Analogue-to-Digital Converters
FoV	Field of View
GmBH	*Gesellschaft mit beschränkter Haftung*
GR	General Relativity
GRB	Gamma Ray Burst
GUT	Grand Unification Theory
HEGRA	High Energy Gamma Ray Astronomy
H.E.S.S.	High Energy Stereoscopic System
HPD	Hybrid Photo-Detector
IAC	Instituto de Astrofísica de Canarias
IACT	Imaging Atmospheric Cherenkov Telescope

i.e.	latin for *id est*, it is used for clarification
INFN	*Istituto Nazionale di Fisica Nucleare*
L0, L1, L2, L3	trigger Levels 0, 1, 2 and 3 respectively
LIDAR	LIght Detection And Ranging
LIV	Lorentz Invariance Violation
LQG	Loop Quantum Gravity
LUT	Look-Up Table
MAGIC	Major Atmospheric Gamma-ray Imaging Cherenkov telescope (it refers to the stereoscopic system unless stated otherwise)
MC	MonteCarlo
Melibea	MErge and Link Image parameter Before Energy Analysis
MHD	Magneto HydroDynamic
MICINN	Ministerio de Ciencia e Innovación
ML	Maximum Likelihood
MPG	Max-Planck-Gesellschaft
MS	MAGIC Summer atmospheric model
MSE	Mean Squared Error
MW	MAGIC Winter atmospheric model
NRAO	Nationa Radio Astronomy Observatory
NSB	Night Sky Background
ORM	Observatorio del Roque de los Muchachos
Osteria	Optimize STandard Energy Reconstruction and Image Analysis
$p/p^+/H^+$	proton
PIC	Port d'Infraestructures Científiques
PMT	PhotoMultiplier Tube
PSF	Point-Spread Function
PULSAR	PULSer And Recorder board
PWN	Pulsar Wind Nebula
QFT	Quantum Field Theory
QG	Quantum Gravity
RF	Random Forest
SI	*Système International d'Unités*
SR	Special Relativity
ST	Sum Trigger
Star	STandard Analysis and Reconstruction
TAC	Time Allocation Committee
TNG	Telescopio Nazionale Galileo
UAB	Universitat Autònoma de Barcelona
VERITAS	Very Energetic Radiation Imaging Telescope Array System
VLA	Karl G. Jansky Very Large Array radio observatory
WS	Weather Station

Metric prefixes

Name	Symbol	Tenth power	Decimal Value
yotta	Z	10^{24}	1,000,000,000,000,000,000,000,000
zetta	Y	10^{21}	1,000,000,000,000,000,000,000
eta	E	10^{18}	1,000,000,000,000,000,000
peta	P	10^{15}	1,000,000,000,000,000
tera	T	10^{12}	1,000,000,000,000
giga	G	10^{9}	1,000,000,000
mega	M	10^{6}	1,000,000
kilo	k	10^{3}	1,000
hecto	h	10^{2}	100
deca	da	10^{1}	10
-	-	10^{0}	1
deci	d	10^{-1}	0.1
centi	c	10^{-2}	0.01
milli	m	10^{-3}	0.001
micro	μ	10^{-6}	0.000 001
nano	n	10^{-9}	0.000 000 001
pico	p	10^{-12}	0.000 000 000 001
fempto	f	10^{-15}	0.000 000 000 000 001
atto	a	10^{-18}	0.000 000 000 000 000 001
zepto	z	10^{-21}	0.000 000 000 000 000 000 001
yocto	y	10^{-24}	0.000 000 000 000 000 000 000 001

List of Figures

List of Tables

Bibliography

[1] M. S. Longair, *High Energy Astrophysics*, vol. 1, 2nd edn. (Cambridge University Press1992).

[2] H. Bradt, *Astrophysics processes: The Physics of Astronomical Phenomena* (Cambridge University Press2008).

[3] R. A. Perley, J. W. Dreher and J. J. Cowan, *The jet and filaments in Cygnus A*, The Astrophysical Journal, **285** (1984): pp. L35–L38, URL http://adsabs.harvard.edu/abs/1984ApJ...285L..35P.

[4] P. L. Biermann et al., *Single and binary black holes and their active environment*, in *Proceedings of the 7eme Colloquium Cosmologie* (N. Sanchez and H. de Vega2002), URL http://arxiv.org/abs/astro-ph/0211503.

[5] R. Antonucci, *Unified models for active galactic nuclei and quasars*, Annual review of astronomy and astrophysics, **31** (1993): pp. 473–521, URL http://adsabs.harvard.edu/full/1993ARA%26A..31..473A.

[6] R. Diehl et al., *COMPTEL observations of galactic ^{26}Al emission*, Astronomy and Astrophysics, **298** (1995): p. 445, URL http://adsabs.harvard.edu/abs/1995A%26A...298..445D.

[7] S. P. Reynolds, *Supernova remnants at high energy*, Annual Review of Astronomy and Astrophysics, **46** (2008) (1): pp. 89–126, doi:http://dx.doi.org/10.1146/annurev.astro.46.060407.145237.

[8] J. Aleksić and others (The MAGIC Collaboration), *Morphological and spectral properties of the W51 region measured with the MAGIC telescopes*, Astronomy & Astrophysics, **541** (2012): p. A13, URL http://arxiv.org/abs/1201.4074.

[9] A. P. Marscher et al., *Observational evidence for the accretion-disk origin for a radio jet in an active galaxy*, Nature, **417** (2002): pp. 625–627, URL http://dx.doi.org/10.1038/nature00772.

[10] W. Kraushaar and G. Clark, *Gamma-ray astronomy*, Scientific American (U.S.), (1962), URL http://www.osti.gov/scitech/servlets/purl/4096241.

[11] R. Sato, *Long term performance of the surface detectors of the Pierre Auger observatory*, in *International Cosmic Ray Conference*, vol. 3, p. 200 (2011).

[12] J. Abraham et al., *The fluorescence detector of the Pierre Auger Observatory*, Nuclear Instruments and Methods in Physics Research Section A: Accelerators, Spectrometers, Detectors and Associated Equipment, **620** (2010) (2–3): pp. 227 – 251, doi:http://dx.doi.org/10.1016/j.nima.2010.04.023.

[13] N. Chiba et al., *Akeno Giant Air Shower Array (AGASA) covering 100 km^2 area*, Nuclear Instruments and Methods in Physics Research Section A: Accelerators, Spectrometers, Detectors and Associated Equipment, **311** (1992) (1–2): pp. 338 – 349, doi:http://dx.doi.org/10.1016/0168-9002(92)90882-5.

[14] T. Antoni et al., *The cosmic-ray experiment KASCADE*, Nuclear Instruments and Methods in Physics Research Section A: Accelerators, Spectrometers, Detectors and Associated Equipment, **513** (2003) (3): pp. 490 – 510, doi:http://dx.doi.org/10.1016/S0168-9002(03)02076-X.

[15] P. Sokolsky, *Final results from the high solution flys eye (HiRes) experiment*, Nuclear Physics B - Proceedings Supplements, **212–213** (2011) (0): pp. 74–78, doi:http://dx.doi.org/10.1016/j.nuclphysbps.2011.03.010.

[16] V. Hess, *Über Beobachtungen der durchdringenden Strahlung bei sieben Freibal-lonfahrten*, Physikalische Zeitschrift, **13** (1912): pp. 1084–1091.

[17] M. Nagano and A. A. Watson, *Observations and implications of the ultrahigh-energy cosmic rays*, Reviews of Modern Physics, **72** (2000) (3), URL http://journals.aps.org/rmp/pdf/10.1103/RevModPhys.72.689.

[18] T. P. collaboration, *Large-scale distribution of arrival directions of cosmic rays detected above 10^{18} eV at the Pierre Auger observatory*, The Astrophysical Journal Supplement Series, **203** (2012) (2): p. 34, URL http://stacks.iop.org/0067-0049/203/i=2/a=34.

[19] G. Cocconi, *Extensive air showers*, in S. Flügge (ed.), *Cosmic Rays I / Kosmische Strahlung I*, *Encyclopedia of Physics*, vol. 9 / 46 / 1, pp. 215–271 (Springer Berlin Heidelberg1961), doi:http://dx.doi.org/10.1007/978-3-642-45964-1_5.

[20] J. F. Carlson and J. Oppenheimer, *On multiplicative showers*, Physical Review, **51** (1937): pp. 220–231, URL http://link.aps.org/doi/10.1103/PhysRev.51.220.

[21] D. Tescaro, *TeV gamma-ray observations of nearby Active Galactic Nuclei with the MAGIC telescope: exploring the high energy region of the multiwavelength picture*, Ph.D. thesis, Universitat Autònoma de Barcelona, 2010.

[22] K. Bernlöhr, *Simulation of imaging atmospheric Cherenkov telescopes with CORSIKA and sim_telarray*, Astroparticle Physics, **30** (2008) (3): pp. 149–158, URL http://arxiv.org/abs/0808.2253.

[23] J. B. Gonzalez, *Study of Very High Energy Gamma Ray Sources: Discovery of the Blazars PKS 1222+21 and 1ES 1215+303*, Ph.D. thesis, Instituto de Astroísica de Canarias, September 2011.

[24] K. Bernlohr, *Impact of atmospheric parameters on the atmospheric Cherenkov technique*, Astroparticle Physics, **12** (2000) (4): pp. 255–268.

[25] T. C. Weekes, M. F. Cawley, D. J. Fegan, K. G. Gibbs, A. M. Hillas, P. K. Kwok, R. C. Lamb, D. A. Lewis, D. Macomb, N. A. Porter, P. T. Reynolds and G. Vacant, *Observation of TeV gamma-rays from the Crab nebula using the atmospheric Cherenkov imaging technique*, The Astrophysical Journal, **342** (1989): pp. 379–395.

[26] J. Aleksić et al., *The major upgrade of the MAGIC telescopes, Part II: The achieved physics performance using the Crab nebula observations*, (Accepted for publication in Astroparticle Physics), (2015), URL http://arxiv.org/abs/1409.5594.

[27] T. M. Collaboration, *MAGIC introduction*, 2013, URL https://magic.mpp.mpg.de/newcomers/introduction/.

[28] J. Barrio et al., *The MAGIC telescope*, design study, MPI-PhE/98-5, (1998).

[29] J. Cortina, F. Goebel and T. Schweizer, *Technical performance of the MAGIC telescopes*, ArXiv e-Prints, (2009), URL http://arxiv.org/abs/0907.1211.

[30] S. Ritt, *Design and performance of the 6 GHz waveform digitizing chip DRS4*, IEEE Nuclear Science Symposium Conference Record, (2008): pp. 1512–1515.

[31] T. Bretz, D. Dorner, R. Wagner and P. Sawallisch, *The drive system of the major atmospheric gamma-ray imaging Cherenkov telescope*, Astroparticle Physics, **31** (2009): pp. 92–101.

[32] A. Billand and others for the MAGIC Collaboration, *The active mirror control of the MAGIC telescope*, in *30th International Cosmic Ray Conference* (2007), URL http://arxiv.org/abs/0709.1574.

[33] R. Paoletti, R. Cecchi, D. Corti, F. Dazzi, M. Mariotti, R. Pegna and N. Turini, *The trigger system of the MAGIC telescope*, IEEE Transactions on Nuclear Science, **54** (2007): pp. 404–409, doi:http://dx.doi.org/10.1109/TNS.2007.892649.

[34] R. López-Coto et al., *The topo-trigger: a new concept of stereo trigger system for imaging atmospheric Cherenkov telescopes*, in preparation.

[35] T. T. Liu, *CDF PULSAR board*, 2004, URL http://hep.uchicago.edu/~thliu/projects/Pulsar/.

[36] M. T. Rissi, *Detection of Pulsed Very High Energy Gamma-Rays from the Crab Pulsar with the MAGIC telescope using an Analog Sum Trigger*, Ph.D. thesis, Swiss Federal Institute of TechnologyZurich, 2009.

[37] E. Aliu and others (The MAGIC Collaboration), *Observation of pulsed gamma-rays above 25 GeV from the Crab pulsar with MAGIC*, Science, **322** (2008): p. 1221.

[38] L. Font, M. Doro, C. Fruck, M. Garczarczyk, D. Garrido and for the MAGIC Collaboration, *Monitoring and calibration of the atmosphere in magic*, in *Proceedings of the 33th International Cosmic Ray Conference in Rio de Janeiro, Brazil* (2013).

[39] C. Fruck, *A novel LIDAR-based atmospheric calibration method for improving the data analysis of MAGIC*, in *Proceedings of the 33th International Cosmic Ray Conference in Rio de Janeiro, Brazil* (2013).

[40] C. Fruck, M. Gaug, R. Zanin, D. Dorner and D. Garrido, *A novel LIDAR-based atmospheric calibration method for improving the data analysis of MAGIC*, in *Proceedings of the 33th International Cosmic Ray Conference in Rio de Janeiro, Brazil* (2013).

[41] G. Giavitto, *Observing the VHE Gamma-Ray Sky with the MAGIC Telescopes: the Blazar B3 2247+381 and the Crab Pulsar*, Ph.D. thesis, Universitat Autònoma de Barcelona, 2013.

[42] V. Fomin, A. Stepanian, R. Lamb, D. Lewis, M. Punch and T. Weekes, *New methods of atmospheric Cherenkov imaging for gamma-ray astronomy. I. The false source method*, Astroparticle Physics, **2** (1994) (2): pp. 137 – 150, doi:http://dx.doi.org/10.1016/0927-6505(94)90036-1.

[43] A. Moralejo, M. Gaug, E. Carmona, P. Colin, C. Delgado, S. Lombardi, D. Mazin, V. Scalzotto, J. Sitarek, D. Tescaro and for the MAGIC collaboration, *MARS, the MAGIC analysis and reconstruction software*.

[44] T. R. Team, *A data analysis framework*.

[45] M. Gaug, *Calibration of the MAGIC Telescope and Observation of Gamma Ray Bursts*, Ph.D. thesis, Universitat Autònoma de Barcelona, March 2006.

[46] R. Mirzoyan and E. Lorenz, *On the calibration accuracy of light sensors in atmospheric Cherenkov, fluorescence and neutrino experiments*, in *Proceedings of the 25th International Cosmic Ray Conference in Durban, South Africa* (1997).

[47] R. Lessard, J. Buckley, V. Connaughton and S. Le Bohec, *A new analysis method for reconstructing the arrival direction of TeV gamma-rays using a single imaging atmospheric cherenkov telescope*, Astroparticle Physics, **15** (2001) (1): pp. 1–18.

[48] A. M. Hillas, *Cherenkov light images of EAS produced by primary gamma*, in *19th International Cosmic Ray Conference Proceedings*, p. 445 (1985).

[49] J. Aleksić and others (The MAGIC Collaboration), *Search for an extended VHE γ-ray emission from Mrk 421 and Mrk 501 with the MAGIC telescope*, Astronomy & Astrophysics, **524** (2010) (A77), URL http://dx.doi.org/10.1051/0004-6361/201014747.

[50] I. Reichardt, *Massive, automatic data analysis for the MAGIC telescopes*, Master's thesis, Universitat Autònoma de Barcelona, December 2009, URL https://magicold.mpp.mpg.de/publications/theses/IReichardt.pdf.

[51] J. Albert and others (The MAGIC Collaboration), *Implementation of the random forest method for the Imaging Atmospheric Cherenkov Telescope MAGIC*, Nuclear Instruments and Methods in Physics Research Section A: Accelerators, Spectrometers, Detectors and Associated Equipment, **588** (2008) (3): pp. 424 – 432, doi:http://dx.doi.org/10.1016/j.nima.2007.11.068.

[52] T.-P. Li and Y.-Q. Ma, *Analysis methods for results in gamma-ray astronomy*, The Astrophysical Journal, **272** (1983): pp. 317–324, URL http://adsabs.harvard.edu/full/1983ApJ...272..317L7.

[53] A. Lyne and M. Roberts, *Jodrell Bank Crab pulsar monthly ephemeris*, 2014, URL http://www.jb.man.ac.uk/~pulsar/crab.html.

[54] M. L. Moya, *Astronomía Gamma con el Telescopio MAGIC: Observaciones de la Nebulosa y Pulsar del Cangrejo*, Ph.D. thesis, Universidad Complutense de Madrid, July 2006.

[55] I. I. Shapiro, *Fourth test of General Relativity*, Physical Review Letters, **13** (1964): pp. 789–791, doi:http://dx.doi.org/10.1103/PhysRevLett.13.789.

[56] R. Manchester, G. Hobbs, A. Teoh and M. Hobbs, *The australia telescope national facility pulsar catalogue*, The Astrophysical Journal, **129** (2005) (4): pp. 1993–2006, URL http://www.atnf.csiro.au/people/pulsar/psrcat/.

[57] W. Baade and F. Zwicky, *On supernovae*, Proceedings of the National Academy of Sciences of the United States of America, **20** (1934): pp. 254–259.

[58] F. Pacini, *Energy emission from a neutron star*, Nature, **216** (1967) (5115): pp. 567–568, URL http://dx.doi.org/10.1038/216567a0.

[59] T. Gold, *Rotating neutron stars as the origin of the pulsating radio sources*, Nature, **218** (1968) (5143): pp. 731–732, URL http://dx.doi.org/10.1038/218731a0.

[60] A. Abdo and others (The Fermi-LAT Collaboration), *The second Fermi pulsar catalogue*, Astrophysical Journal Supplement, **208** (2013) (2), URL http://arxiv.org/abs/1305.4385.

[61] M. Ruderman, *Neutron starquakes and pulsar periods*, Nature, **223** (1969): pp. 597–598.

[62] A. G. Lyne and F. Graham-Smith, *Pulsar Astronomy*, 3rd edn. (Cambridge University Press2006).

[63] R. Hulse and J. Taylor, *Discovery of a pulsar in a binary system*, The Astrophysical Journal, **195** (1975): pp. L51–L53, URL http://adsabs.harvard.edu/full/1975ApJ...195L..51H.

[64] J. H. Taylor, L. A. Fowler and P. M. McCulloch, *Measurements of general relativistic effects in the binary pulsar PSR1913+16*, Nature, **277** (1979): pp. 437–440, URL http://dx.doi.org/10.1038/277437a0.

[65] J. Weisberg and J. H. Taylor, *The relativistic binary pulsar B1913+16: Thirty years of observations and analysis*, in F. A. Rasio and I. H. Stairs (eds.), *Binary Radio Pulsars*, vol. 328, p. 25 (2004), URL http://arxiv.org/abs/astro-ph/0407149.

[66] K. Brecher, R. A. Fesen, S. P. Maran and J. C. Brandt, *Ancient records and the Crab nebula supernova*, The Observatory, **103** (193): pp. 106–113, URL http://adsabs.harvard.edu/full/1983Obs...103..106B.

[67] T. Schweizer, N. Bucciantini, W. Idec, K. Nilsson, A. Tennant, M. Weisskopf and R. Zanin, *Characterization of the optical and X-ray properties of the northwestern wisps in the Crab nebula*, Monthly Notices of the Royal Astronomical Society, **433** (2012) (4): pp. 3325–3335, URL http://mnras.oxfordjournals.org/content/433/4/3325.abstract.

[68] R. Bühler and R. Blandford, *The surprising Crab pulsar and its nebula: a review*, Reports on Progress in Physics, **77** (2014) (6): p. 066,901, URL http://stacks.iop.org/0034-4885/77/i=6/a=066901.

[69] A. Abdo and others (The Fermi-LAT Collaboration), *Fermi large area telescope observations of the Crab pulsar and nebula.*, The Astrophysical Journal, **708** (2010): pp. 1254–1267.

[70] E. Aliu and others (The VERITAS Collaboration), *Detection of pulsed gamma-rays above 100 GeV from the Crab pulsar*, Science, **334** (2011): p. 69.

[71] J. A. et. al. (The MAGIC Collaboration), *Phase-resolved energy spectra of the Crab pulsar in the range of 50-400 GeV measured with the MAGIC telescopes*, Astronomy & Astrophysics, **540** (2012): p. A69.

[72] J. Aleksić and others (The MAGIC Collaboration), *Detection of bridge emission above 50 GeV from the Crab pulsar with the MAGIC telescopes*, Astronomy & Astrophysics, **565** (2014): p. L12, URL http://adsabs.harvard.edu/abs/2014A%26A...565L..12A.

[73] J. Aleksić and others (The MAGIC Collaboration), *Observations of the Crab pulsar between 25 and 100 GeV with the MAGIC I telescope*, The Astrophysical Journal, **742** (2011) (1): p. 43, URL http://stacks.iop.org/0004-637X/742/i=1/a=43.

[74] P. Goldreich and W. H. Julian, *Pulsar Electrodynamics*, The Astrophysical Journal, **157** (1969): p. 869, doi:http://dx.doi.org/10.1086/150119.

[75] S. S. Komissarov, *Time-dependent, force-free, degenerate electrodynamics*, Monthly Notices of the Royal Astronomical Society, **336** (2002): pp. 759–766, URL http://adsabs.harvard.edu/abs/2002MNRAS.336..759K, astro-ph/0202447.

[76] F. A. Aharonian, S. V. Bogovalov and D. Khangulyan, *Abrupt acceleration of a /'cold/' ultrarelativistic wind from the Crab pulsar*, Nature, **482** (2012) (7386): pp. 507–509, URL http://dx.doi.org/10.1038/nature10793.

[77] P. A. Sturrock, *A Model of Pulsars*, The Astrophysical Journal, **164** (1971): p. 529.

[78] J. K. Daugherty and A. K. Harding, *Gamma-ray pulsars: Emission from extended polar cap cascades*, The Astrophysical Journal, **458** (1996): p. 278, doi:http://dx.doi.org/10.1086/176811.

[79] K. S. Cheng, C. Ho and M. Ruderman, *Energetic radiation from rapidly spinning pulsars. I - Outer magnetosphere gaps. II - VELA and Crab*, The Astrophysical Journal, **300** (1986): pp. 500–539, doi:http://dx.doi.org/10.1086/163829.

[80] K. S. Cheng, M. Ruderman and L. Zhang, *A three-dimensional outer magnetospheric gap model for gamma-ray pulsars: Geometry, pair production, emission morphologies and phase-resolved spectra*, The Astrophysical Journal, **537** (2000) (2): p. 964, URL http://stacks.iop.org/0004-637X/537/i=2/a=964.

[81] J. Dyks and B. Rudak, *Two-pole caustic model for high-energy light curves of pulsars*, The Astrophysical Journal, **598** (2003) (2): p. 1201, URL http://stacks.iop.org/0004-637X/598/i=2/a=1201.

[82] D. Viganò, D. F. Torres, K. Hirotani and M. E. Pessah, *An assessment of the pulsar outer gap model – i. assumptions, uncertainties, and implications on the gap size and the accelerating field*, Monthly Notices of the Royal Astronomical Society, **447** (2015) (3): pp. 2631–2648, URL http://mnras.oxfordjournals.org/content/447/3/2631.abstract.

[83] D. Viganò, D. F. Torres, K. Hirotani and M. E. Pessah, *An assessment of the pulsar outer gap model – II. Implications for the predicted gamma-ray spectra*, Monthly Notices of the Royal Astronomical Society, **447** (2015) (3): pp. 2649–2657, URL http://mnras.oxfordjournals.org/content/447/3/2649.abstract.

[84] A. G. Muslimov and A. K. Harding, *High-altitude particle acceleration and radiation in pulsar slot gaps*, The Astrophysical Journal, **606** (2004): pp. 1143–1153.

[85] K. Hirotani, *Outer-gap versus slot-gap models for pulsar high-energy emissions: The case of the Crab pulsar*, The Astrophysical Journal Letters, **688** (2008) (1): p. L25, URL http://stacks.iop.org/1538-4357/688/i=1/a=L25.

[86] WILLIAM OF OCCAM, *Quaestiones et decisiones in quattuor libros Sententiarum Petri Lombardi: Centilogium theologicum* (Johannes Trechsel1495).

[87] C. ROVELLI, *Notes for a brief history of quantum gravity*, Proceedings of the Ninth Marcel Grossman Meeting, **A** (2002): pp. 742–768, URL http://arxiv.org/abs/gr-qc/0006061.

[88] T. THIEMANN, *Introduction to modern canonical quantum general relativity*, Tech. rep., Max-Planck Inst. Gravitationsphysik Lab., Potsdam, 2001, URL http://arxiv.org/pdf/gr-qc/0110034.pdf.

[89] A. EINSTEIN, *Näherungsweise Integration der Feldgleichungen der Gravitation*, pp. 99–108 (Wiley-VCH Verlag GmbH & Co. KGaA2006), URL http://dx.doi.org/10.1002/3527608958.ch7.

[90] J. H. SCHWARZ, *From superstring to M-theory*, Physics Reports, **315** (1999): pp. 107–121, URL http://arxiv.org/abs/hep-th/9807135.

[91] D. S. BERMAN and M. J. PERRY, *Generalized geometry and M-theory*, Journal of High Energy Physics, **74** (2011) (6), doi:http://dx.doi.org/10.1007/JHEP06%282011%29074.

[92] A. ASHTEKAR, *New Hamiltonian formulation of general relativity*, Physical Review D, **36** (1987): p. 1587.

[93] C. ROVELLI, *Loop quantum gravity*, Living Reviews in Relativity, **11** (2008) (5), URL http://relativity.livingreviews.org/Articles/lrr-2008-5/.

[94] A. ASHTEKAR, J. ENGLE and C. VAN DEN BROECK, *Quantum horizons and black hole entropy: Inclusion of distortion and rotation*, Classical and Quantum Gravity, **22** (2005) (L27), URL http://arxiv.org/abs/gr-qc/0412003.

[95] L. SMOLIN, *Discreteness of area and volume in quantum gravity*, Nuclear Physics B, **442** (1995): pp. 593–622.

[96] L. J. GARAY, *Quantum gravity and minimum length*, International Journal of Modern Physics A, **10** (1994): pp. 145–166, URL http://arxiv.org/abs/gr-qc/9403008.

[97] A. ASHTEKAR and J. LEWANDOWSKI, *Quantum theory of geometry: I. Area operators*, Classical and Quantum Gravity, **14** (1997): pp. A55–A82, URL http://arxiv.org/abs/gr-qc/9602046.

[98] M. BOJOWALD, *Absence of singularity in loop quantum cosmology*, Physical Review Letters, **86** (2001): pp. 5227–5230, URL http://arxiv.org/abs/gr-qc/0102069.

[99] I. Agullo, A. Ashtekar and W. Nelson, *Quantum gravity extension of the inflationary scenario*, Physical Review Letters, **109** (2012): p. 251,301, doi:http://dx.doi.org/10.1103/PhysRevLett.109.251301.

[100] L. Smolin, *Newtonian gravity in loop quantum gravity*, 2010, URL http://arxiv.org/abs/1001.3668.

[101] A. Ashtekar, T. Pawlowski and P. Singh, *Quantum nature of the Big Bang*, Physical Review Letters, **96** (2006): p. 141,301, URL http://arxiv.org/abs/gr-qc/0602086.

[102] G. Amelino-Camelia, *Quantum-spacetime phenomenology*, Living Reviews in Relativity, **16** (2013) (5), URL http://relativity.livingreviews.org/Articles/lrr-2013-5/.

[103] R. Gambini and J. Pullin, *Nonstandard optics from quantum spacetime*, Physical Review D, **59** (1999).

[104] G. Amelino-Camelia, J. Ellis, N. Mavromatos, D. Nanopoulos and S. Sarkar, *Potential sensitivity of gamma ray buster to wave dispersion in vacuo*, Nature, **393** (1998): pp. 763–765.

[105] D. Mattingly, *Modern tests of Lorentz invariance*, Living Reviews in Relativity, **8** (2005) (5), URL http://www.livingreviews.org/lrr-2005-5.

[106] A. Kostelecký and C. Lane, *Constraints on Lorentz violation from clock-comparison experiments*, Physical Review D, **60** (1999): p. 116,010, URL http://link.aps.org/doi/10.1103/PhysRevD.60.116010.

[107] D. Bear, R. Stoner, R. Walsworth, V. A. Kostelećky and C. Lane, *Limit on Lorentz and CPT violation of the neutron using a two-species noble-gas maser*, Physical Review Letters, **85** (2000): pp. 5038–5041, URL http://link.aps.org/doi/10.1103/PhysRevLett.85.5038.

[108] R. Bluhm, A. Kostelecký and N. Russell, *CPT and Lorentz tests in penning traps*, Physical Review D, **57** (1998): p. 3932, URL http://arxiv.org/abs/hep-ph/9809543.

[109] P. Antonini, M. Okhapkin, E. Göklü and S. Schiller, *Test of constancy of speed of light with rotating cryogenic optical resonators*, Physical Review A, **71** (2005): p. 050,101, URL http://link.aps.org/doi/10.1103/PhysRevA.71.050101.

[110] C. D. Lane, *Probing Lorentz violation with Doppler-shift experiments*, Physical Review D, **72** (2005): p. 016,005, URL http://link.aps.org/doi/10.1103/PhysRevD.72.016005.

[111] R. Bluhm, K. V.A. and C. Lane, *CPT and Lorentz tests with muons*, Physical Review Letters, **84** (2000): p. 1098, URL http://link.aps.org/doi/10.1103/PhysRevA.71.050101.

[112] D. Anderson, M. Sher and I. Turan, *Lorentz and CPT violation in the Higgs sector*, Physical Review D, **70** (2004): p. 016,001, URL http://arXiv.org/abs/hep-ph/0403116.

[113] W. Coburn and S. Boggs, *Polarization of the prompt gamma-ray emission from the gamma-ray burst of 6 December 2002*, Nature, **423** (2003): pp. 415–417, URL http://arxiv.org/abs/astro-ph/0305377.

[114] P. Laurent, D. Götz, P. Binétruy, S. Covino and A. Fernandez-Soto, *Constraints on Lorentz invariance violation using INTEGRAL/IBIS observations of GRB041219A*, Physical Review D Rev. D, **83** (2011): p. 121,301, doi:http://dx.doi.org/10.1103/PhysRevD.83.121301.

[115] G. Gubitosi and F. Paci, *Constraints on cosmological birefringence energy dependence from CMB polarization data*, Journal of Cosmology and Astroparticle Physics, **2013** (2013) (2): p. 20, URL http://stacks.iop.org/1475-7516/2013/i=02/a=020.

[116] S. Choubey and S. King, *Gamma-ray bursts as probes of neutrino mass, quantum gravity and dark energy*, Physical Review D, **67** (2003): p. 073,005.

[117] G. Hinshaw et al., *Nine-year Wilkinson microwave anisotropy probe (WMAP) observations: Cosmological parameter results*, Astrophysical Journal Supplement Series, **208** (2013) (19), URL http://arxiv.org/abs/1212.5226.

[118] J. Aleksić and others (The MAGIC Collaboration), *Black hole lightning due to particle acceleration at subhorizon scales*, Science, **346** (2014) (6213): pp. 1080–1084, URL http://www.sciencemag.org/content/346/6213/1080.abstract.

[119] F. Aharonian and others (The H.E.S.S. Collaboration), *An exceptional very high energy gamma-ray flare of PKS 2155-304*, The Astrophysical Journal Letters, **664** (2007) (2): p. L71, URL http://stacks.iop.org/1538-4357/664/i=2/a=L71.

[120] A. Abramowski and others (The H.E.S.S. Collaboration), *Search for Lorentz invariance breaking with a likelihood fit of the PKS 2155-304 flare data taken on MJD 53944*, Astroparticle Physics, **34** (2011) (9): pp. 738 – 747, URL http://dx.doi.org/10.1016/j.astropartphys.2011.01.007.

[121] J. D. Scargle, J. P. Norris and J. T. Bonnell, *An algorithm for detecting quantum gravity photon dispersion in gamma-ray bursts: DisCan*, The Astrophysical Journal, **673** (2008) (2): p. 972, URL `http://stacks.iop.org/0004-637X/673/i=2/a=972`.

[122] A. Abdo and others (The Fermi-LAT Collaboration), *A limit on the variation of the speed of light arising from quantum gravity effects*, Nature, **462** (2009): pp. 331–334.

[123] V. V. et. al., *Constraints on lorentz invariance violation from Fermi-Large area telescope observations of gamma-ray bursts*, Physical Review D, **87** (2013): p. 122,001.

[124] P. Kaaret, *Pulsar radiation and quantum gravity*, Astronomy & Astrophysics, **345** (1999): pp. L32–34.

[125] A. McCann and for the VERITAS Collaboration, *Observations of the Crab pulsar with VERITAS*, in *4th Fermi Symposium in Monterey, CA* (2012).

[126] M. Martínez and M. Errando, *A new approach to study energy-dependent arrival delays on photons from astrophysical sources*, Astroparticle Physics, **31** (2009): pp. 226–232.

[127] K. Olive and Particle Data Group, *Review of Particle Physics*, Chinese Physics C, **38** (2014) (9): p. 090,001, doi:http://dx.doi.org/10.1088/1674-1137/38/9/090001.

[128] J. Albert and others (The MAGIC Collaboration), *Probing quantum gravity using photons from a flare of the active galactic nucleus Markarian 501 observed by the MAGIC telescope*, Physics Letters B, **668** (2008): pp. 253–257.

[129] J. Albert and others (The MAGIC Collaboration), *Variable very high energy gamma-ray emission from Markarian 501*, The Astrophysical Journal, **669** (2007) (2): p. 862, URL `http://dx.doi.org/10.1086/521382`.

[130] U. L. de Almeida and M. Daniel, *A simple method to test for energy-dependent dispersion in high energy lightcurves of astrophysical sources*, Astroparticle Physics, **35** (2012) (12): pp. 850—860, doi:http://dx.doi.org/10.1016/j.astropartphys.2012.03.011.